Measurement of the Isolated Direct Photon Cross Section with Conversions in $p\bar{p}$ Collisions at $\sqrt{s} = 1.8$ TeV

A thesis presented
by

Carter Randolph Hall

to
The Department of Physics
in partial fulfillment of the requirements
for the degree of
Doctor of Philosophy
in the subject of

Physics

Harvard University
Cambridge, Massachusetts
May 2002

Thesis advisor
Melissa Franklin

Author
Carter Randolph Hall

Measurement of the Isolated Direct Photon Cross Section with Conversions in $p\bar{p}$ Collisions at $\sqrt{s} = 1.8$ TeV

Abstract

We present a measurement of the isolated direct photon cross section in $p\bar{p}$ collisions at $\sqrt{s} = 1.8$ TeV using data collected between 1994 and 1995 by the Collider Detector at Fermilab (CDF). The measurement is based on events where the photon converts into an electron-positron pair in the material of the inner detector, resulting in a two track event signature. To remove $\pi^0 \rightarrow \gamma\gamma$ and $\eta \rightarrow \gamma\gamma$ events from the data we have developed a novel background subtraction technique based in electron E/p. We find that the shape of the cross section as a function of photon p_T is poorly described by next-to-leading-order QCD predictions, but agrees well with previous CDF measurements. This is strong evidence that improvements in the calculation are needed to explain the data.

Contents

List of Figures

List of Tables

Acknowledgments

My greatest debt is to my advisor, Prof. Melissa Franklin, who got me admitted to Harvard and kicked me out the door six years later. This thesis would not have been possible without her guidance. Her boundless enthusiasm for physics is an inspiration, and her uncanny ability for asking the right question at the right time corrected my trajectory on more occasions than I can remember. Fortunately, she is not shy about reminding me.

I would also like to thank the other members of the Harvard CDF group, who collectively raise the coolness level of Fermilab by a factor of two. The first mention goes to Robyn Madrak and Kevin Burkett, with whom I've worked the longest, and who showed me how much fun drift chambers can be. I am still learning how to do physics from their example. (By the way, Robyn alone is responsible for 75% of the group's coolness.) I've also learned a tremendous amount from our other postdocs - Petar Maksimović, Tommaso Dorigo, João Guimarães da Costa, Werner Riegler, Lester Miller, and Abraham Gallas. I'm sure I've forgotten several of João's names, and for that I apologize. I should also acknowledge my Iberian colleagues for their fashion sense. (I'm a slow student, but I'm trying.) I'd like to thank Fotios Ptohos, Maria Spiropulu, and Andrew Gordon for making me feel welcome when I joined the group five years ago. Ayana Holloway and Abraham deserve special mention for their indulgence of my weakness for polish sausages, while Stephen Bailey is largely to blame for the next 200 pages, since he once asked me "Isn't there any way you can get a thesis out of these conversions?". Thanks to Sal Rappoccio, who had to listen while Melissa and I debated the merits of the isolation cut for a month, and still managed to write an entire monograph about the last 50 years of particle physics on the white board. The faculty members of the group - John Huth, Micheal Schmitt, and Andy Foland - also deserve thanks for their knowledge, guidance, and intuition. Andy in particular was a tremendous help both for his ideas and for agreeing to serve on my committee at the last minute. Thanks to my other committee member, Prof. John Doyle, for his help improving the thesis, and to George Brandenburg, Sanjib Mishra, Hitoshi Yamamoto, and Gary Feldman for creating a rich intellectual environment at HEPL.

Needless to say, this thesis was made possible by the efforts of the CDF collaboration and the Fermilab staff, who proposed, designed, built, and operated the experiment, beginning when I was three years old. In particular I'd like to thank several people whose results are used directly in this thesis: Karen Byrum, Wendy Taylor, Steve Kuhlmann, Dana Partos, Barry Wicklund, William Trischuk, and Andreas Warburton. If not for their work this analysis would not have been feasible. I'd also like to single out Steve and Bob Blair for advising me at length on the photon cross section. I couldn't have picked a more supportive analysis group on CDF. I also managed to stumble into a wonderful upgrade project, the COT, where I worked with Bob Wagner and Aseet Mukherjee, the two physicists I respect the most on CDF. Avi Yagil, Bill Ashmanskas, and Larry Nodulman also devoted considerable time to helping me with the electron data.

Thanks to my revolving cast of housemates in West Chicago for making it possible

for me to live within two blocks of the taqueria. In addition to Stephen and Lester, I'd like to thank Mike Kirby for introducing me to the subtle pleasures of major league baseball. Unbelievably, I now enjoy watching White Sox games in text form on the web. Peter Tamburello also played a large role here. Also thanks to Shin-Shan (Eiko) Yu for taking me to dim sum in Chinatown, and to the Drug Sniffing Dogs for reassuring me that even the Ramones need a horn section.

Thanks to the HEPL staff - Guy Sciacca, John Oliver, Jack O'Kane, Sarah Harder, Dan Henessey, and Robyn Simpson for their tolerance of bright eyed graduate students. Thanks in particular to Rick Haggerty and Steve Sansone for teaching me how experiments are built, and for inviting me to the Friday afternoon 'staff meetings'.

From Virginia Tech I'd like to thank David Jenkins, Brian Dennison, and John Simonetti for giving me a taste of what science research is like. Thanks to Luke Mo for arranging for me to spend a summer at Fermilab. I should also mention my friend Abe Falcone, who loves physics and life more than anyone I know. I hope that Abe and I can work on an experiment together one day. Among my friends at Harvard I'd like to single out Natasha Lepore, Alexandra Vega, Zac Dutton, Todd and Nancy Squires, and Lester Chen, who didn't forget me when I moved to the Chicago suburbs for three years.

Finally my thanks to Mom, Dad, Andy, and Emily who have given me so much support these last six years. They also gave me a car and an incisor, without which I would not be able to smile at commencement. I love you all.

Chapter 1

Introduction

The subject of this thesis is a measurement of the isolated direct photon cross section at the Fermilab Tevatron collider. The photon cross section is a classic test of perturbative quantum chromodynamics (QCD), and has the potential to provide valuable information on the non-perturbative structure of the proton. We begin this chapter with an introduction to the photon cross section, and conclude with an overview of the remainder of the thesis.

1.1 Introduction to the photon cross section

A schematic diagram of a proton - anti-proton ($p\bar{p}$) collision is shown in Figure 1.1. The particles approach each other horizontally and interact at the center of the Figure. At the Fermilab Tevatron the center-of-mass energy of the $p\bar{p}$ system is 1.8 TeV.

There are many possible results of the interaction. For example, the proton and anti-proton may deflect from their straight trajectories without creating any new particles. This type of reaction is known as elastic scattering. In this thesis we will be interested in inelastic events where the collision produces a large number of new, and sometimes unstable, particles. In a small fraction of inelastic events a high energy photon will be produced with a large momentum transverse to the axis of the two beams. This is the situation illustrated in Figure 1.1. It is the goal of this thesis to measure the cross section for this to occur as a function of the transverse momentum of the photon.

Our reasons for studying $p\bar{p}$ collisions fall into two large categories. In 'particle measurements' we attempt to understand the properties, behavior, and interactions of the particles produced in the collision. For example, we may be trying to understand the weak force by studying the W and Z bosons which transmit it. In these measurements the $p\bar{p}$ collision is simply a convenient manner for producing the particle of interest. In 'production measurements' we are not interested in the produced

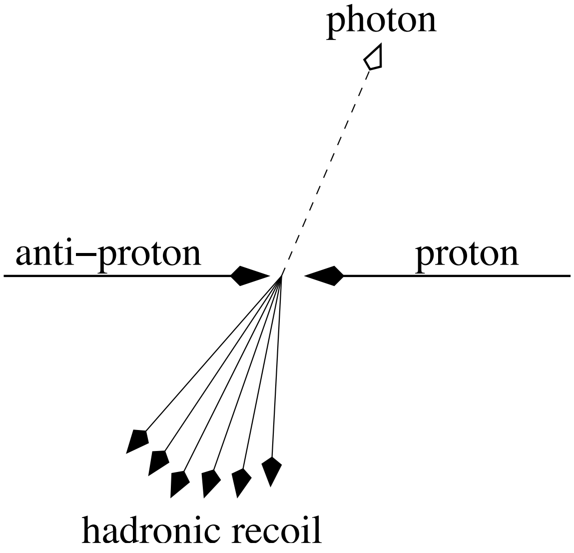

Figure 1.1: Diagram of a proton - anti-proton collision. The particles approach each other along the horizontal and interact at the center of the Figure. In the collision shown here a photon is produced transverse to the beamline. A number of other particles are also produced in the opposite direction, as required by momentum conservation in the transverse plane.

particle itself as much as we are interested in the mechanism by which it was created. Here we are trying to understand the dynamics of the collision itself. These dynamics are governed by QCD, and production experiments are necessarily tests of QCD. Moreover, since QCD is by now a well established theory, modern production experiments primarily test of our ability to calculate with the theory. The photon cross section measurement is a production experiment.

The proton is a composite particle made up of quarks, anti-quarks, and gluons, known collectively as partons. Strictly speaking it is the interactions of the partons which is predicted by QCD. In a high energy $p\bar{p}$ collision the partons in the proton can be considered to be free particles, and the result of the collision can be predicted by assuming that the interaction takes place between a single parton from the proton and a single parton from the anti-proton. In general the reacting partons do not carry the entire momentum of the $p\bar{p}$ system, so in a given collision the center-of-mass energy of the hard scattering is often much smaller than the sum of the beam energies. Since the observed reaction cross sections depend both on the center-of-mass energy of the collision, and on the species of partons involved, in order to predict the results of the collision we must know the probability of finding each parton species inside the proton and its momentum distribution. The momentum distributions of the various partons inside the proton are known as the parton distribution functions (PDFs). An example of a proposed PDF for the gluon is shown in Figure 1.2.

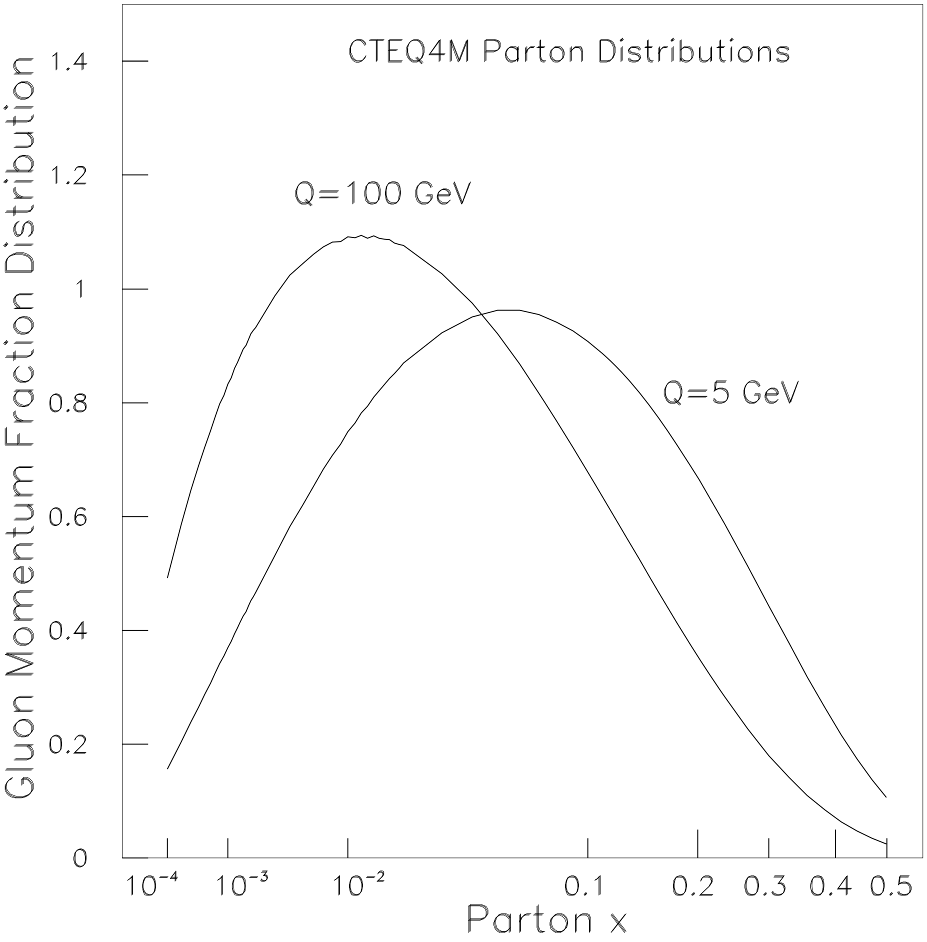

Figure 1.2: An example of the gluon distribution of the proton, proposed by the CTEQ collaboration [1]. The variable on the x-axis is parton x, which is the fraction of the proton's momentum which is carried by the gluon. The two curves correspond to two different energy scales at which the PDF may be evaluated.

The form of the PDFs should be predicted by QCD itself since they are the result of the strong dynamics which bind the partons into the proton. However, the strong force is non-perturbative at low energies, so only lattice QCD calculations are feasible. In lieu of this, we attempt to extract the PDFs in an empirical manner from the observed cross sections themselves. This sounds like a circular procedure, since we hope to use the PDFs to predict the cross sections, but the agreement of a wide variety of measurements on the same PDFs confirms that they are fundamental. Furthermore, the exact form of the PDFs depend on the energy scale of the collisions involved, and this dependence is correctly predicted by perturbative QCD. This serves as a check on the soundness of the formalism.

Photon production is a unique process in that it depends on the gluon PDF at the lowest order in perturbation theory. The gluon distribution is poorly known, so we hope to utilize the photon cross section to constrain it. Unfortunately this program has been difficult to realize. Photon experiments have found that the observed cross section is not in good agreement with next-to-leading order QCD calculations, even allowing for the uncertainty in the gluon PDF. Therefore the nature of the gluon inside the proton remains an open question for the time being. The final result of this thesis continues this trend, with the measured cross section being larger than most predictions.

1.2 Overview of the thesis

The thesis is organized in the following manner.

- Chapter 2: Review of theory and formalism of direct photons.
- Chapter 3: Description of the accelerator and CDF detector.
- Chapter 4: Definition of event variables and the cuts used to isolate the final data samples.
- Chapter 5: Description of the Monte Carlo simulation.
- Chapter 6: Results of the background subtraction used to remove meson decays from the data sample.
- Chapter 7: Calculation of the acceptance and efficiency to retain signal events after all cuts are applied.
- Chapter 8: Evaluation of the total conversion probability.
- Chapter 9: Evaluation of the systematic errors.
- Chapter 10: Cross section measurement and comparison with theory.
- Chapter 11: Conclusions

Chapter 2

Direct photon theory

In this chapter we begin with a brief review of the methods used to calculate observables in QCD. We then describe the physics of direct photons at hadron machines, and specifically at hadron colliders.

2.1 QCD scattering formalism

With quantum chromodynamics it is possible to calculate the cross sections for processes which involve hadronic particles in the initial or final state. If the process is written as

$$A(p_A) + B(p_B) \to C(p_C) + X \tag{2.1}$$

where A, B, and C are initial and final state particles, p_A, p_B, and p_C, are their momenta, and X represents all unobserved particles, then according to the parton model the cross section may be written as

$$\begin{aligned} & E_C \frac{d\sigma}{d^3 p_C} = \\ & \sum_{abcd} \int dx_a \, dx_b \, dz_c \, f_{a/A}(x_a, \mu_f^2) f_{b/B}(x_b, \mu_f^2) D_{C/c}(z_C, \mu_F^2) \frac{\hat{s}}{z_c^2 \pi} \frac{d\sigma}{d\hat{t}}(ab \to cd) \\ & \times \delta(\hat{s} + \hat{t} + \hat{u}) \end{aligned} \tag{2.2}$$

In this expression, a,b,c,and d are the partons which participate in the hard scattering process and $\hat{s}$, $\hat{t}$, and $\hat{u}$ are the Mandelstam variables defined by $\hat{s} = (p_a + p_b)^2$, $\hat{t} = (p_a - p_c)^2$, and $\hat{u} = (p_b - p_c)^2$. The delta function is the appropriate phase space expression for two-body scattering and ensures energy conservation.

$f_{a/A}(x_a, \mu_f^2)$ is the parton distribution function (PDF) which gives the probability of finding parton a within hadron A with momentum fraction x_a. The PDF is evaluated at the factorization scale μ_f^2. The dependence of the PDFs on this scale is an artifact of the procedure for handling certain mass singularities in the calculation. For example, consider an initial state quark line which radiates a gluon. If the gluon becomes collinear with the quark, then the internal quark line will be on-shell and there will be a correction proportional to $\ln s/m_{quark}^2$. However, in QCD the quarks are considered to be massless, so this term invalidates the calculation. The factorization theorem holds that these singularities are universal in that they are the same for all processes, and can be absorbed into the PDFs. The PDFs are not calculable in QCD, so they must be determined empirically from experiment. However, their dependence on the factorization scale is governed by the DGLAP[2] evolution equations, so PDFs measured at one scale can be used to predict the results of experiments at other scales.

$D_{C/c}(z_C, \mu_F^2)$ is the fragmentation function which gives the probability that parton c will produces final state particle C with momentum fraction z_C during the fragmentation process. μ_F^2 is the fragmentation scale analogous to the factorization scale μ_f^2. Like the PDFs, fragmentation functions are not calculable but their scale dependence is. If the final state observable C is directly associable with the hard scattered parton, as in the case of jet production, then no fragmentation function is necessary to compare theory and experiment. Final state photons can also be produced in the hard scatter, and this process requires no fragmentation function. However, photons are also produced during the fragmentation of quarks and gluons, and the inclusive photon cross section depends on $D_{\gamma/q}$ and $D_{\gamma/g}$.

The partonic cross section $d\sigma/d\hat{t}(ab \to cd)$ is a function of the Mandelstam variables and must be calculated to a given order in perturbation theory by including all the appropriate Feynman diagrams. For example, the process $q\bar{q} \to q'\bar{q}'$ has one leading order Feynman diagram, and its cross section is

$$\frac{d\sigma}{dt}(q\bar{q} \to q'\bar{q}') = \frac{\pi\alpha_s^2}{\hat{s}^2}\frac{4}{9}\frac{\hat{t}^2+\hat{u}^2}{\hat{s}^2} \tag{2.3}$$

In this expression α_s is the strong coupling constant. The effect of higher order diagrams may be included by introducing a running coupling constant $\alpha_s(Q^2)$. The dependence of the running coupling constant on Q^2 is specified by the renormalization group equation:

$$Q^2\frac{d\alpha_s(Q^2)}{dQ^2} = \beta(\alpha_s(Q^2)) \tag{2.4}$$

The function β must be calculated at each order in perturbation theory. To two loop order β is given by[3]

$$\beta(\alpha_s(Q^2)) = -b_0\alpha_s(Q^2) - b_1\alpha_s^3(Q^2) \tag{2.5}$$

and the first two perturbative constants are

$$b_0 = \frac{33 - 2N_f}{12\pi}, b_1 = \frac{153 - 19N_f}{24\pi^2} \tag{2.6}$$

where N_f is the number of quark flavors with $m_q^2 < Q^2$. At leading order (that is, $b_1 = 0$), the renormalization group equation is solved by

$$\alpha_s(Q^2) = \frac{1}{b_0 \ln(Q^2/\Lambda^2_{QCD})} \tag{2.7}$$

Here Λ_{QCD} sets the scale of the QCD interaction, and is typically chosen to be approximately $200\,MeV$. In this leading order expression a change in Q^2 of order one (for example, $Q^2 \to 4Q^2$) results in a change of α_s of order α_s^2. For this reason, leading order QCD calculations are highly unstable and are not useful for quantitative comparisons with experiment. Fortunately, next-to-leading order (NLO) calculations are available for almost all processes of interest, and some next-to-next-to-leading order calculations have now been performed.

We see that a typical QCD calculation involves up to three arbitrary scales: the factorization scale, the fragmentation scale, and the renormalization scale. If a given calculation were carried out to all orders in perturbation theory, then the final result would not have any dependence on these scales. By truncating the perturbation series at a fixed order we are left with predictions which exhibit a residual dependence on the scales. This variation is a measure of the size of the uncalculated terms in the expansion. Of course, the best method of estimating the error on the result is to calculate the next term in the series and confirm that it is small.

There is no compelling reason why all three scales must be exactly the same. However, the scales should not be chosen to be very different from each other because this would introduce an unphysical hierarchy into the problem. A common choice is to set all three scales equal to the p_T of one of the final state objects (particle or jet) which is observed by the experiment. Another procedure is to choose each scale such that the cross section has no first-order dependence on the scale: $d\sigma/d\mu^2(\mu_0^2) \equiv 0$. This procedure, known as optimization[4], assumes that if the known terms in the perturbative expansion do not depend on μ^2 to first order, then the unknown terms will have a very small dependence. Some cross sections have no such extrema, or the extrema occur for unphysical values of μ^2, and in the optimization scheme these calculations are considered unreliable.

2.2 Direct photon physics

Photons offer some unique advantages over jets for the study of QCD physics at hadron machines. First, the number of initial and final states for photon production is relatively small. The four tree-level diagrams for the direct production of photons at hadron colliders are shown in Figures 2.1 and 2.2. Two of the diagrams are the QCD

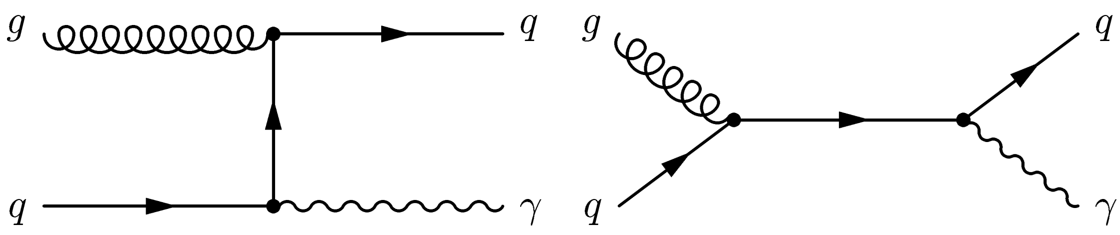

Figure 2.1: Compton diagrams.

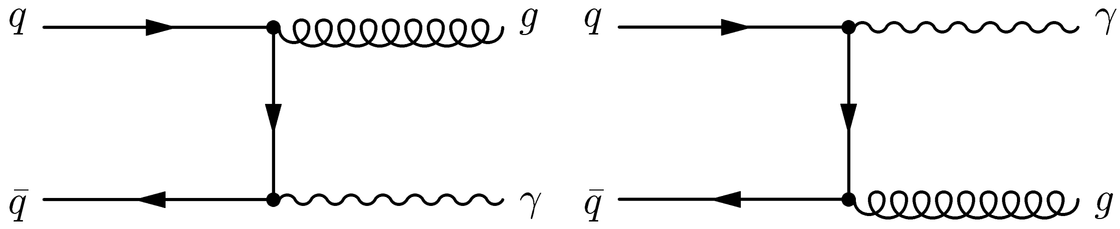

Figure 2.2: Annihilation diagrams.

analog of Compton scattering in QED, and the other two are due to $q\bar{q}$ annihilation. This is in contrast to jet production, where all possible 2 → 2 processes contribute to the cross section. Secondly, the presence of the electromagnetic vertex in the photon diagrams makes the perturbative calculation more reliable, since this coupling is smaller than the strong coupling constant α_s.

Photons also offer some experimental advantages. Since photons do not hadronize, they represent a direct probe of the hard scattering without ambiguities due to jet definitions. Furthermore, photon energies can be measured with electromagnetic rather than hadronic calorimeters, resulting in greatly improved energy resolution.

In addition to being directly produced in the hard scattering, photons may also be produced during the fragmentation of a final state parton as shown in Figure 2.3. These processes are described as 2 → 2 hard scattering convoluted with the fragmentation functions $D_{\gamma/q}$ and $D_{\gamma/g}$. Since fragmentation functions are non-perturbative, their appearance partially spoils the theoretical simplicity of direct photon physics.

The fragmentation functions are determined in the following way. Diagrams with

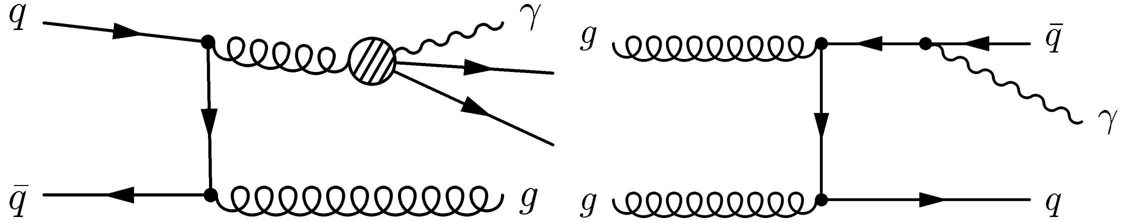

Figure 2.3: Bremsstrahlung diagrams.

prompt photon radiation from a quark line (such as the diagram on the right in Figure 2.3) are calculated perturbatively. This process is experimentally constrained by $e^+e^- \to qq\gamma$ studies at LEP and other electron machines[18]. Secondly, photons produced during the soft QCD of hadronization (shown schematically on the left in Figure 2.3) are modeled with the vector meson dominance (VMD) ansatz[19]. VMD states that in certain circumstances photons can be considered to be a linear combination of vector mesons such as the $\rho(770)$, $\omega(782)$, and $\phi(1020)$. Therefore $D_{\gamma/q}$ is determined from $D_{\rho/q}$, $D_{\omega/q}$, and $D_{\phi/q}$ which are measured at e^+e^- machines[20]. The dependence of the fragmentation functions on the fragmentation scale is then given by NLO evolution equations. Finally, high z fragmentation photons have been observed inside jets by ALEPH[21] providing a direct check of the formalism.

The experimental study of photons is also complicated by the prompt two photon decay of light mesons such as the π^0 and η. These particles interact strongly, so they are produced in great numbers at hadron machines. All photon experiments must have highly effective methods to eliminate these decays from their datasets.

The primary motivation for most photon measurements is their potential to constrain the gluon distribution of the proton ($g(x)$). This is due to the gluon's appearance in the initial state of the tree level compton diagrams. The compton diagrams dominate the photon cross section at low-to-moderate p_T, as shown in Figure 2.4, so photon production is a strong candidate process to reveal $g(x)$.

Deep inelastic scattering (DIS) and Drell-Yan experiments can also constrain the gluon, but since lepton probes do not couple directly to color charge these measurements rely on higher order effects. Nevertheless, data from ZEUS, H1, and other DIS experiments have placed significant constraints on $g(x)$ at small x where gluons are numerous. Above $x = 0.1$, however, there is little information from DIS, and variations of up to 50% are consistent with the data. This is illustrated in a study by the CTEQ collaboration [29] shown in Figure 2.5.

Serious attempts to extract $g(x)$ from photon data became possible in the mid 1980's when the NLO QCD calculation was completed[22]. Since that time, a large variety of experiments have measured the photon cross section at both fixed target and collider energies. A list of relevant experiments is given in Table 2.1, and a compilation of their data (taken from reference [17]) is shown in Figure 2.6. Fixed target experiments offer the greatest potential for constraining the gluon at high x due to their large interaction rate, and about half a dozen experiments have published data which is sensitive at $x > 0.1$.

Unfortunately, these data have yet not resolved the question of the gluon distribution. This is because not all the data are in good agreement with the NLO QCD prediction, and no reasonable variation of $g(x)$ is sufficient to bring them into agreement. Generally, the measured cross sections lie above the theoretical predictions. This is particularly true in the case of the E706 data, where excesses of up to a factor of five are observed.

The fact that some experiments observe an excess cross section has led to spec-

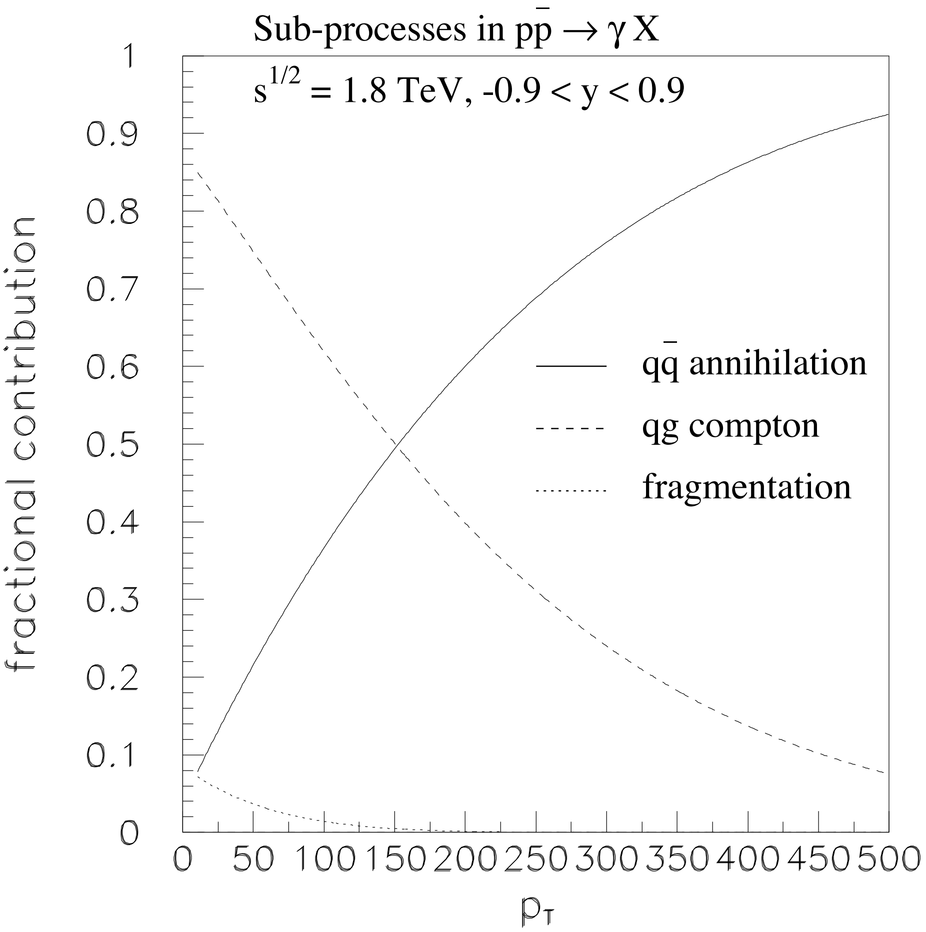

Figure 2.4: The relative contributions of the three photon processes as a function of p_T, for $p\bar{p}$ collisions at $\sqrt{s} = 1.8$ TeV. The bremsstrahlung process, labelled fragmentation here, is suppressed by an isolation cut, as discussed in section 2.3. These curves are approximate.

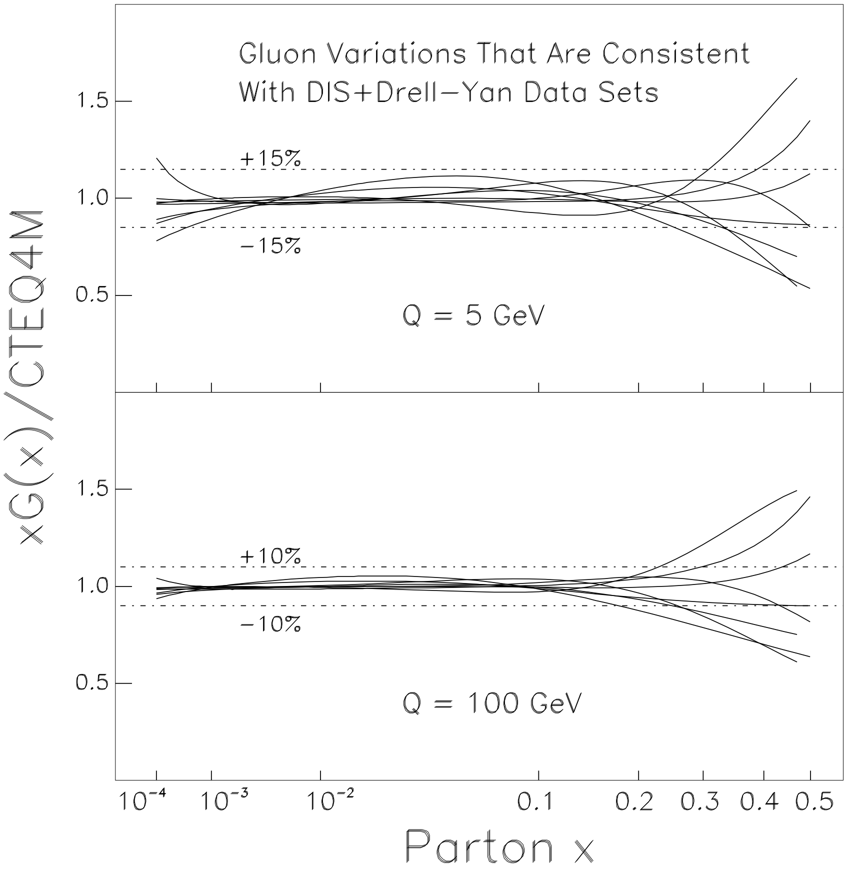

Figure 2.5: A study of the uncertainty of the gluon distribution of the proton, by the CTEQ collaboration [29].

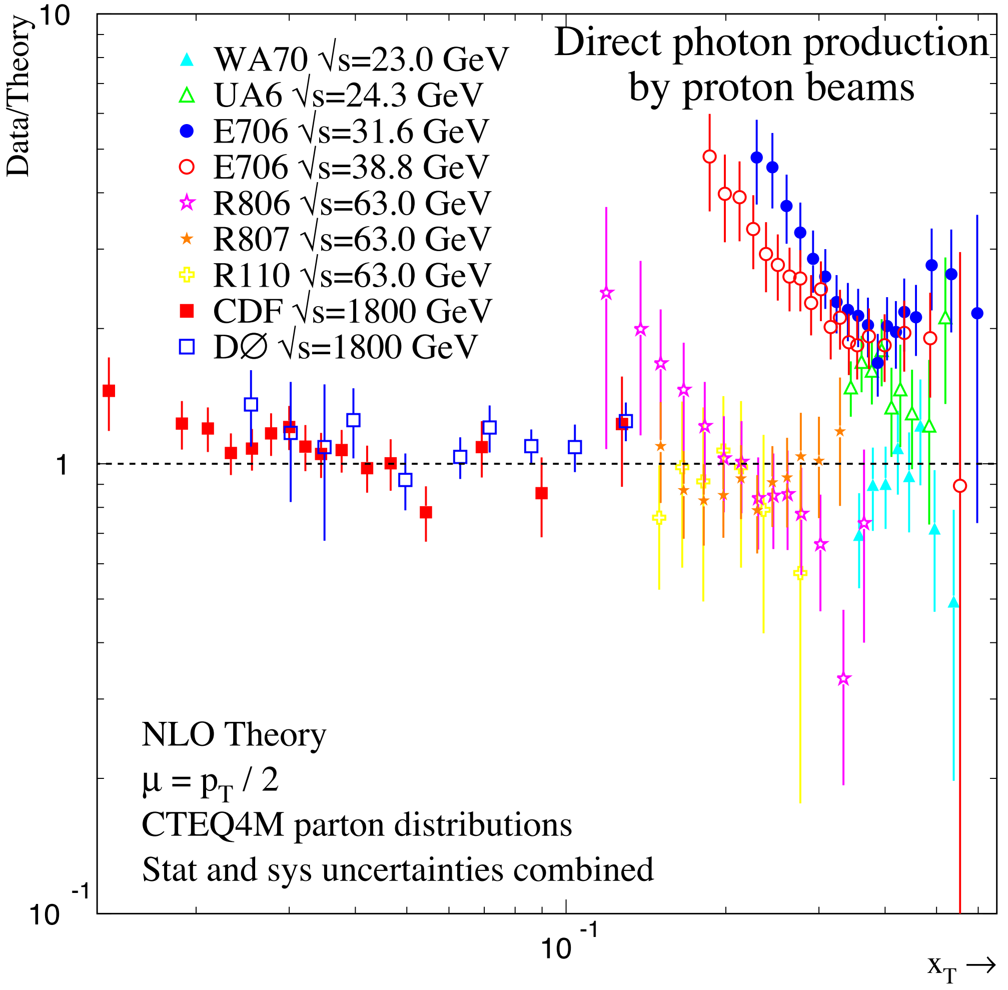

Figure 2.6: A compilation of photon data from many experiments compared to NLO QCD predictions. To compare measurements at different values of $\sqrt{s}$, the data is plotted as a function of $x_T = 2p_T/\sqrt{s}$. This variable is approximately equal to the gluon momentum fraction of the proton to which the data is sensitive. The CDF and D0 data shown here are from Run Ia (1992-93). This plot is taken from reference [17].

Experiment	Accelerator	initial state	$\sqrt{s}$	year	ref
R806	ISR	pp	63 GeV	1982	[5]
WA70	SPS	pp	23 GeV	1988	[6]
UA1	$Sp\bar{p}S$	$p\bar{p}$	630 GeV	1988	[7]
R110	ISR	pp	63 GeV	1989	[8]
R807	ISR	pp	63 GeV	1990	[9]
UA2	$Sp\bar{p}S$	$p\bar{p}$	630 GeV	1991	[10]
UA6	$Sp\bar{p}S$	pp	24.3 GeV	1998	[11]
UA6	$Sp\bar{p}S$	$p\bar{p}$	24.3 GeV	1998	[11]
E706	Tevatron fixed target	pBe	31.6 GeV	1998	[12]
E706	Tevatron fixed target	pBe	38.8 GeV	1998	[12]
D0	Tevatron collider	$p\bar{p}$	1800 GeV	2000	[13]
D0	Tevatron collider	$p\bar{p}$	630 GeV	2001	[14]
CDF	Tevatron collider	$p\bar{p}$	1800 GeV	2001	[15]
CDF	Tevatron collider	$p\bar{p}$	630 GeV	2001	[15]

Table 2.1: Direct photon experiments.

ulation that the initial state partons may possess a small amount of transverse momentum (k_T) before scattering[23], [12]. If this is the case, the smearing of the initial state center-of-mass energy would increase the cross section because of its steep slope as a function of p_T.

The colliding partons may possess some 'intrinsic k_T' due to the fact that they are bound within a nucleon of finite size. However, this effect is believed to be too small to explain the observed enhancement. Another possibility is that the initial state partons radiate soft gluons before scattering. In this case the recoil of the system would give rise to an effective k_T which is not properly accounted for by conventional NLO QCD calculations. Some theorists have estimated that this effect could account for the observed discrepancies[24]. However, a complete and rigorous treatment requires a full re-calculation of the NLO matrix elements.

It should be noted that the k_T hypothesis remains somewhat controversial. The authors of reference [25] take the following approach. They argue through optimization that the NLO QCD calculation is not reliable for all the data points measured by the experiments. They disregard these data, and find that among the remaining data only the E706 experiment is anomalous. They also argue that E706 is inconsistent with other experiments, and conclude that no serious discrepancy exists between data and theory.

2.3 Photon calculations for hadron colliders

Photon experiments at the Fermilab Tevatron collider ($p\bar{p}$ at $\sqrt{s} = 1.8\,TeV$) face difficulties not found in fixed target experiments.[1] For example, fixed target experiments generally measure the cross section for photon p_T less than 10 GeV. At these energies, the background $\pi^0 \to \gamma\gamma$ and $\eta \to \gamma\gamma$ decays produce two photons which can be resolved by the calorimeter. Collider experiments must contend with meson decays at energies from 10 to 100 GeV where the two showers overlap in the calorimeter and cannot be rejected on an event-by-event basis. Consequently collider measurements must perform a statistical background subtraction in order to measure the cross section.

In addition, the presence of hadronic jets at collider energies complicates the observation of the 'bremsstrahlung' process, where a photon is produced during the fragmentation of a quark or gluon. These photons are usually found inside a jet where they are difficult to identify. Furthermore, the trigger rate for this process would overwhelm typical data acquisition systems due to spurious triggers caused by π^0's and η's. Therefore collider experiments do not attempt to measure the fully inclusive photon cross section. Instead they measure the 'isolated' part of the cross section, where the photon is found far away from other hadronic activity in the event.[2]

This experimental reality necessitated a great deal of theoretical work to implement an isolation cut on the calculation, and a simple and consistent NLO treatment became available in the mid 1990s[26], [27]. The isolated cross section is calculated from the fully inclusive cross section by introducing a subtraction term as follows:

$$d\sigma_{dir}^{iso} = d\sigma_{dir} - d\sigma_{dir}^{sub}(\delta, \epsilon) \tag{2.8}$$

In this expression δ is the isolation cone radius surrounding the photon, and ϵ is the ratio of hadronic energy to the photon energy which is allowed inside the cone. At leading order one may introduce the isolation cut simply by changing the lower limit of the integral over Z_C in equation 2.2. At next-to-leading order (2 → 3 processes) one must consider the possibility that the third parton in the final state may contribute energy to the isolation cone. In this case an approximate but accurate expression for the dependence of $d\sigma_{dir}^{sub}$ on δ and ϵ is [27]

$$d\sigma_{dir}^{sub}(\delta, \epsilon) = A \ln\delta + B + C\delta^2 \ln\epsilon \tag{2.9}$$

where A, B, and C are functions of the kinematic variables.

---

[1] Needless to say, fixed target experiments also involve unique experimental challenges.

[2] Fixed target experiments also apply some minimal isolation cuts, such as requiring that no tracks point at the photon candidate in the calorimeter. These cuts are generally less restrictive than the isolation cuts applied by collider experiments, and the fixed target cross sections are corrected for their inefficiency.

Despite the theoretical difficulties introduced by the isolation cut, it has the fortunate side effect of reducing the contribution of the poorly-understood bremsstrahlung diagrams to the cross section. At the Tevatron collider the bremsstrahlung diagrams are expected to contribute about 20% of the isolated cross section at 15 GeV, whereas they are responsible for up to 50% of the fully inclusive cross section[28].

2.4 Photon measurements at the Tevatron collider

In recent years the D0 and CDF collaborations have performed measurements of the isolated photon cross section at both $\sqrt{s} = 1800$ GeV and 630 GeV . Two techniques are employed to subtract the π^0 and η decays from the data. The longitudinal segmentation of the D0 calorimeter can be used to determine at what depth the photon candidate initially converted into an electron-positron pair. Since a two-photon shower will begin earlier, on average, than a single photon shower, this information can be used to measure the signal to background ratio of a given photon sample. The CDF electromagnetic calorimeter is not longitudinally segmented, but it does have a pre-shower detector located between the solenoid and the calorimeter which can be utilized in a similar fashion. Furthermore, the CDF calorimeter has a layer of strip and wires chambers embedded at a depth of six radiation lengths which provide a measurement of the transverse size of the shower at shower maximum. At low p_T, a π^0 or η shower will appear to be broader than a single photon, and this information can be used to subtract the mesons from the photon sample below 35 GeV. The CDF and D0 cross section measurements are in agreement with each other, but both see an excess of events at low p_T compared to NLO QCD.

In this thesis we report on a new measurement of the isolated photon cross section in $p\bar{p}$ collisions at $\sqrt{s} = 1.8$ TeV using data collected with the CDF experiment. The new measurement uses events where the photon converts in the detector material before the central tracking chamber. The resulting electron and positron are reconstructed by the tracking chamber as well as the calorimeter. These type of events are explicitly rejected by conventional photon analyses, and therefore they represent a statistically independent data sample. In addition, the redundant tracking and calorimeter measurements make possible a novel background subtraction technique. Specifically, in a single photon event the p_T measured by the tracking chamber will be consistent with the E_T measured by the calorimeter. In a meson decay, however, the second unconverted photon deposits extra energy in the calorimeter not seen by the tracking chamber. This 'E/p' background subtraction relies on our understanding of π^0 and η decay kinematics, and is largely independent from the shower shape variables used by previous measurements. Therefore the new measurement provides a good test of the standard background subtraction techniques.

The conversion measurement suffers from small statistics - the inner detector was designed to be light, so only about 5% of all photons convert before the tracking chamber. However, the photon cross section is very large at low p_T, so we are not statistically limited in this region. Furthermore, much of the physics interest in the cross section is focussed on the low p_T region due to the previously observed anomaly, so a new measurement which is sensitive only in this region is quite useful.

In terms of the gluon distribution of the proton, collider experiments have less sensitivity than fixed target experiments in the high x region. The x region probed is given roughly by $2p_T/\sqrt{s}$, so measurements at the Tevatron collider are sensitive to x between 10^{-2} and 10^{-1}. In this region there are already significant constraints on the gluon from DIS experiments. Nevertheless, collider measurements are still useful since they provide independent information. Moreover, since many photon measurements are in poor agreement with NLO QCD calculations, collider data can provide a testing ground for new ideas which hope to reconcile theory and experiment.

Chapter 3

Experimental Apparatus

The data for this thesis was collected by the Collider Detector at Fermilab (CDF), a general purpose experiment designed to study $p\bar{p}$ collisions at $\sqrt{s} = 1.8$ TeV. The collisions are produced by the Fermilab Tevatron accelerator. The data was collected in 1994-95, a period known as Run Ib. In this chapter we describe briefly the accelerator and the detector, with emphasis on those aspects which are of particular relevance to the photon cross section measurement.

3.1 The accelerator

A schematic drawing of the Fermilab accelerator complex is shown in Figure 3.1. The proton beam begins as a collection of H^- ions produced by ionizing hydrogen gas. The ions are electrostatically accelerated to an energy of 750 keV with a Cockcroft-Walton device. A linear accelerator ('linac') brings the ion energy to 400 MeV, at which time electrons are stripped from the ions to produce a proton beam. The protons are inserted into a synchotron with a radius of 75 meters known as the booster, where they are further accelerated to 8 GeV and formed into bunches. Six bunches are then injected into the main ring, another synchotron with a radius of one kilometer. The main ring accelerates the protons to 150 GeV and delivers them to the Tevatron. The Tevatron is an accelerator located in the same tunnel as the main ring, and therefore has the same radius. Unlike the main ring, the Tevatron magnet coils are made from a niobuim-titanium alloy wire, a material which becomes superconducting when cooled to four degrees kelvin. This allows for a larger dipole field (up to 4.2 Tesla), and consequently the Tevatron can store a proton beam with energies up to 980 GeV. The data used in this measurement was collected with a final beam energy of 900 GeV.

The anti-proton beam is created by extracting protons from the main ring at an energy of 120 GeV and colliding them with a fixed target. Many types of particles are produced in the collisions, and occasionally an anti-proton is produced. The anti-

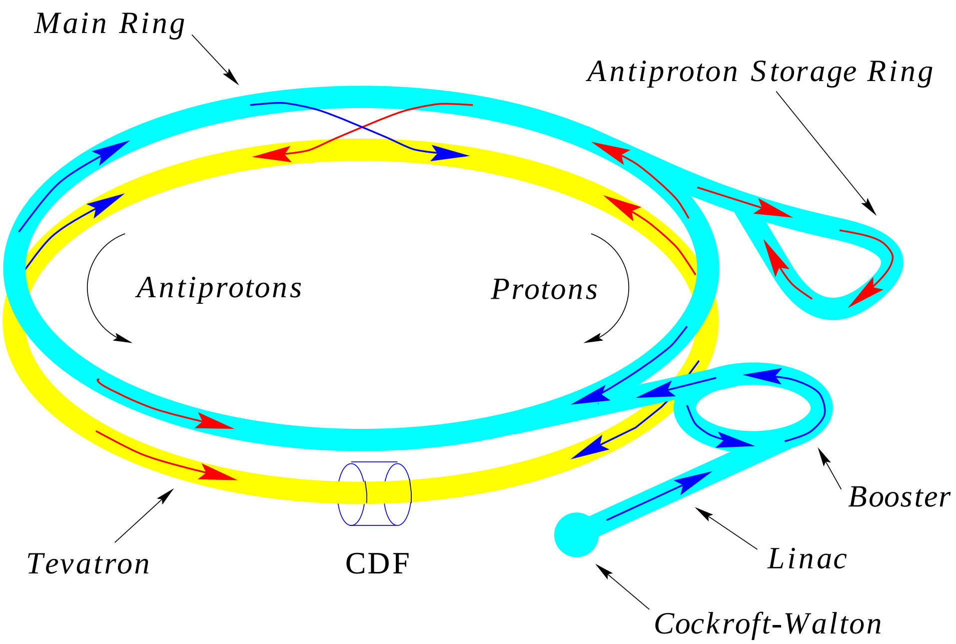

Figure 3.1: A schematic drawing of the Fermilab accelerator complex.

protons are collected by a triangular shaped synchotron known as the debuncher, which has a mean radius of 75 meters. The debuncher reduces the momentum spread of the anti-protons through stochastic cooling, producing a monochromatic 8 GeV beam. The anti-protons are transferred to another 75 meter synchotron called the accumulator which cools the beam further and stores it for later use. Approximately 10^5 protons-on-target are required to collect one anti-proton in the accumulator. When an anti-proton beam of sufficient intensity has been created, six bunches of anti-protons are transferred to the main ring traveling in the opposite direction as the protons. The main ring accelerates the bunches to 150 GeV, and then injects them into the Tevatron where they are accelerated to their final energy of 900 GeV.

The proton and anti-proton bunches are focussed with quadrupole magnets and made to collide every 3.5 μs at the center of the CDF detector, which surrounds the beam pipe. A typical proton bunch contains 2×10^{11} particles, while a typical anti-proton bunch contains 2×10^{10} antiparticles. During Run Ib, the maximum collider instantaneous luminosity was $\sim 2.8 \times 10^{31} cm^{-2} s^{-1}$. At these luminosities, an average of 2 or 3 $p\bar{p}$ interactions occur in each beam crossing. The interactions are distributed along the z axis of the detector in an approximately gaussian shape with width $\sim$ 30 cm.

Figure 3.2: One quarter of the CDF detector. The detector is forward-backward symmetric, and has azimuthal symmetry about the z axis.

3.2 Detector Overview

One quarter of the CDF detector is shown in Figure 3.2. In this view the protons and anti-protons travel along the z axis and collide at the interaction point in the lower left corner. The detector is forward-backward symmetric, and has azimuthal symmetry about the z axis. The positive z axis of the CDF standard coordinate system is defined by the direction of the proton beam, which points east, while the x axis points north, and the y axis up. In Figure 3.2, the variable η (pseudo-rapidity) is related to the polar angle θ by

$$\eta = -\ln\tan\left(\theta/2\right) \tag{3.1}$$

The detector is a hybrid magnetic spectrometer-calorimeter. The spectrometer is composed of a silicon vertex detector, a vertex time projection chamber, and a large open-cell drift chamber located inside an approximately uniform solenoidal magnetic field of 1.4 Tesla. The calorimeter is divided longitudinally into electromagnetic and hadronic modules, and is further subdivided in η and ϕ into projective towers which point back to the nominal interaction point at $z = 0$. The calorimetry is outside of the superconducting solenoid, and in the central region ($|\eta| < 1$) particles pass through the solenoid coil before reaching the calorimeter. Additional layers of drift chambers outside the calorimeter are used for muon identification. A layer of steel outside the central calorimeter provides shielding for a final layer of muon chambers, and also acts a flux return for the solenoid.

3.3 Tracking

The CDF tracking system consists of three subdetectors. The largest of these is the Central Tracking Chamber (CTC), an open cell drift chamber whose purpose is to reconstruct with high efficiency the trajectories of central charged particles with transverse momentum greater than 400 MeV. Inside the CTC sits the Vertex Time Projection Chamber (VTX), and the Silicon Vertex Detector (SVX), which provide precise vertex information. We describe these detectors in detail below.

3.3.1 The Central Tracking Chamber (CTC)

The CTC is a cylindrical drift chamber which occupies the region between r = 28 cm and r = 138 cm and $|z| < 1.6m$, which provides for charged particle tracking out to $|\eta| < 1.1$. 84 layers of sense wires run between the endplates located at $z = \pm 1.6m$. The layers are grouped into cells, and the cells are arranged into superlayers, as shown in Figure 3.3. Of the 84 layers, 60 are parallel to the z axis and provide track position information in the x-y plane. These axial layers are arranged in 5 superlayers of 12 wires each. The remaining 24 layers are tilted by ±3° from axial, and provide both $r\phi$ and z information. These stereo layers are arranged into four superlayers of six wires each.

Charged particles travel on a helical trajectory in a uniform magnetic field. A helix is described by 5 parameters, and at CDF the parameters are labelled crv, d_0, ϕ_0, $\cot\theta$, and z_0. The first three parameters describe the circular projection of the helix in the x-y plane, and are shown schematically in figure 3.4. crv is the inverse diameter of the circle and is signed according to the track charge. d_0 is the signed impact parameter, and ϕ_0 is the azimuthal direction of the particle at the point of closest approach to the origin. The sign convention of the impact parameter is as follows: for a positive particle the impact parameter is positive if the circle does not contain the origin; for a negative particle the impact parameter is positive if the circle does contain the origin. $\cot\theta$ and z_0 are the cotangent of the polar angle and the z position of the particle at the point of closest approach to the z axis.

Track reconstruction begins by searching for sets of hits on sense wires within a single axial superlayer which form a line segment. Next, line segments found in all five axial superlayers which fall on the arc of a circle are joined to form an axial track.

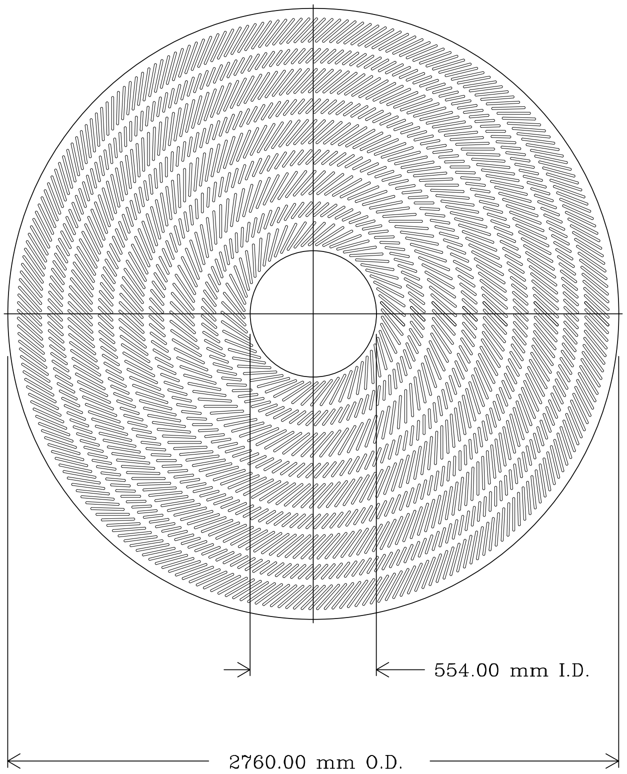

Figure 3.3: An x-y view of the CTC endplate. Each line represents one cell; the cells are arranged into nine superlayers. The five wide superlayers are axial; each axial cell contains 12 sense wires. The other four superlayers are stereo; each stereo cell contains six sense wires.

The hit information from the stereo layers is added to measure z_0 and $\cot\theta$. Because the stereo superlayers have only six sense wires each, it is inefficient to search for stereo line segments. Instead, individual stereo hits are attached to the axial tracks. The efficiency of this process is enhanced if the z_0 of the track is already known, so the reconstruction code begins by assuming that the track originated at one of the vertices found by the VTX. After all possible hits have been attached to the various tracks, a final fit is performed and the five helix parameters are extracted along with an estimate of their errors.

The transverse momentum (p_T) of a particle is inversely proportional to the curvature of its trajectory, where the proportionality constant is determined by the magnetic field. For the 1.4 Tesla field at CDF, the conversion formula is

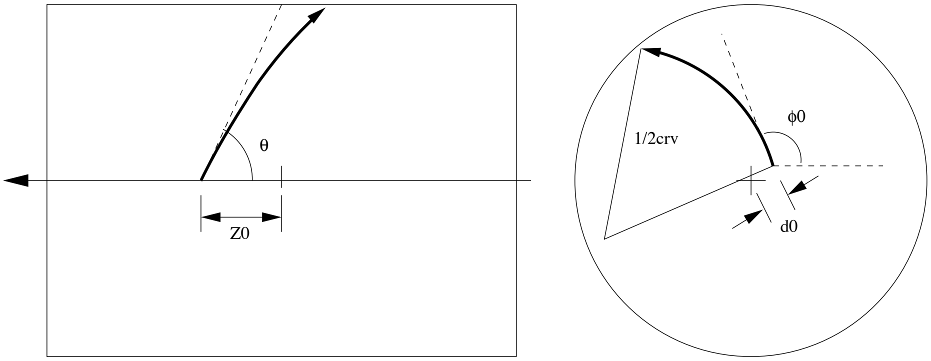

Figure 3.4: A schematic diagram of the five helix parameters. On the left is an r-z view of the CTC, with the horizontal line being the z axis. The heavy arrow is the particle trajectory. On the right is an x-y view, with the cross at the center of the circle being the origin.

$$p_T = \frac{0.002116 GeV/cm}{|crv|} \tag{3.2}$$

where crv is the curvature. The full 3-momentum is then given by

$$p = p_T \sqrt{1 + \cot^2\theta} \tag{3.3}$$

3.3.2 The Vertex Time Projection Chamber (VTX)

The VTX is composed of eight octagonal time projection chambers stacked end-to-end in the z-direction. A diagram of one VTX module is shown in Figure 3.5. The modules are located inside the inner diameter of the CTC, occupying the space from r = 11 cm to r = 25 cm and $|z| < 1.44$ m. Anodes are located at each end of the module, and ionized electrons drift along the z axis to a plane of sense wires and cathode pads located at the center of the module. The wires planes in each octant run azimuthally, and therefore the ϕ resolution of the chamber is poor. The z information, which is measured by timing the electron drift, is precise because the drift velocity is well-known, and the radial information is measured by the wires and pads. Consequently the VTX is efficient for reconstructing tracks in the r-z plane. These tracks are projected to the z axis and the position of the interaction vertices is measured to within one millimeter.

As noted above, the z position of the vertices found by the VTX is used to improve the stereo pattern recognition of the CTC. We will also use the VTX event vertex to convert the total energy measured by the calorimeter to transverse energy.

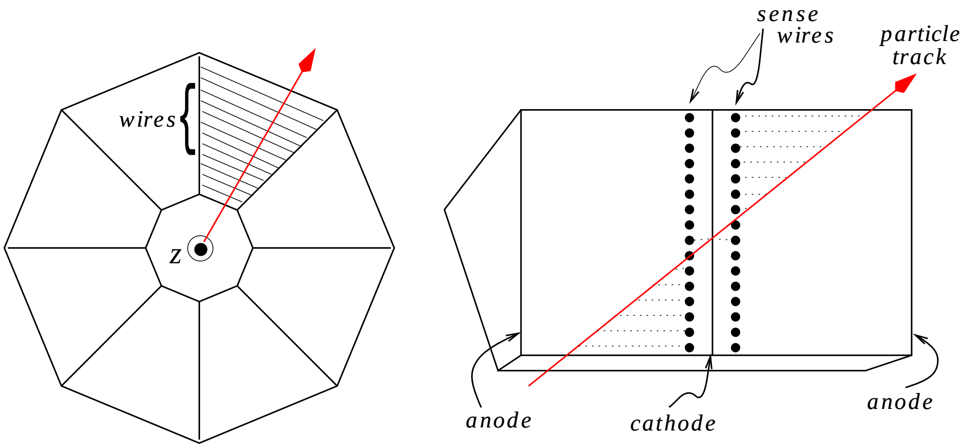

Figure 3.5: A diagram of one VTX module. On the left is a view of the module in the x-y plane, showing the orientation of the sense wires. On the right is an r-z view of one octant of the module, showing the direction of the electron drift to the sense plane and cathode.

3.3.3 The Silicon Vertex Detector (SVX)

The SVX detector is a silicon microstrip device which provides precise $r\phi$ tracking information close to the interaction point. The silicon sensors are assembled into ladders which are 25.5 cm in length. The ladders are held at each end by a beryllium bulkhead, and four layers of ladders form one barrel. The entire device consists of two identical barrels covering a region between r = 3 cm and r = 7.8 cm. The barrels meet at $z = 0$, where there is a gap of 2.15 cm for read-out cables. A diagram of a barrel and a ladder is shown in Figure 3.6.

The silicon strips run along the z axis, and therefore provide $r\phi$ tracking information. A charged particle passing through an active silicon layer creates electron-hole pairs which are observed as a current in the affected strips. Typically a current is found in more than one strip, so several strips are combined together to form a hit cluster. The particle position is taken to be the centroid of the cluster, which is measured by weighting each strip by its collected charge. The position resolution of a cluster is about 15 μm. These clusters are used to improve the impact parameter, p_T, and ϕ_0 resolution of tracks which were found by the CTC.

For the photon cross section measurement, we will be concerned mostly with the tracks of conversion electrons. These particles are produced when a photon converts into an electron-positron pair in the material of the beam pipe, SVX, VTX, and CTC inner cylinder. Since many of these conversions occur outside the SVX, we will not attempt to attach SVX clusters to any of these tracks. Instead, we use the SVX to measure the location of the beam on a run-by-run basis, and when we reconstruct a conversion photon, we require that it point back to the beam spot. This constraint

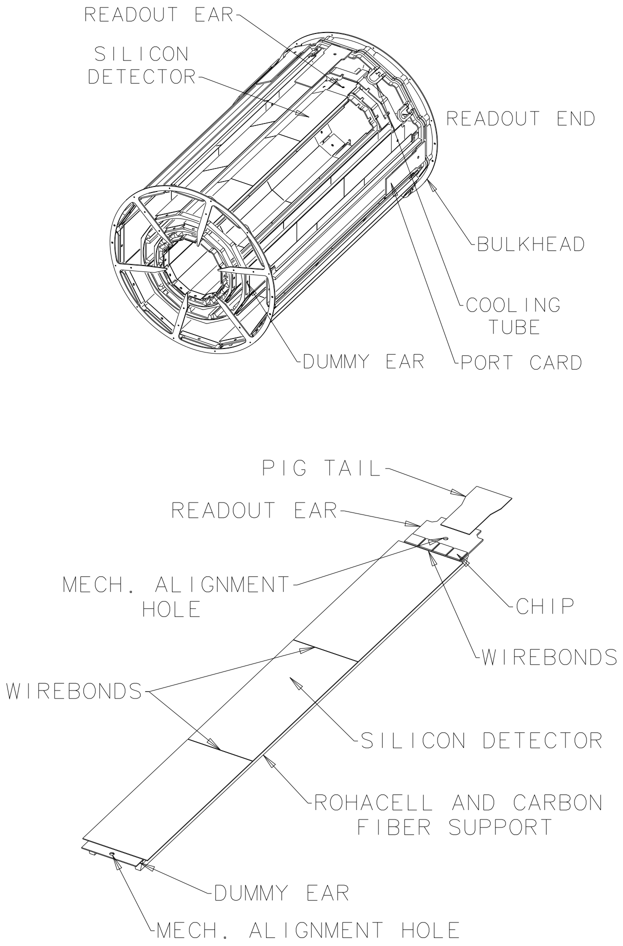

Figure 3.6: The SVX detector. The upper diagram shows a barrel, which consists of four layers of silicon ladders mounted at each end on beryllium bulkheads.The lower diagram is a close-up view of a ladder.

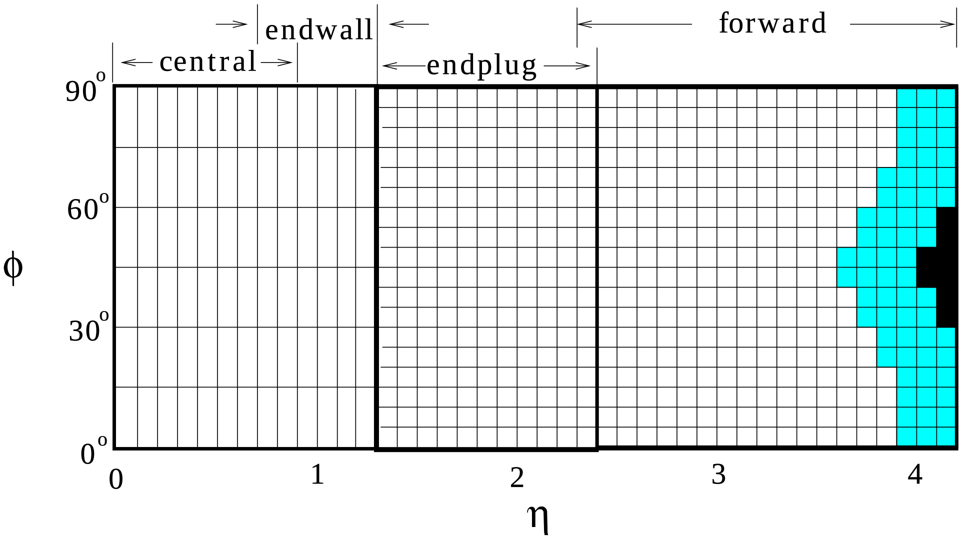

Figure 3.7: Schematic diagram of the $\eta\phi$ segmentation of the CDF calorimeter. The shaded regions at high η have only partial depth coverage.

improves the momentum resolution of the CTC without explicitly attaching silicon clusters to conversion tracks.

3.4 Calorimetry

As shown in Figure 3.7, the CDF calorimeter is subdivided in η into central, wall, plug, and forward detectors. We will measure the photon cross section in the central region, so we use the central calorimeter to measure the photon energy. We use the central, wall, and plug calorimeters to measure the isolation of the photon, and all four calorimeters are used to measure $\not\!\!E_T$.

3.4.1 Central Electromagnetic Calorimeter (CEM)

The CEM is a sampling calorimeter designed to measure accurately the energy of central photons and electrons. The detector is composed of 48 identical wedges, each of which subtends 15° in ϕ and 246 cm in z. Twelve wedges stacked together form an arch. and the four arches meet at $z = 0$ and $x = 0$ to form one barrel which covers $|\eta| < 1$. Because the arches meet at $z = 0$, the region $|z| < 4$ cm is uninstrumented. This is known as the 90° crack. There are also smaller cracks between the wedges due to their steel skins. For accurate energy measurements we will avoid events which have electromagnetic showers in these regions.

The CEM is located outside the solenoid beginning at a radius of 173 cm. A diagram of a CEM wedge is shown in Figure 3.8. The active volume of the wedge

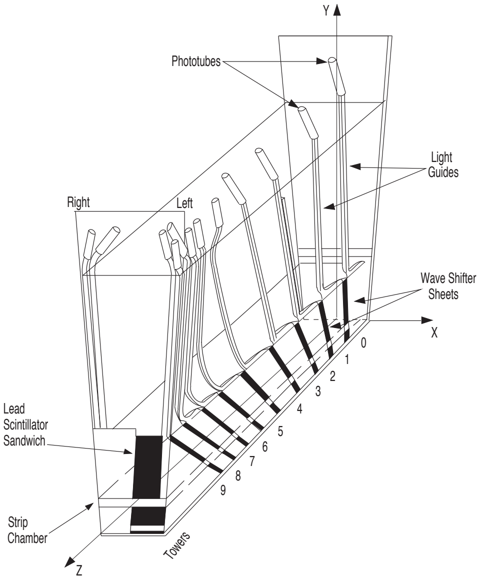

Figure 3.8: A diagram of a single CEM wedge. The ten towers are labelled 0 through 9, and the location of the CES strip chambers is also shown.

consists of a stack of 30 1/8 thick lead plates interleaved with 5 mm thick polystyrene scintillator. The scintillator is divided in z into ten projective towers, each of which subtends approximately 0.1 units of η. The scintillator is attached to wavelength shifters at both azimuthal ends, and each wavelength shifter is observed by a phototube. The higher η towers have selected layers of lead replaced with acrylic in order to keep the amount of absorber constant as a function of polar angle.

The towers in the wedge shown in Figure 3.8 are labelled 0 through 9. Tower 9 is incomplete; it has only about 60% of the absorber and scintillator that the other towers have. We consider this tower to be outside the fiducial volume of the detector. In addition, one wedge is missing two towers in order to allow cryogenics and power to reach the solenoid. This region is known as the chimney module, and is also excluded from the fiducial region.

As shown in Figure 3.8, a proportional strip chamber (CES) is inserted into the stacks between the eighth layer of lead and the ninth layer of scintillator. This location is at a depth of six radiation lengths, and corresponds to the longitudinal shower maximum. A detailed view of a CES chamber is shown in Figure 3.9. The chambers consist of crossed anode wires and cathode strips. The wires run along z spaced at 1.45 cm and measure the azimuthal position of the electromagnetic shower within the CEM wedge. The cathode strips run in the ϕ direction and measure the z position of the shower. The cathode spacing is 1.67 cm in towers zero through four, and 2.01 cm in towers five through nine. We will use the CES for electron identification and to identify multiple showers occurring in one CEM tower.

Figure 3.9: A detailed view of one CES chamber.

The CEM energy resolution is described by

$$\left(\frac{\sigma(E)}{E}\right)^2 = \left(\frac{13.5\%}{\sqrt{E\sin\theta}}\right)^2 + \kappa^2 \tag{3.4}$$

The first term was measured in a test beam, and the second term accounts for tower-to-tower variations. κ has been measured to be $1.6 \pm 0.3\%$.

3.4.2 Central and Wall Hadronic Calorimeters (CHA and WHA)

The CHA and WHA are sampling calorimeters located behind the CEM which provide for hadronic energy measurements out to $|\eta| < 1.3$. The CHA is contained within the same wedges that house the CEM, while the WHA is an independent unit. As shown in Figure 3.2, towers zero through five are contained entirely within the CHA, while towers six through eight are completed by the WHA. Tower nine passes through only the WHA. Like the CEM, the CHA and WHA are based on a scintillator-absorber sandwich. The CHA and WHA employ steel as the absorber, with a plate thickness of 2.5 cm in the CHA and 5.1 cm in the WHA. Both detectors use 1 cm thick scintillator. The energy resolution for single charged pions was measured in a test beam to be

$$\left(\frac{\sigma(E)}{E}\right)^2 = \left(\frac{50\%}{\sqrt{E\sin\theta}}\right)^2 + 3\%^2 \tag{3.5}$$

3.4.3 Plug Electromagnetic and Hadron Calorimeters (PEM and PHA)

The η coverage of the CDF calorimeter is continued beyond $|\eta| > 1.1$ by the plug and forward calorimeters. The plug calorimeter instruments the region $1.1 < |\eta| < 2.4$. Although the boundary between the central and plug calorimeters is small, a significant reduction in response is observed for showers occurring there. This feature of the calorimeter is known as the 30° crack.

The plug is divided into two identical parts, one for the east side of the detector and one for the west. It is segmented into projective towers which point back to the nominal interaction point with a tower size of 0.1 units in η and 5° in ϕ. The plug is also segmented in depth into electromagnetic (PEM) and hadronic (PHA) modules.

Like the central calorimeter, the plug is a sampling calorimeter with lead as the absorber in the electromagnetic portion and steel in the hadronic portion. However, instead of a scintillator active medium, the plug uses gas proportional tubes. The tubes consist of a conductive plastic filled with a 50/50 mixture of argon-ethane gas and a central high voltage wire which act as an anode. Each layer of tubes is located next to a set of cathode pads, and these pads are etched to form the projective geometry of the calorimeter. During an electromagnetic or hadronic shower the gas in the proportional tubes is ionized by the charged particles of the shower. The ionization electrons induce signals on both the wires and cathode pads, and the charge observed on the pads is used to estimate the energy and location of the shower. In the PEM the various layers of pads are ganged together into three groups to provide three energy measurements as a function of depth, while in the PHA all layers are summed for one measurement.

The resolution of the plug has been measured in a test beam with electrons and pions. The PEM resolution is

$$\left(\frac{\sigma(E)}{E}\right)^2 = \left(\frac{22\%}{\sqrt{E\sin\theta}}\right)^2 + (2\%)^2 \tag{3.6}$$

and the PHA resolution is

$$\left(\frac{\sigma(E)}{E}\right)^2 = \left(\frac{90\%}{\sqrt{E\sin\theta}}\right)^2 + (4\%)^2 \tag{3.7}$$

3.4.4 Forward Electromagnetic and Hadronic Calorimeter (FEM and FHA)

The forward calorimeter instruments the η region between 2.4 and 4.2 with electromagnetic and hadronic modules. Like the plug, the forward calorimeter is composed of two identical detectors for the east and west sides of the collision hall and uses the same proportional tube - cathode pad readout technology. The electromagnetic and hadronic modules use lead and steel as their respective absorbers, and the cathode pads are ganged together to form two energy measurements as a function of depth in each module. At the highest η regions the towers of the forward calorimeter are truncated in depth in order to provide space for the Tevatron's low-beta quadrupole magnets.

The resolution of the FEM as determined by test beam is

$$\left(\frac{\sigma(E)}{E}\right)^2 = \left(\frac{26\%}{\sqrt{E\sin\theta}}\right)^2 + (2\%)^2 \tag{3.8}$$

and the FHA resolution is

$$\left(\frac{\sigma(E)}{E}\right)^2 = \left(\frac{137\%}{\sqrt{E\sin\theta}}\right)^2 + (4\%)^2 \tag{3.9}$$

3.5 Beam-beam counters (BBC)

In addition to providing energy measurements, the forward calorimeter also acts a mount for a system of large scintillator telescopes which covers the η region between 3.2 and 5.9. Since any inelastic interaction will produce charged particles in this region, a coincidence between the east and west 'beam-beam counters' signals a $p\bar{p}$ interaction.

This information serves two purposes. First, it triggers the data acquisition system to produce a minimum-bias data sample consisting of typical $p\bar{p}$ events, which is useful to study the general properties of the experimental environment. Secondly, the BBC also measure the instantaneous luminosity of the Tevatron collider, a number which goes directly into all CDF cross sections.

The procedure for extracting the luminosity is as follows. The BBC data is used to count the number of beam crossings in which no inelastic $p\bar{p}$ interaction occurred. Since the number of interactions per crossing is Poisson distributed, by measuring the number of 'misses' we can infer the average number of interactions per crossing. The total inelastic cross section is known from a previous CDF measurement to be 51.15 ± 1.6 mb [32], so the average number of interactions translates directly to a measurement of the instantaneous luminosity. To determine the total luminosity of a CDF dataset we integrate over the instantaneous luminosity observed during the live-time of the detector in that data. This procedure is accurate to 4.1%, and we take that as a systematic error on our cross section measurements.

3.6 Trigger

As noted above, the Tevatron produces a beam crossing every $3.5\mu s$, and several $p\bar{p}$ interactions may occur during each crossing. The data from the various detector components is written to magnetic tape for offline study, but the amount of data and the speed of the tape drives is such that only about 10 events per second can be saved. Therefore it is necessary to begin the data reduction process in real time as the data is collected. For this purpose CDF has implemented a three level trigger system which selects only the most interesting events for archiving. Since the physics goal of the experiment are broad, there are many different ways for a given event to pass the trigger. We will discuss here only the trigger paths used for the direct photon cross section measurement: an 8 GeV electron trigger, and a 23 GeV photon trigger.

3.6.1 8 GeV electron trigger

The first level of the trigger (Level 1) is required to decide within the $3.5\mu s$ bunch crossing time whether or not the most recent event should be discarded. For the 8 GeV electron sample Level 1 requires that energy be deposited in the CEM. For the purpose of measuring CEM energy quickly, the trigger organizes the 10 towers in each CEM wedge into 5 pairs of neighboring towers. These pairs of towers are referred to as 'trigger towers', and the energy in the two towers is summed together. To convert the total energy to transverse energy (E_T), the trigger multiplies the observed signal amplitude in each trigger tower by a value for $\sin\theta$ that was calculated by assuming that the interaction occurred at $z = 0$. If the estimated E_T is greater than 8 GeV, then the event is sent to trigger level 2 (Level 2).

The Level 2 trigger takes $\sim 20\mu s$ to make a decision, and during this time all new beam crossings are ignored. The Level 2 trigger possesses a hardware calorimeter cluster finder, allowing for a re-evaluation of the energy found at Level 1. The cluster finder combines neighboring trigger towers using two algorithms. The first algorithm requires a 'seed' tower of at least 5 GeV, and neighboring towers with more than 4 GeV are added to it. The second algorithm requires an 8 GeV seed tower and 7 GeV neighboring towers. The cluster finder also measures the hadronic fraction of the cluster by comparing the energy in the CHA and WHA towers to the energy in the CEM. For the 8 GeV electron trigger, we require that the energy be less than 12.5% hadronic. The cluster finder produces a list of the location and E_T of all clusters.

During Run Ib a second hardware cluster finder known as the XCES was used to locate showers observed by the wire chambers in the CES. The XCES produces a list of the ϕ position of all such CES clusters.

Level 2 also makes use of a hardware track finder called the Central Fast Tracker (CFT). The CFT searches the hit information from the CTC for evidence of high p_T tracks. It does this by comparing the observed hit patterns in the axial superlayers to the expected hit patterns of real tracks. The CFT produces a list of candidate tracks with their p_T and location in the chamber. These tracks are extrapolated to the radius of the CEM and compared with the location of the CEM and CES clusters. For the 8 GeV electron trigger, Level 2 requires a CFT track with $p_T > 7.5$ GeV which points toward a CEM cluster with $E_T > 8.0$ GeV and a XCES cluster. Events passing these requirement are sent to the third trigger level (L3) for further processing.

At L3 the event data is passed to a 'farm' of 64 Silicon Graphics processors which analyze the event with a simplified version of the full offline reconstruction code. The offline CEM clustering and CTC tracking routines are run giving improved measurements of the electron E_T and p_T. In addition, several electron quality variables are calculated and L3 rejects events which appear to be fake electrons. These quality variables are discussed in detail in section 4.3.3. L3 passes electron candidates with have $E_T > 8.0$ GeV and $p_T > 6.0$ GeV. These events are then written to tape.

3.6.2 23 GeV photon trigger

We use a second trigger with an E_T threshold of 23 GeV to measure the photon cross section at high p_T. This trigger allows, but does not require, that a track be associated with the EM cluster, and we refer to it as a 'photon' trigger.

Like the 8 GeV electron trigger, this trigger requires an 8 GeV EM cluster at Level 1. The Level 2 trigger raises the E_T threshold to 23 GeV, and also requires an associated XCES cluster. In addition, the 23 GeV photon trigger adds an isolation requirement to the EM cluster in order to reduce the trigger rate to an acceptable level. The isolation of the photon is calculated by a neural net board, which sums the energy found in the calorimeter in a 5×5 grid surrounding the photon candidate. The neural net calculates an isolation quality variable which is then used to discriminate against un-isolated EM clusters. The neural net cut corresponds to roughly 4 GeV of energy in a cone of radius $\Delta R = 0.4$ surrounding the photon. For this trigger no events are rejected by Level 3, so all events passing Level 2 are written to tape.

3.6.3 Trigger summary

The trigger requirements of our two datasets are summarized in Table 3.1.

8 GeV electron data	
Level 1	8 GeV trigger tower
Level 2	8 GeV Level 2 CEM cluster 7.5 GeV CFT track XCES cluster
Level 3	$E_T > 8.0$ GeV $p_T > 6.0$ GeV electron ID cuts
23 GeV photon data	
Level 1	8 GeV trigger tower
Level 2	23 GeV Level 2 CEM cluster neural net isolation XCES cluster
Level 3	no requirements

Table 3.1: Summary of the trigger requirements of the two datasets.

Chapter 4

Event variables and data selection

The selection of the events to be used in the photon cross section measurement begins with the online trigger system described in the previous chapter. We make further cuts offline in order to isolate a sample of events in which the signal can be reliably separated from the background. Some cuts are chosen to discriminate against background while efficiently retaining the signal events. Others, such as fiducial requirements, are made in order to insure that the event has been well measured by the detector. During data selection it is important to only make cuts whose efficiency to accept real signal events can be measured in the data or can be predicted by the Monte Carlo. The efficiency of the signal to pass all the selection cuts will be used to correct the observed number of signal events to the number of produced signal events, and the error on the efficiency translates directly to an error on the final cross section.

We begin this chapter with a discussion of the variables we will use to select the data and measure the cross section. We then explain in detail each cut.

4.1 Event variables

4.1.1 E_T

The electron transverse energy is measured by the CEM. Typically the energy of an electromagnetic shower is deposited in one or two CEM towers. To be safe we use a three tower cluster: a seed tower whose energy is required to be greater than 5 GeV, and its two neighboring towers in η. Clusters do not include towers from neighboring wedges. Clusters are also not allowed to cross the 90° crack, so if the seed tower is tower 0 in Figure 3.8, then only two towers are included in the cluster.

Each phototube produces a voltage signal whose time integral is proportional to the number of photons incident upon its photocathode. The photons produced by the scintillator in the electromagnetic shower are attenuated as they travel to the wavelength shifter located at the end of the tower. Consequently the energy observed at each end depends on the location of the shower inside the tower. If x is the position of the shower measured along the length of the scintillator from the center of the tower, then with an appropriate energy calibration the integrated signal seen by the two phototubes A and B located at $x = \pm 24.5$ cm is

$$A = Ee^{\lambda x} \tag{4.1}$$

$$B = Ee^{-\lambda x} \tag{4.2}$$

where E is the energy of the shower and λ is the attenuation length of the scintillator. For the CEM, $\lambda = 68$ cm. The geometric mean of the two phototube energies gives the energy of the shower independent of its location: $E = \sqrt{AB}$.

The total cluster energy is the sum of the energies observed in each tower. Cluster energy is converted to transverse energy according to $E_T = E/\sqrt{1 + \cot^2\theta}$, where $\cot\theta$ is taken from the highest p_T track pointing at the cluster.

Small changes are made to the measured E_T to correct for time and position dependent changes in the response of the CEM. The time-dependent corrections are measured using the E_T/p_T of isolated (non-conversion) electrons by assuming that the p_T measurement is independent of time. (This is assured by CTC calibrations based on the $J/\psi \rightarrow \mu^+\mu^-$ resonance.) Studies show that the gain of the CEM decreased by 4% during Run Ib. This is illustrated in Figure 4.1 where the mean E_T/p_T between 0.9 and 1.1 of $W \rightarrow e\nu$ and conversion electrons is shown versus run number. After applying the correction E_T/p_T is independent of time. Similarly, the CEM response also depends on the location of the cluster within a CEM wedge. This 'mapping' correction was measured in the test beam as well as data, and is shown as a function of the ϕ and z position of the shower within the tower in figures 4.2 and 4.3.

The E_T distribution of the two final data samples is shown in Figure 4.4

4.1.2 Raw and vertexed p_T

The transverse momentum of all tracks is measured by the CTC. The CTC reconstruction code performs the pattern recognition and track fitting described in chapter 2. This results in measurement of the five track parameters for each track and an estimate of their 5×5 covariance matrix. We will refer to this momentum measurement as the 'raw p_T'.

Most of the tracks that we will be concerned with in this thesis are the result of a photon conversion. When a photon converts in material, the final state electron and positron are produced parallel to each other. This unique geometry allows us to add a constraint to the CTC track fit which improves the momentum resolution of our measurement. This is done in the following way. We hypothesize the location of the conversion in the detector and the 3-momenta of the two produced particles. We require that the momentum vectors be parallel, but we do not require that they

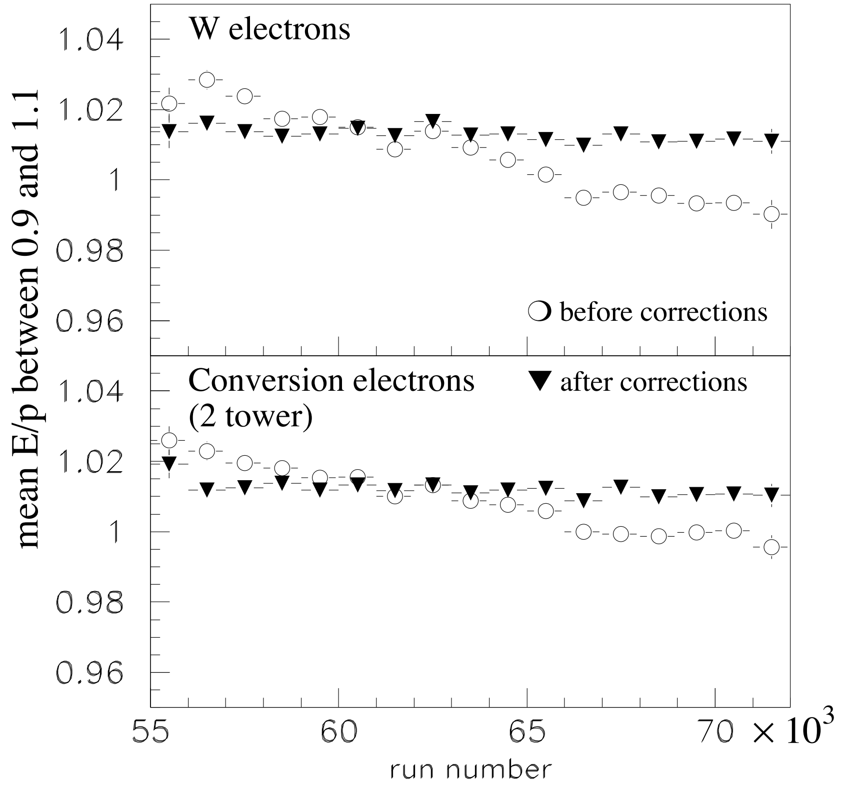

Figure 4.1: The mean E_T/p_T of CEM electrons plotted versus run number. Run 55000 occurred in January 1994, and run 72000 was in July 1995. Both $W \rightarrow e\nu$ and conversion electrons are shown, before and after the CEM energy corrections are applied.

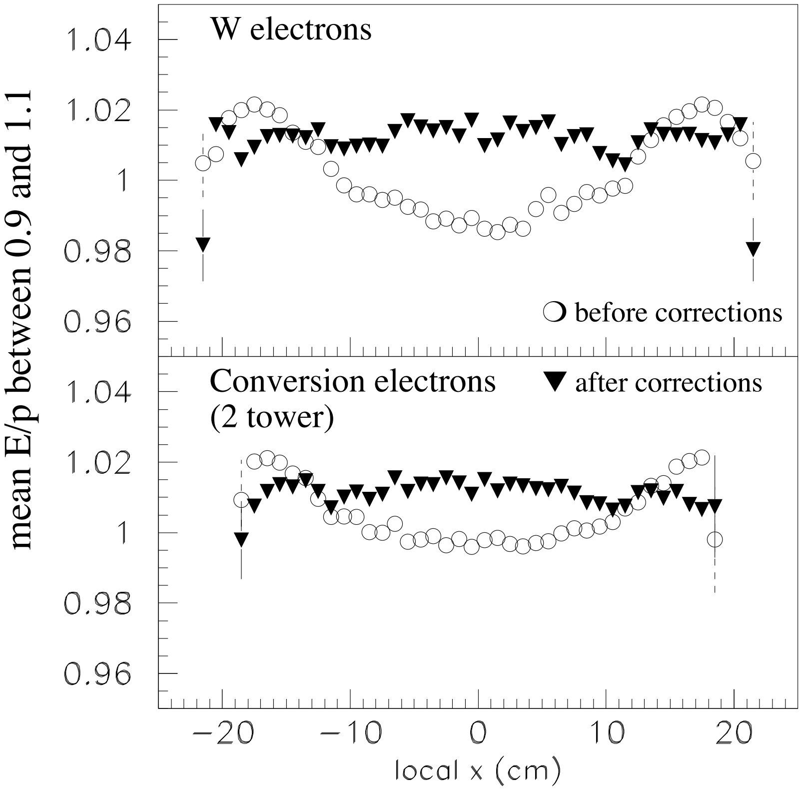

Figure 4.2: The mean E_T/p_T of CEM electrons plotted versus the ϕ position of the cluster inside the CEM tower. Here ϕ is transformed to the distance from the center of the tower (local x) by multiplying by the radius of the CEM from the center of CDF. Both $W \rightarrow e\nu$ and conversion electrons are shown, before and after the CEM energy corrections are applied.

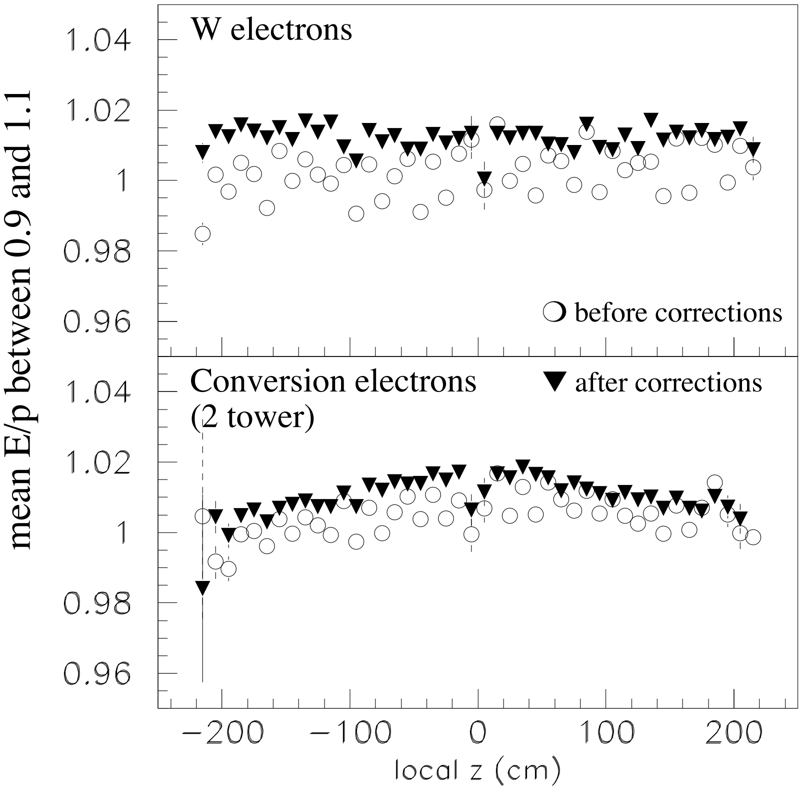

Figure 4.3: The mean E_T/p_T of CEM electrons plotted versus the z position of the cluster in the CEM (local z). Both $W \rightarrow e\nu$ and conversion electrons are shown, before and after the CEM energy corrections are applied. Unlike the W electrons, the mean E_T/p_T of conversion electrons appears to depend on local z before and after the correction. This may indicate that the conversion p_T measurement has a bias which depends on η.

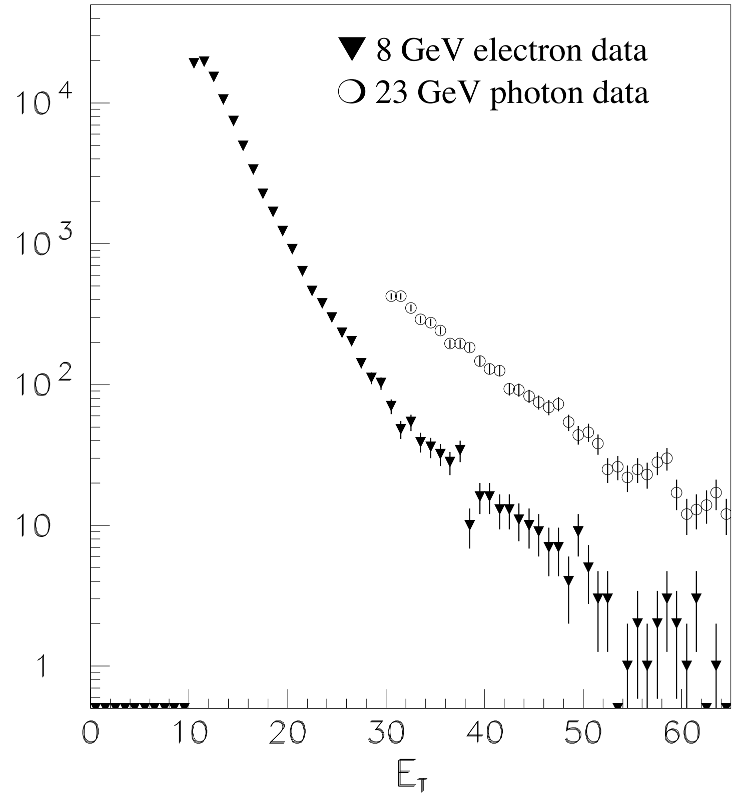

Figure 4.4: The electron E_T distribution of conversion events.

point back to the beam spot [1]. We then extrapolate the tracks to the CTC, and we compare the hypothesized track parameters to those measured by the CTC. To perform the comparison, we use a χ^2 defined by

$$\chi^2 = \Delta\vec{\alpha_1} \cdot \tilde{C_1}^{-1} \cdot \Delta\vec{\alpha_1} + \Delta\vec{\alpha_2} \cdot \tilde{C_2}^{-1} \cdot \Delta\vec{\alpha_2} \tag{4.3}$$

where $\Delta\alpha_{1,2}$ is the difference between the measured and hypothesized track parameters for the two tracks, and $\tilde{C}_{1,2}$ are the covariance matrices. We vary the location of the conversion and the momenta of the two tracks until the χ^2 is minimized. This results in an improved estimate of the p_T of the two tracks and the location of the

---

[1] The lack of a beam constraint in the vertex fit was an oversight. By using a beam constraint in addition to the vertex constraint the p_T resolution may improve by as much as 15%. This would improve the statistical errors associated with the E/p background subtraction. However, the final errors on the cross section are systematically limited.

conversion inside the detector. We will refer to this p_T measurement as the 'vertexed p_T'.

The conversion geometry which allows us to perform the vertex fit also creates some difficulties. Because the electron and positron have opposite charge, they bend in opposite directions and separate from each other in the solenoidal field of the tracking detectors. However, depending on the momenta of the tracks and the location of the conversion point, these particles are often very close to each other as they pass through the first superlayers of the CTC. This situation creates difficulties for pattern recognition and track fitting. For example, once a given wire has registered the presence of a hit that wire becomes insensitive to further hits which follow in the next ~ 20 nanoseconds. Since the drift velocity of the ionization electrons in the gas is 50 μm/ns, this means that two hits cannot be distinguished if they are separated by less than a millimeter within a cell. Consequently, the pattern recognition will assign the hit to one of the two tracks and record a miss for the other track. Since the tracking code is not optimized to handle such situations, this often results in a biased fit for the track p_T and a distorted covariance matrix.

One effect of this distortion is shown in Figure 4.5. In the top plot we show the E/p distribution of the 23 GeV photon data sample using both the raw and vertexed p_T. The peak at E/p = 1 is due to the single photon signal, and the long tail at high E/p is from backgrounds. After vertexing the tracks the E/p peak becomes 30% more narrow, indicating that the tracking resolution has improved. In addition, the mean of the peak shifts by about 4%. In the lower half of the plot the change in the p_T due to the vertex fit is shown.

The conversion p_T bias is also displayed in Figure 4.6. Here we plot the average fractional change in the p_T of each track after vertexing as a function of the track p_T. Both the 8 GeV electron data and 23 GeV photon data are shown, and we find that the bias increases with p_T and is much larger in the 23 GeV photon data. This is expected if the bias is due to hit overlap in the CTC. For example, when the secondary track is soft (1 GeV) it separates from the trigger electron quickly. This is a common situation in the 8 GeV electron data due to the 2 tower requirement (which is discussed in section 4.2). In the 23 GeV photon data we often have two stiff tracks, which may not be distinguishable until the third or fourth layer of the CTC. Therefore hit level effects become very important in these data.

If the raw p_T and the covariance matrix were unbiased then we would expect the vertex fit to improve the p_T resolution but not shift the mean. Therefore the shift observed in the data is an indication of the non-ideal nature of conversion tracks. For most purposes we use the vertexed p_T because we expect that the vertex constraint will have the effect of removing some of the distortion.

The radius of conversion distribution of the 8 GeV electron data is shown in Figure 4.7, before and after vertexing. (The un-vertexed radius of conversion is the radius at which the two tracks are parallel to each other.) Various structures are visible in the plot, including the SVX, VTX, and CTC inner cylinder. There is also a Dalitz peak

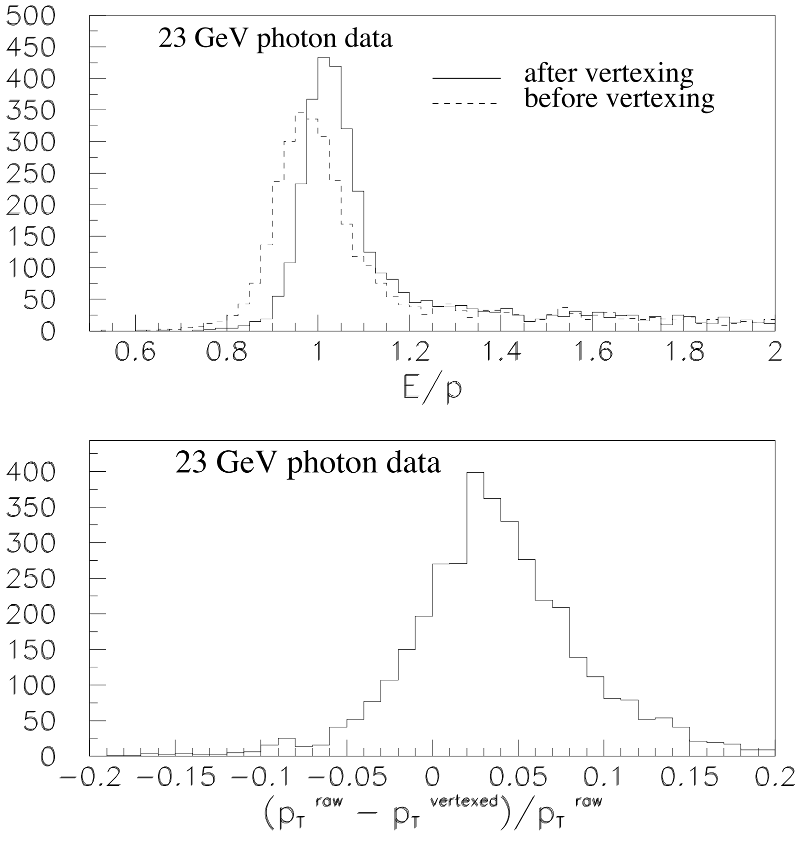

Figure 4.5: Effects of conversion track distortion. Top: E/p distribution of the 23 GeV photon data before and after the vertex fit. The fit improves the width of the E/p peak by 30%, and shifts the mean by 4%. Below: fractional change in the conversion p_T after vertexing. The non-zero mean indicates that the raw CTC fit is biased for conversion tracks.

due to $\pi^0 \to e^+e^-\gamma$ decays and $\gamma^* \to e^+e^-$ at zero radius. The vertex fit improves the resolution enough that the VTX outer can and the CTC inner cylinder become distinguishable.

In Figure 4.8 we show the impact parameter of the conversion photon, before and after performing the vertex fit. The impact parameter is measured from the beam position, which is determined on a run-by-run basis with the SVX detector. The width of the beam spot is tens of microns, so the 0.5 mm width in the observed impact parameter is dominated by the CTC resolution. The vertex fit makes a very small improvement in the resolution.

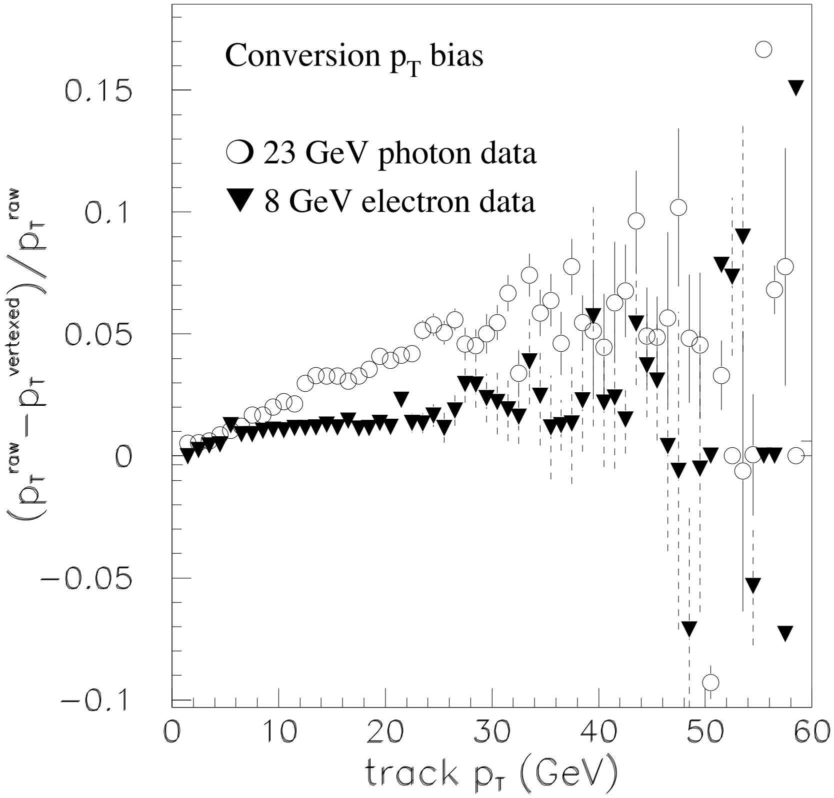

Figure 4.6: Conversion p_T bias versus p_T. The points are the average fractional change in the conversion track p_T after the vertex fit. Both conversion tracks are included, so each event contributes two entries. The bias increases with track p_T, and is larger for the 23 GeV photon data. This is consistent with the bias being associated with hit overlap in the inner superlayers of the CTC.

4.1.3 *sep*

In a photon conversion, the final state electron and positron are produced parallel to each other at a single point. We define *sep* as the measured distance between the tracks in the x-y plane at the point where they are parallel. Since the particles are created at a single point, the true value of *sep* is zero for a real conversion. As shown in Figure 4.9, *sep* is positive if their trajectories overlap each other, and negative otherwise. The *sep* distribution of CTC inner cylinder conversion candidates is shown in Figure 4.10.

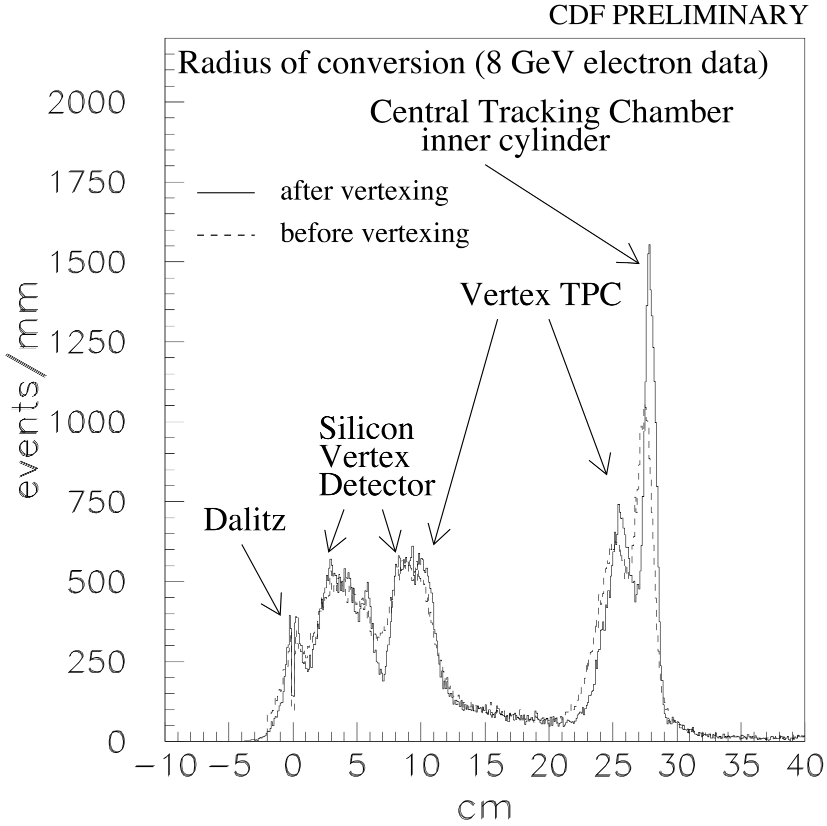

Figure 4.7: Vertexed and un-vertexed radius of conversion distribution in 8 GeV electron data. The peak at r = 0 labelled 'Dalitz' is due to $\pi^0 \rightarrow e^+e^-\gamma$ decays and $\gamma^* \rightarrow e^+e^-$

4.1.4 $\Delta \cot \theta$

The solenoidal magnetic field separates the electron and positron in the x-y plane, but not in z. Consequently the two tracks have identical $\cot \theta$. $\Delta \cot \theta$ is the difference in the track $\cot \theta$'s, and its true value is zero for a real conversion. The $\Delta \cot \theta$ distribution observed for CTC inner cylinder conversion candidates is shown in Figure 4.10.

4.1.5 z_0

In most events we have two measurements of the electron track z_0; one provided by the VTX and one returned by the CTC track fit. If the CTC z_0 is within 5 cm

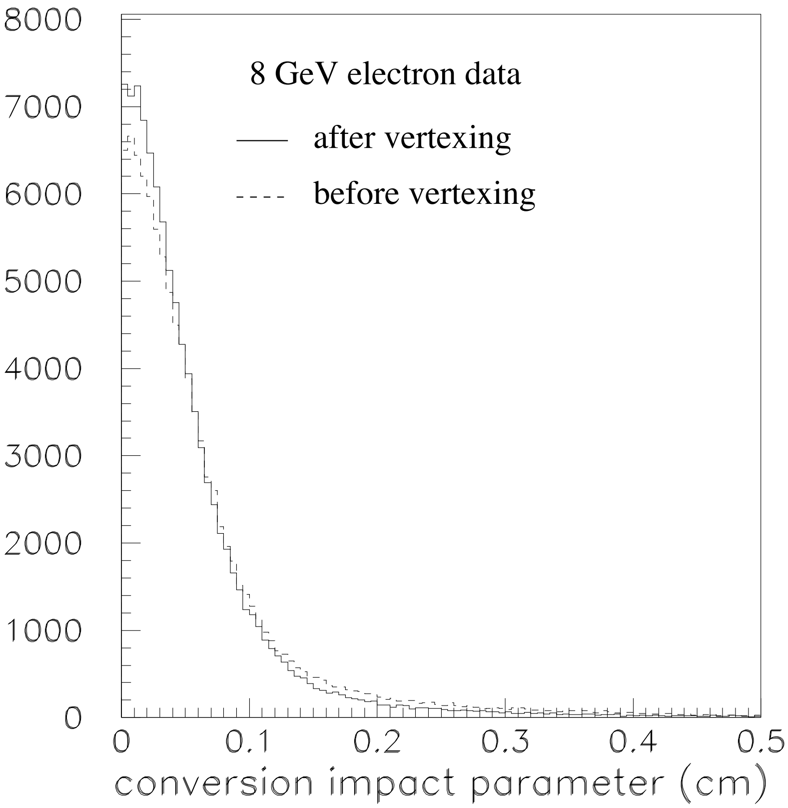

Figure 4.8: Conversion photon impact parameter, before and after vertexing. The width is dominated by the CTC resolution, and not the width of the beam spot, which is tens of microns.

of a VTX vertex, then we take the VTX z_0 as the electron z_0. Otherwise we take z_0 from the CTC track fit. This occurs in 5% of all events.

The z_0 distribution of the final 8 GeV electron data sample is shown in Figure 4.11. The z_0 distribution of a typical data sample is approximately gaussian distributed about $z = 0$ with a width of 30 cm. In a conversion data sample, however, the z_0 of the electron is highly correlated with the z position of the conversion point. The material in the inner detector is not uniform in z, and we see an image of this material on the beamline when reconstructing z_0. The sharp drop in z_0 near $|z| = 30$ cm is due to the SVX detector, which is located between -30 cm $< z_0 <$ 30 cm. In the Figure we have compared the data distribution to the Monte Carlo prediction. The Monte Carlo material has not been carefully tuned in z, but the location of the SVX

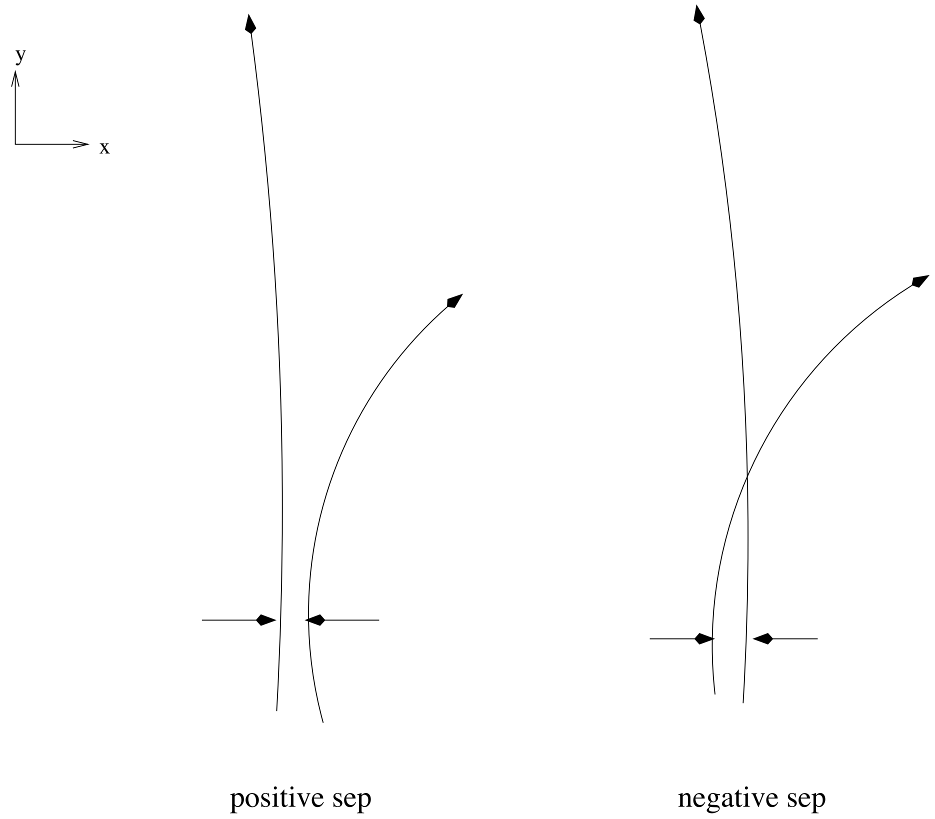

Figure 4.9: The *sep* sign convention. The arcs are the measured trajectories of the conversion electron and positron in the x-y plane. *sep* is the distance between the tracks at the point where they are parallel. *sep* is positive if the tracks do not overlap, and negative otherwise.

detector is included correctly. The Monte Carlo predicts a sharp drop at $|z_0| = 30$ cm, but it does not get the overall shape perfectly correct.

4.1.6 η

The pseudorapidity (η) is defined according to equation 3.1. θ in that equation is the angle between the z axis (beamline) and the line connecting the z_0 of the electron at the beamline and the electron cluster in the calorimeter. The η distribution of the final 8 GeV electron data sample is shown in Figure 4.12. In a conversion data sample the η distribution is enhanced at large $|\eta|$ due to the larger amount of material seen by photons which travel through the material at an angle.

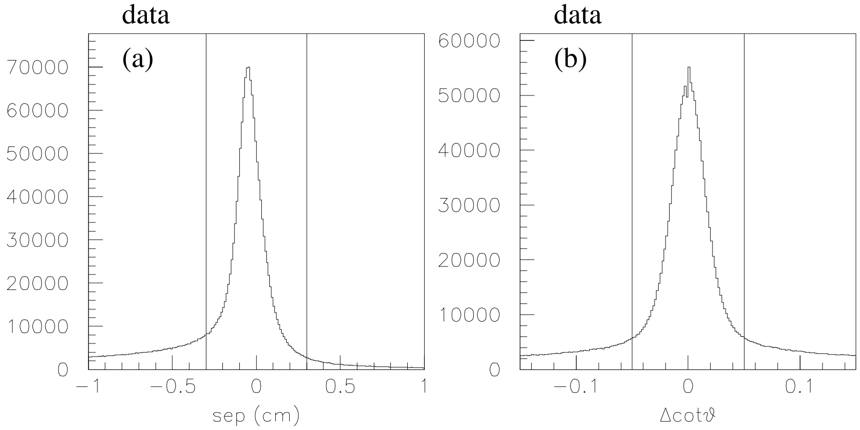

Figure 4.10: The conversion identification variables *sep* and $\Delta\cot\theta$. *sep* is the distance between the two tracks in the x-y plane at the radius at which they are parallel, and $\Delta\cot\theta$ is the difference in the track $\cot\theta$'s. These distributions were obtained from CTC inner cylinder conversion candidates. The vertical lines are the cuts applied to these variables. The long tails beyond the cut values are dominated by fake conversions.

4.1.7 Electron identification variables

In this section we describe the six electron identification variables which are used by the 8 GeV electron Level 3 trigger to reject fake electrons. The six variables are plotted for the final conversion sample from the 8 GeV electron data and 23 GeV photon data in Figures 4.14 and 4.15.

χ^2_{wires} and χ^2_{strips}

The CES strip and wire chambers are located within the CEM towers at a depth of $6X_0$. Because of their fine segmentation, they provide information on the lateral shape and location of the electromagnetic shower whose energy is measured by the CEM. About 95 % of an electromagnetic shower is contained laterally within two Moliere radii from the center of the shower. For the CEM, the Moliere radius is about two centimeters, and since the CES wire pitch is 1.45 cm, we find the energy deposited on multiple CES channels. Therefore the offline reconstruction code uses a seed and shoulder algorithm to combine energetic channels into clusters. The clustering in done independently in both 'views' (strip and wire). Clustering begins with channels which have more than 500 MeV of energy, and grow on both sides to include a total of 11 channels. A plot of the energy versus channel number gives us the lateral profile of the shower at shower maximum. This profile is compared to shower profiles measured

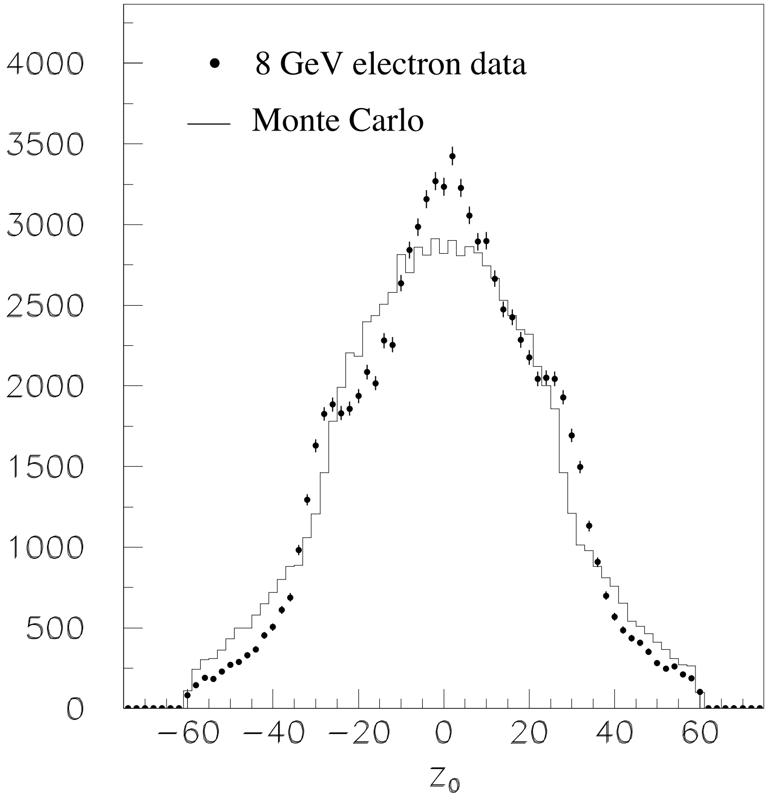

Figure 4.11: The electron z_0 distribution of conversion events. The non-gaussian shape is due to z of the material in the inner detector.

in a test beam with single electrons, and a pseudo-χ^2 is calculated for each view to describe the agreement with the single-shower hypothesis. A χ^2_{wires} and χ^2_{strips} less than four is expected for a single shower event. A poor value of χ^2_{wires} or χ^2_{strips} usually indicates that two showers have been included in the same CES cluster. This can occur if the event is the result of a meson decay such as $\pi^0 \to \gamma\gamma$.

Δx and Δz

Most of the electromagnetic showers that we are concerned with in this thesis are the result of electrons which are observed tracked by the CTC. The electron tracks can be extrapolated to the radius of the CES (183 cm), and the expected position of the track can be compared with the measured position of the CES cluster. The difference in the extrapolated track position and the CES cluster position is known

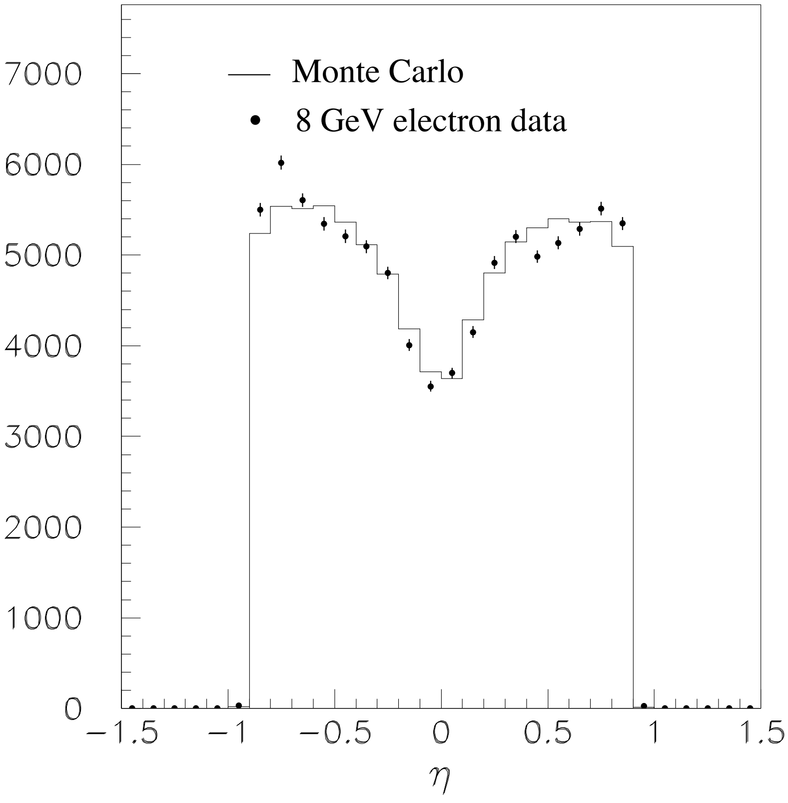

Figure 4.12: The electron η distribution of conversion events. The η distribution of conversions is enhanced at large $|\eta|$ due to the larger amount of material seen by photons which travel through the material at an angle.

as Δx in the wire view and Δz in the strip view. For real electrons, Δx and Δz are typically less than a couple of centimeters. Most of the mismatch is due to multiple scattering of the electron in the material of the solenoid and the CEM.

L_{shr}

As noted above, an electromagnetic shower is expected to deposit its energy in one or two CEM towers which neighbor each other in z. The manner in which the energy is shared between those towers is determined by the position of the shower relative to the tower boundary and the angle of incidence of the particle which initiated the shower. In order to quantify the agreement between the lateral energy distribution observed in a given CEM cluster and the expectation for single shower, CDF uses a quality variable known as L_{shr} (*lateral sharing*) which is defined as

$$L_{shr} = 0.14 \sum_k \frac{M_k - P_k}{\sqrt{0.14^2 E_T + (\Delta P_k)^2}} \tag{4.4}$$

The index k runs over the two or three towers in the CEM cluster, and M_k is the fractional energy found in tower k. P_k is the prediction for M_k which is a function of the z position of the cluster measured in the CES and the z_0 of the cluster measured with the VTX. In the denominator, $0.14^2 E_T$ represents the square of the energy resolution of the CEM, while ΔP_k is the error on the prediction P_k. The values used for P_k are taken from test beam electrons. For single electromagnetic showers, the L_{shr} distribution is centered at zero. CEM clusters with more than one shower have positive L_{shr}.

had/em

In the central calorimeter, most of the energy in an electromagnetic shower is deposited in the CEM. Hadronic showers, on the other hand, start deeper and travel further in the calorimeter, and consequently leave significant energy in the CHA and WHA. To quantify the nature of the shower, we use a variable called *had/em*, which is the energy measured in the CHA and WHA towers behind the CEM cluster towers divided by the energy measured in the CEM. For an entirely electromagnetic shower we expect *had/em* to be no more than a few percent.

4.1.8 local x and local z

In addition to measuring the lateral profile of the electromagnetic shower, CES clusters are also used to measure the location of the shower within the CEM wedge. The center of the shower is taken to be the centroid of the strips (or wires) in the cluster, where each channel is weighted by its energy. This provides a position measurement with an accuracy of a few millimeters. In the wire view the position of the cluster is called 'local x', which is measured in centimeters from the center of the CEM wedge. The edges of the CEM wedge occur at $x = \pm 24.2$ cm. The strips measure 'local z', which is the position of the cluster along the beam direction. The center of the detector is at $z = 0.0$ and the edges of the CEM are at $z = \pm 246$ cm.

4.1.9 N_{trk}

To insure that the CES and CEM measurements are reliable we veto events in which extraneous tracks point to the towers which make up the CEM cluster. We refer to the total number of three dimensional tracks reconstructed by the CTC which extrapolate to the CEM cluster as N_{trk}, and we require N_{trk} to be equal to the number of conversion tracks (one or two) which point to the cluster.

4.1.10 $E_T^{cone0.4}$

To measure the isolation of the photon we perform a scalar sum of the transverse energy in all calorimeter towers which satisfy $\Delta R < 0.4$, where $\Delta R = \sqrt{\Delta\eta^2 + \Delta\phi^2}$. $\Delta\eta$ and $\Delta\phi$ are calculated for each tower in the following manner.$\Delta\eta$ is the difference between the tower η and the CEM cluster η as measured by the CES strip chambers. The tower η is calculated from the event vertex by assuming that the energy was deposited in the center of the tower in z. Energy in the hadronic section of the calorimeter is assumed to be deposited at a depth of 1.5 interaction lengths, and electromagnetic energy is assumed to be at a depth of six radiation lengths. Similarly $\Delta\phi$ is the difference between the tower ϕ and the CEM cluster ϕ measured by the CES wire chambers. The tower ϕ is determined using the ratio of the energies observed in the two phototubes A and B attached to the azimuthal ends of the tower. As seen from equations 2.1 and 2.2, $A/B = \exp 2\lambda x$. Since the attenuation length λ of the scintillator is known, A/B measures the local x of the energy deposit, which is converted to global ϕ.

Excluded from the isolation sum are the two or three towers which make up the CEM cluster. However, in some events the softer conversion track lands outside the CEM cluster but within $\Delta R < 0.4$, artificially enhancing the energy sum. In this case we also exclude from the sum the tower hit by the conversion track, as well as the closest tower in η. The final summed energy is referred to as $E_T^{cone0.4}$.

4.1.11 $\not{E}_T$

Since the calorimeter measures both energy and position, we can use it to infer the production of non-interacting particles (such as neutrinos) by imposing energy conservation in the plane transverse to the beamline. We refer to the calorimeter energy imbalance observed in a given event as the 'missing E_T' ($\not{E}_T$). The $\not{E}_T$ is calculated by performing a vector sum in the transverse plane of all energy deposited at $|\eta| < 3.6$. To be included in the sum a tower must exceed a threshold of 100 MeV in the CEM, CHA, and WHA, 300 MeV in the PEM, 500 MeV in the PHA and FEM, and 800 MeV in the FHA. The negative of this vector sum is the $\not{E}_T$ vector. Note that in $p\bar{p}$ collisions a non-negligible amount of energy escapes unobserved down the beam-pipe as the remnants of the initial state particles, and this prevents us from measuring the missing energy in the z direction.

4.2 1 tower and 2 tower events

In a photon conversion the electron and positron are created nearly parallel to each other. If the conversion occurs in the CDF inner detector these charged particles become separated in the x-y plane due to the solenoidal magnetic field. When the tracks reach the central calorimeter the distance between them ranges from a few centimeters to several meters, depending on the stiffness (p_T) of the tracks and the location of the conversion point. Since a single CEM tower is 49 cm wide in the x-y plane the electron and positron may shower in the same calorimeter tower or the may be in separate towers. We refer to conversion with both tracks pointing to the same tower as '1 tower' events, and conversions with the tracks in separate towers as '2 tower' events. This is shown schematically in Figure 4.13.

These two conversion geometries lead to significantly different systematics. The most important effect is on the behavior of the electron ID variables. The CES electron quality variables (χ^2_{wires}, χ^2_{strips}, Δx, and Δz) are designed to distinguish single electromagnetic showers from double showers occurring in the same CEM tower. This allows us to reject electron candidates which are due to a $\pi^0 \rightarrow \gamma\gamma$ shower overlapping with a random charged track. As a side effect these variables also reject 1 tower conversion events. The 8 GeV electron trigger applies these quality cuts at Level 3, so we cannot release them. Therefore for the 8 GeV electron data we restrict ourselves to the 2 tower geometry only. This causes a loss of acceptance for these data at high p_T, but below 18 GeV the 2 tower geometry is preferred and the acceptance is relatively large.

The 23 GeV photon trigger makes no electron quality cuts, so in these data we can recover the 1 tower events which we rejected from the 8 GeV electron data. Above 23 GeV the 1 tower configuration is dominant, so at these p_T our acceptance is large. Furthermore, we impose the requirement that our final 23 GeV photon data sample be 1 tower only. This ensures that our two data samples have no events in common, producing statistically independent measurements of the cross section which we can compare to cross check our understanding the systematics.

For the remainder of this thesis we will refer to the two datasets as either '1 tower' and '2 tower', or '8 GeV electrons' and '23 GeV photons'.

4.3 8 GeV electron sample selection

4.3.1 Trigger

The 8 GeV electron data selection begins with the three-level trigger system described in the previous chapter. At Level 1 the trigger requires 8 GeV of transverse energy in the CEM. The Level 2 trigger also requires an associated CFT track with $p_T > 7.5$ GeV, and an XCES cluster in the CES wire chambers. The Level 3 silicon graphics processor farm runs a version of the offline reconstruction code and makes the following electron quality cuts:

- $E_T > 8.0$ GeV
- $p_T > 6.0$ GeV
- $l_{shr} < 0.2$

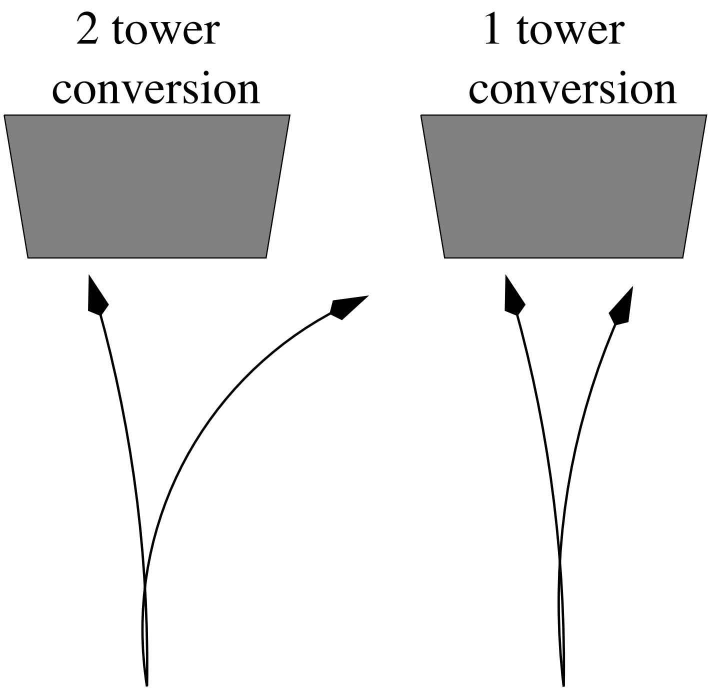

Figure 4.13: Schematic diagram 1 and 2 tower conversions. The shaded trapezoids represent a single tower in the CEM, while the arcs are the trajectories of the conversion electron and positron.

- $had/em < 0.125$
- $\Delta x < 3.0$ cm
- $\Delta z < 10.0$ cm
- $\chi^2_{wires} < 10$
- $\chi^2_{strips} < 10$

The six electron ID variables for the 8 GeV electron data are compared to $Z \rightarrow e^+e^-$ electrons in figure 4.14. In addition, the same comparison is made for the 23 GeV photon dataset in Figure 4.15. In that Figure there is a clear distortion of the χ^2_{wires} and Δx variables due to the presence of the second EM shower in a 1 tower event. The other variables are consistent with the electron hypothesis. Since the 23 GeV photon trigger makes no cuts on these variables, we impose none offline.

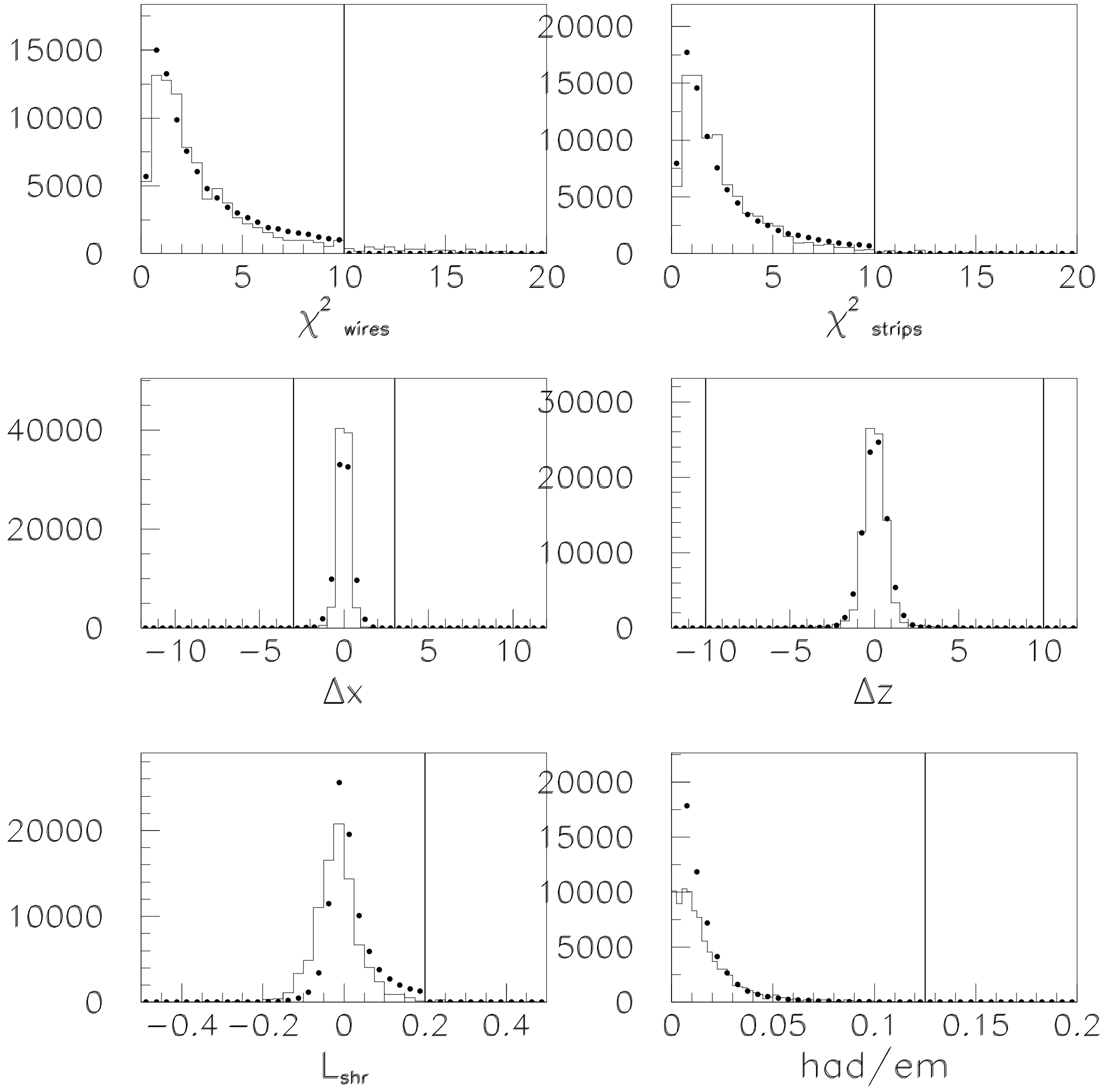

Figure 4.14: The six electron ID variables. The solid histograms are the electron ID variables for $Z \rightarrow e^+e^-$ electrons in the data, and the points are for the final 8 GeV conversion data sample. The vertical lines indicate the location of the cut applied by the Level 3 trigger to the 8 GeV electron data. The L_{shr} variable is skewed for the conversion electrons due to the presence of π^0s in the data sample, and *had/em* is larger for Z electrons due to the leakage energy expected for high E_T showers.

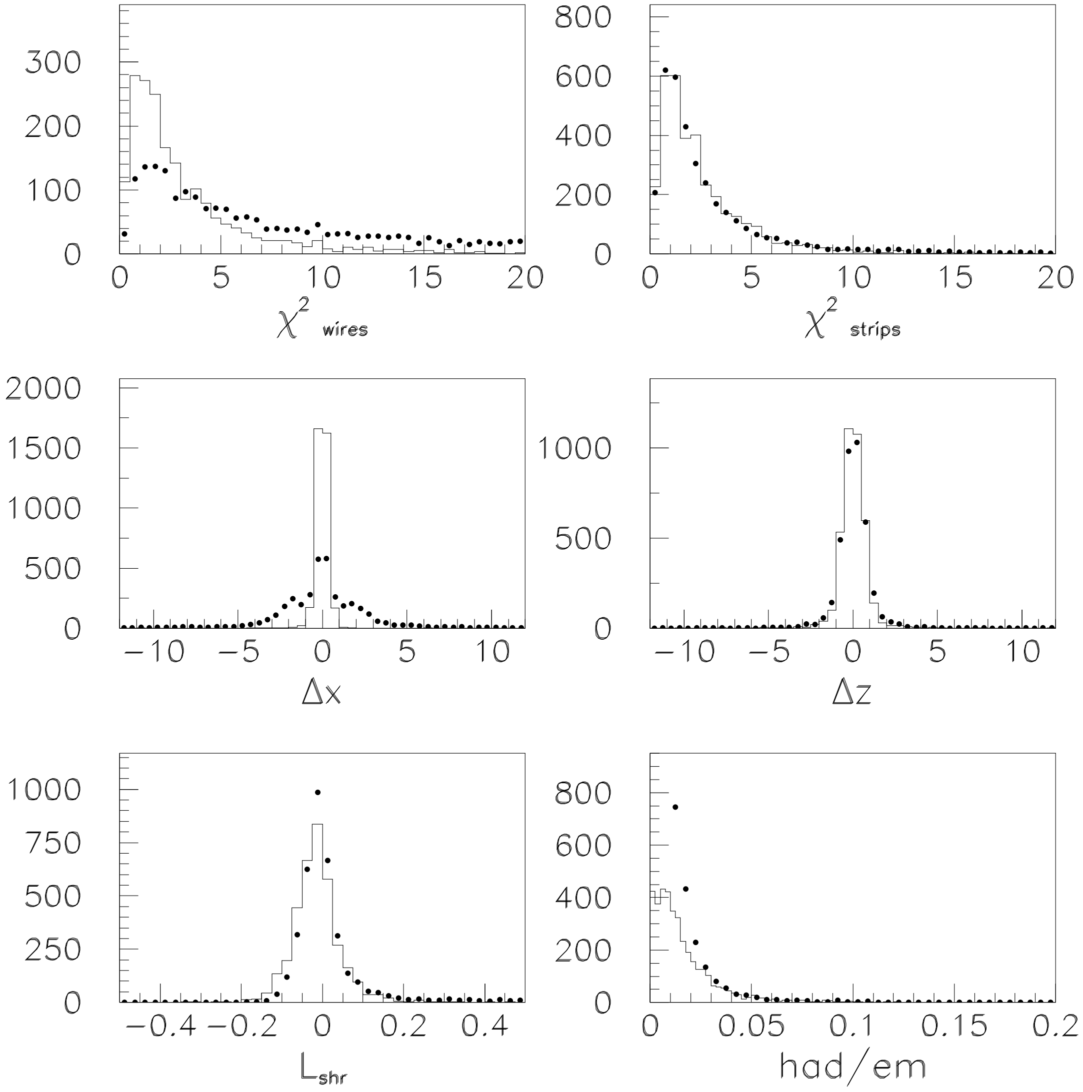

Figure 4.15: The six electron ID variables. The solid histograms are the electron ID variables for $Z \rightarrow e^+e^-$ electrons in the data, and the points are for the final 23 GeV conversion data sample. The χ^2_{wires} and Δx distributions are distorted for this 1 tower data due to the presence of the second EM shower. We make no cuts on these variables for this data.

4.3.2 Conversion identification cuts

We begin the offline data reduction with a search for events containing conversions. We calculate *sep* and $\Delta \cot\theta$ for each pair of opposite sign CTC tracks. We accept as conversion candidates track pairs which satisfy $|sep| < 0.3$ cm and $|\Delta \cot\theta| < 0.05$.

The *sep* and $\Delta \cot\theta$ distributions for conversion candidates occurring in the CTC inner cylinder are shown in Figure 4.10, along with the cut values.

Candidates which pass the *sep* and $\Delta \cot\theta$ cuts are then vertexed. The vertexing routine makes two quality cuts before attempting the vertex fit. The first requires that the z_0's of the two tracks differ by no more than 20 cm. The second requires that the initial guess for the radius of conversion be greater than -2.0 cm. The initial guess radius of conversion is the radius at which the raw CTC tracks are parallel to each other. This radius is considered negative if the momentum vector of the photon points toward the beam spot instead of away from it.

We apply the following geometric and kinematic cuts to the conversion candidate:

- $p_T^{sec} > 0.4$ GeV
- $2.0 < r_{cnv} < 30.0$ cm
- $|\eta| < 0.9$

p_T^{sec} is the p_T of the softer of the two conversion tracks. The p_T^{sec} cut insures that both tracks are in the plateau region of the CTC tracking efficiency. r_{cnv} is the vertexed radius of conversion, and η is the pseudo-rapidity of the conversion photon. The lower limit on r_{cnv} removes $\pi^0 \rightarrow e^+e^-\gamma$ decays and $\gamma^* \rightarrow e^+e^-$ events from the data sample.

Finally, for the 8 GeV electron data we require that the higher p_T conversion track (trigger electron) point at a CEM cluster, and that the lower p_T track (secondary) point at a separate CEM tower (2 tower requirement). The trigger electron is required to extrapolate to within 17.5 cm of the tower center, while the secondary track is required to be more than 31.5 cm away from the tower center. (The tower edge is located at 24.2 cm.)

- $|x_{el}| < 17.5$ cm
- $|x_{sec}| > 31.5$ cm

4.3.3 Electron cuts

We make several offline cuts to the CEM cluster which is associated with the conversion candidate. We require that the cluster be contained within the fiducial volume of the CEM, which excludes the following regions:

- local $|x| > 21.0$ cm (wedge edge)
- local $|z| < 9cm$ (90° crack)
- local $|z| > 217cm$
- tower 7 of chimney module

Finally, we require that the electron z_0 (as measured by the VTX) be within 60 cm of the center of the detector. This cut insures that the projective tower geometry of the calorimeter remains valid for the event.

4.3.4 Isolation cuts

The goal of this thesis is to measure the cross section for isolated prompt photons. The term 'isolated' refers to the energy of other particles which are created in the same direction as the photon. The primary backgrounds to the prompt photon signal are π^0 and η decays to two photons. Since π^0's and η's are hadronic particles, they are produced primarily in jets, particularly at high p_T. Therefore, to reject background while retaining signal we eliminate events in which the conversion candidate is found near other energy deposits in the calorimeter.

We make two isolation cuts on the conversion: a cut on $E_T^{cone0.4}$ and N_{trk}. For the 2 tower conversion data the $E_T^{cone0.4}$ cut has two possibilities. If the secondary track extrapolates to a tower which is outside the 0.4 cone, then we require $E_T^{cone0.4} < 1.0$ GeV. However, if the secondary track is within the 0.4 cone, then we exclude from the cone energy sum that tower and its closest neighbor in η. To account for the loss of area, we lower the cut value to 0.87 GeV. This value was chosen to produce the same efficiency for signal as the 1.0 GeV cut in the standard case. The efficiency study is described in section 7.2.5.

The $E_T^{cone0.4}$ distribution of the two datasets is shown in Figure 4.16.

The second isolation cut is on N_{trk}, the number of three dimensional tracks which extrapolate to the CEM cluster. In 2 tower events we require $N_{trk} = 1$ to eliminate events with extraneous tracks.

4.3.5 $\not{E}_T$ cut

In the 8 GeV electron data we require $\not{E}_T < 25$ GeV. This cut reduces a background due to $W \rightarrow e\nu$ events which populates the 2 tower case at high p_T. This background is described in section 9.2. The $\not{E}_T$ distribution of the data is shown in Figure 4.17.

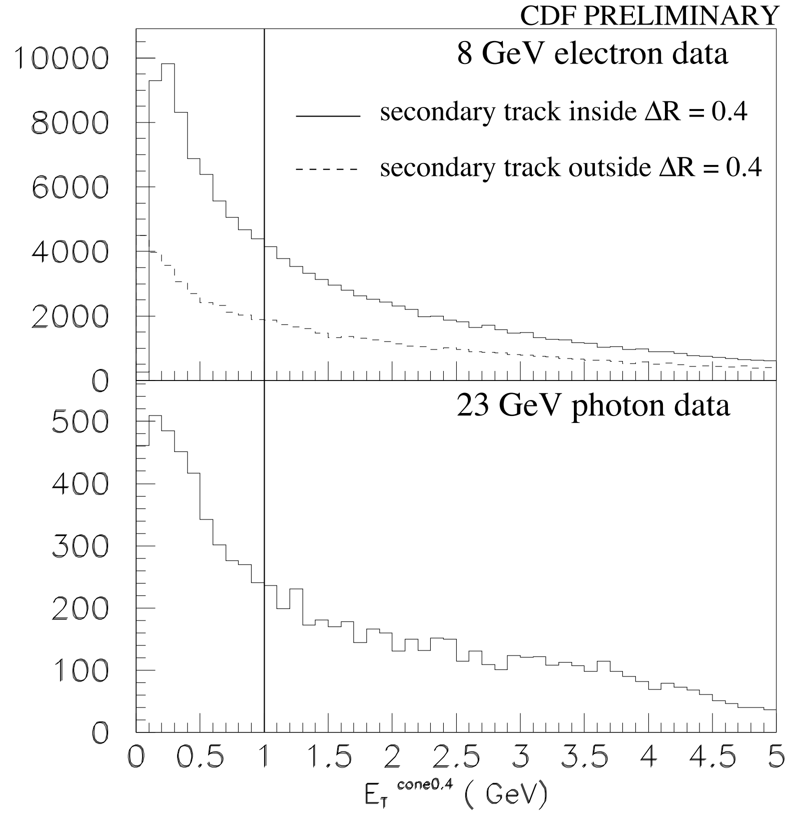

Figure 4.16: The $E_T^{cone0.4}$ distributions of the two datasets. The vertical line marks the cut value. Top: the 8 GeV electron data (2 tower). In this dataset $E_T^{cone0.4}$ is shown with the soft secondary track inside and outside the cone. When the track is inside the cone, the cut is lowered from 1.0 GeV to 0.87 GeV to account for the loss of two towers from the sum. In this plot the data is shown shifted by 0.13 GeV so that the cut for both cases appears at 1.0 GeV. Bottom: the 23 GeV photon data (1 tower).

4.3.6 8 GeV electron data selection summary

The 8 GeV electron data selection is summarized in Table 4.1, and the number of events remaining after each cut are listed in Table 4.2.

8 GeV electron data	
Level 1	8 GeV trigger tower
Level 2	8 GeV Level 2 CEM cluster 7.5 GeV CFT track XCES cluster
Level 3	$E_T > 8.0$ GeV $p_T > 6.0$ GeV
Fiducial (2 tower)	$\|x_{el}\| < 17.5$ cm $\|x_{sec}\| > 31.5$ cm 9 cm $< \|z\| <$ 217 cm chimney tower excluded $\|z_0\| < 60$ cm
Conversion	$\|sep\| < 0.3$ cm $\|\Delta \cot\theta\| < 0.05$ $p_T^{sec} > 0.4$ GeV $\|\eta\| < 0.9$ 2 cm $< r_{cnv} <$ 30 cm successful vertex fit
Electron	$E_T > 8.0$ GeV $p_T^{el} > 6.0$ GeV $l_{shr} < 0.2$ $had/em < 0.125$ $\Delta x < 3.0$ cm $\Delta z < 10.0$ cm $\chi^2_{wires} < 10$ $\chi^2_{strips} < 10$
Isolation	$E_T^{cone0.4} < 1.0$ or 0.87 GeV $N_{trk} = 1$
$\not\!\!E_T$	$\not\!\!E_T < 25$ GeV

Table 4.1: 8 GeV electron dataset selection.

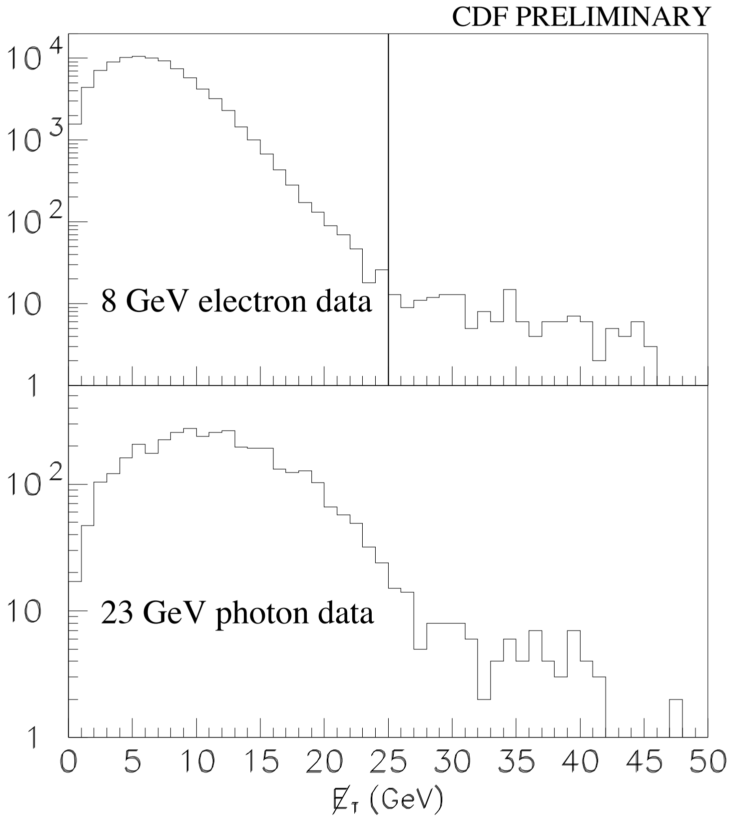

Figure 4.17: The $\not\!\!E_T$ distribution of the two datasets. Top: the 8 GeV electron data (2 tower). The vertical line marks the $\not\!\!E_T$ cut placed on this data. Bottom: the 23 GeV photon data (1 tower). We make no $\not\!\!E_T$ cut on this dataset.

4.4 23 GeV photon sample selection

The 23 GeV photon sample selection similar to the 8 GeV electron sample, but with fewer cuts. As discussed in section 4.3.1, this trigger makes no electron ID cuts at Level 3, and we impose none offline. We apply the same conversion cuts as in the 8 GeV electron case, except that we require that the events be 1 tower only:

- $|x_{el}| < 17.5$ cm
- $|x_{sec}| < 17.5$ cm

Otherwise the fiducial cuts are the same. The isolation cuts on the 23 GeV photon data are simple: we require $E_T^{cone0.4} < 1.0$ GeV and $N_{trk} = 2$. We make no $\not\!\!E_T$ cut on this dataset. The 23 GeV photon data selection is summarized in Table 4.3, and the number of events remaining after each cut is listed in Table 4.4.

Selection	number of events
pass Levels 1,2,3	4,738,521
conversion with CEM cluster	1,250,597
2 cm $< r_{cnv} <$ 30 cm	1,015,386
$p_T^{sec} > 0.4$ GeV	971,219
$\|\eta\| < 0.9$	809,426
central fiducial CEM cluster	756,404
2 tower	367,040
$\|z_0\| < 60$ cm	353,935
$\not{E}_T < 25$ GeV	353,135
$E_T > 8$ GeV, $p_T^{el} > 6$ GeV	343,370
electron ID cuts	334,033
10 GeV < photon $p_T <$ 65 GeV	299,028
$E_T^{cone0.4} < 1.0$ GeV	106,532
$N_{trk} = 1$	89,412
0.5 < E/p < 2.0	88,662

Table 4.2: 8 GeV electron data reduction

23 GeV photon data	
Level 1	8 GeV trigger tower
Level 2	23 GeV Level 2 CEM cluster neural net isolation XCES cluster
Level 3	no requirements
Fiducial (1 tower)	$\lvert x_{el}\rvert < 17.5$ cm $\lvert x_{sec}\rvert < 17.5$ cm 9 cm $< \lvert z\rvert <$ 217 cm chimney tower excluded $\lvert z_0\rvert < 60$ cm
Conversion	$\lvert sep\rvert < 0.3$ cm $\lvert\Delta \cot\theta\rvert < 0.05$ $p_T^{sec} > 0.4$ GeV $\lvert\eta\rvert < 0.9$ 2 cm $< r_{cnv} <$ 30 cm successful vertex fit
Electron	$E_T > 28$ GeV $p_T > 8$ GeV
Isolation	$E_T^{cone0.4} < 1.0$ GeV $N_{trk} = 2$

Table 4.3: 23 GeV photon dataset selection.

Selection	number of events
pass Levels 1,2	2,416,846
conversion with CEM cluster	255,380
2 cm $< r_{cnv} <$ 30 cm	173,795
$p_T^{sec} > 0.4$ GeV	167,079
$\lvert\eta\rvert < 0.9$	143,237
central fiducial CEM cluster	137,187
1 tower	33,711
$\lvert z_0\rvert < 60$ cm	32,493
$E_T > 28$ GeV, $p_T^{el} > 8$ GeV	17,787
30 GeV < photon $p_T <$ 65 GeV	14,416
$E_T^{cone0.4} < 1.0$ GeV	3,911
$N_{trk} = 2$	3,115
0.5 < E/p < 2.0	2,775

Table 4.4: 23 GeV photon data reduction

Chapter 5

Monte Carlo Simulation

In this chapter we describe the Monte Carlo simulations used to understand the data. In the direct photon cross section measurement the Monte Carlo serves two main purposes: it predicts the E/p distributions of signal and background, and it calculates the geometric acceptance for the single photon signal. Therefore the Monte Carlo plays a crucial role in both the signal extraction and in the cross section calculation.

In this thesis we measure the photon cross section using events in which the photon has converted into an electron-positron pair in the material of the inner detector. The manner in which the photon energy is divided between the final state electron and positron is known as the conversion asymmetry. Many of the offline geometrical cuts that we make, as well as the 8 GeV electron trigger, bias the observed asymmetry of the of the conversions. To infer the total cross section it is important that we understand these biases. To simulate the bias we use a theoretical calculation of the conversion asymmetry distribution as a central part of the Monte Carlo. In this way we correctly account for the correlation between the conversion asymmetry and the detector geometry cuts.

To perform the background subtraction we fit the E/p distribution observed in the data to the sum of the E/p distributions for signal and background as predicted by the Monte Carlo. Therefore the reliability of the background subtraction is determined by the quality of the E/p simulation in the Monte Carlo. The detectors used to measure E/p, the CEM and CTC, are among the best understood at CDF. The behavior of both has been calibrated extensively in the data with $Z \to e^+e^-$, $W \to e\nu, \mu\nu$, and $Z, J/\psi, \Upsilon \to \mu^+\mu^-$ events.

We expect the single photon signal to have an E/p distribution which is sharply peaked at unity, with a width consistent with the known resolutions of the CEM and CTC. This distribution is simple enough that it could plausibly be modeled as a gaussian without a simulation. We use the Monte Carlo's prediction in order to include small effects like bremsstrahlung.

Background events also have a simple E/p shape. In the case of a two photon meson decay, the calorimeter will measure the energies of both photons, and thereby observe the transverse momentum of the meson. The tracking chamber, however, reconstructs the momentum of only one of the final state photons. Therefore, by comparing the CEM energy to the CTC momentum we measure the decay asymmetry of the meson. Meson decay kinematics are well known, so we expect the Monte Carlo to give reliable predictions for the meson E/p.

There are two cases where effects which are not modeled by the simulation can have important p_T dependent consequences on the E/p shape and acceptance: the trigger efficiency and the CTC tracking efficiency. Both of these efficiencies have been measured in the data previous to this work, and the authors of those studies report the efficiencies as a function of the E_T and p_T of the electron and track. We apply these parameterized forms to the results of the Monte Carlo simulation to assess their effects.

Although the detector simulation that we employ simulates most of the variables that we use to isolate our data sample, for many of those variables the simulation gives predictions that can only be trusted qualitatively. To evaluate the signal efficiency of most of our cuts we do not rely on the Monte Carlo. Rather we use a variety of studies done in the data, and these studies are described in chapter 7.2.

The CDF detector simulation that we use is known as QFL. This set of routines produces simulated data files which have the same format as real data files, and therefore the results of the simulation can be analyzed with the same offline reconstruction code. In order to maximize the speed and efficiency of the simulation, QFL does not attempt to simulate in detail the physical processes that occur inside each detector during an event. Instead, it takes the 'true' generator level quantities and smears them by the known resolutions of the detectors to produce simulated measurements. For example, the CTC simulation takes the true trajectory of a charged particle and produces a smeared 'track' without generating a set of hits or running the track reconstruction code. This approach is adequate for most purposes, and it has the advantage of reproducing exactly the resolution observed in the data. We will note the limitations of this type of simulation when appropriate. Also, we have altered several QFL routines in order to better simulate the photon cross section measurements. We will note these cases in passing.

5.1 CEM simulation

The CEM simulation adds up the energies of the electrons and photons which land in each tower of the CEM and smears the sum according to equation 3.4. The output of the simulation has the same format as real data from the detector, and the same electron reconstruction code will subsequently cluster groups of CEM towers into CEM clusters. We now discuss several subtleties of the CEM simulation.

Each CEM tower is observed by two photomultiplier tubes, one at each azimuthal end. The energy in the tower is calculated according to the geometric mean of the total charges integrated by the two PMTs. The energy seen by each phototube depends strongly on the distance between the phototubes and the location of the electromagnetic shower in the tower due to the light attenuation of the scintillator. As discussed in section 4.1.1, by taking the geometric mean of the two PMTs, we get an energy measurement which is largely independent of the position of the EM cluster within the tower. A small position dependence remains (a few percent variation from the center of the tower to the edge), and this is removed later by the energy correction code.

While QFL attempts to simulate the measurement of each CEM phototube, the only quantity which it should reproduce well is the geometric mean. QFL includes the form of the residual position dependence of the energy measurement, so we subsequently run the energy correction code on the Monte Carlo as well as the data.

The lack of a well calibrated model for each individual PMT has important consequences in events where two EM showers occur in the same tower but well separated from each other. In this case the geometric mean will not give an unbiased estimate of the total energy. To predict that bias it is necessary to model the two PMTs individually, and QFL cannot do this exactly. Since in 1 tower conversion events we have the electron and positron showers in the same CEM tower, we must consider systematic effects which may result from the lack of a better PMT simulation.

At the edge of the tower the response of the CEM falls rapidly. QFL models this with a steep function fit from test beam data, but the slope of the function is too large to reproduce exactly. We will avoid events in the data which have energy deposited near the edge of the tower.

A real EM shower will typically deposit energy in two neighboring CEM towers. The manner in which the energy is shared between the two depends on the location of the energy deposit and the angle of incidence of the initiating particle. The L_{shr} variable describes whether the energy sharing in a given cluster is consistent with expectations for a single shower. QFL's simulation of the energy sharing is not good enough to compare with data, so only the sum of the tower energies in a cluster is reliable. A similar statement is true of the energy which leaks out the back of the CEM into the hadronic calorimeter.

5.2 CES simulation

As described in section 3.4.1, the CEM has a layer of strip and wire chambers (CES) embedded at a depth of six radiation lengths, a location which corresponds to shower maximum for typical shower energies encountered at the Tevatron. The CES gives us finely segmented information about the position and transverse shape of a shower occurring inside a single CEM tower. Only a detailed shower simulation could hope to predict the behavior of these chambers from first principles. In QFL the strip and wire energy observations are simulated by drawing from a 'frozen shower' database of CES measurements done with single test beam electrons. This insures that the Monte Carlo gives an accurate representation of the behavior of the real detector. In events where two showers overlap in the CES, the energy from two of the frozen showers is summed. The same cluster reconstruction code runs on both the data and Monte Carlo, and this code calculates electron ID variables such as χ^2_{wires}, χ^2_{strips}, Δx, and Δz.

In the data the CEM and CES measurements are correlated because they observe the same shower. For example, if a particular shower fluctuates such that the CEM measurement is high, then the energy observed in the CES may also be high. In QFL the CEM and CES simulations are performed separately from each other, so there can be no correlations between the two. We do not use the CES energy measurement in this thesis, so we do not expect this effect to be important.

However, there is an important correlation between the CES electron ID measurements and E/p for a $\pi^0 \rightarrow \gamma\gamma$ event. This is because the E/p of a meson is a measurement of its decay asymmetry, and that asymmetry determines the angle between the two photons as well as their energy sharing. These in turn have a substantial impact on the results of the CES observations. Therefore in the data the E/p and CES measurements are tied together by the decay kinematics of the meson. We expect QFL to understand this correlation because the meson decay is simulated correctly.

The 8 GeV electron trigger that we use makes cuts on CES electron ID variables at Level 3. We will apply these cuts in the Monte Carlo in order to predict their effect on the E/p distributions of signal and background. However, when determining the efficiency of these cuts to retain signal, we will not rely on QFL to make predictions. Instead we will measure their efficiency in the data with a sample of electrons where the cuts have not been applied. This study is described in section 7.2.3.

5.3 CTC simulation

The QFL simulation of the central tracking chamber (CTC) takes the true track parameters of charged particles with $p_T > 400$ MeV, and smears them according to the resolution of the CTC. The track produced by the simulation is identical in format to that produced by the tracking reconstruction code which is runs on the data. Therefore the same analysis routines, such as conversion finding or electron reconstruction, can run on the data and Monte Carlo.

The smearing of the five track parameters is done by calculating a 5×5 covariance matrix for each track. The covariance matrix for a track depends on the location and accuracy of the the hits which make up the track. In QFL the resolution of each hit is set to 220 microns, a value which was observed in the hit residuals in the data. To simulate the hit pattern for a track, QFL first calculates which of the 84 layers of wires the track passed through. (A track may pass through less than 84 layers if it exits the chamber through the endplate, but this is uncommon for a central conversion track.) To get the final hit pattern QFL throws away the hits on some wires based on the hit efficiencies of each wire layer observed in the data. This hit pattern then determines the track covariance matrix.

Once the covariance matrix is calculated, QFL draws a set of five random numbers which have the exact correlations described by the covariance matrix. These random numbers are added to the true track parameters of the Monte Carlo particle to produce the final smeared track.

We now discuss some limitations of QFL's tracking simulation.

5.3.1 CTC tracking efficiency

QFL produces a track for every charged particle with $p_T > 400$ which passes through the volume of the CTC. The tracking efficiency of the real CTC, however, turns on between 300 and 400 MeV, and plateaus around 95%, as shown in Figure 5.1. This plot shows the results of a study of the CTC tracking efficiency done by the University of Toronto[30]. The study was performed by embedding the hits from a Monte Carlo track inside the hit data from a real event. Then the tracking reconstruction code is run, and the efficiency for finding the new track is measured as a function of the p_T of the track. The curves shown here represent the average tracking efficiency over the course of Run Ib.

The tracking efficiency is slightly different for positive and negative tracks. This is due to the fact that the cells of the CTC are tilted at 45° with respect to the radial direction in the direction that positively charged particles bend in the magnetic field. Therefore, positive particles are less likely to cross cell boundaries than negative particles, so they have a slightly larger hit efficiency.

Since QFL does not take account of the tracking efficiency above 400 MeV, we impose the efficiency during the data analysis stage by rejecting events randomly according to the efficiency shown in Figure 5.1. This makes up one part of our efficiency calculation. Furthermore, we place a lower p_T cut of 400 MeV on all tracks in the data and Monte Carlo so that the exact form of the efficiency turn-on does not influence our measurement.

5.3.2 Two track separation

A second limitation of QFL's CTC simulation is the neglect of hit level effects. One such effect which could have a significant impact on the photon cross section measurement is the two-track separation. In order for two nearby tracks to be distinguished they should be separated by approximately three millimeters. Since the electron and positron from a photon conversion are produced parallel to each other and are only separated by the effect of the magnetic field, in many cases they are not distinguishable until the second or third layer of the CTC. Although we do not

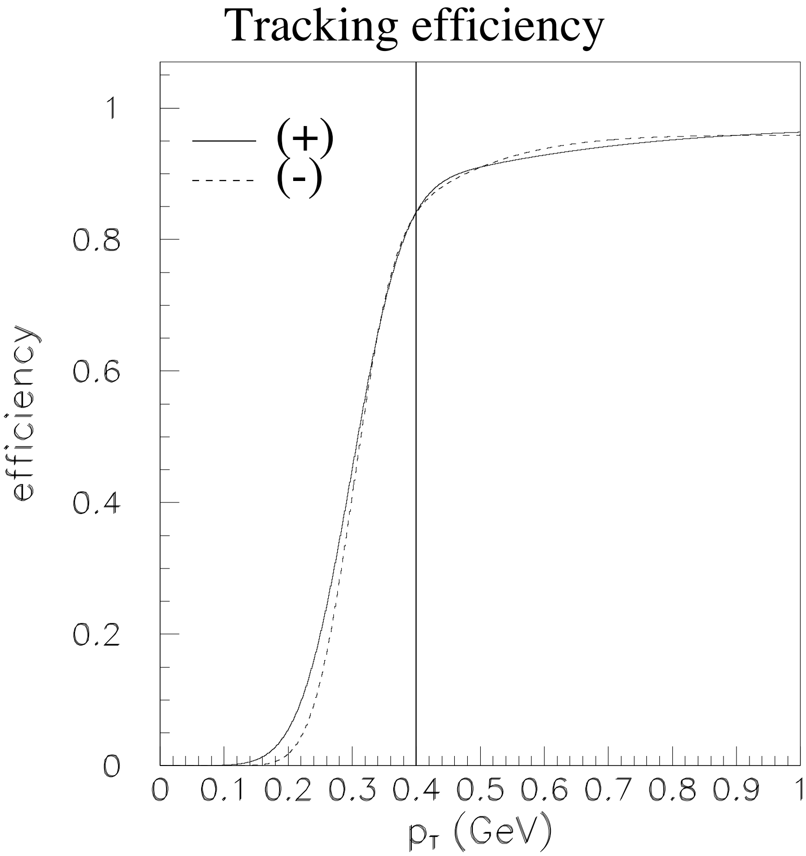

Figure 5.1: The CTC tracking efficiency as a function of the track p_T. The two curves correspond to positive and negative tracks. The vertical line at 0.4 GeV shows the value of the lower p_T cut placed on all conversion tracks. The curves plotted here are parameterizations of the efficiency measured in track embedding studies done by the University of Toronto [30].

expect a loss of tracking efficiency due to this effect, the overlapping hits produced by the two tracks can result in unusual tracking systematics which are not seen in generic tracks.

One consequence of this in the data is shown in Figure 4.10, where the *sep* distribution of CTC inner cylinder conversion candidates in the data is shown. *sep* is the distance between the two conversion tracks at the point where they are parallel, so the true value of *sep* in all events should be zero. In the Figure the mean value of *sep* is clearly shifted away from zero. This indicates that the conversion tracks reconstructed in the data must be distorted. As shown in Figure 5.2, QFL does not predict such a bias. However, also shown in Figure 5.2 is the result of a more sophisticated CTC simulation (known as CDFSIM) which generates hits to be reconstructed by the tracking algorithm. The *sep* distribution of conversions simulated with CDFSIM shows a similar negative bias as seen in the data.

As the *sep* variable indicates, the tracks found in the data have some subtleties which are not understood by QFL. As discussed in section 4.1.2, conversion track distortion also produces a bias on the p_T measurement. We will consider this when evaluating the systematic errors on the cross section measurement.

5.3.3 CTC covariance scale

One of the mysteries which remain in regard to the behavior of the CTC is the exact nature of the track parameter errors. Since the CTC provides up to 84 hits on a track, it is simple to measure the hit resolution in the data by removing a single wire from the track fit and comparing the extrapolated track position to the observed hit location. The track parameter errors should be calculable based on this hit resolution and hit efficiencies as discussed above. However, it was found that in order to explain the width of resonances such as the J/ψ, and to attach SVX hits to CTC tracks, the calculated covariance matrix of CTC tracks must be inflated by about a factor of two.

Although the source of this 'CTC covariance scale' is not understood, we must account for it in our CTC simulation. We use the E/p distribution of high E_T conversions to determine the best covariance scale for our measurement. We select conversion events from the 8 GeV electron trigger which have p_T between 36 GeV and 46 GeV. In this p_T range the energy resolution of the CEM is much better than the momentum resolution of the CTC, so we expect the width of the E/p peak to be determined primarily by the CTC resolution. We require that the the electron and positron tracks point toward separate CEM towers. In figure 5.3(a) the E/p distribution of the data is compared to the Monte Carlo which has been generated with a CTC covariance scale of 1.8. To match the Monte Carlo to the data we fit the E/p peak to a gaussian between $0.85 < E/p < 1.15$. In Figure 5.3(b) we show the results of the Monte Carlo fit as a function of the Monte Carlo covariance scale. Also shown as a horizontal line is the value observed in the data. We find that the preferred covariance scale is 1.8, a value which is not atypical for CDF analyses.

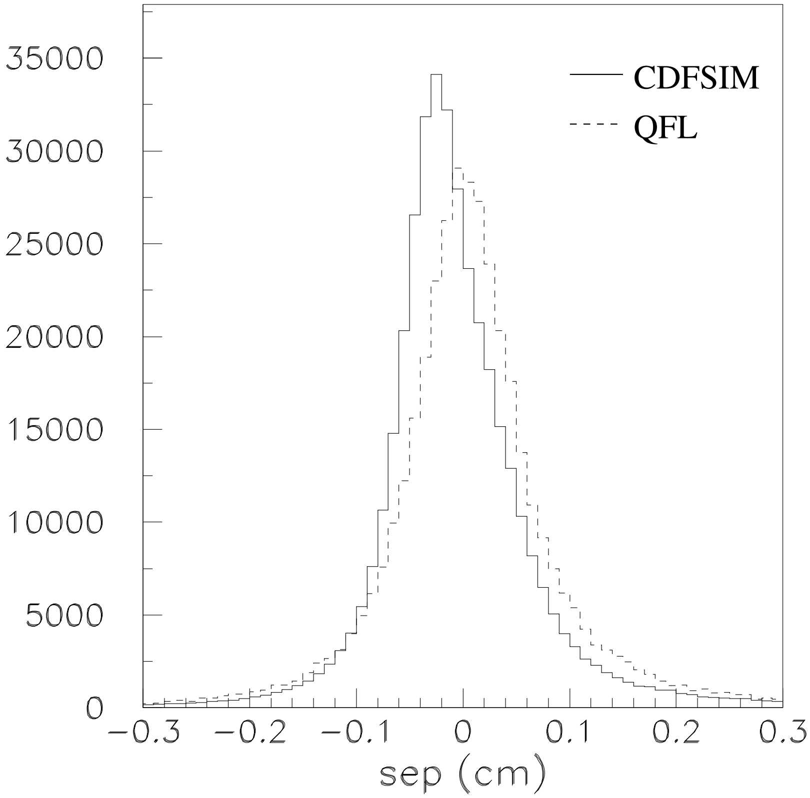

Figure 5.2: The x-y separation (*sep*) of photon conversion tracks as simulated by QFL and by CDFSIM. CDFSIM generates hits on wires which are reconstructed by the tracking code, whereas QFL simulates tracking by simply smearing the true track parameters. CDFSIM predicts that *sep* will be biased towards negative values as seen in the data, and QFL does not.

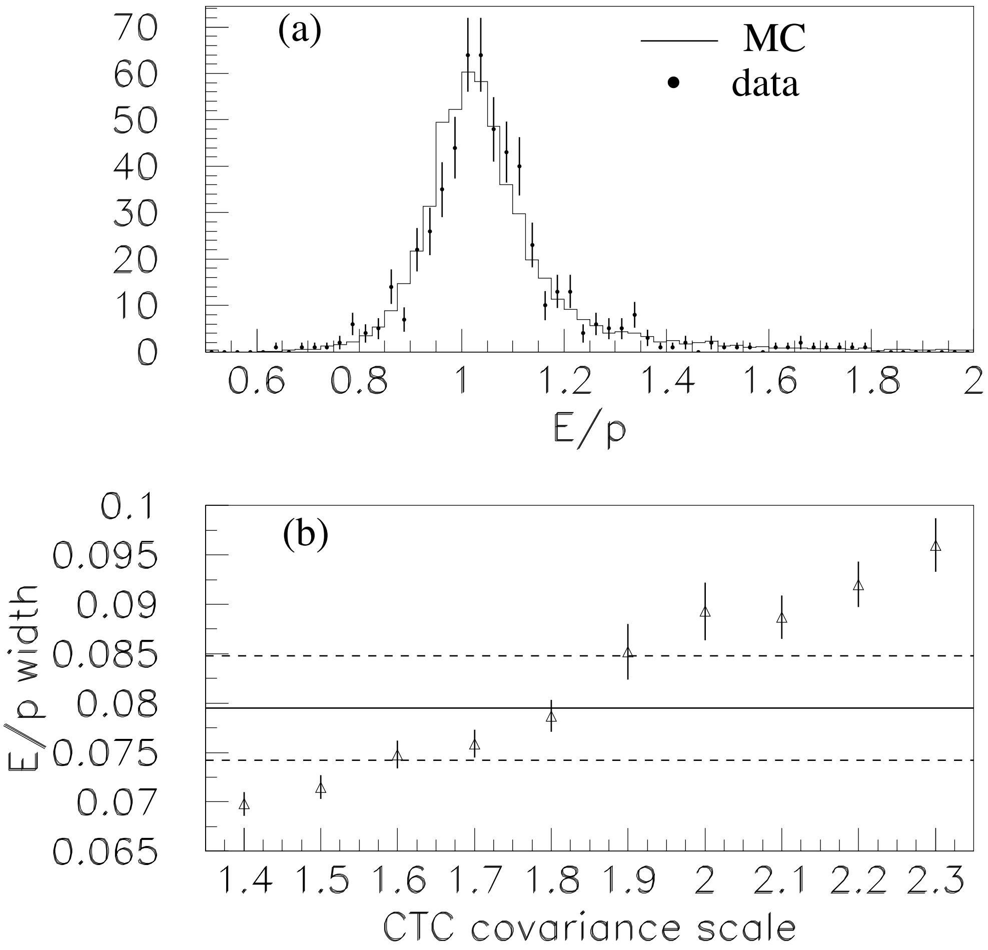

Figure 5.3: Setting the CTC covariance scale of the Monte Carlo. (a) The E/p distribution of the data compared to the Monte Carlo for 36 GeV $< p_T <$ 46 GeV. In this Figure the Monte Carlo was generated with a covariance scale of 1.8. (b) The width of a gaussian fit to the Monte Carlo E/p distribution between 0.85 and 1.15 as a function of the Monte Carlo CTC covariance scale. The horizontal line is the width returned by a similar fit in the data.

5.4 Trigger parameterization

QFL does not implement a simulation of the CDF trigger system. A separate software package, known as TRGSIM, attempts to simulate the CDF trigger hardware, but this simulation is not reliable enough to use in physics measurements. Consequently CDF measurements which require knowledge of the trigger behavior rely on trigger studies performed in the data with an independent data sample. This is the approach that we take in the photon cross section measurement.

Typically the efficiency of the a trigger can be parameterized in terms of one or more simple variables. These variables are chosen to be the reconstructed physics variables which correspond most closely to the detector information on which the trigger hardware based its decision. For example, the Level 1 and Level 2 electron triggers pass or fail events based on the energy seen in the calorimeter and the momentum of the tracks which are found by the track reconstruction hardware (CFT). Therefore the electron triggers efficiency is measured in terms of the offline E_T and p_T of the reconstructed electron candidate. When parameterized by appropriate variables the trigger efficiency should appear as a sharp turn-on followed by a plateau which represents the asymptotic efficiency.

In the photon cross section measurement we use an 8 GeV electron trigger and a 23 GeV photon trigger. The efficiencies of these triggers were measured previous to this work, and we adopt the results of those studies[16],[31].[1] For the 23 GeV photon trigger we do not know the functional form of the trigger efficiency turn-on, so we avoid events which are not in the plateau regions with lower cuts on the E_T of the event. For the 8 GeV electron trigger we retain events in the turn-on region in order to have sensitivity at the lowest possible photon p_T. We use the results of a study which measured the trigger behavior at all E_T and p_T.

In the case of the 8 GeV electron trigger, the requirement of a 7.5 GeV track produces a significant bias on the asymmetry of the conversion when the photon p_T is near the trigger threshold. This track requirement also biases the asymmetry of the meson decay in the case of a $\pi^0 \rightarrow \gamma\gamma$ or $\eta \rightarrow \gamma\gamma$ event, and this has the consequence of cutting off the high E/p tail of the background near the trigger threshold. Therefore the trigger effects both our signal acceptance and the E/p background subtraction. Ultimately we can compare the E/p distributions of data and monte carlo to judge how well the trigger is modeled.

The Level 1 trigger for all of the datasets used in this thesis is an 8 GeV calorimeter trigger. This trigger is known to have an asymptotic efficiency of 100%, and we will not consider it further. The Level 3 electron trigger applies electron ID cuts to the electron candidate. We re-apply these cuts offline, and we measure their efficiency in a separate study described in section 7.2.3.

---

[1] In the case of the 8 GeV electron trigger, the efficiency was measured using a sample of isolated (non-conversion) electrons. We repeated the study with conversion electrons, and found that the trigger behavior is the same.

We now describe the form of each Level 2 trigger efficiency used in the photon cross section measurement.

5.4.1 8 GeV electron trigger

This trigger has three Level 2 requirements: a calorimeter cluster with $E_T > 8$ GeV, a CFT track with $p_T > 7.5$ GeV, and a CES cluster matched to the track. We parameterize the calorimeter and track thresholds in terms of electron E_T and p_T. The CES cluster measurement is correlated with the energy observed in the CEM, and therefore for convenience we parameterize it in terms of E_T as well. In addition, there is a small inefficiency which occurs when an electron hits the calorimeter near a trigger tower boundary. This is also parameterized by E_T. The efficiency curves of these four thresholds were measured with a pre-scaled sample of 5 GeV electrons, and are shown in Figure 5.4. The asymptotic efficiency of the trigger was taken from a sample of volunteer electrons collected with a muon trigger, and was found to be 0.9137 ± 0.0088. This value is consistent with a separate measurement of the asymptotic CFT efficiency.

To apply these results to the Monte Carlo, we calculate the probability of an event passing the trigger based on its E_T and p_T as the product of the curves shown in 5.4 and the asymptotic efficiency. We then randomly reject events based on this probability.

5.4.2 23 GeV photon trigger

This trigger requires a 23 GeV calorimeter cluster, a CES cluster, and that the calorimeter cluster be isolated. The asymptotic efficiency of these requirements was measured with a prescaled sample of events collected with 10 GeV and 23 GeV thresholds without the XCES and isolation requirements. The result is 0.914 ± 0.043, and we randomly reject events in the Monte Carlo according to this probability.

5.5 Material distribution

The distribution of material in the inner detector, which acts as our conversion medium, plays a crucial role in the Monte Carlo because it affects our signal acceptance. The radius of conversion and acceptance become correlated due to the fact that we make cuts on where the conversion tracks are allowed to point in the calorimeter. For example, for events in the 8 GeV electron sample we require that the electron and positron be in separate CEM towers (2 tower requirement). A photon which converts near the origin is more likely to satisfy this requirement than a conversion in the CTC inner cylinder. Therefore to calculate the acceptance for signal we must have a realistic model of the material distribution in the monte carlo.

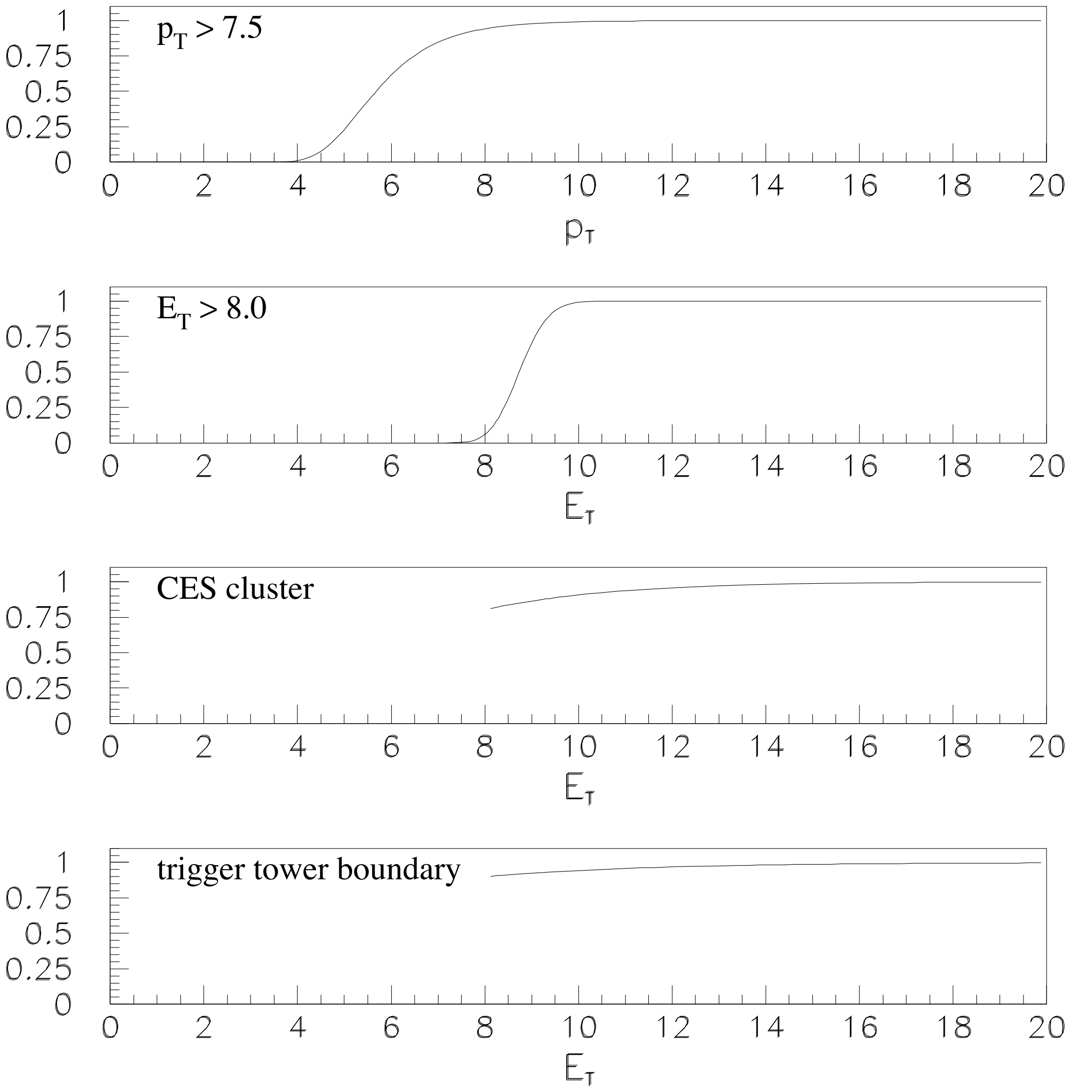

Figure 5.4: The threshold shapes of the 8 GeV electron trigger. The four curves correspond to CFT > 7.5 GeV, CEM > 8 GeV, CES cluster, and trigger tower boundary efficiencies. The asymptotic efficiency, not shown here, is 0.9137 ± 0.0088. The total trigger efficiency is the product of the these functions.

QFL includes a model of the inner detector material based on our knowledge of the construction of the detector. We have altered this model in order to reproduce better the material observed in the data. We have done this by changing the radiation lengths of various structures in the model, and in some cases moving their location. To compare the model to the data we generate direct photon events with PYTHIA, simulate their conversion and reconstruction with QFL, and then compare the reconstructed radius of conversion distribution with that of the data. To do the comparison we apply all the cuts used to isolate our final sample, since some of the cuts will alter the observed radius of conversion distribution.

The material in the Monte Carlo is simulated as a series of thin cylinders. In the data the material is smoothly distributed, and this makes it difficult to compare the radius of conversion distributions directly. Instead we compare the integrated radius of conversion distributions. This is shown in Figure 5.5.

Our final result for the photon cross section is inversely proportional to the material scale of the inner detector through the total conversion probability. For the cross section measurement we do not ask the Monte Carlo to predict the conversion probability. Instead we put in the correct number by hand, which was in measured in data. The measurement of the conversion probability is described in section 8. Therefore our final results are not very sensitive to the material scale in the Monte Carlo.

However, the amount of material also determines the amount of bremsstrahlung, and therefore the material scale can have a small effect on the E/p distribution of the data. Since we use E/p to perform the background subtraction by fitting to Monte Carlo templates, we have set the material scale of the Monte Carlo to reproduce the total conversion probability of the data.

To confirm that the Monte Carlo material scale is correct we compare our results to a separate Monte Carlo developed to measure the mass of the W boson at CDF [37]. In that work it was found that the average number of radiation lengths which $W \rightarrow e\nu$ electrons pass through before the CTC tracking volume is 7.2%. After running the same $W \rightarrow e\nu$ events through our tuned version of QFL we also find an average radiation length of 7.2%.

5.6 Conversion asymmetry

Many trigger and reconstruction effects bias the conversion asymmetry observed in the data, and we rely on the Monte Carlo to account for these effects. Fortunately, the conversion asymmetry is well known both from theory and experiment. The analytic calculation of the asymmetry is shown in Figure 5.6. This plot shows the fraction of the photon's energy which is given to the positron in the conversion process. The asymmetry has a very small dependence on the photon's energy and the atomic number of the conversion medium, and in the Figure these have been set to 30 GeV

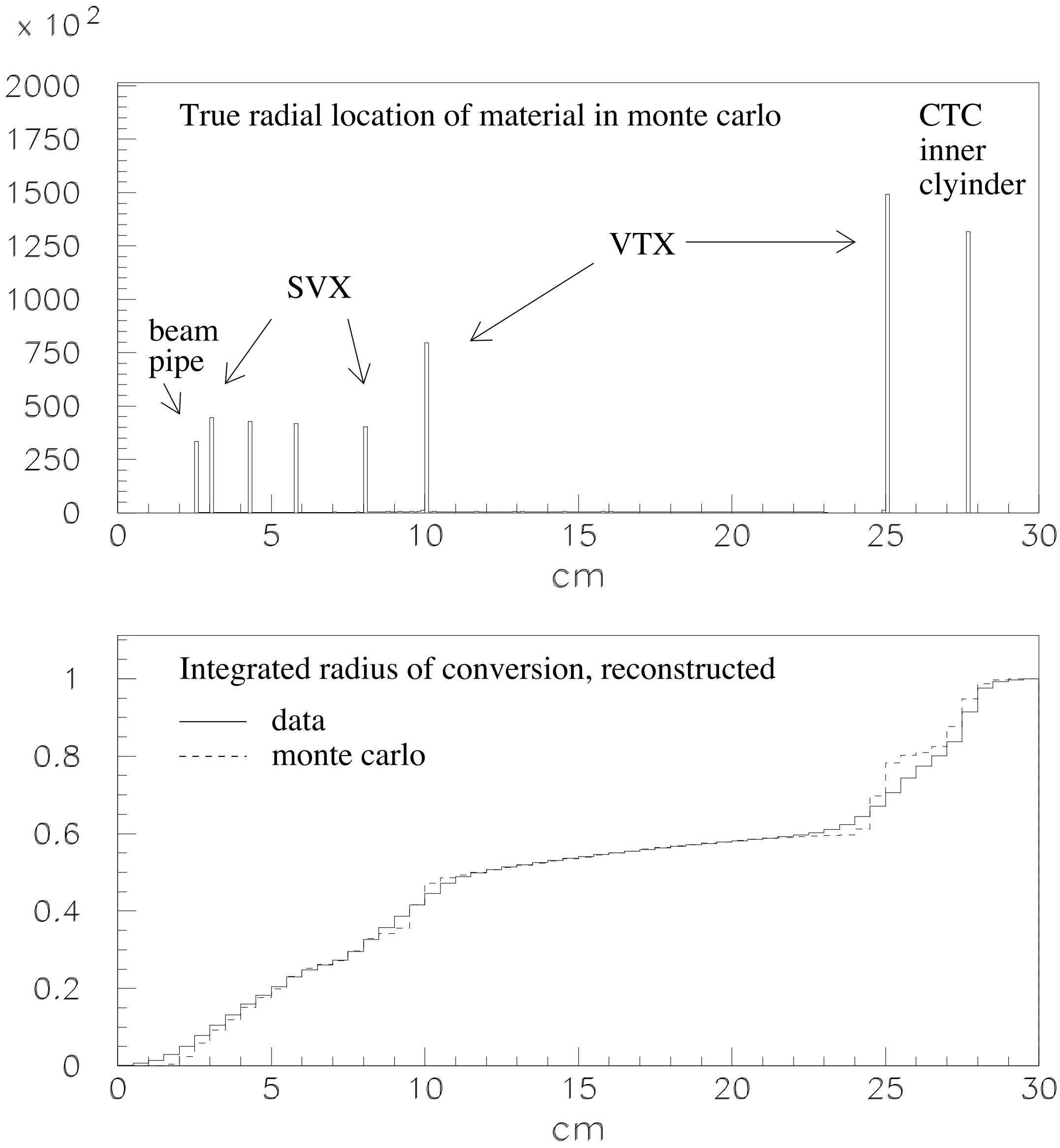

Figure 5.5: The material distribution in the Monte Carlo. The top plot shows the true radial location of the material in the Monte Carlo. The bottom plot shown the integrated radius of conversion in the Monte Carlo after reconstruction compared to that in the data.

and Z = 13. To simulate the conversion process QFL draws a random number which is distributed from 0.0 to 0.5 as shown in Figure 5.6, and assigns that fraction of the photon's energy to the electron or positron. The QFL calculation accounts for the energy dependence of the asymmetry, but all material is assumed to have an atomic number of 13.

5.7 Event simulation

We use PYTHIA version 6.115 to generate our signal Monte Carlo sample of direct photon events. PYTHIA generates a direct photon event whose p_T and η distribution is given by a leading order QCD calculation. PYTHIA also generates a hadronic recoil on the opposite side so that the energy in the event is balanced, but we will not use this part of the simulation in our measurement. We initialize PYTHIA to generate photons with $p_T > 9.0$ GeV and $|\eta| < 1.3$.

To simulate background events we use a single particle generator known as FAKE_EVENT. FAKE_EVENT produces a given particle with a p_T and η spectrum which is chosen by the user. We generate π^0's and η's separately with a power law p_T spectrum. The choice of the power law is discussed in section 5.9. The η spectrum is chosen to be flat from -1.0 to 1.0.

The π^0's decay promptly to $\gamma\gamma$ and γe^+e^- with branching fractions of 98.8% and 1.2 % respectively. η's also decay promptly to a variety of final states, including $\gamma\gamma$ (40 %), $3\pi^0$ (32 %), $\pi^+\pi^-\pi^0$ (23 %), and $\pi^+\pi^-\gamma$ (5%). The $3\pi^0$ mode tends to give a very large E/p outside the signal region, and the charged pion modes are eliminated by the no-extra-tracks requirement on the electron cluster. Therefore the most important decay mode for both the π^0 and the η is the two gamma mode. This two-body decay is calculated in the rest frame of the meson and then boosted into the lab frame.

Both the signal and background Monte Carlos produce events which are symmetric in azimuth, and the location of the collision along the beam axis is chosen randomly with a gaussian of width 30 cm, which matches the data. All particles produced by the generator are then stepped through the detector simulation.

As charged particles pass through the inner detector material model they are allowed to undergo multiple scattering and energy loss due to ionization. In addition, electrons are allowed to undergo bremsstrahlung. The brem length of each electron (the amount of material the electron will pass through before bremming) is chosen randomly upon the electron's creation from an exponentially falling distribution. Since the brem p_T spectrum is steeply falling, the average brem length depends strongly on the minimum brem photon energy which is simulated. In QFL this is set to 100 MeV.

As the electron is stepped through the inner detector a running count is kept of the material it has passed through. The material in each layer is multiplied by $1/\sin\theta$

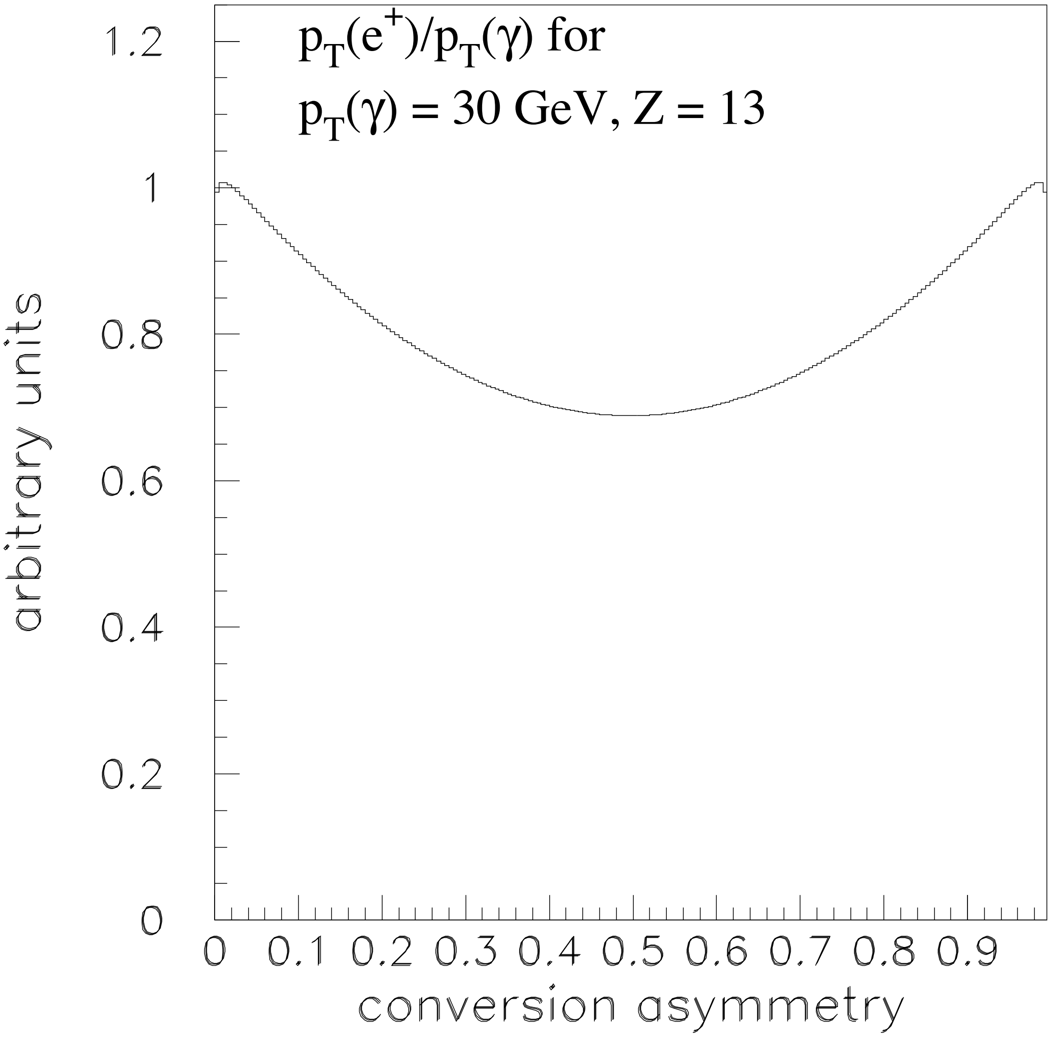

Figure 5.6: The conversion asymmetry distribution. The curve is the differential probability of the positron receiving a given fraction of the photon's energy in the conversion process. The curve is calculated assuming $p_T(\gamma) = 30$ GeV and Z = 13.

, where θ is the polar angle of the electron, to account for the angle of incidence. If in a given layer the material count exceeds the brem length, then the electron gives up some of its energy to a photon. The photon spectrum is given by

$$p(y)\,dy\,dT = \frac{dy\,dT}{y}[(1-y)(\frac{4}{3}+k)+y^2] \tag{5.1}$$

where y is the fraction of the electron's energy which is transferred to the photon and dT is the thickness of the material measured in radiation lengths. k is a small constant which depends on the material, and is set to 3% for the inner detector. The photon is generated parallel to the electron, and is tracked through the detector separately.

To confirm that bremsstrahlung is implemented correctly in the Monte Carlo, we compare the Monte Carlo bremsstrahlung spectrum to equation 5.1. To perform the comparison we generate 100,000 electrons and pass them through a single layer of material at normal incidence. The study is repeated with four different layer thicknesses. As shown in Figure 5.7, the Monte Carlo spectrum agrees well with the analytic formula. In these plots the theoretical prediction has been normalized to the total number of generated events, so the agreement indicates that both the spectrum and the total rate are correct in the Monte Carlo.

All photons are allowed to convert in the inner detector material. This process is handled in a similar fashion as the electron bremsstrahlung. Upon creation of the photon QFL chooses a conversion length from an exponentially falling distribution, the decay constant of which is determined by the conversion cross section. The cross section has a very small dependence on photon energy, and this is taken into account. As the photon is stepped through the inner detector a running count is maintained of the amount of material seen by the photon. If the material count exceeds the conversion length for a given photon, then QFL converts the photon into an electron-positron pair with the asymmetry distribution shown in Figure 5.6. These electrons are subsequently stepped through the rest of the detector independently.

Since conversion electrons are produced inside of material, they should be allowed to brem before exiting their layer of origin. QFL considers the material layers to be infinitely thin, so special precautions are necessary. To account for this possibility, the material count of a conversion electron is initialized upon its creation to a random fraction of the material count of its layer of origin. This insures, for example, that conversion electrons which are created in the final material layer have the opportunity to brem.

Since only about 5% of the produced photons will convert, the generation of a conversion Monte Carlo sample is inefficient. Fortunately, the high p_T photon produced by PYTHIA is the first particle simulated by QFL. We have altered QFL so that if this photon does not convert in the inner detector, then all further simulation of that event is stopped, and another event is generated by PYTHIA. With this convention the CPU time of the simulation is dominated by PYTHIA.

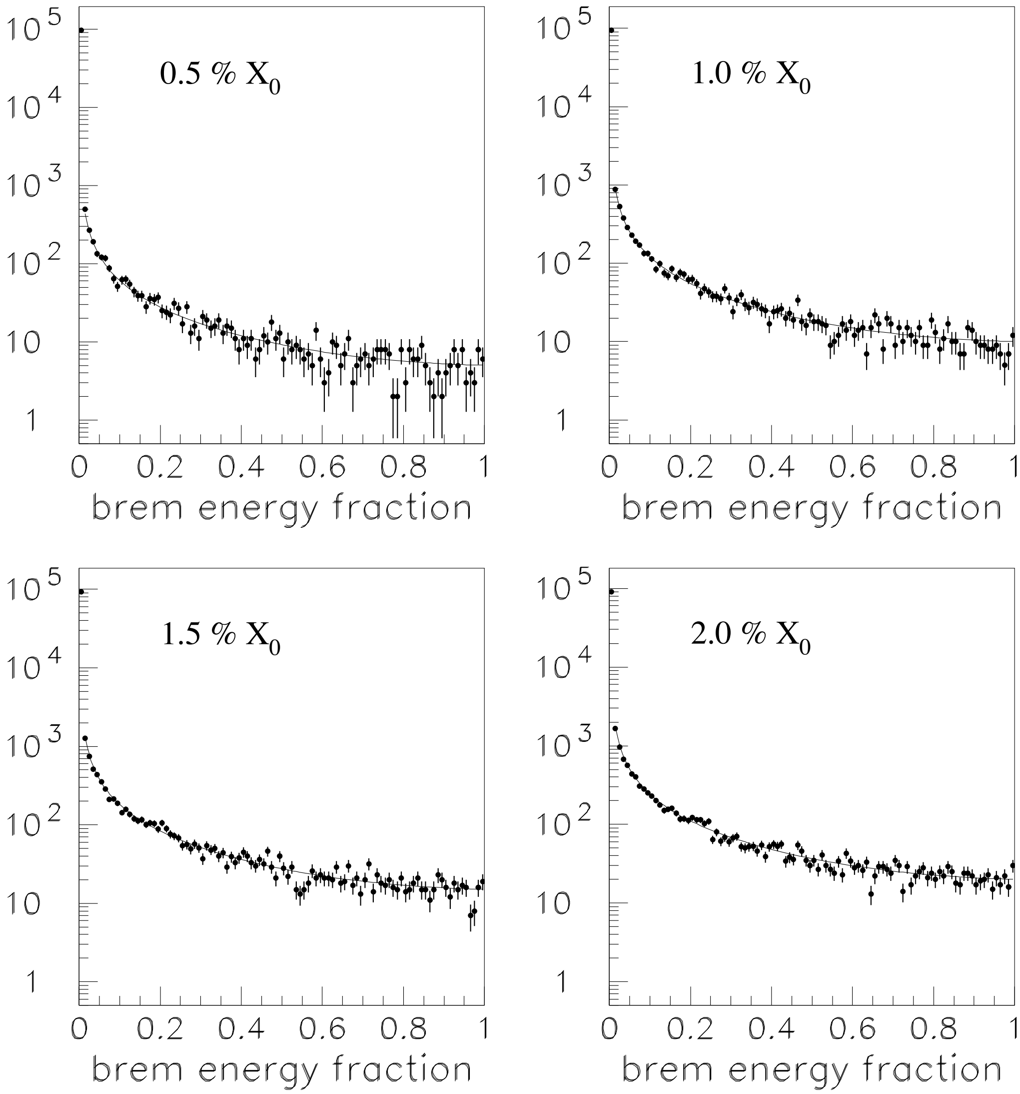

Figure 5.7: The Monte Carlo bremsstrahlung spectrum. The points represent the fraction of the electron's energy which is transferred to the photon during bremsstrahlung in a single thin layer of material. The solid curves are the analytic formulae for the spectrums given in equation 5.1. The four plots correspond to four different radiator thicknesses.

All charged particles which reach the volume of the CTC are sent to the CTC simulation, which produces a track object if the particle has $p_T > 400$ MeV. Electrons and photons are extrapolated to the calorimeter, and their energy is smeared by the CEM simulation and energy deposits are made on the strips and wires in the CES. The hadronic particles produced by PYTHIA are also tracked by the CTC, and their energy deposition in the calorimeter is also simulated, but our results will not rely on this aspect of the simulation. After all particles are simulated by QFL, the detector 'data' is reconstructed by the same routines which run on real data.

5.8 Check on E/p simulation with $W \rightarrow e\nu$ electrons

As a final check on the ability of the simulation to predict E/p, we compare the E/p distribution of $W \rightarrow e\nu$ electrons in the data to that of the Monte Carlo simulation. This is a powerful test since none of the simulation's parameters have been tuned with this dataset. On the other hand, there are several characteristics of W electrons which are not representative of conversion electrons. First, the W electron sample has internal as well as external bremsstrahlung. This means that the E/p tail of W electrons will be larger than conversion electrons. Secondly, W electron tracks do not suffer from the unusual tracking systematics found in conversion electrons. This means that we should expect E/p biases in the conversion data that are not seen in the W electrons.

We use a Monte Carlo calculation of $W \rightarrow e\nu(\gamma)$ production. The W p_T spectrum of the Monte Carlo has been chosen to match that observed in the CDF W data, and internal bremsstrahlung is done according to the calculation of Berends and Kleiss [38]. The data was collected with two Level 3 triggers, neither of which make cuts on electron ID variables, so we need not apply such cuts offline. The selection of the data and Monte Carlo is listed in Table 5.1. The variable M_T is the W transverse mass, and is defined by

$$M_T = \sqrt{(E_T + \not{E}_T)^2 - (\vec{E_T} + \vec{\not{E}_T})^2} \tag{5.2}$$

where $\vec{E_T}$ is the transverse energy vector of the electron, $\vec{\not{E}_T}$ is the missing energy vector, and E_T and $\not{E}_T$ are their magnitudes. In this Monte Carlo the missing energy measurement is not simulated, so we use the true neutrino p_T in its place. To improve the p_T resolution of the CTC we beam constrain the W electrons in the data and Monte Carlo. This serves in the place of the conversion vertex fit.

The E/p of data and Monte Carlo are compared in Figure 5.8. The Monte Carlo is normalized to the data. Overall the agreement between data and Monte Carlo is good, although the high E/p tail is 10% larger in data than Monte Carlo.

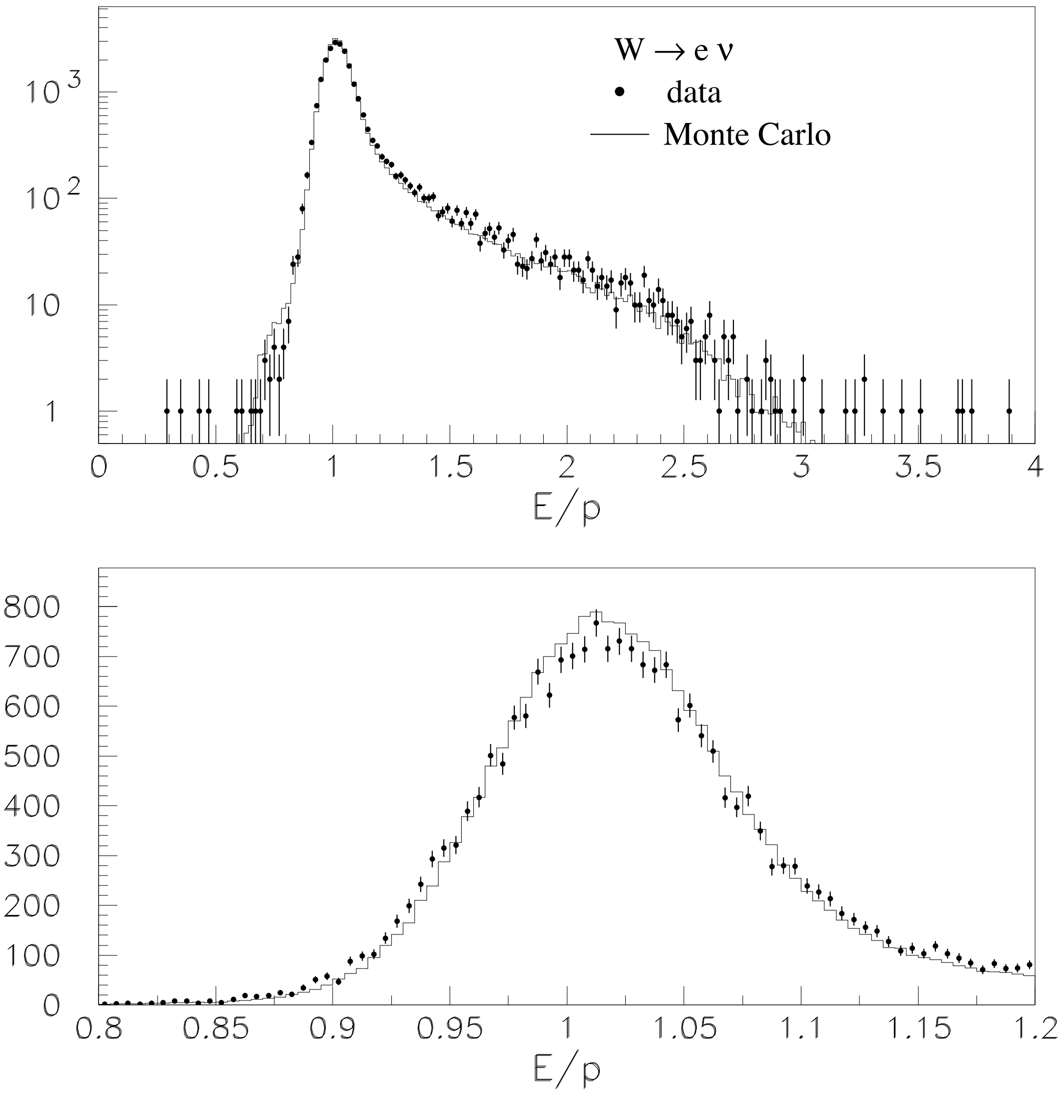

Figure 5.8: W electron E/p in data and Monte Carlo. The top plot shows the entire spectrum on a log scale. The lower plot shows a close up of the peak region on a linear scale.

$\|z_0\| < 60$ cm
local $\|x\| < 21$ cm
9 cm $<$ | local $z\| < 230$ cm
central detector
$E_T > 25$ GeV
$\not\!\!E_T > 25$ GeV
$p_T > 15$ GeV
$N_{trk} = 1$
$E_T^{cone0.4} < 1.0$ GeV
65 GeV $< M_T <$ 100 GeV

Table 5.1: W event selection

5.9 η/π^0 ratio and meson p_T spectrum

As the final elements of the background simulation we must choose the production ratio and p_T spectrum with which to generate. Fortunately the cross section measurement is quite insensitive to both of these parameters. For example, before performing the background subtraction we bin the data by E_T. This means that in each bin we have approximately monochromatic π^0's and η's, so their p_T spectrum has very little effect on the outcome. The production ratio of π^0s and ηs also has only a small effect on the outcome of the background subtraction. This is because the η and π^0 mesons have similar E/p distributions due to their identical meson decay kinematics.

To determine the η/π^0 ratio and meson p_T spectrum we use double conversion events ($\pi^0, \eta \rightarrow \gamma\gamma \rightarrow e^+e^-e^+e^-$) in the data. The diphoton mass spectrum from these events in the data is shown in figure 5.9. To make this plot we use the same cuts as for a single conversion except for the isolation cut. We modify the isolation cut to account for the presence of conversion tracks in the 0.4 cone. In events where one or more conversion tracks extrapolates to a tower outside the CEM cluster but within $\Delta R = 0.4$, we subtract its measured p_T from the isolation energy. We then cut on $E_T^{cone0.4} < 1.0$ GeV. In this way we measure the η/π^0 ratio under similar isolation requirements that we find in our photon cross section measurement.

To insure good mass resolution we fit each photon candidate to a conversion vertex and require that the photon point back to the beamspot. We first fit the spectrum to the sum of two lorentzians and a third order polynomial. The background spectrum is shown as the dotted line in Figure 5.9. The double conversion η/π^0 ratio is observed to be 0.205 ± 0.023. This number is not the production ratio due to the $\eta \rightarrow \gamma\gamma$ branching ratio of 39.33% and acceptance differences between η's and π^0's due to the χ^2_{strips}, χ^2_{wires}, and isolation cuts. We account for these effects with the QFL detector

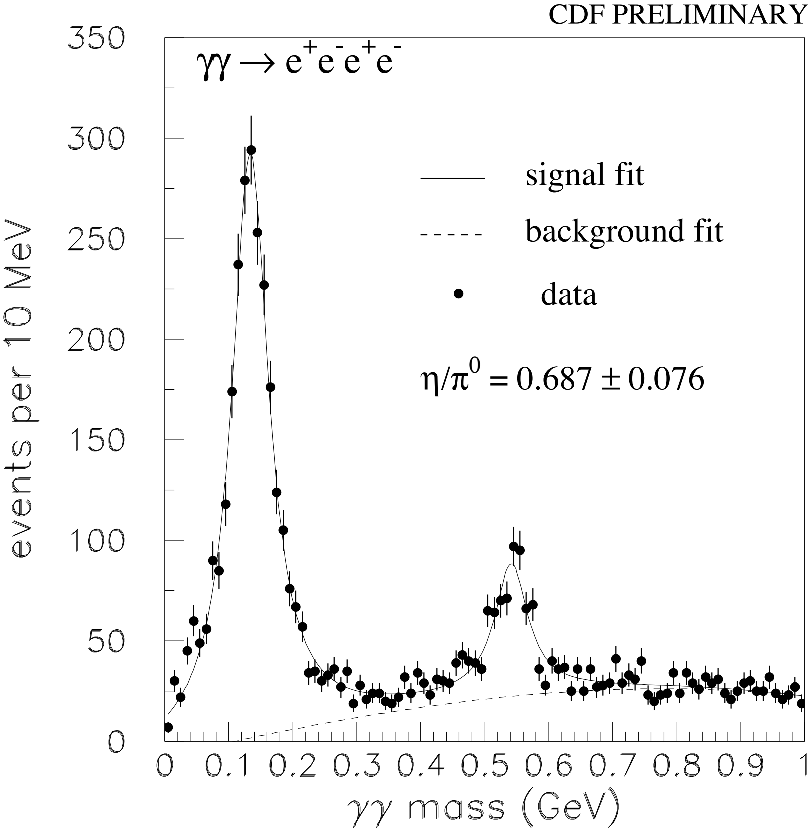

Figure 5.9: The diphoton mass spectrum of double conversion events in the data. The data is fit to two lorentzians plus a third order polynomial. The polynomial is shown as the dotted line. The pi^0 and η peaks are visible at 0.135 GeV and 0.547 GeV respectively. The ratio of the areas of the two peaks, along with the Monte Carlo prediction for the ratio of acceptances, gives an η/π^0 production ratio of 0.687 ± 0.076.

simulation, and we find that the η/π^0 production ratio is measured to be 0.678±0.076. Previous CDF photon cross section analyses use an η/π^0 ratio of 1.02±0.15±0.23[42], which is in agreement with our result. .

The meson p_T spectrum is also taken from double conversion events. We select double conversion events in the data and Monte Carlo with $M < 240$ MeV (π^0 candidates) and 480 MeV $< M <$ 620 MeV (η candidates). The p_T spectrum of the double conversion events in the Monte Carlo is compared to the data in Figure 5.10 The Monte Carlo has been generated with a power law spectrum, where the exponent is 6. We use this spectrum for the photon cross section measurement.

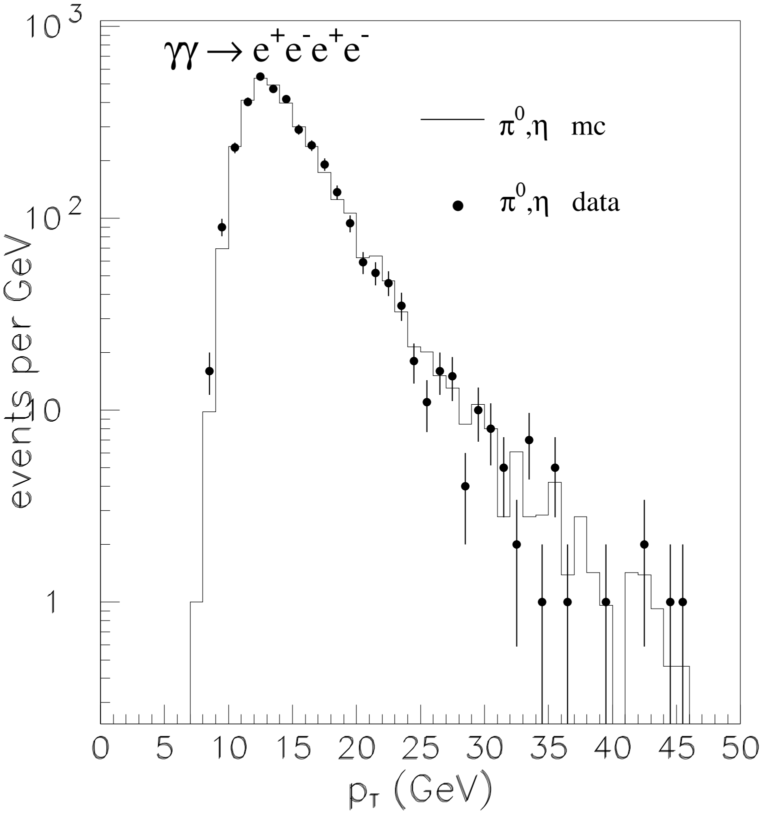

Figure 5.10: The meson p_T spectrum in data and Monte Carlo, from double conversion events. Events with a diphoton mass between $M < 240$ MeV (π^0 candidates) and 480 MeV $< M <$ 620 MeV (η candidates) have their p_T plotted here. The Monte Carlo has been generated with a power law spectrum, with an exponent of six.

Chapter 6

Background Subtraction

The backgrounds to prompt photons at hadron machines are the π^0 and η mesons. These are light hadronic particles ($m(\pi^0) = 135$ MeV, $m(\eta) = 547$ MeV), so their production cross section is very large in $p\bar{p}$ collisions. Unfortunately, they decay immediately to photons: the $\pi^0 \rightarrow \gamma\gamma$ branching ratio is 98.8%, and the $\eta \rightarrow \gamma\gamma$ branching ratio is 39.33%. The p_T at which we wish to measure the photon cross section is much larger than the masses of these mesons, so the angle between the two photons from the meson decay is small. Typically both photons will land in the same CEM tower, and at very high energies the two electromagnetic showers will merge. As a result, a meson decay appears to be a single photon in the calorimeter. Since the production cross sections for these particles far exceed the cross section that we wish to measure, this is a serious concern.

We are rescued by the fact that hadronic particles are usually found in jets that are the result of the hadronization of a scattered high energy quark or gluon. A prompt photon, on the other hand, does not interact through the color force, so no hadronization occurs as it leaves the interaction point. Therefore, to reject π^0 and η decays while retaining signal events, we require that the observed photon be isolated from other energy in the calorimeter[1]. This is the motivation for the isolation cut described in section 4.3.4.

Occasionally a π^0 or an η meson will appear isolated. This occurs when a scattered parton hadronizes in such a way that most of its energy is transferred to a single meson. Typically these events cannot be distinguished from prompt photons on an event by event basis. Instead, we devise background subtraction methods which can statistically separate the mesons from the photons.

This chapter describes a new background subtraction technique developed to distinguish a meson decay from a single photon. This method takes advantage of the tracking information available in a photon conversion event by comparing the E_T measured in the calorimeter to the p_T measured in the tracking chamber. In the case

---

[1] Prompt photons produced through the 'bremsstrahlung' diagrams are not always isolated, so we must consider the effect of the isolation cut when comparing data to theory.

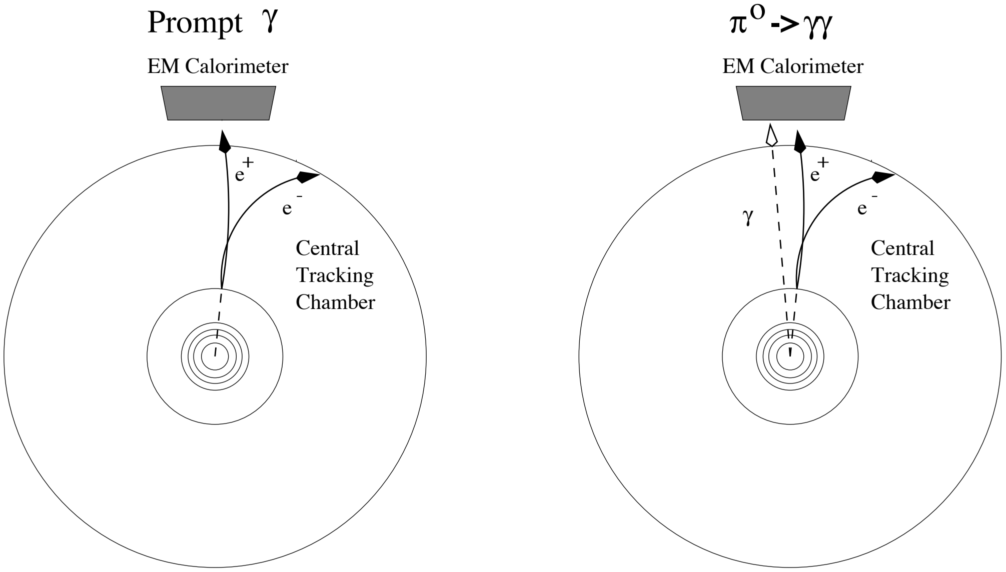

Figure 6.1: Schematic comparison of a prompt photon conversion to a conversion from $\pi^0 \rightarrow \gamma\gamma$ decay.

of a single photon, the energy should be consistent with the momentum within detector resolution. In a meson decay, the unconverted photon will pass through the CTC unseen, but will deposit its energy in the CEM. In these events, the energy exceeds the momentum. This is shown schematically in Figure 6.1.

For each event in the data, we calculate the quantity E/p, where E is the E_T measured by the CEM, and p is the p_T measured by the CTC. We divide the data into bins of photon transverse energy, and in each bin we attempt to explain the E/p distribution of the data in terms of the sum of a signal distribution and a background distribution. An example of these distributions taken from the Monte Carlo is shown in Figure 6.2. The signal distribution is sharply peaked at E/p = 1 while the meson distribution has a long tail at E/p > 1. The width of the signal peak is determined by the resolutions of the CEM and the CTC which are known. The shape of the meson distribution is determined primarily by two-body decay kinematics, with some alteration due to trigger and reconstruction effects. We rely on the Monte Carlo to predict the E/p distributions of signal and backgrounds.

We use two methods to extract the signal from the E/p distribution: an E/p tail count, and a χ^2 fit. The tail count method determines the signal-to-background ratio by requiring that the number of events observed in the E/p tail (E/p > 1.2) be the same in the data and Monte Carlo, while also requiring the total number of events be the same. The χ^2 fit method allows the normalization of the signal and background Monte Carlo shapes to float until the χ^2 between data and Monte Carlo is minimized. We describe the results of both of these methods for the two data

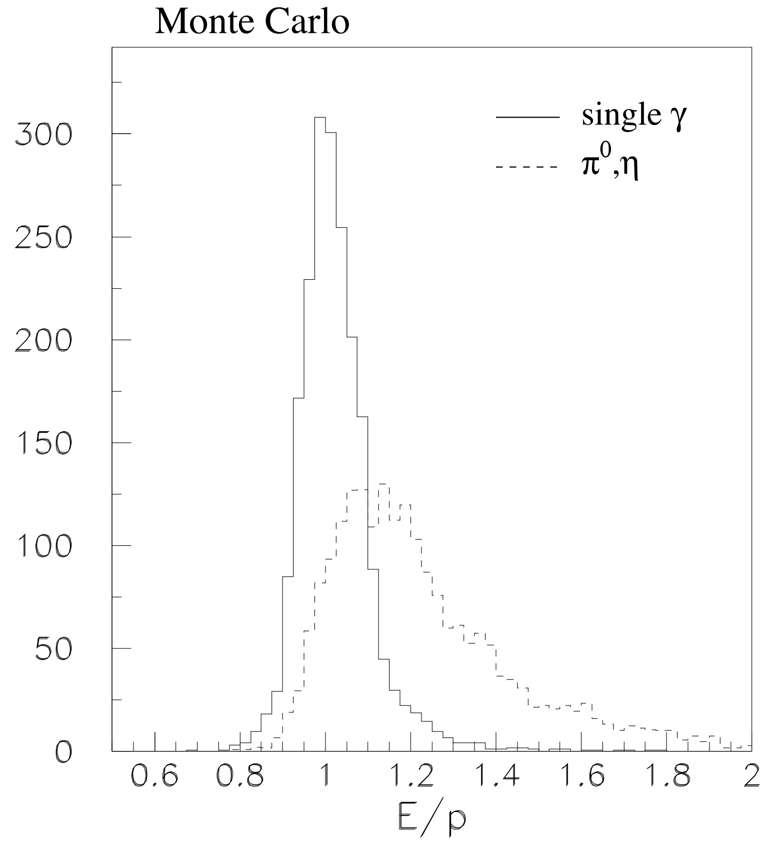

Figure 6.2: An example of the E/p distributions of signal and background in one p_T bin, from Monte Carlo.

samples in the following sections.

6.1 Event binning

Since we have both an energy measurement and a momentum measurement for the conversion photon, we can choose to bin the events according to the $p_T(\gamma)$ or $E_T(\gamma)$. We bin according to E_T for the following reason. In the case of a meson decay, both photons usually land in the same CEM cluster, and consequently the E_T measures the meson p_T. Therefore by binning in E_T we get approximately monochromatic mesons in each bin, and this reduces our sensitivity to the meson p_T spectrum. However, for the 8 GeV electron dataset, our fiducial cuts require that the two conversion tracks point at different CEM towers. Since we make no attempt to measure the E_T of the softer track with the calorimeter, when binning the event we correct for the lost E_T by adding the vertexed momentum of the soft track to the E_T of the trigger electron. For the 23 GeV photon data we require that both tracks point to the same CEM tower, and we use the E_T of that cluster to bin the event.

6.2 Tail count method

For this background subtraction method we set the signal-to- background ratio such that the number of events in the E/p tail is the same in the data and Monte Carlo, while also constraining the total number of events to be the same. This is done in the following manner. The Monte Carlo predicts the fraction of the events which would have and E/p < 1.2 if the data were pure signal or pure background. We measure this fraction in the data and find that the data lies between the signal and background Monte Carlo fractions. The number of signal candidates is then given by

$$N_\gamma = N_{data}\left(\frac{f_d - f_b}{f_s - f_b}\right) \tag{6.1}$$

where N_γ is the number of signal candidates, N_{data} is the total number of events in the data, and f_d, f_b, and f_s are the fraction of events in the data, background Monte Carlo, and signal Monte Carlo which have an E/p < 1.2. This equation says that the fraction observed in the data is the weighted average of the two Monte Carlo predictions, where the weights are the number of signal events and the number of background events.

6.2.1 8 GeV electron data

This data sample is the most difficult to model. Since this is our lowest p_T trigger, we rely solely on the 8 GeV data to measure the cross section for p_T below 20 GeV. In

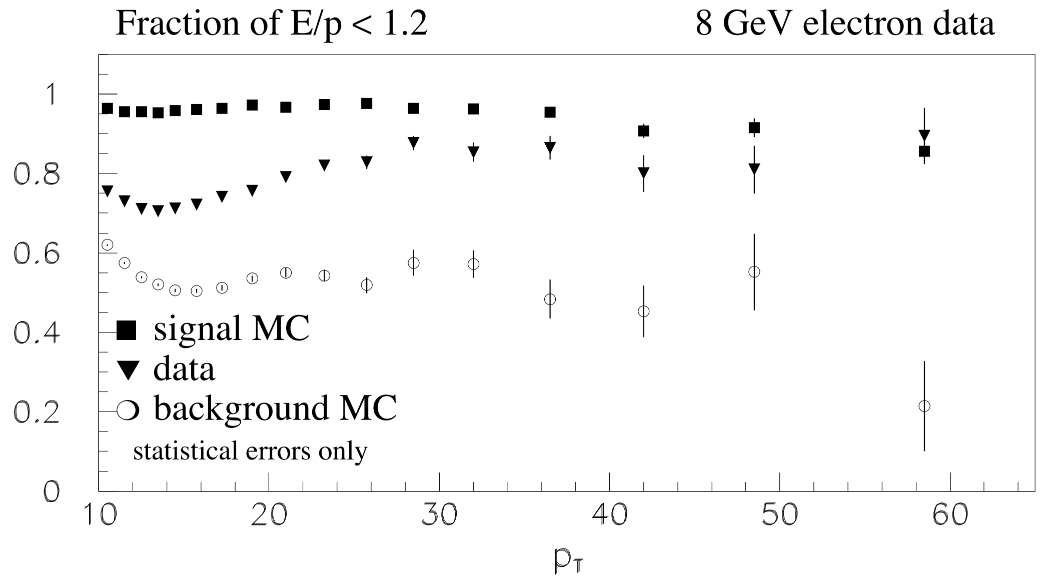

Figure 6.3: Tail count background subtraction for 8 GeV electron data. Fraction of E/p < 1.2 for data, signal Monte Carlo, and background Monte Carlo.

this dataset we retain events which are in the threshold region of the trigger efficiency in order to extend our sensitivity to the lowest possible energies. Furthermore, the p_T cuts applied to the electron by the trigger has the effect of cutting off the high E/p tail in the lowest p_T bins, meaning that our background subtraction becomes less powerful, and we become more sensitive to systematic effects. In addition, the electron ID cuts applied to this dataset can alter the E/p distributions of the background. We ask the Monte Carlo to predict this sculpting.

The Monte Carlo predictions for the signal and background fractions for the 8 GeV electron data are shown in Figure 6.3, along with the inferred number of signal candidates.

To get qualitative information on the robustness of the background subtraction, we compare the E/p distributions of data and monte carlo in each p_T bin. These plots are shown on linear and log scales in Figures 6.4 to 6.12. In the Monte Carlo the signal and background distributions have been added together in the ratio determined by the tail count method. In general we see good agreement between data and Monte Carlo in all p_T bins. In particular, the shape of the high E/p tail of the data appears to be predicted nicely by the Monte Carlo. This is particularly noticeable in the lowest p_T bins, where the tail is cut off by the Level 2 and Level 3 trigger cuts on the p_T of the electron track. The fact that the Monte Carlo matches the data in this region indicates that the Level 2 trigger parameterization is adequate.

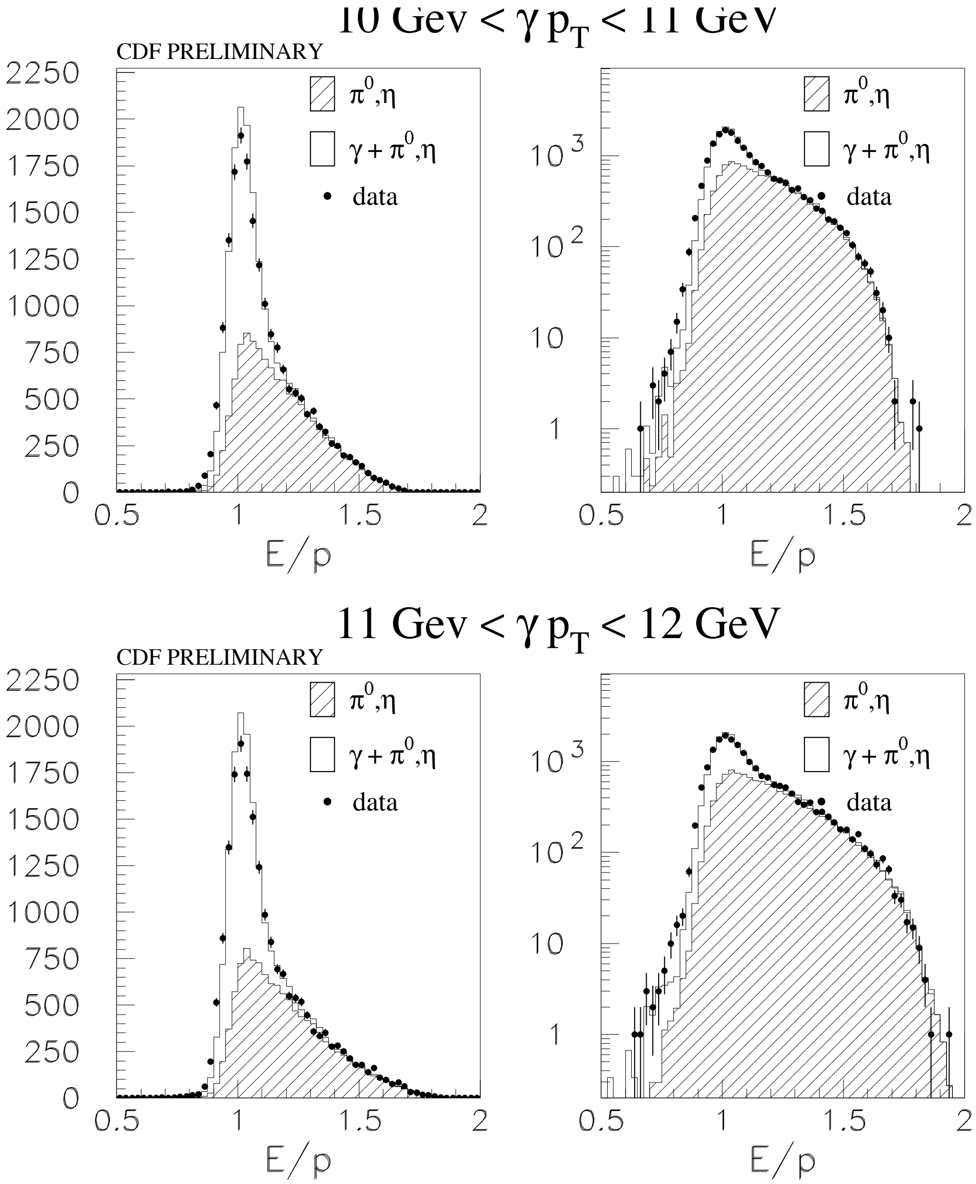

Figure 6.4: A comparison of E/p in the data and Monte Carlo in each photon p_T bin, for the 8 GeV electron dataset. The plot on the right is the log of the plot on the left.

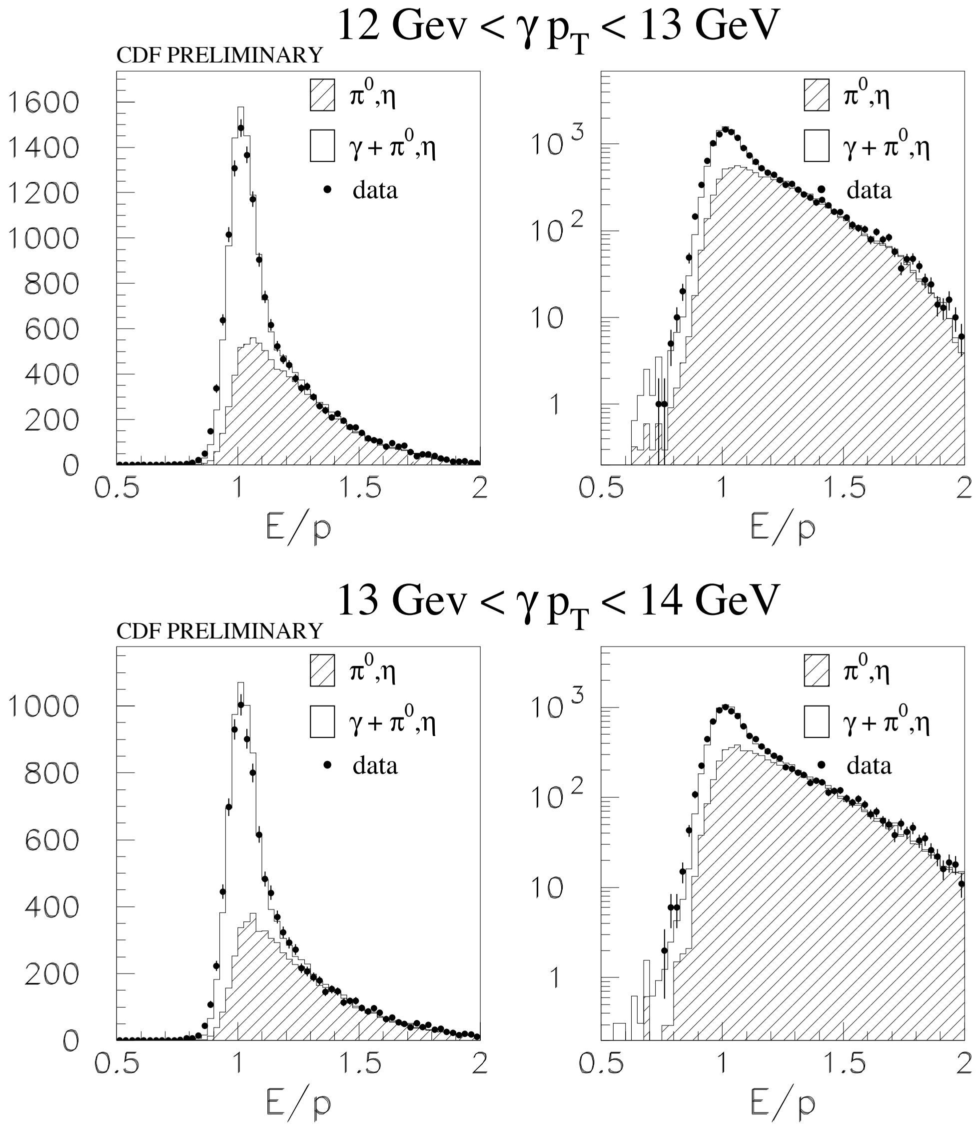

Figure 6.5: A comparison of E/p in the data and Monte Carlo in each photon p_T bin, for the 8 GeV electron dataset. The plot on the right is the log of the plot on the left.

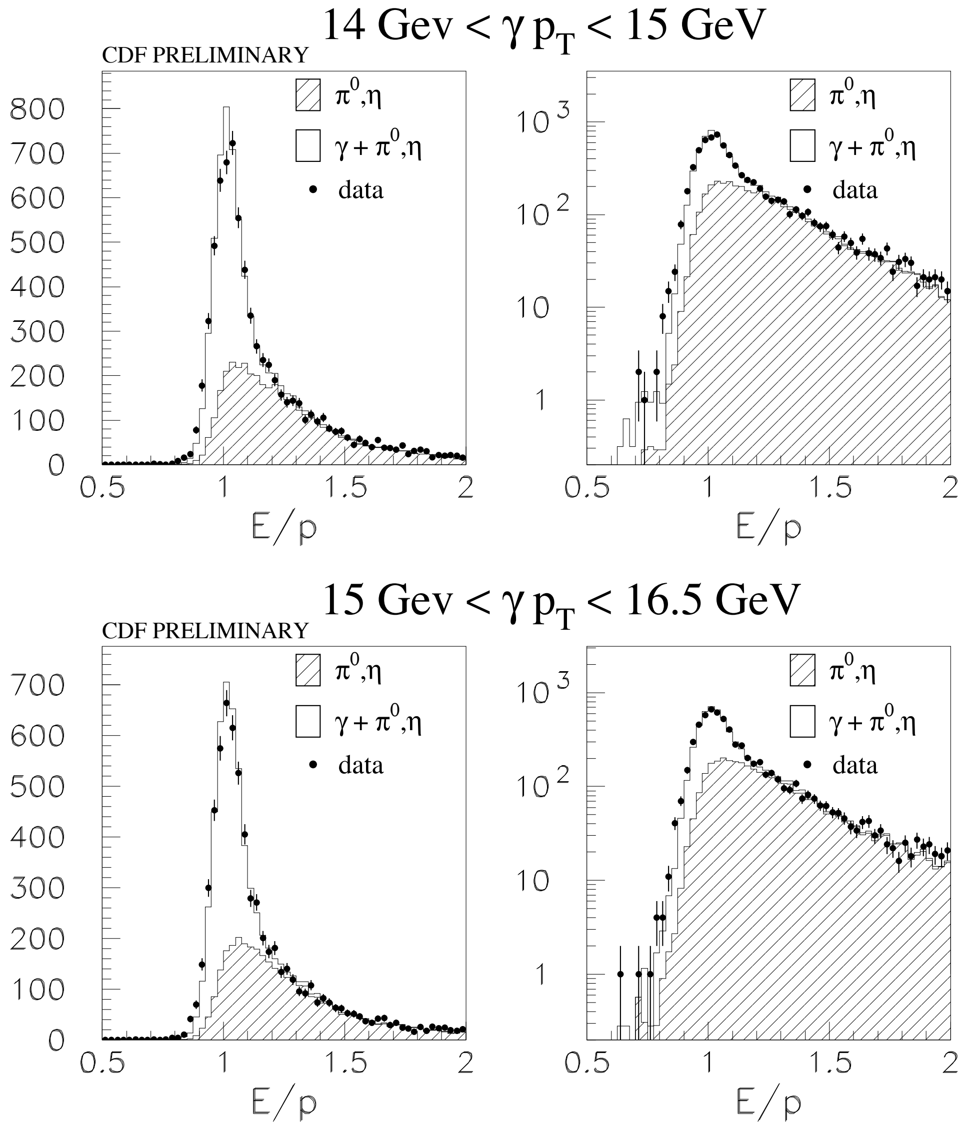

Figure 6.6: A comparison of E/p in the data and Monte Carlo in each photon p_T bin, for the 8 GeV electron dataset. The plot on the right is the log of the plot on the left.

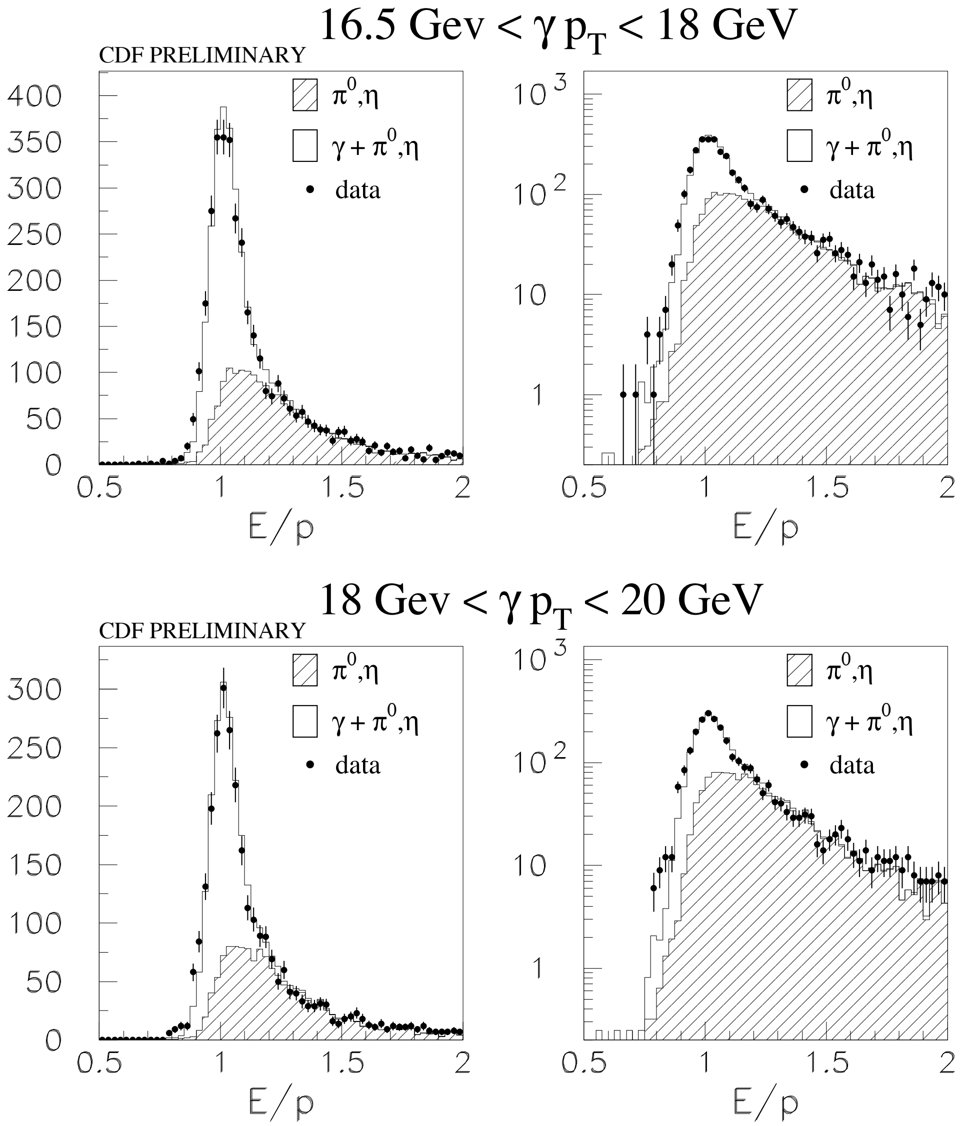

Figure 6.7: A comparison of E/p in the data and Monte Carlo in each photon p_T bin, for the 8 GeV electron dataset. The plot on the right is the log of the plot on the left.

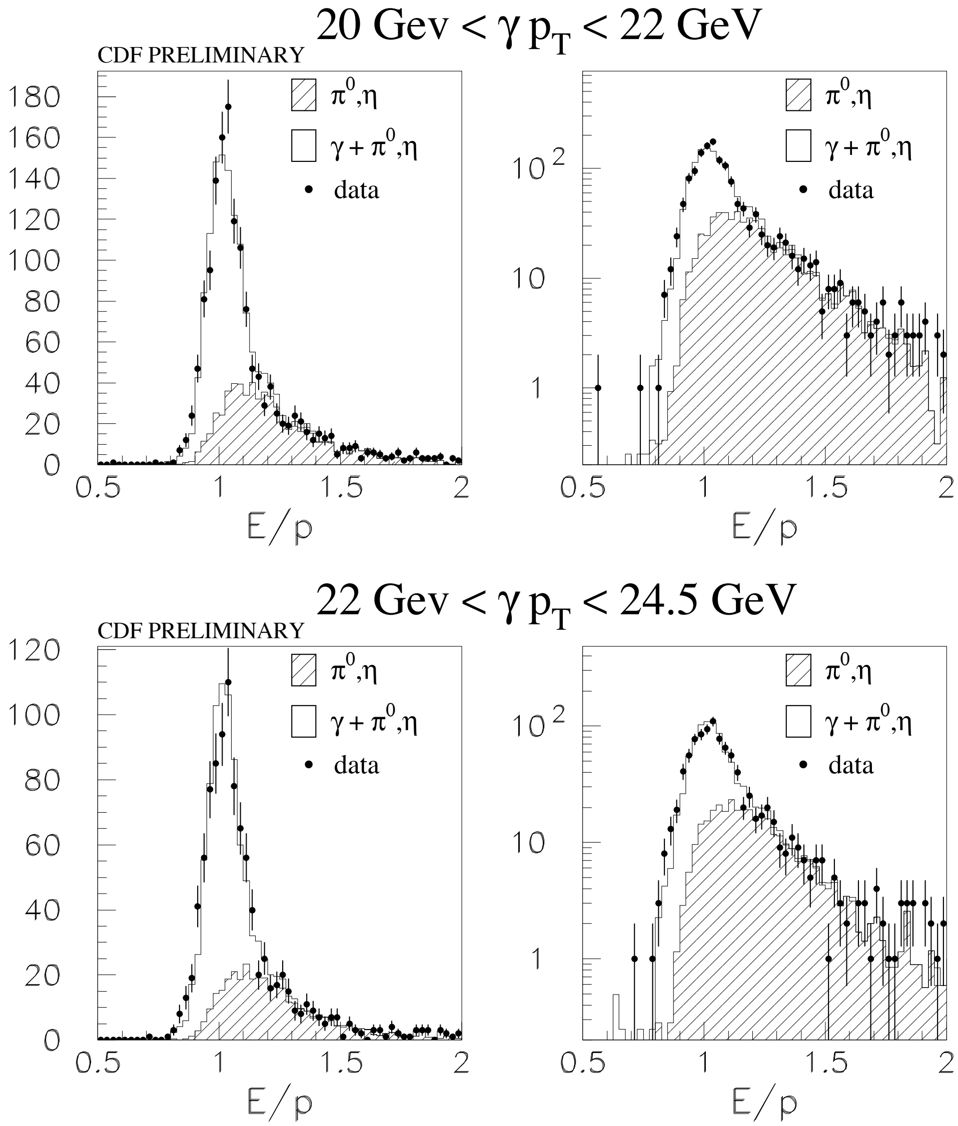

Figure 6.8: A comparison of E/p in the data and Monte Carlo in each photon p_T bin, for the 8 GeV electron dataset. The plot on the right is the log of the plot on the left.

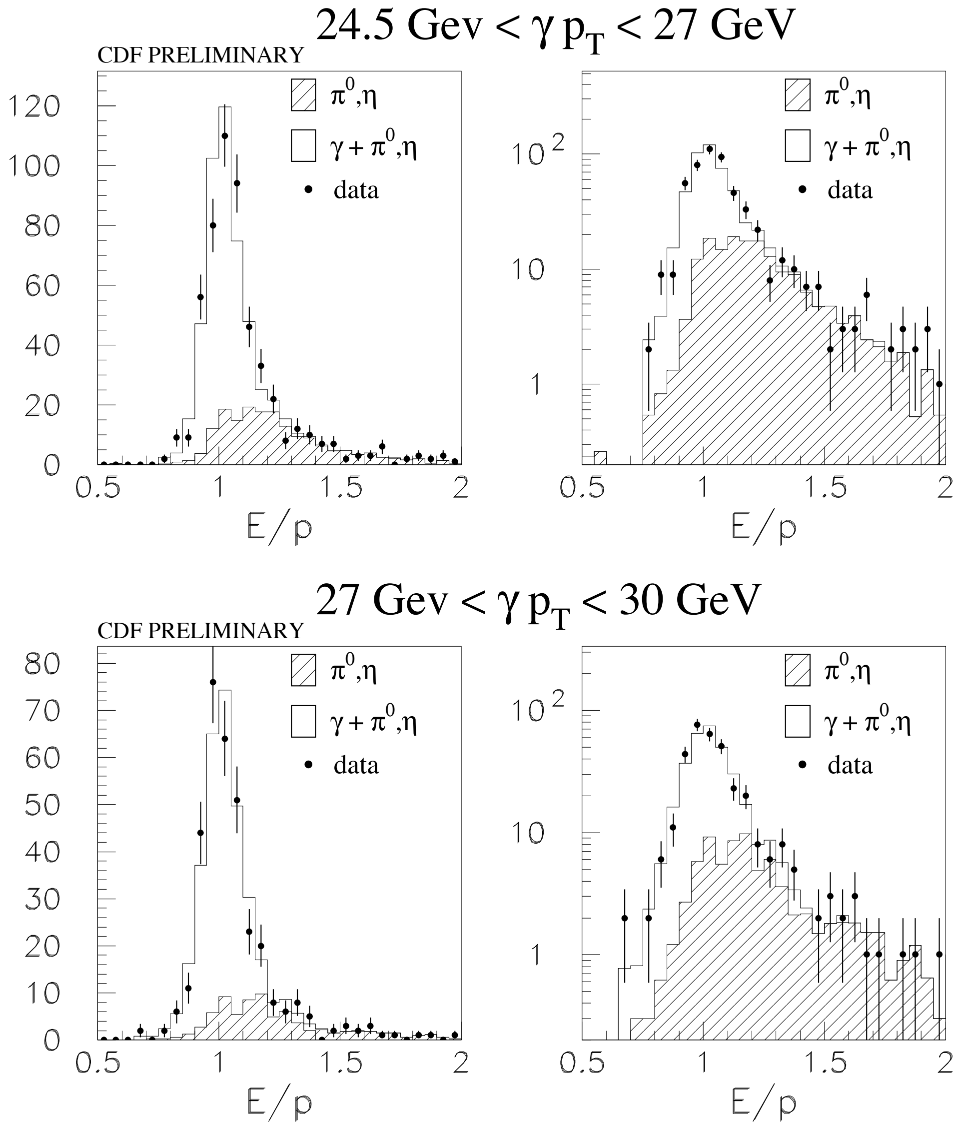

Figure 6.9: A comparison of E/p in the data and Monte Carlo in each photon p_T bin, for the 8 GeV electron dataset. The plot on the right is the log of the plot on the left.

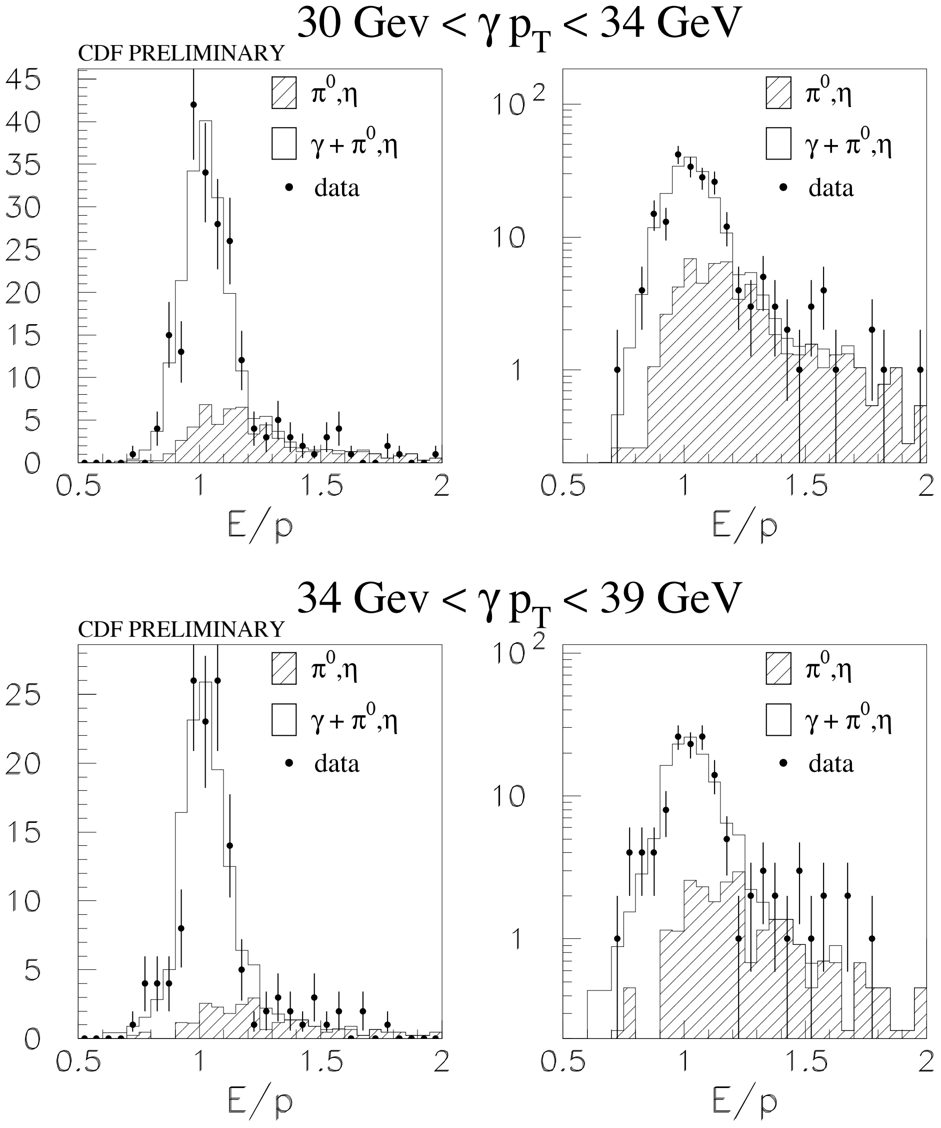

Figure 6.10: A comparison of E/p in the data and Monte Carlo in each photon p_T bin, for the 8 GeV electron dataset. The plot on the right is the log of the plot on the left.

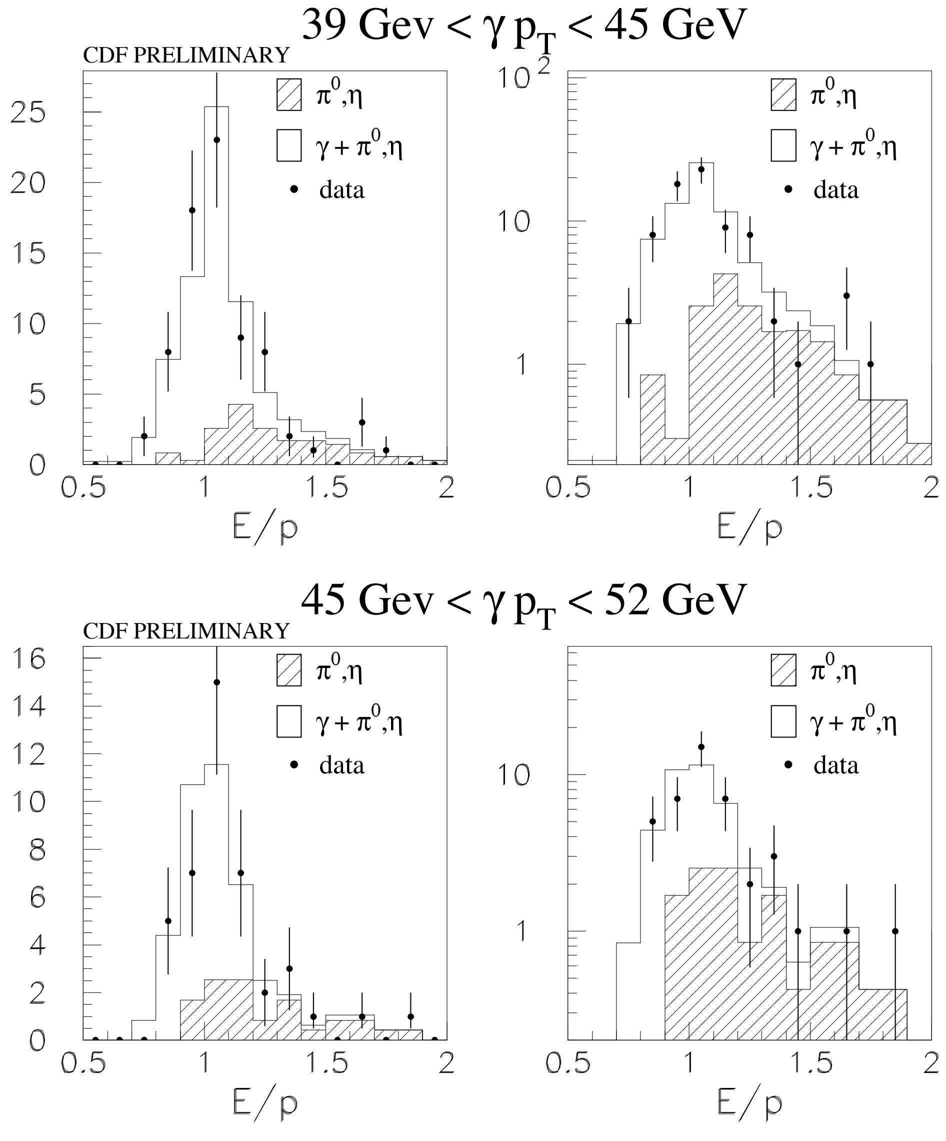

Figure 6.11: A comparison of E/p in the data and Monte Carlo in each photon p_T bin, for the 8 GeV electron dataset. The plot on the right is the log of the plot on the left.

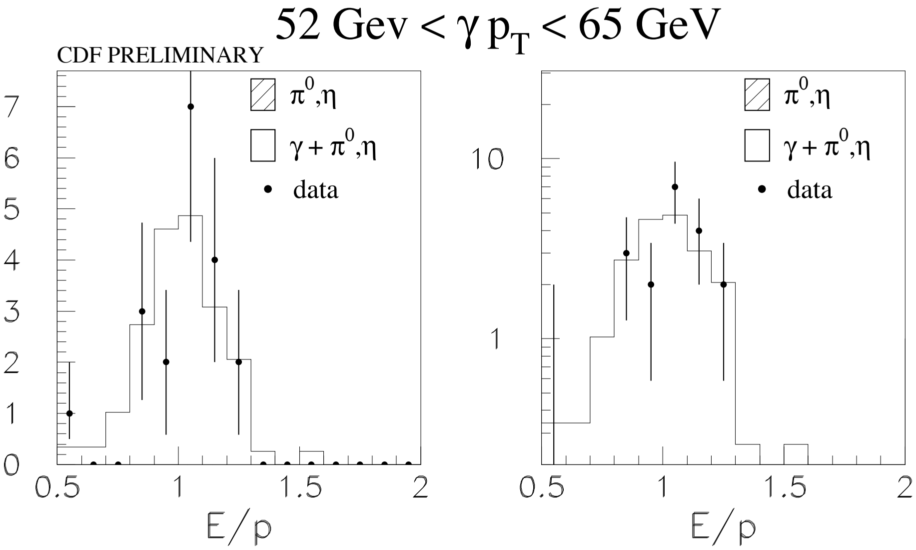

Figure 6.12: A comparison of E/p in the data and Monte Carlo in each photon p_T bin, for the 8 GeV electron dataset. The plot on the right is the log of the plot on the left.

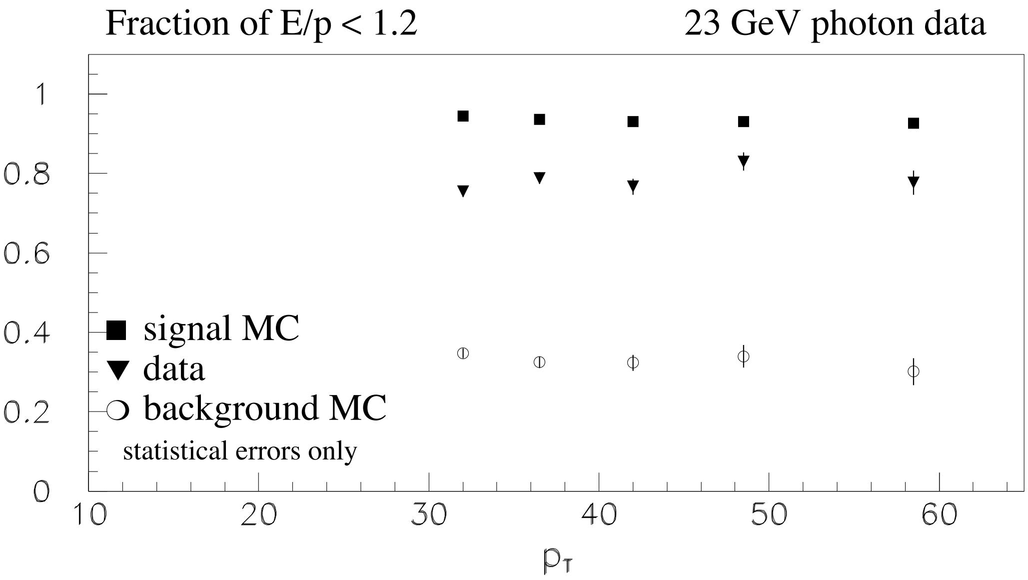

Figure 6.13: Tail count background subtraction for 23 GeV electron data. Fraction of E/p < 1.2 for data, signal Monte Carlo, and background Monte Carlo.

6.2.2 23 GeV photon data

This data sample has no Level 3 electron ID cuts to be modeled, and there are no track requirements in the trigger, meaning that the high E/p tail of the meson distribution is not suppressed. Consequently the background subtraction is particularly robust in this data.

The Monte Carlo predictions for the E/p fractions are shown in figure 6.13, and the resulting E/p plots are shown in 6.14 to 6.16.

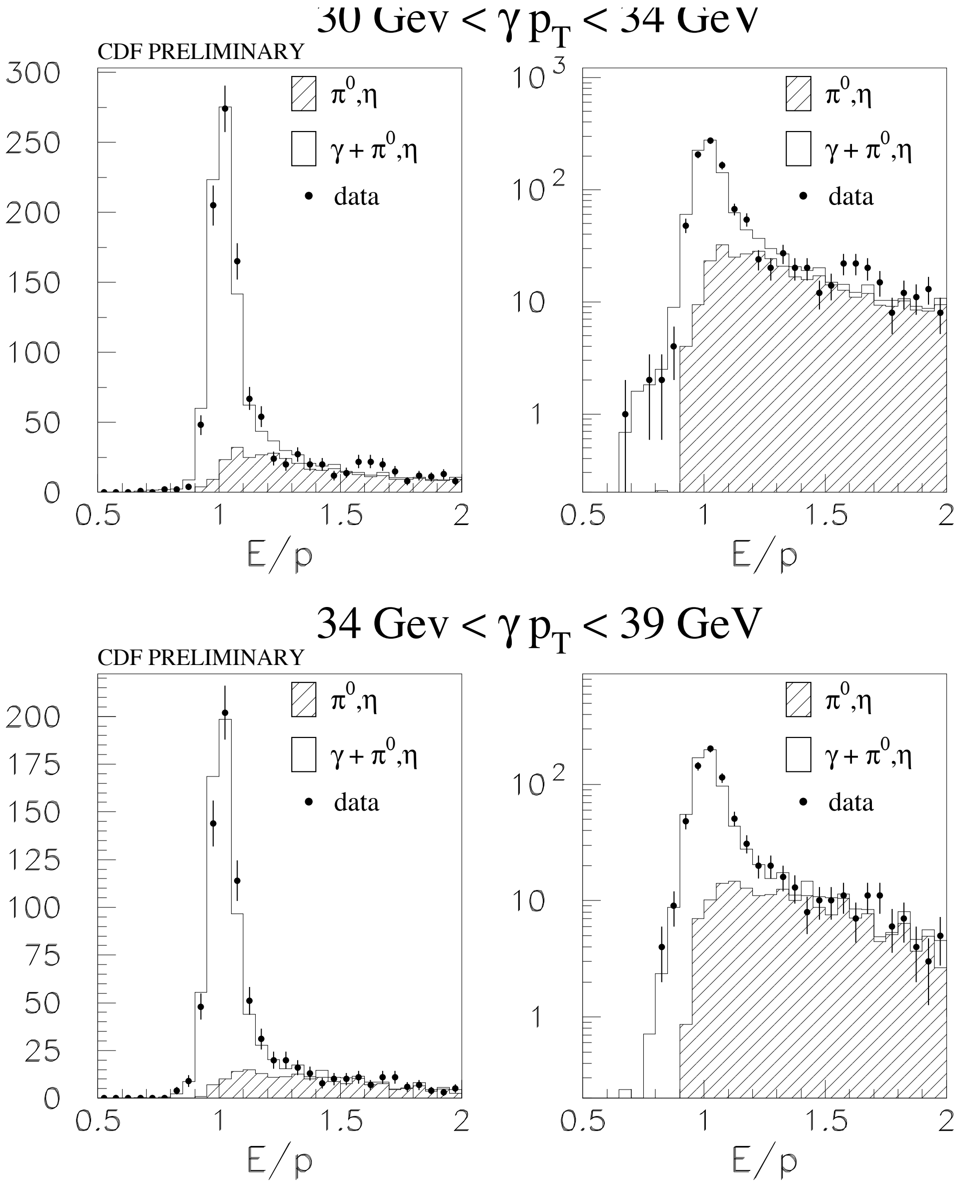

Figure 6.14: A comparison of E/p in the data and Monte Carlo in each photon p_T bin, for the 23 GeV photon dataset. The plot on the right is the log of the plot on the left.

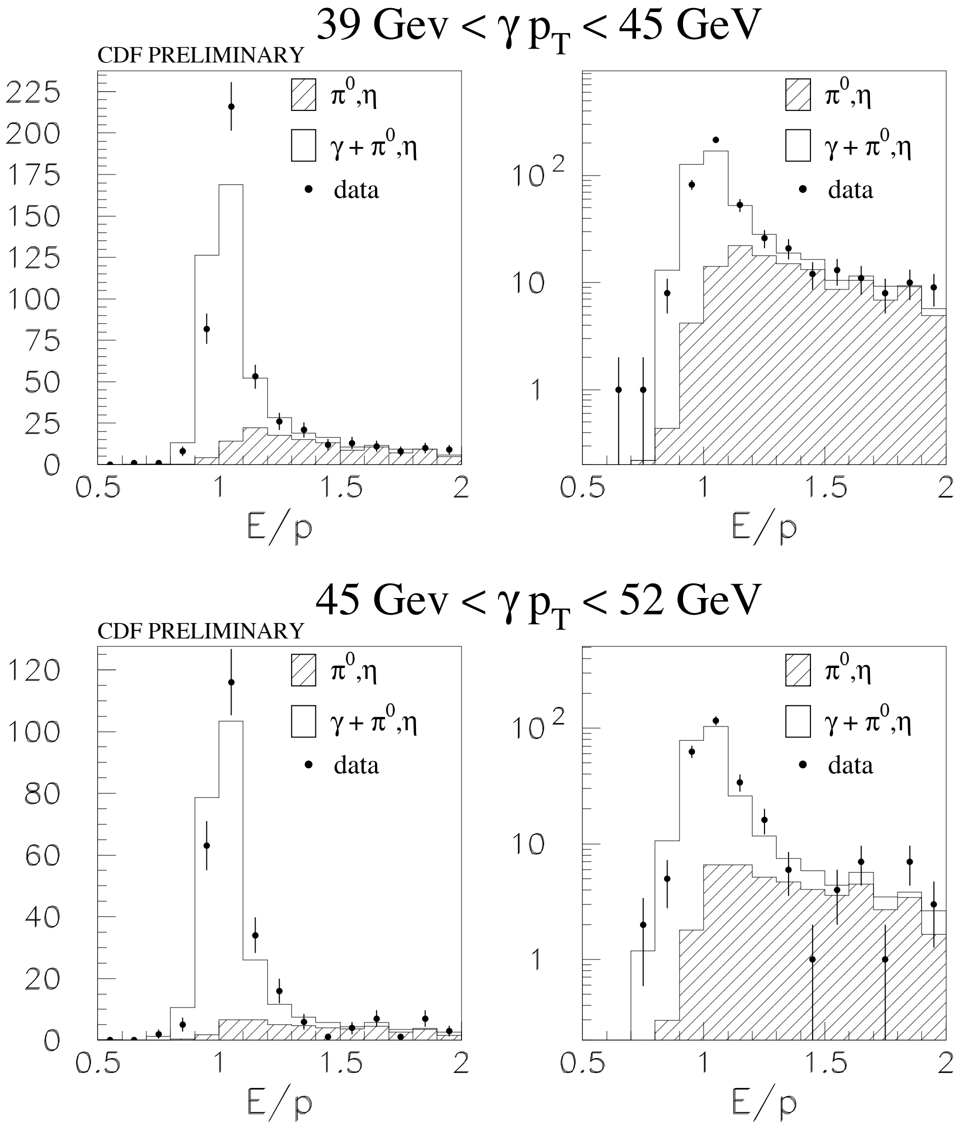

Figure 6.15: A comparison of E/p in the data and Monte Carlo in each photon p_T bin, for the 23 GeV photon dataset. The plot on the right is the log of the plot on the left.

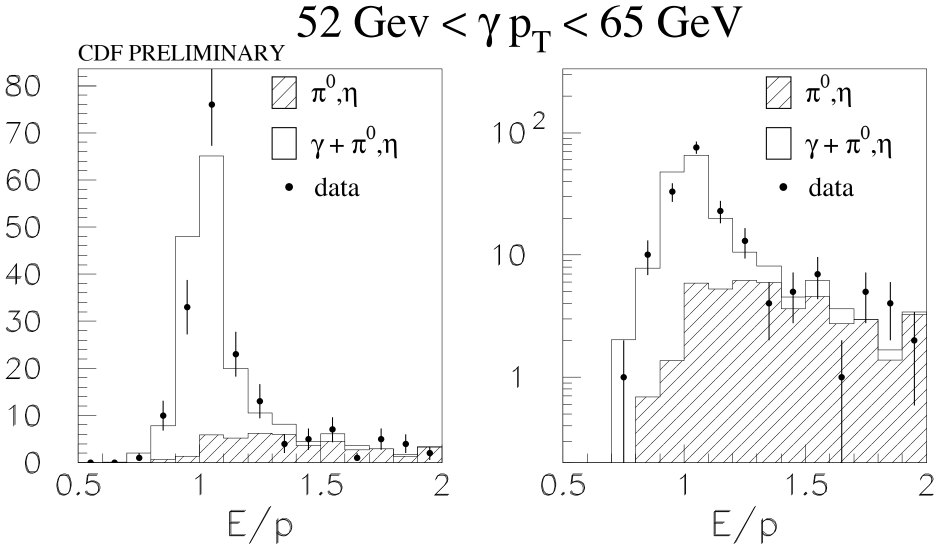

Figure 6.16: A comparison of E/p in the data and Monte Carlo in each photon p_T bin, for the 23 GeV photon dataset. The plot on the right is the log of the plot on the left.

dataset	p_T	Total events	Signal candidates	statistical error (%)
8 GeV electron	10-11	19110	7490.4	2.4
(2 tower)	11-12	19681	8014.8	2.2
	12-13	15216	6246.4	2.3
	13-14	10523	4491.8	2.6
	14-15	7324	3344.0	2.8
	15-16.5	6578	3120.2	2.8
	16.5-18	3657	1847.7	3.6
	18-20	2790	1414.9	4.1
	20-22	1472	849.3	5.1
	22-24.5	966	620.2	5.5
	24.5-27	530	358.6	6.8
	27-30	341	264.6	8.0
	30-34	205	147.6	11.2
	34-39	133	107.8	11.7
	39-45	75	57.3	17.6
	45-52	42	29.8	28.1
	52-65	19	20.1	25.2
23 GeV photon	30-34	1090	742.5	4.4
(1 tower)	34-39	765	580.3	4.8
	39-45	471	343.7	6.4
	45-52	265	220.0	7.7
	52-65	184	140.1	9.8

Table 6.1: Results of the tail count background subtraction.

6.2.3 Tail count summary

The final results of the tail count background subtraction are listed in Table 6.1.

6.3 χ^2 fit method

For a second background subtraction method we perform a χ^2 fit to the E/p distribution of the data, allowing the normalization of the signal and background Monte Carlos to float. The number of signal candidates found by the fit is compared to the tail count result for the 8 GeV electron data in Figure 6.17. The χ^2 fit finds a few percent fewer signal candidates than the tail count method. The confidence level of the fits is also shown in Figure 6.17. The confidence level is good except for the first few p_T bins. By inspecting the E/p plots for these bins we see that the data appears to be shifted slightly toward lower p_T compared to the Monte Carlo in these

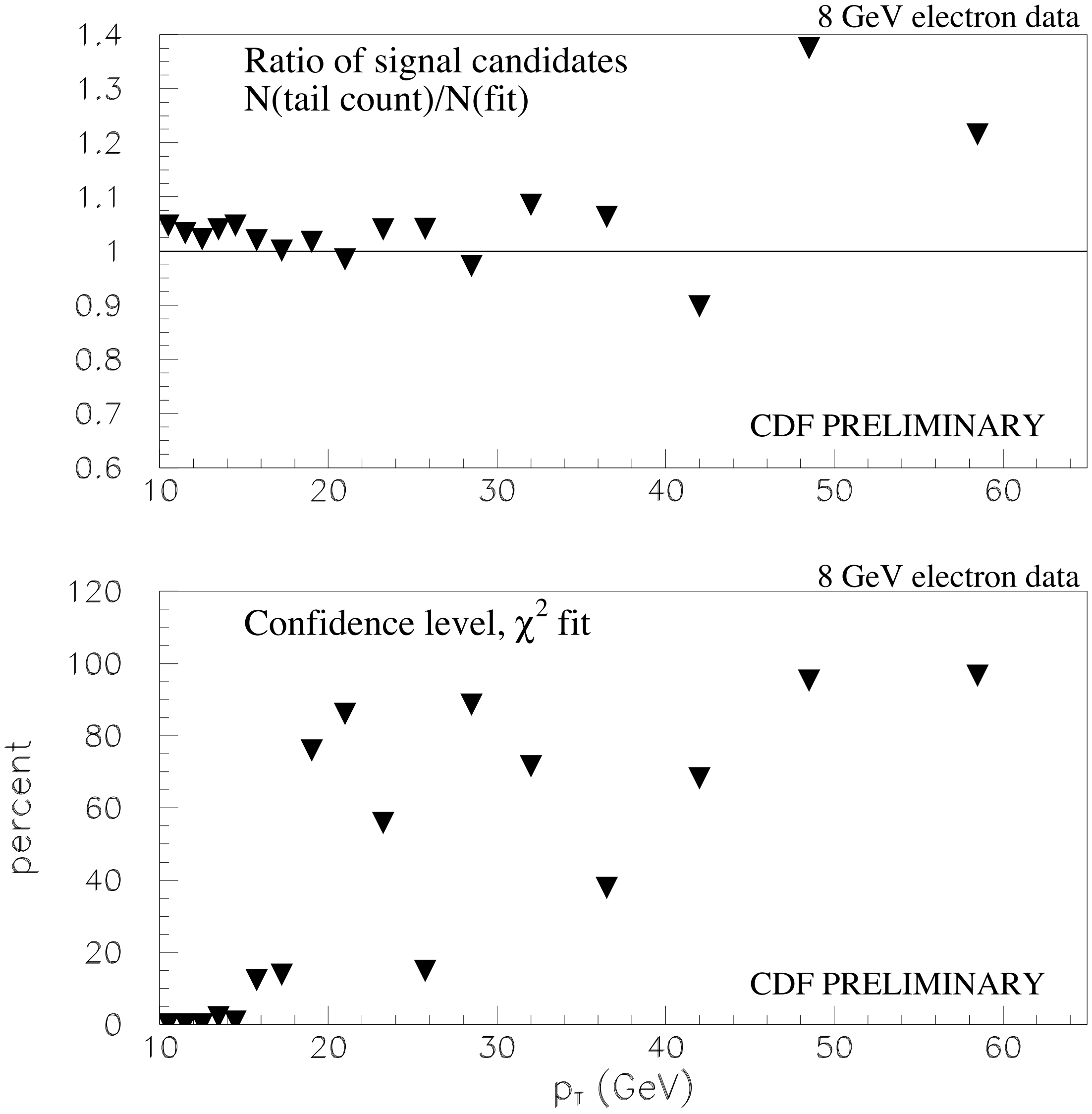

Figure 6.17: Results of the χ^2 fit on the 8 GeV electron data. The top plot shows the number of signal candidates returned by the fit compared to the number found by the tail count. The lower plot shows the confidence level of the fits.

bins. In section 6.4 we discuss the systematic error we take on the cross section to account for shortcomings in the Monte Carlo E/p model.

In Figure 6.18 we show the results of the χ^2 fit for the 23 GeV photon sample. In these data several of the fits return poor confidence levels. The systematic error for

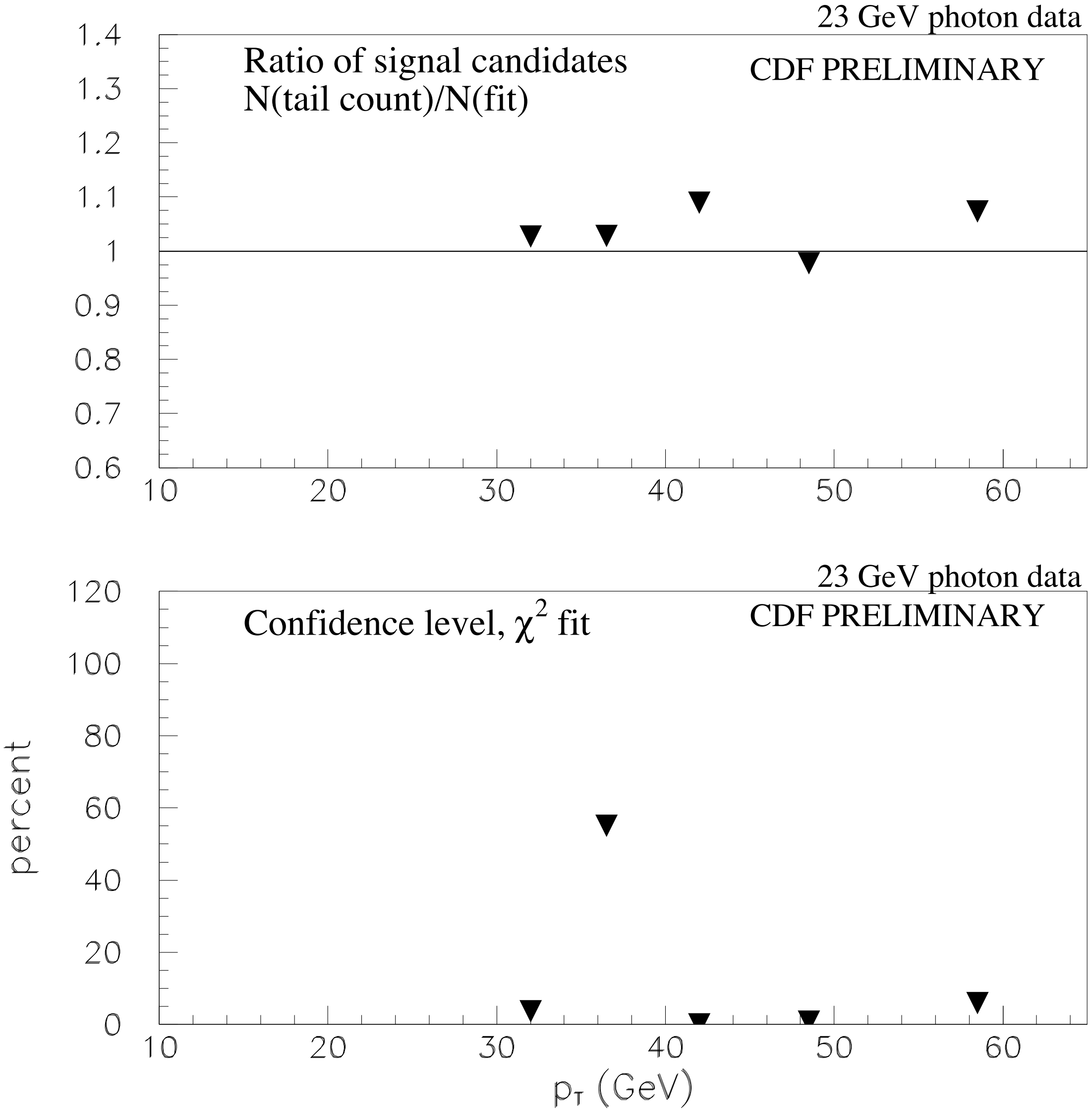

Figure 6.18: Results of the χ^2 fit on the 23 GeV photon data. The top plot shows the number of signal candidates returned by the fit compared to the number found by the tail count. The lower plot shows the confidence level of the fits.

these data is also discussed in section 6.4.

dataset	p_T	Total events	Signal candidates	statistical error (%)
8 GeV electron (2 tower)	10-11	19110	7152.3	2.2
	11-12	19681	7761.2	2.1
	12-13	15216	6110.5	2.2
	13-14	10523	4319.7	2.6
	14-15	7324	3194.5	2.9
	15-16.5	6578	3059.3	2.8
	16.5-18	3657	1846.4	3.5
	18-20	2790	1391.2	4.1
	20-22	1472	862.9	5.1
	22-24.5	966	596.3	6.0
	24.5-27	530	344.6	7.7
	27-30	341	272.2	8.8
	30-34	205	135.9	13.5
	34-39	133	101.4	14.4
	39-45	75	63.9	18.7
	45-52	42	21.7	53.3
	52-65	19	16.6	33.5
23 GeV photon (1 tower)	30-34	1090	723.0	4.8
	34-39	765	564.3	5.3
	39-45	471	315.5	7.4
	45-52	265	224.9	8.5
	52-65	184	130.5	11.3

Table 6.2: Results of the χ^2 fit background subtraction.

6.4 Background subtraction systematics

Since we use E/p to separate signal and background, we are sensitive to the QFL simulation of the CTC and CEM. There are several effects in the data that QFL does not model well. For example, conversion tracks are known to have unusual systematics due to the presence of overlapping hits in the CTC inner superlayers. This can cause the pattern recognition software to pull the two tracks together, increasing their p_T and decreasing E/p, as shown in Figures 4.5 and r4.6. This type of effect is predicted by CDFSIM, a hit-level CTC simulation. Also, in 1 tower events we have two EM showers in the same CEM tower but well separated in ϕ. In this case, the CEM energy measurement, which is the geometric mean of the phototube energies with small corrections, produces a biased E_T measurement. As discussed in section 5.1, QFL simulates the response map of the CEM, but it does not simulate the two phototubes correctly individually. Therefore it cannot reproduce the E_T bias exactly.

Another unusual feature of E/p is shown in Figure 6.19. We divide the 8 GeV electron data into two samples by the charge of the higher p_T track and plot the average E/p between 0.9 and 1.1 as a function of photon p_T. At low p_T the difference in the mean E/p between positive and negative charges is about 0.2%, which is a fairly small discrepancy. However, at moderate p_T the splitting increases up as much as 1%. At high p_T the statistics becomes too small to draw any conclusions. Since the calorimeter is not sensitive to the charge of the showering particle, this splitting must be related to CTC tracking systematics. However, the Monte Carlo simulation of the CTC treats positive and negative tracks the same, and therefore cannot reproduce an effect such as this.

To quantify the effect of all E/p biases on the cross section, we assume that they can be modeled as a scale factor on E/p in the data. This assumption is motivated by the observation that in the p_T bins with poor χ^2 fits, such as the lowest bins in the 8 GeV electron data, the signal peak appears to be shifted in the data compared to the Monte Carlo. To determine what scale factor the data prefers , we use the Kolmogorov-Smirnov (KS) statistic. The KS statistic is defined as the maximum difference between the integrated Monte Carlo and data E/p distributions. We calculate the KS statistic by integration the E/p distributions from 0.5 to 2.0. We apply scale factors to the data in 0.1% steps between 95% and 105%, and we choose in each p_T bin the scale factor which has the minimum KS statistic. These scale factors are shown for both datasets in Figure 6.20, and are tabulated in Table 6.3.

For the 8 GeV electron data the scale factors are between 0.99 and 1.01 in most p_T bins, while the 23 GeV photon data prefer a scale of 0.98 in the highest p_T bins. Since the 23 GeV photon data is 1 tower only and high p_T, in this data the separation between the electron and positron tracks is minimal. Therefore we expect that effects related to the finite two-track resolution of the CTC to manifest themselves here. In the 8 GeV electron data the KS scales are greater than one in most p_T bins. We expect the p_T biases in this data to be smaller because the second track is soft and separates from the trigger electron relatively quickly. We also do not expect to have any calorimeter biases since there is only one EM shower in the CEM cluster in a 2 tower event. Therefore we have no good explanation for the KS scales observed in these data.

To determine the effect of the E/p scales on the cross section, we scale E/p in the data by ±1% for the 8 GeV electron data and ±2% for the 23 GeV photon, and repeat the background subtraction. The fractional change in the number of signal candidates found for both datasets is shown in Figure 6.21. We take these numbers as a systematic error on the cross section.

As shown in Figures 6.17 and 6.18, some of the background subtraction χ^2 fits have poor confidence levels. This is particularly true for the lowest three p_T bins of the 8 GeV electron data. To determine if these poor fits can be explained as an E/p scale we repeat the fits after applying the E/p scales found with the KS statistic. The confidence levels of the fits with and without the scales are shown in Table 6.4. We find that in most cases the confidence level improves after applying the

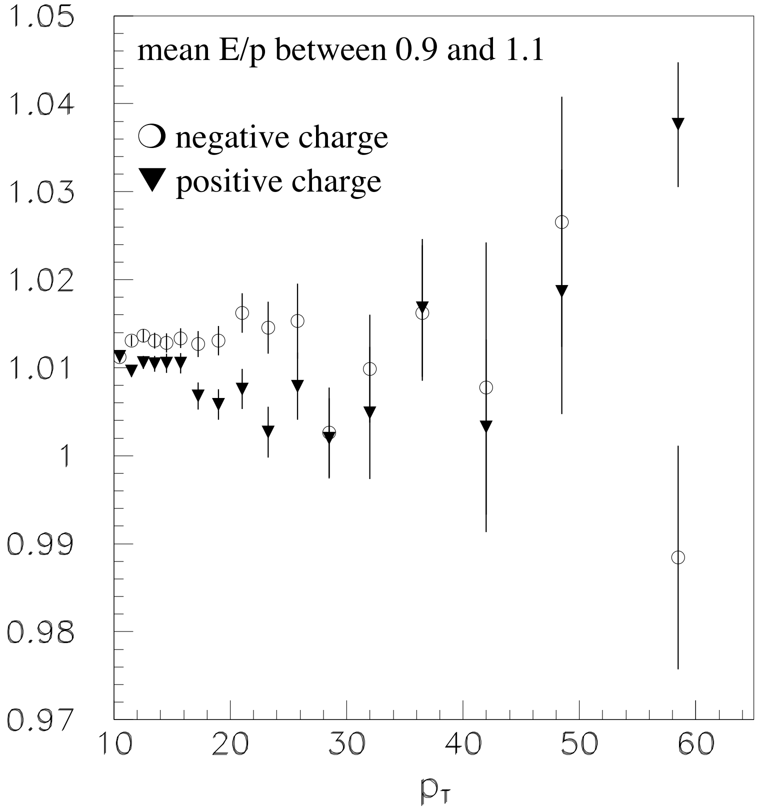

Figure 6.19: Mean E/p between 0.9 and 1.1 versus photon P_T. The 8 GeV electron data is divided into two samples according to the charge of the higher p_T conversion track.

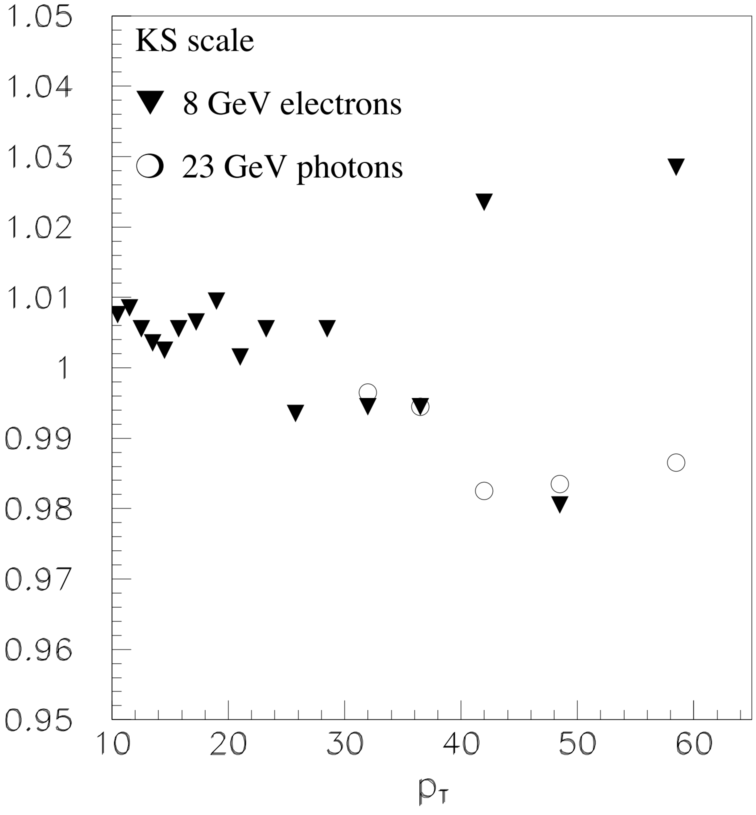

Figure 6.20: E/p scales determined by the KS statistic.

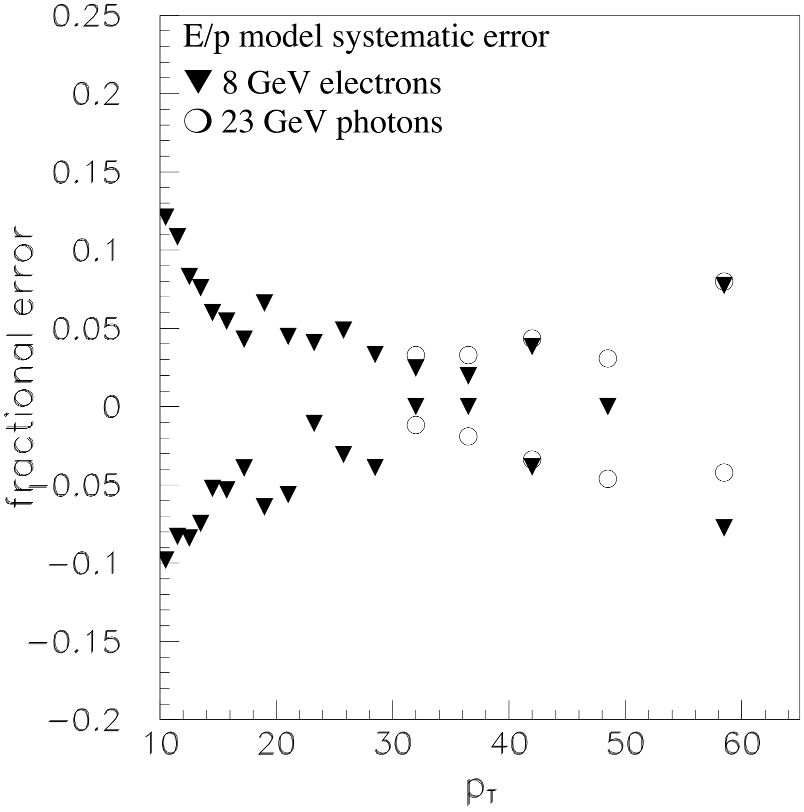

Figure 6.21: E/p model systematic error. The change in the number of signal candidates found by the tail count background subtraction after scaling E/p in the data by ±1% for the 8 GeV electron data ±2% for the 23 GeV photon data.

dataset	p_T	E/p scale
8 GeV electron (2 tower)	10-11	1.0075
	11-12	1.0085
	12-13	1.0055
	13-14	1.0035
	14-15	1.0025
	15-16.5	1.0055
	16.5-18	1.0065
	18-20	1.0095
	20-22	1.0015
	22-24.5	1.0055
	24.5-27	0.9935
	27-30	1.0055
	30-34	0.9945
	34-39	0.9945
	39-45	1.0235
	45-52	0.9805
	52-65	1.0285
23 GeV photon (1 tower)	30-34	0.9965
	34-39	0.9945
	39-45	0.9825
	45-52	0.9835
	52-65	0.9865

Table 6.3: E/p scales determined by the KS statistic.

KS scales. However, some are still too low to be considered a statistical fluctuation. This indicates that the E/p model errors are not always due to a simple scale. For example, it may be that the CEM and CTC resolutions are not exactly gaussian for conversions as assumed by the Monte Carlo. This type of problem could cause poor fits in bins where the data statistics is large, but we would not expect it to cause a bias in the extraction of the number of signal candidates if the effect is relatively small.

6.5 Fake Conversions

In this chapter we have assumed that all backgrounds to the prompt photon signal are due to π^0 and η decays to two photons. However, fake conversions represent another possible background source. A fake conversion is a real or fake electron which has a nearby track that satisfies the conversion identification cuts. Since the

dataset	p_T	C.L before E/p scale (%)	C.L after E/p scale (%)
8 GeV electron (2 tower)	10-11	8.955×10^{-8}	7.870×10^{-2}
	11-12	3.710×10^{-14}	4.293×10^{-4}
	12-13	3.725×10^{-3}	3.463×10^{-3}
	13-14	2.05	17.5
	14-15	0.760	3.44
	15-16.5	12.2	20.9
	16.5-18	13.8	67.6
	18-20	75.9	3.87
	20-22	86.0	84.1
	22-24.5	55.8	73.9
	24.5-27	14.8	81.9
	27-30	88.6	81.9
	30-34	71.5	96.4
	34-39	37.8	32.6
	39-45	68.2	69.9
	45-52	95.2	95.4
	52-65	96.6	80.4
23 GeV photon (1 tower)	30-34	4.01	9.86
	34-39	62.7	33.2
	39-45	1.664E-02	35.4
	45-52	0.665	60.4
	52-65	15.5	78.6

Table 6.4: Confidence level of the background subtraction fits before and after applying the E/p scales determined with the KS statistic.

secondary track in a fake conversion is likely to be a hadron, we can investigate the fake contamination of our sample by examining the electromagnetic nature of the secondary tracks.

For the purpose of this study we require that the secondary track point to the fiducial part of the neighboring tower in the ϕ direction. We measure the E_T of the track by adding the E_T of the tower to which the track points and its closest neighbor in η. We compare this E_T to the secondary's vertexed p_T.

The E/p of the secondary tracks is shown in Figure 6.22. We see that the bulk of the secondary tracks have an E/p consistent with unity, indicating that the tracks are electrons. However, there is a small tail at low E/p and a spike at E/p = 0, and these events may be enriched in fake conversions. To determine if these events are fake conversions, we compare the radius of conversion distribution of the events with E/p > 0.6 to the events with E/p < 0.6. The radius of conversion of a fake should not be correlated with the material distribution of the detector, and we expect that most will occur near the origin. As shown in Figure 6.22, the low E/p events have a radius of conversion distribution which is consistent with the detector material, indicating that these events are real conversions. We conclude that there is no evidence for significant fake conversion contamination in our data sample, so we ignore this background source in the cross section measurement.

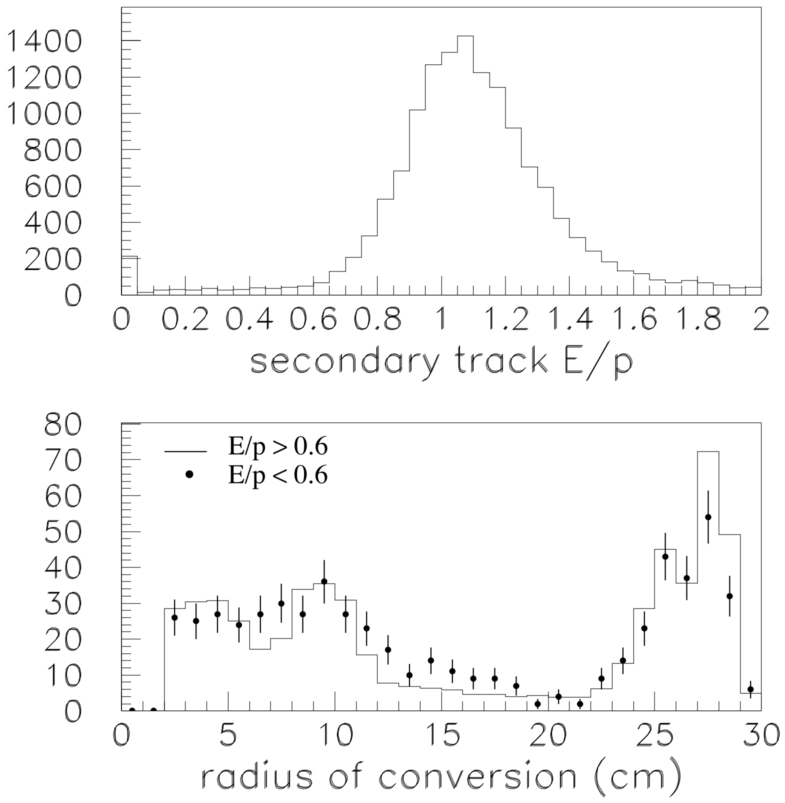

Figure 6.22: Search for fake conversions in the 2 tower data sample. Top: the E/p distribution of the secondary tracks in the final 2 tower dataset. The broad peak at E/p = 1 indicates that the secondary tracks are dominated by real electrons. Bottom: Comparison of the radius of conversion distributions of events with secondary E/p $<$ 0.6 and E/p $>$ 0.6, normalized to equal area. The distributions are consistent with each other, and therefore the low E/p events are likely to be real conversions.

Chapter 7

Acceptance and efficiency

By making cuts on the event variables described in chapter 4, we attempt to isolate a sub-sample of events which are well measured by the detector and have a manageable level of backgrounds from π^0s and ηs. These backgrounds are then removed statistically with the E/p method described in chapter 6. The final result of this procedure is a signal event count in each p_T bin. To complete the cross section measurement we must extrapolate this event count into the regions of parameter space which were removed as a side effect of our data selection.

We classify the extrapolation as the acceptance and the efficiency. By acceptance we mean those efficiencies which are determined primarily by the design and geometry of the detector. The largest component of the acceptance is the probability that a signal event will occur in the fiducial volume of the detector. Also included in the acceptance is the dynamic range of the detector. For example, the CTC cannot reliably track charged particles below 400 MeV, so conversions which produce tracks below this threshold are considered outside the acceptance. Generally the acceptance cannot be changed without changing the detector itself.

The efficiency, on the other hand, refers to the fraction of signal events remaining after we apply quality cuts to the data sample. In the case of the photon cross section, this category includes conversion and electron identification cuts, the isolation cut, the extra track cut, and the $\not\!\!E_T$ cut. Also included in the efficiency are effects related to the detector performance such as the trigger and tracking efficiencies.

There is also an important practical distinction between the acceptance and efficiency. In this thesis we rely on the Monte Carlo to predict the acceptance, while the efficiency is measured directly in the data with a variety of independent studies.

7.1 Acceptance

We take the signal acceptance from the PYTHIA+QFL Monte Carlo. In each p_T bin we count the number of Monte Carlo events generated with $|\eta| < 0.9$ which converted in the inner detector. We then count the number of events in which an electron cluster was found in the calorimeter with two tracks above 400 MeV pointing to the fiducial part of the calorimeter, for both the 1 tower and 2 tower geometries. The ratio of the number of reconstructed events to the number of generated events is the acceptance, and is shown for both geometries as a function of p_T in Figure 7.1. In equation form the acceptance can be written

$$\mathcal{A} = \frac{N_{MC}(CEM, p_T^{sec} > 0.4, |\eta| < 0.9)}{N_{MC}(|\eta| < 0.9)} \tag{7.1}$$

When binning the Monte Carlo by p_T, we use the true p_T of the generated photon. This gives us the acceptance unsmeared by detector resolution. However, the calorimeter resolution is good enough such that binning by the reconstructed p_T has a negligible effect on the inferred acceptance.

As seen in Figure 7.1, the 1 tower acceptance is larger than the 2 tower acceptance below 18 GeV, with the 2 tower geometry being preferred at higher p_T. This is due to the fact that at high p_T the curvature of the conversion tracks becomes small, so they are likely to point at the same CEM tower. In the highest p_T bin the ratio of acceptances between the two geometries is a factor of seven. Since we can use both the 8 GeV electron data and the 23 GeV photon data to measure the cross section above 30 GeV, by comparing the two cross section measurements we can cross check the robustness of the Monte Carlo's acceptance calculation.

As a further check on the acceptance calculation we compare the conversion asymmetry observed in the data to that predicted by the Monte Carlo. The asymmetry is defined as the fraction of the photon momentum which is transferred to the positron in the conversion process. The theoretical prediction for the asymmetry is shown in Figure 5.6. In the data several effects bias the observed asymmetry and result in a loss of acceptance. In the lowest p_T bins we are biased toward very asymmetric conversions by the 7.5 GeV track requirement in the Level 2 trigger. The 1 tower and 2 tower requirements also bias the asymmetry, with the 2 tower data (8 GeV electrons) becoming increasingly asymmetric as the p_T increases, and the 2 tower data (23 GeV photons) recovering the symmetric portion of the spectrum above 30 GeV.

The conversion asymmetry of the 8 GeV electron data and 23 GeV photon data is compared to the Monte Carlo in each p_T bin in figures 7.2 through 7.8. In general there is good agreement between the data and Monte Carlo.

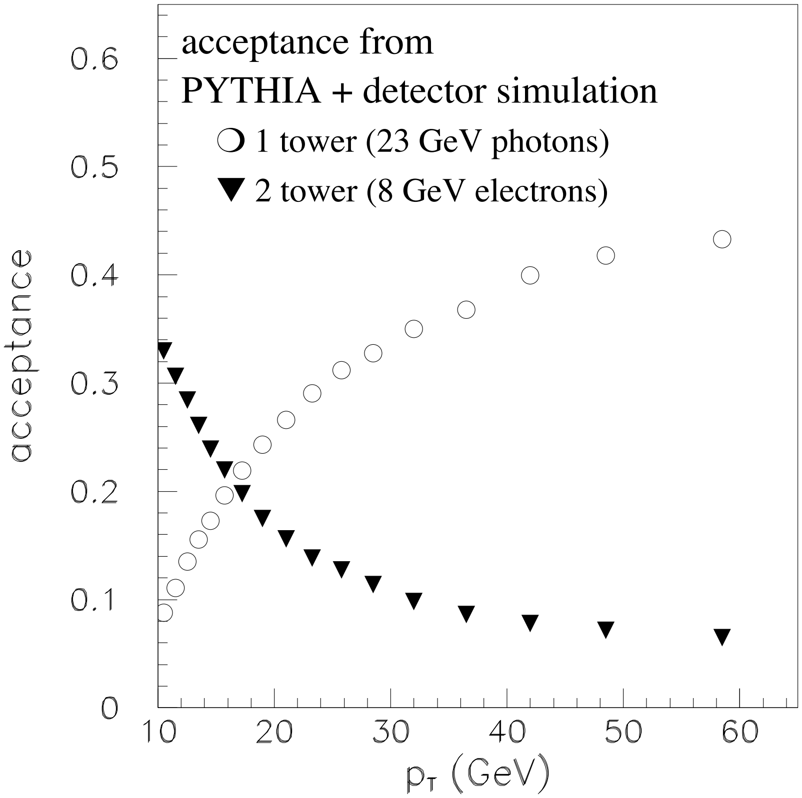

Figure 7.1: The signal acceptance for 1 tower and 2 tower events as a function of p_T, from the PYTHIA+QFL Monte Carlo. Note that the 1 tower acceptance is shown at low p_T, although the trigger threshold for that dataset is 23 GeV.

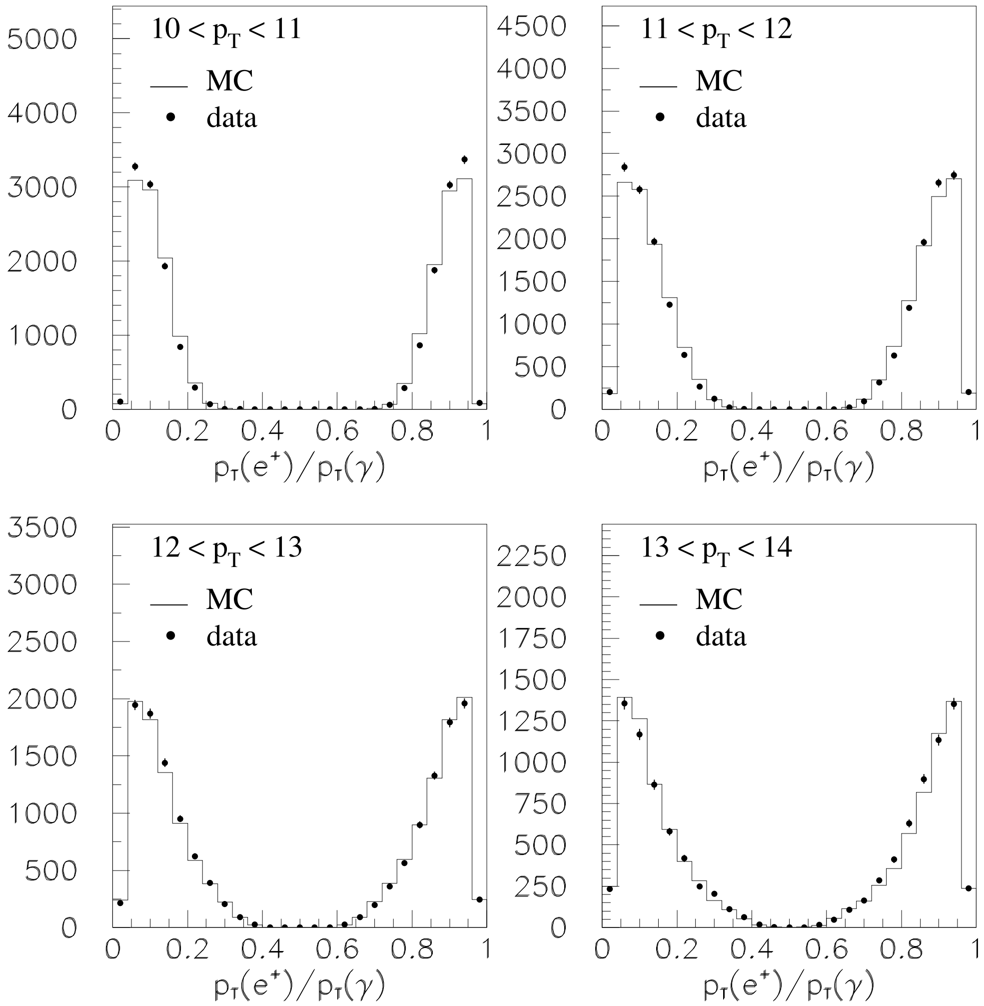

Figure 7.2: Conversion asymmetry in data and Monte Carlo in each p_T bin for the 8 GeV electron data.

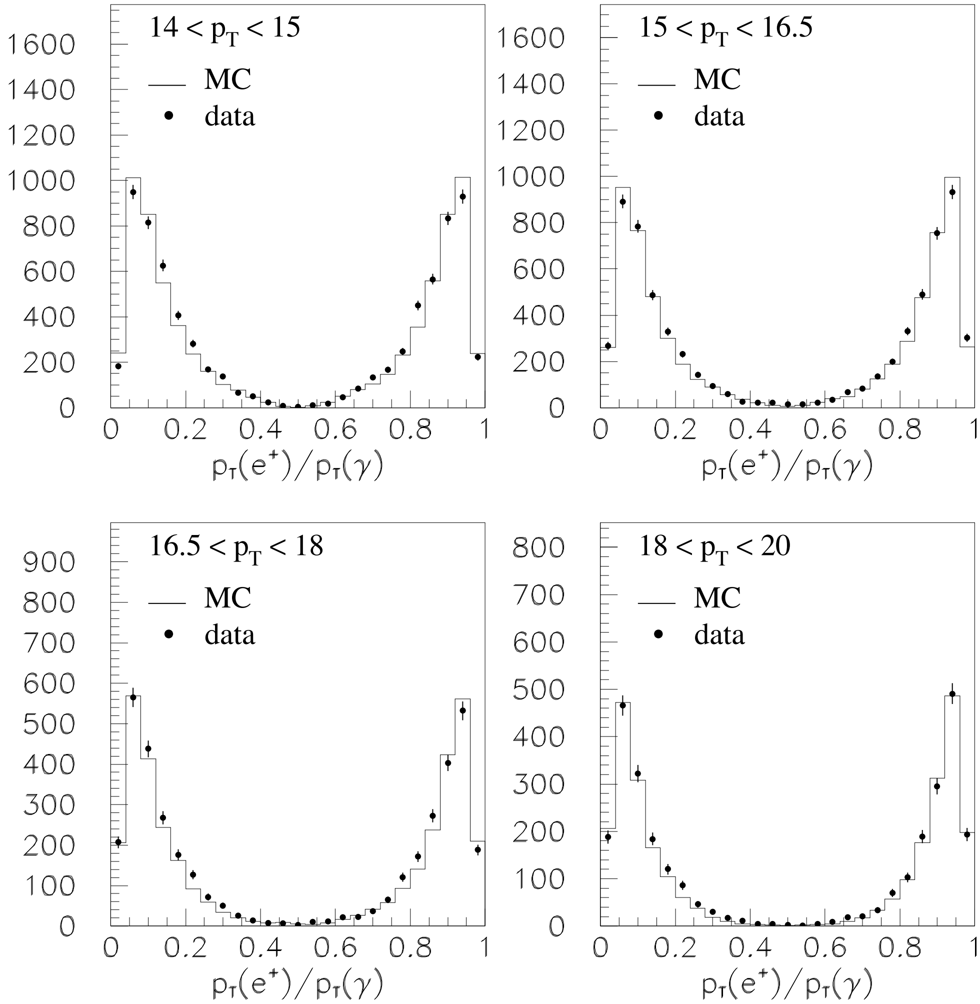

Figure 7.3: Conversion asymmetry in data and Monte Carlo in each p_T bin for the 8 GeV electron data.

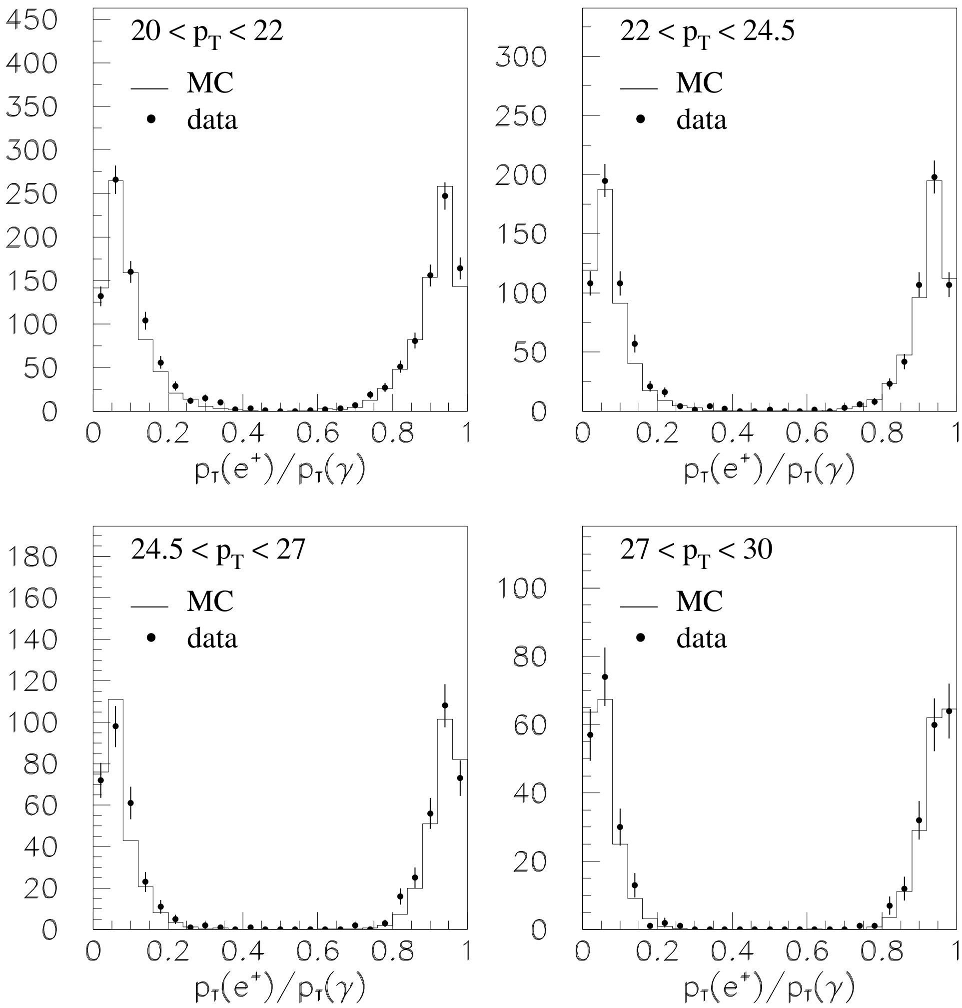

Figure 7.4: Conversion asymmetry in data and Monte Carlo in each p_T bin for the 8 GeV electron data.

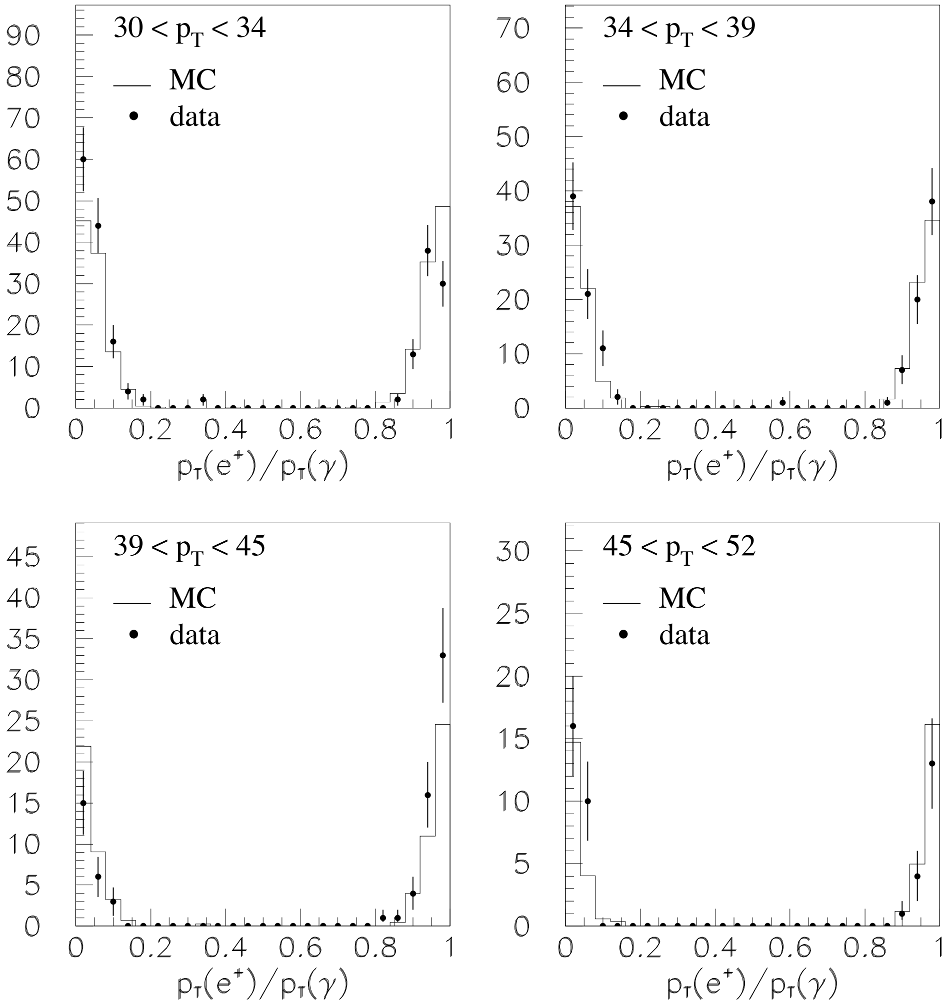

Figure 7.5: Conversion asymmetry in data and Monte Carlo in each p_T bin for the 8 GeV electron data.

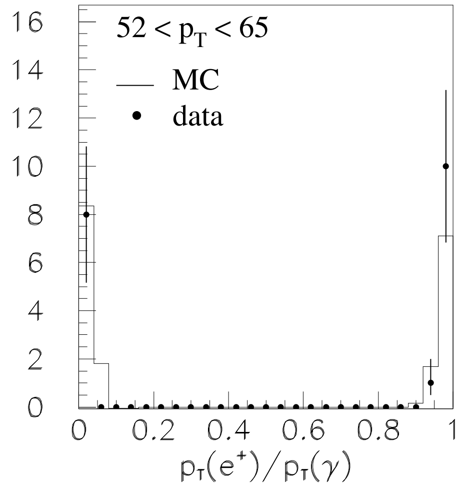

Figure 7.6: Conversion asymmetry in data and Monte Carlo in each p_T bin for the 8 GeV electron data.

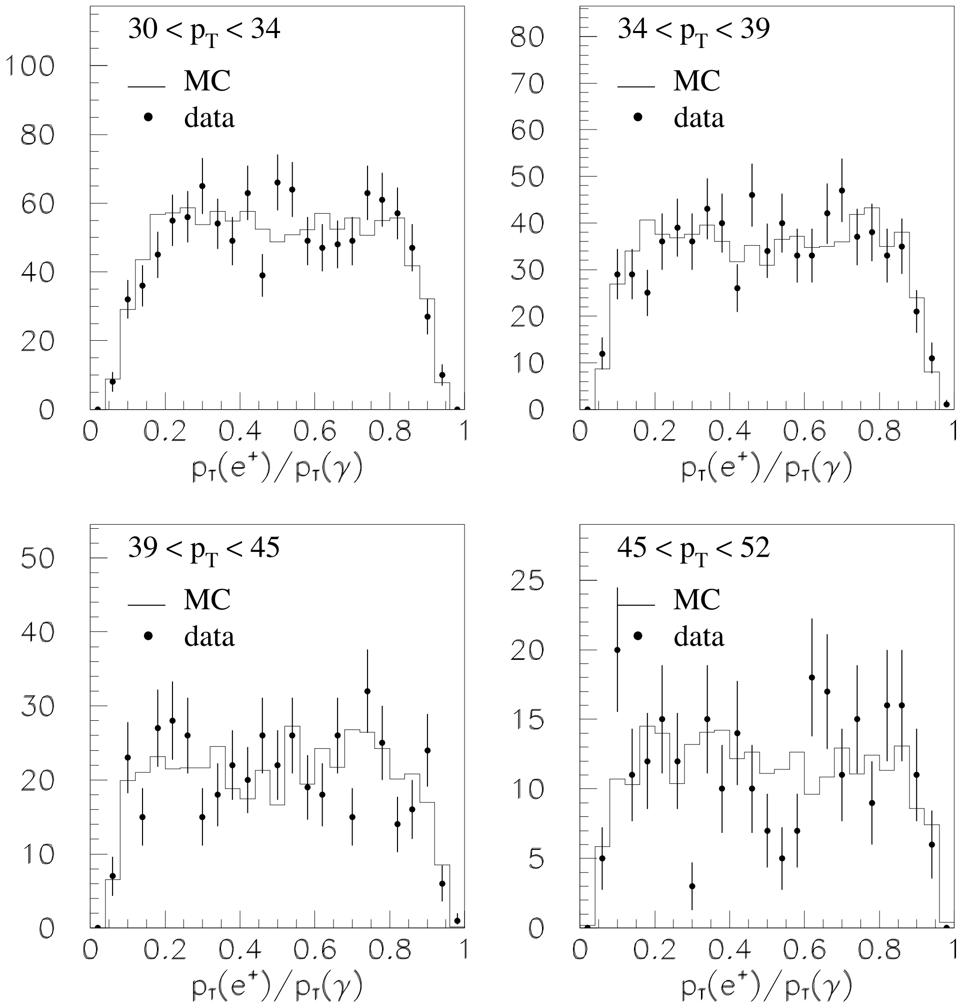

Figure 7.7: Conversion asymmetry in data and Monte Carlo in each p_T bin for the 23 GeV photon data.

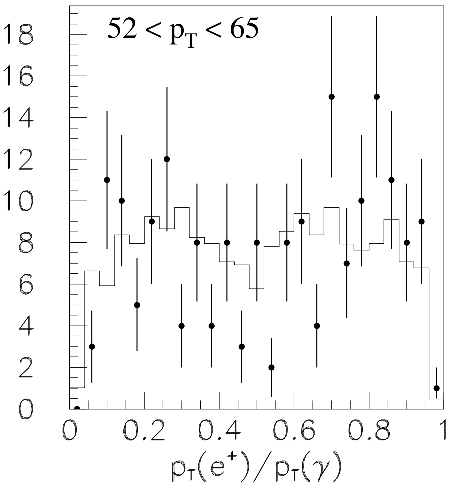

Figure 7.8: Conversion asymmetry in data and Monte Carlo in each p_T bin for the 23 GeV photon data.

7.2 Efficiencies

The signal efficiencies of all remaining data selection cuts are taken from a variety of special studies performed in the data. These studies rely on a number of independent data samples, including minimum bias data, inclusive muon data, $Z \rightarrow e^+e^-$ data, and $W \rightarrow e\nu$ data. Some of these studies were performed specifically for this thesis, and in other cases the results of previous work have been adopted here.

7.2.1 z_0 cut

We require that the event vertex be within 60 cm of the center of the detector along the z axis in order to maintain the projective geometry of the calorimeter. Since the illuminated region is approximately gaussian with a width of 30 cm, we expect this cut will retain about 95% of all events. The efficiency of the cut was measured with a special study of Run Ib minimum bias data, and the result is $\epsilon_{z_0} = 0.937 \pm 0.011$ [33].

7.2.2 Conversion identification efficiency

The efficiency to pass the conversion identification cuts (*sep* and $\Delta \cot \theta$ cuts) along with the efficiency of the conversion vertex fit is taken from the data using CTC inner cylinder conversions. We use the inner cylinder because it is a distinct structure which is easily distinguishable from the neighboring material and fakes, even after relaxing the conversion identification cuts.

We loosen the *sep* and $\Delta \cot \theta$ cuts to 1.0 cm and 0.15, respectively, and plot the un-vertexed radius of conversion in Figure 7.9. The un-vertexed radius of conversion is the radius at which the two un-vertexed tracks are parallel. To reduce the number of fake conversions, in this plot we require that the secondary track deposit more than 1 GeV of energy in the CES strip chambers. The CTC inner cylinder and VTX outer wall are seen between 20 cm and 30 cm. To eliminate fake conversions we fit the sidebands to a third order polynomial, excluding from the fit the region between 19 cm and 31 cm. We subtract the fitted polynomial from the data and find 189,599 conversion candidates. We then apply the *sep* and $\Delta \cot \theta$ cuts, and require that the vertex fit is successful. We repeat the sideband fit and find 184,737 conversion candidates. We take the ratio, 0.974, as the efficiency of the conversion ID cuts. Note that the sidebands contain both real and fake conversions, so a sideband subtraction will subtract real conversions from the signal region as well fakes. In effect, we are using the difference in material between the signal region and sideband region as our figure of merit.

We check to see if the conversion identification cut efficiency depends on photon p_T. We repeat the above procedure after dividing the data into p_T bins. We find that the efficiency varies by about ±2% from the average value.

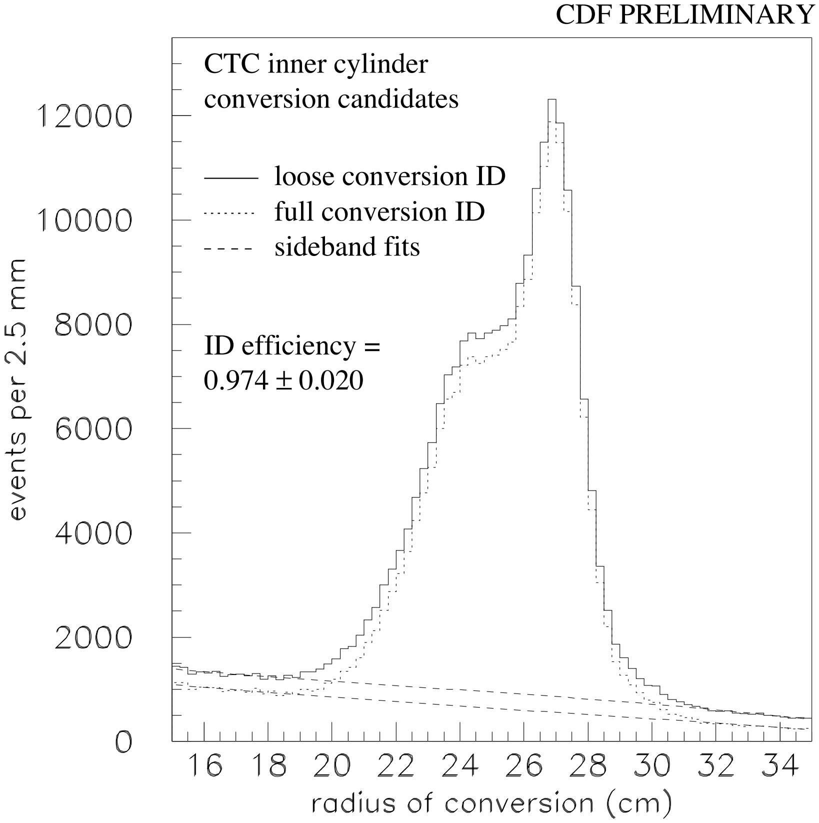

Figure 7.9: The efficiency of the conversion identification cuts, from inner cylinder conversions in the data. The plot shows the un-vertexed radius of conversion with very loose conversion identification compared to the full standard cuts. Fake conversions are removed with the sideband fits, and the ratio of peaks is taken as the efficiency.

We also check the conversion ID efficiency for dependence on the radius of conversion. We again relax the *sep* and $\Delta\cot\theta$ cuts to 1.0 cm and 0.15. To get a pure sample of real conversions we use double conversion events which have a diphoton mass within 50 MeV of the π^0 mass. We require that all four tracks deposit more than 1 GeV of energy in the strip chambers, and we measure the conversion ID efficiency of those photons with p_T above 8.0 GeV. For photons with radius of conversion between 2 cm and 12 cm we find an ID efficiency of $96.7 \pm 0.8\%$, and for conversion between 22 cm and 29 cm we find $95.4 \pm 1.1\%$.

To account for these variations we assign a systematic uncertainty of ±2% to the conversion ID cut efficiency.

7.2.3 Trigger efficiency

The Level 2 trigger efficiencies our two datasets have been measured previously. In the case of the 8 GeV electron data, we take the Level 2 efficiency from a study of 5 GeV electrons and inclusive muons, as described in section 5.4.1. The efficiency of the electron identification cuts applied at Level 3 is measured with $Z \rightarrow e^+e^-$ data. We take the Level 2 efficiency of the 23 GeV photon dataset from a previous study.

8 GeV electron trigger efficiency

The Level 2 efficiency of the 8 GeV electron trigger was measured and parameterized in terms of the single electron E_T and p_T [31] as discussed in section 5.4.1. For the photon cross section measurement we must transform those variables onto the photon p_T. The relationship between the photon p_T and the electron E_T and p_T is determined by the conversion asymmetry distribution, which is included in the Monte Carlo as discussed in section 5.6. Therefore we use the Monte Carlo to do the transformation. The results are shown in Figure 7.10. The efficiency becomes flat above 16 GeV because a 16 GeV photon is guaranteed to have at least one conversion track above the 7.5 GeV track p_T requirement. Note that the parameterized trigger efficiency only applies to conversions which are in the fiducial part of the calorimeter. We can express this as

$$\epsilon(L2(8GeV)) = \frac{N_{MC}(L2, \mathcal{A})}{N_{MC}(\mathcal{A})} \tag{7.2}$$

The Level 3 electron trigger applies E_T, p_T, and electron identification cuts to the data. The efficiency of the E_T and p_T cuts is given by the PYTHIA+QFL Monte Carlo, while the electron identification efficiency is determined with a study of $Z \rightarrow e^+e^-$ events found in the 8 GeV electron dataset. We select Z candidates with an invariant mass between 80 GeV and 100 GeV. We require that both electrons be central and fiducial, and that they have $E_T > 20$ GeV and $p_T > 15$ GeV. We then ask that one of the electrons pass the following tight electron ID cuts:

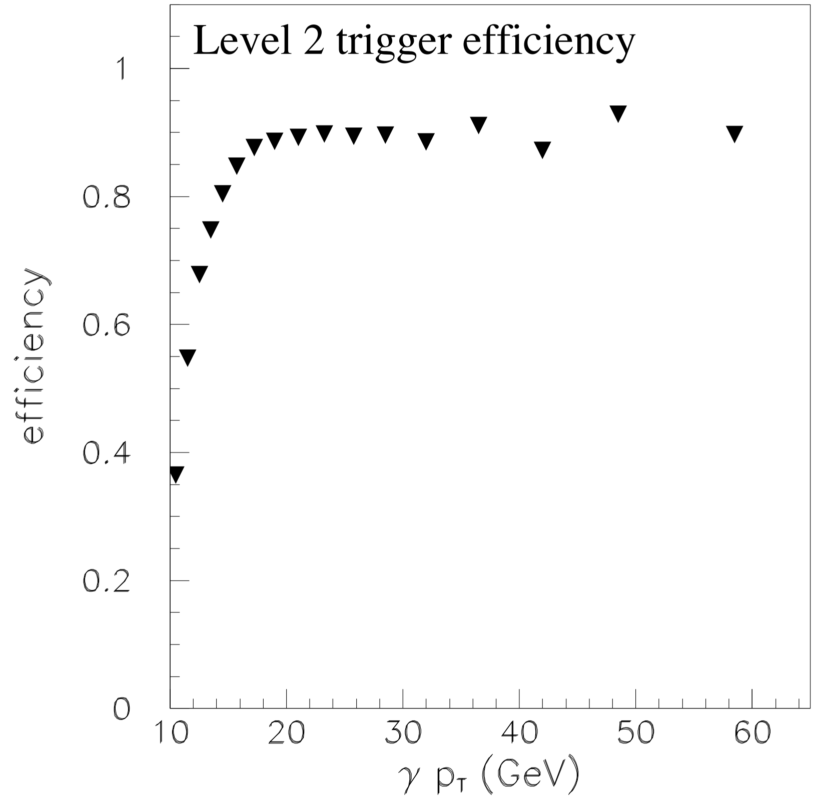

Figure 7.10: The efficiency of the Level 2 8 GeV electron trigger, in terms of the photon p_T.

- $l_{shr} < 0.1$
- $had/em < 0.05$
- $|\Delta x| < 1.5$ cm
- $|\Delta z| < 3.0$ cm
- $\chi^2_{strip} < 4.0$
- $\chi^2_{wire} < 4.0$

We assume that the other electron in the event is unbiased, and we use it to measure the efficiency of the Level 3 electron ID cuts.

The efficiency measurement is complicated by the presence of internal and external bremsstrahlung in the Z electrons. This causes the EM shower to broaden in the CES wire view, and the χ^2_{wires} cut tends to become inefficient. However, conversion electrons have no internal bremsstrahlung, and only a fraction of the external brems (since they do not pass through all the detector material), so we are interested in the Level 3 efficiency of low brem electrons.

To study the effect of bremsstrahlung on the Z electron ID efficiency, we plot the efficiency as a function of E/p in Figure 7.11. Also shown is the electron ID efficiency with the χ^2_{wire} cut released. The χ^2_{wires} cut is seen to cause a dramatic drop in the efficiency at E/p > 1.2. Below E/p = 1.2, the efficiency is flat at 0.849, and we take this to be the Level 3 electron ID efficiency of low brem electrons.

$$\epsilon(L3(8GeV)) = \frac{N_{MC}(L3, \mathcal{A}, L2, E/p < 1.2)}{N_{MC}(\mathcal{A}, L2, E/p < 1.2)} \tag{7.3}$$

Since the rate of external bremsstrahlung depends on the amount of material seen by the conversion electron, we can study the effect in the Monte Carlo by asking QFL to predict the variation in the χ^2_{wires} cut efficiency as a function of the radius of conversion. We see a 3% difference between SVX conversions and CTC inner cylinder conversions, and we take this as a systematic error. Our final result for the electron identification efficiency is 0.849 ± 0.03

23 GeV photon trigger efficiency

The 23 GeV photon trigger has Level 2 requirements on E_T, CES energy (XCES), and isolation. The E_T and XCES efficiency were measured with a prescaled 10 GeV photon trigger, while the isolation efficiency was measured with a prescaled non-isolated 23 GeV trigger [16]. The efficiency is found to be 0.914 ± 0.043 above 30 GeV. This trigger has no Level 3 requirements, so we take the Level 3 efficiency to be 1.0.

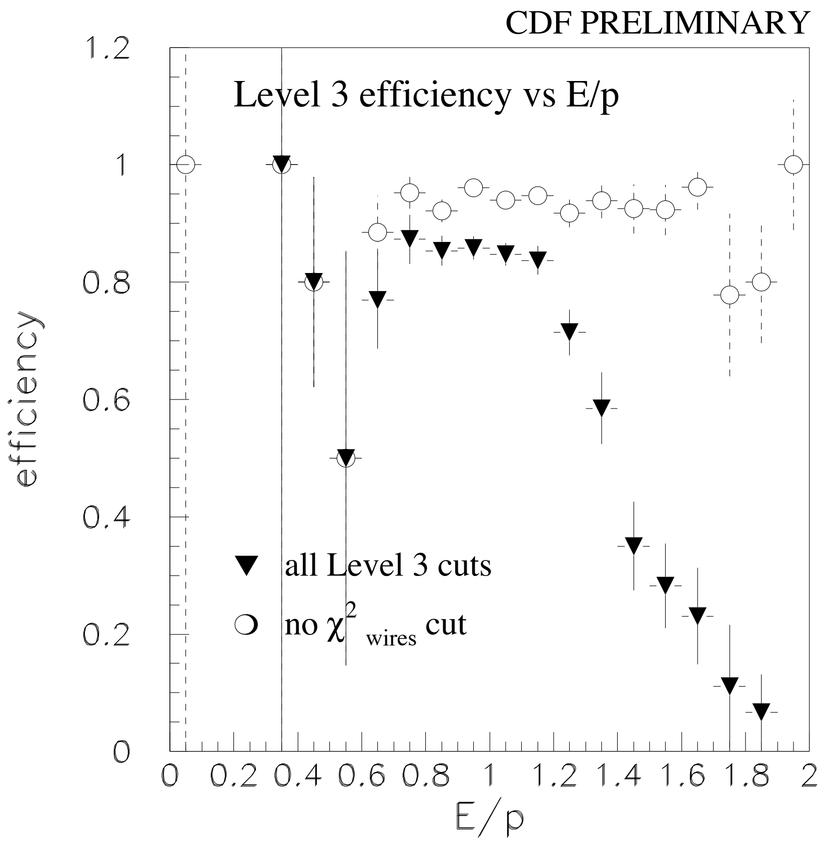

Figure 7.11: The efficiency of the Level 3 electron identification cuts measured with $Z \rightarrow e^+e^-$ data, as a function of electron E/p. Also shown is the same efficiency with the χ^2_{wires} cut released. The χ^2_{wires} cut becomes inefficient at high E/p due bremsstrahlung, and we use events with E/p $<$ 1.2 to measure the efficiency.

7.2.4 Tracking efficiency

The CTC tracking efficiency was measured with a track embedding study [30] described in section 5.3.1. This study parameterized the CTC efficiency as a function of track p_T, and we apply the efficiency to both conversion tracks. We use the PYTHIA+QFL Monte Carlo to transform the efficiency in terms of the photon p_T. The efficiency is almost flat as a function of photon p_T, with a plateau value of 92%.

7.2.5 Isolation cut efficiency

We use an isolation cut which depends on the geometry of the conversion. In 1 tower events and 2 tower events where the secondary conversion track lands outside a 0.4 cone centered on the trigger electron, we cut at $E_T^{cone0.4} < 1.0$ GeV. In 2 tower events where the secondary conversion track points to a tower within a radius of 0.4, we exclude from the cone energy sum the tower hit by the secondary track and its nearest neighbor in η. We then lower the cut value to 0.87 GeV to account for the loss of these towers.

To measure the efficiency of the isolation cut we assume that the energy we find in the calorimeter due to the underlying event and multiple $p\bar{p}$ interactions is the same in minimum bias data as in direct photon events. In the minimum bias data we choose randomly an η and ϕ for a hypothetical electron candidate. We calculate the location of the candidate in the calorimeter, and form a 'CEM cluster' from the tower hit by the electron and its neighboring towers in η. We then add up the E_T in all calorimeter towers which satisfy $\Delta R < 0.4$, excluding from the sum those towers which are in the CEM cluster. We measure the fraction of events in which this energy sum is less than 1 GeV as a function of the number of reconstructed vertices in the event. This efficiency is shown in Figure 7.12. We convolute this efficiency with the number-of-vertices distribution [1] of the 8 GeV conversion data to obtain an efficiency of 0.859. This is expressed as

$$\epsilon(E_T^{cone0.4}) = \frac{\sum_{i=0}^{N_{vertices}} N_i^{8GeV} \cdot \frac{N_i^{mb}(E_T^{cone0.4}<1)}{N_i^{mb}}}{\sum_{i=0}^{N_{vertices}} N_i^{8GeV}} \tag{7.4}$$

Also shown in Figure 7.12 is the efficiency for events to pass a cut of 0.87 GeV where two extra towers have been excluded from the energy sum, as is the case in a 2 tower conversion with its secondary track within the 0.4 cone. The efficiency of this cut as a function of the number of reconstructed vertices is the same as the first case, and we also take its efficiency to be 0.859.

---

[1] When counting the number of vertices we only include those VTX vertices which pass certain quality cuts. At CDF these vertices are known as class 12.

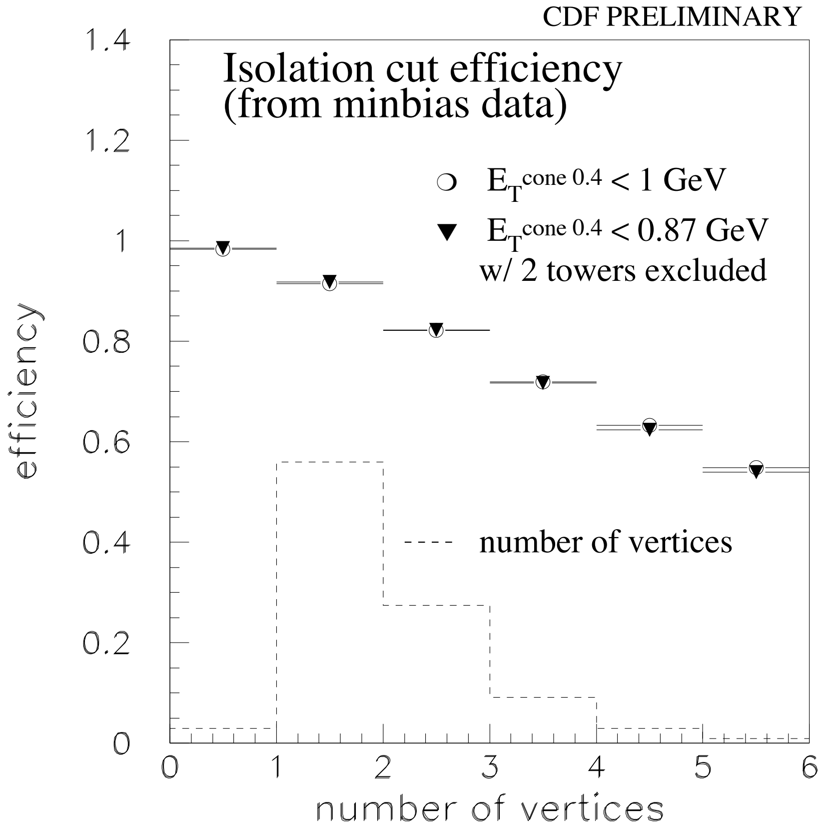

Figure 7.12: The isolation cut efficiency as a function of the number of reconstructed vertices in the event, from minbias data. The efficiency is measured by randomly choosing the location of an electron candidate in each event and adding up the energy found in the calorimeter within a cone of radius 0.4. The efficiency is shown for a 1 GeV cut, and also an 0.87 GeV cut for the case where two towers have been excluded from the cone energy sum. The dashed histogram is the number-of-vertices distribution in conversion events normalized to unit area.

7.2.6 N_{trk} cut efficiency

To measure the efficiency of the N_{trk} cut we assume that the probability of finding a random track pointing at the CEM cluster is the same in $Z \rightarrow e^+e^-$ events as in direct photon events. We select Z candidates with fiducial central electrons satisfying $E_T > 25$ GeV and $p_T > 20$ GeV. We measure the efficiency of requiring that no extra tracks point to the CEM clusters as a function of the number of reconstructed vertices in the event. This efficiency is shown in Figure 7.13. We convolute the efficiency with the number-of-vertices distribution of the 8 GeV conversion events to get an efficiency of 0.896

$$\epsilon(N_{trk}) = \frac{\sum_{i=0}^{N_{vertices}} N_i^{8GeV} \cdot \frac{N_i^Z(N_{trk}=1)}{N_i^Z}}{\sum_{i=0}^{N_{vertices}} N_i^{8GeV}} \tag{7.5}$$

7.2.7 $\not\!\!E_T$ cut efficiency

We apply a $\not\!\!E_T$ cut to the 8 GeV electron data sample in order to reduce a background due to $W \rightarrow e\nu$ events. We measure the efficiency of the cut with two datasets: a conversion sample with large $E_T^{cone0.4}$ and a double conversion π^0 sample. Both of these datasets are dominated by dijet events where the observed $\not\!\!E_T$ is determined by the calorimeter resolution. These datasets have a mostly electromagnetic jet on one side of the event, so the $\not\!\!E_T$ resolution should be similar to what we find in photon events. The efficiency is expressed as

$$\epsilon(\not\!\!E_T) = \frac{N(\not\!\!E_T < 25, \mathcal{A})}{N(\mathcal{A})} \tag{7.6}$$

and is plotted as a function of photon p_T in Figure 7.14. The two datasets agree on the efficiency, but the un-isolated conversion sample has superior statistics. We fit a polynomial to these data points above 20 GeV and take this as the efficiency.

7.2.8 Summary of efficiencies

The results of the efficiency studies are summarized in Table 7.1.

7.3 Total acceptance times efficiency

The total acceptance times efficiency as a function of photon p_T is shown for both datasets in Figure 7.15, and are listed in Tables 7.2 and 7.3. These results do not include the probability of conversion, which is discussed in chapter 8.

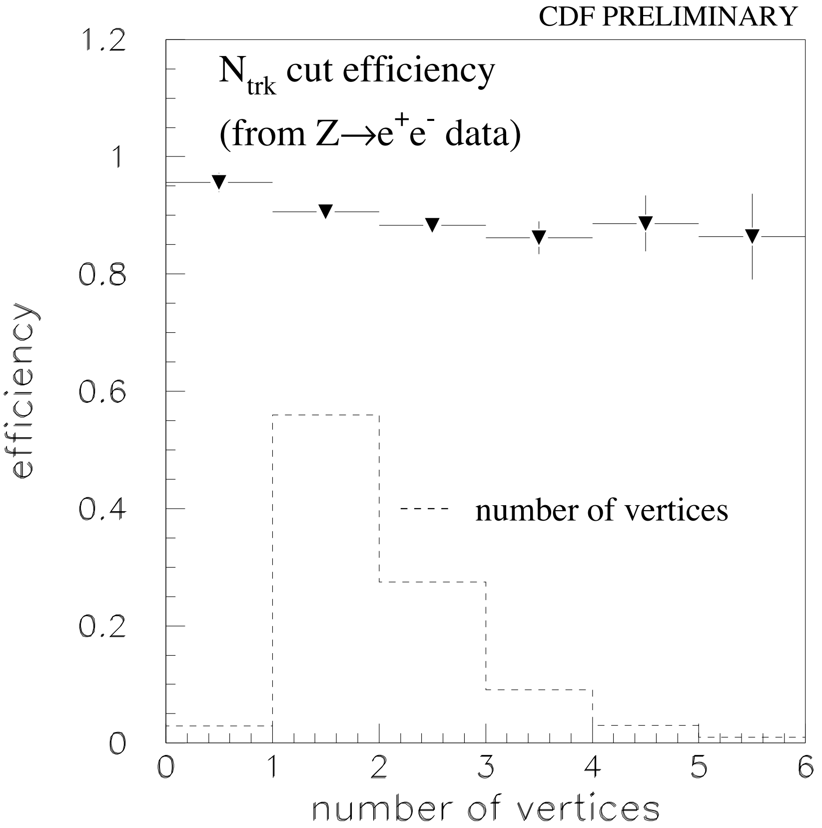

Figure 7.13: Efficiency to pass the N_{trk} cut as a function of the number of reconstructed vertices in the event, from Z events in the inclusive electron data. The dashed histogram is the number-of-vertices distribution in conversion events normalized to unit area.

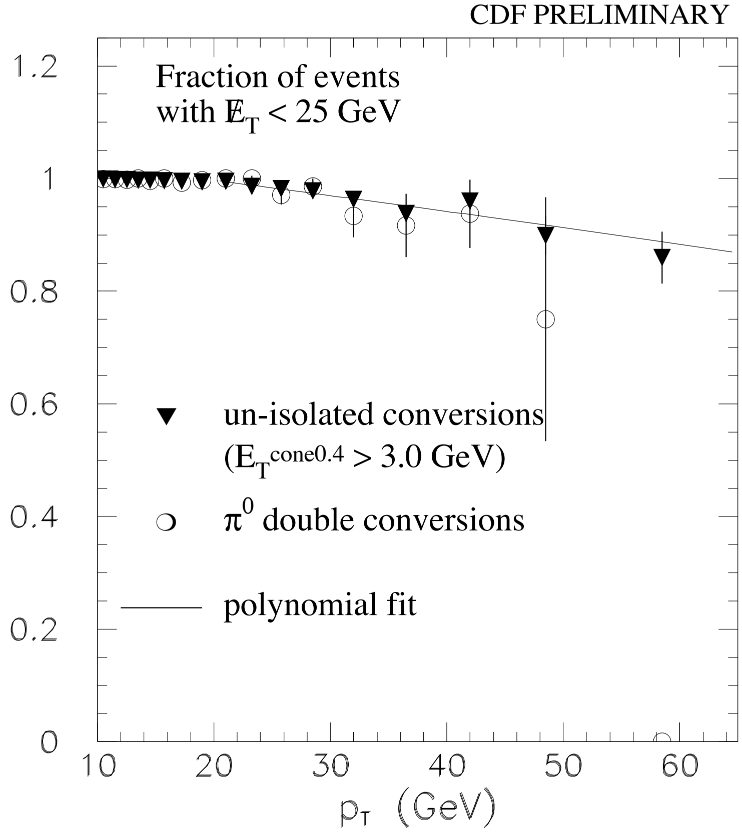

Figure 7.14: The $\not{E}_T$ cut efficiency as measured with two data samples: an un-isolated conversion sample and π^0 double converison events. Both data samples are taken from the 8 GeV electron data.

source	8 GeV	23 GeV	efficiency	method
z_0	*	*	0.937 ± 0.011	minbias data
conversion ID	*	*	0.974 ± 0.020	inner cylinder conversions
Level 2 (8 GeV)	*		p_T dependent	5 GeV electron and inclusive muon data
Level 3 (8 GeV)	*		0.849 ± 0.030	Second leg of $Z \rightarrow e^+e^-$ data
Level 2 (23 GeV)		*	0.914 ± 0.043	prescaled 10 GeV and 23 GeV photon triggers
Tracking (CTC)	*	*	$\sim 92\%$	track embedding study
Isolation	*	*	0.859	minbias data
N_{trk}	*	*	0.896	$Z \rightarrow e^+e^-$ data
$\not\!\!E_T$ (8 GeV)	*		p_T dependent	double conversion π^0 data

Table 7.1: Summary of cut efficiencies.

p_T	$\mathcal{A}$	z_0	cnv	L2	L3	CTC	Iso	N_{trk}	$\not\!\!E_T$	total
10-11	0.330	0.937	0.974	0.377	0.839	0.917	0.859	0.896	1.0	0.067
11-12	0.306	0.937	0.974	0.559	0.842	0.920	0.859	0.896	1.0	0.094
12-13	0.284	0.937	0.974	0.685	0.846	0.922	0.859	0.896	1.0	0.106
13-14	0.261	0.937	0.974	0.757	0.847	0.923	0.859	0.896	1.0	0.109
14-15	0.239	0.937	0.974	0.799	0.848	0.924	0.859	0.896	1.0	0.108
15-16.5	0.220	0.937	0.974	0.847	0.849	0.922	0.859	0.896	1.0	0.105
16.5-18	0.198	0.937	0.974	0.876	0.849	0.925	0.859	0.896	1.0	0.096
18-20	0.175	0.937	0.974	0.886	0.849	0.924	0.859	0.896	1.0	0.086
20-22	0.156	0.937	0.974	0.896	0.849	0.924	0.859	0.896	0.995	0.077
22-24.5	0.138	0.937	0.974	0.896	0.849	0.926	0.859	0.896	0.988	0.068
24.5-27	0.127	0.937	0.974	0.894	0.849	0.930	0.859	0.896	0.982	0.063
27-30	0.114	0.937	0.974	0.887	0.849	0.921	0.859	0.896	0.974	0.056
30-34	0.098	0.937	0.974	0.883	0.849	0.916	0.859	0.896	0.965	0.047
34-39	0.086	0.937	0.974	0.923	0.849	0.911	0.859	0.896	0.952	0.041
39-45	0.078	0.937	0.974	0.881	0.849	0.926	0.859	0.896	0.937	0.036
45-52	0.072	0.937	0.974	0.891	0.849	0.917	0.859	0.896	0.919	0.032
52-65	0.065	0.937	0.974	0.897	0.849	0.942	0.859	0.896	0.892	0.030

Table 7.2: Acceptance and efficiency of 8 GeV electron data sample.

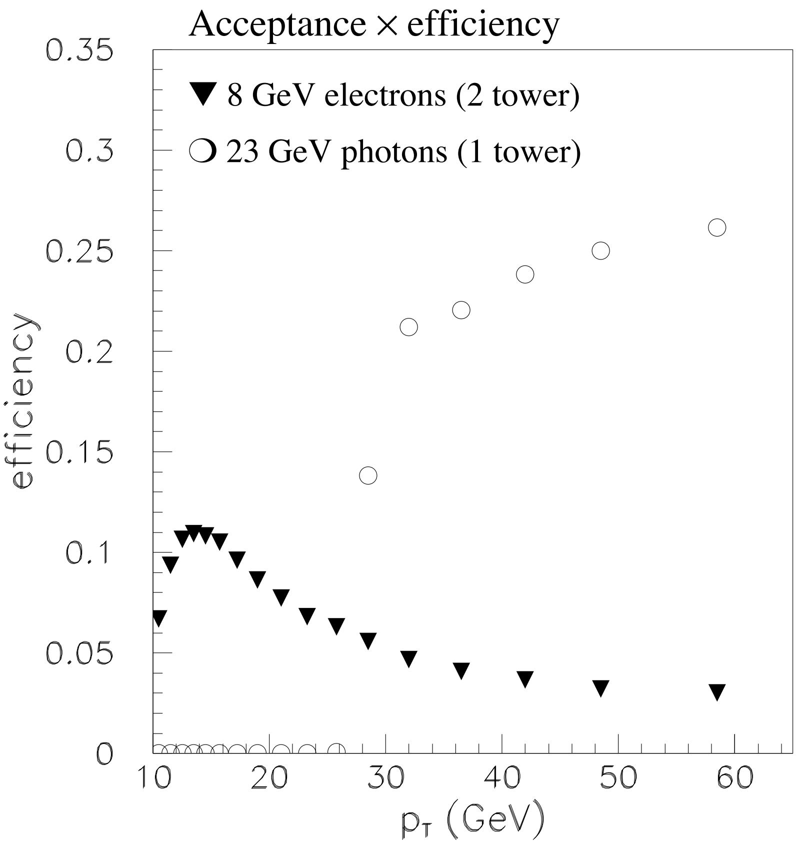

Figure 7.15: The total acceptance times efficiency for signal as a function of photon p_T, for both 1 tower and 2 tower events. The probability of conversion is not included.

p_T	$\mathcal{A}$	z_0	cnv	L2	CTC	Iso	N_{trk}	total
30-34	0.350	0.937	0.974	0.914	0.941	0.859	0.896	0.212
34-39	0.368	0.937	0.974	0.914	0.937	0.859	0.896	0.220
39-45	0.400	0.937	0.974	0.914	0.934	0.859	0.896	0.238
45-52	0.418	0.937	0.974	0.914	0.930	0.859	0.896	0.250
52-65	0.433	0.937	0.974	0.914	0.924	0.859	0.896	0.261

Table 7.3: Acceptance and efficiency of 23 GeV photon data sample. The probability of conversion is not included.

Chapter 8

Conversion probability

In this chapter we evaluate the total conversion probability for direct photons in the CDF inner detector. The conversion probability is a type of detector efficiency, therefore the final cross section measurement is inversely proportional to it. Since the probability is small ($\sim 5\%$), its value has an enormous impact on the measurement.

The conversion probability is related to the total amount of material in the CDF inner detector according to

$$cnvprb = 1 - e^{-7X/9} \tag{8.1}$$

where X is the total material measured in radiation lengths. The total material (often referred to as the *material scale*) is usually quoted as the average number of radiation lengths seen by the particles produced in a physics process. Since the η distributions and the z_0 distributions can vary from one data sample to another, the average material seen can vary somewhat from measurement to measurement. Nevertheless, they should all be very similar.

This chapter begins with a description of the standard method for measuring the material scale at CDF, which is based on inner detector conversions normalized to the material in the CTC inner cylinder. Next we present independent evaluation of the conversion probability based on π^0 Dalitz decays. Then we summarize all other evidence concerning conversion probability, and conclude by choosing a value for the conversion probability which is consistent with all these data.

8.1 Standard CDF conversion probability

The standard method for measuring the material scale of the CDF inner detector is to count the number of conversions found in the 8 GeV electron data sample. The measurement is calibrated using an *a priori* accounting of the material in the CTC inner cylinder based on our knowledge of its construction [34]. The inner cylinder is composed mostly of carbon fiber reinforced plastic (CFRP), with smaller amounts of epoxy, rohacell, copper clad kapton, and aluminum. The final result is $X_{CTCIC} = 1.22 \pm 0.06\% X_0$, where the error is dominated by the uncertainty on the thickness of the CFRP tube. The global inner detector material scale is determined by comparing the total number of conversions found in the data to the number found in the CTC inner cylinder.

The material scale study uses an inclusive conversion data sample which includes as a small subset the 2 tower events used in this thesis to measure the photon cross section. Since the two data sets are not identical, we must account for possible differences between them. The most important is the fact that the two datasets may have different η distributions. Since a photon traveling through the material at non-zero η sees the material enhanced by a factor of $1/\sin\theta$ due to the angle of incidence, the effective conversion probability depends on the average η of the conversion sample.

We account for this with a two step procedure. First, when measuring the material scale with inclusive conversions we remove the effect by weighting each conversion by its observed η. Therefore our global material scale, which is $X_T = 6.024 \pm 0.043 \pm 0.325\% X_0$ [35], represents the effective amount of material seen by a particle traveling through the detector transverse to the beamline. To get the appropriate material scale for the cross section measurement, we multiply this number by the average $1/\sin\theta$ of direct photons. According to the PYTHIA Monte Carlo, photons with $|\eta| < 0.9$ have an average $1/\sin\theta$ of 1.132, giving us $X_\gamma = 6.82 \pm 0.37\% X_0$. The conversion probability is $1 - e^{-7X_\gamma/9} = 5.17 \pm 0.28\%$.

8.2 Material measurement with Dalitz decays

A π^0 which Dalitz decays ($\pi^0 \to e^+e^-\gamma$), followed by a conversion of the on-shell photon in the detector material, reproduces the four-track topology of a double conversion $\pi^0 \to \gamma\gamma$ decay. If the reconstruction efficiencies of these two decays are the same, then the ratio of $\gamma\gamma$ events to Dalitz events should be the ratio of the conversion probability and $\gamma\gamma$ branching ratio to the Dalitz branching fraction:

$$\frac{\pi^0 \to \gamma\gamma \to e^+e^-e^+e^-}{\pi^0 \to e^+e^-\gamma \to e^+e^-e^+e^-} = \frac{BR(\gamma\gamma)}{BR(Dalitz)} \times \frac{cnvprb^2}{cnvprb} \tag{8.2}$$

$$= \frac{98.8\%}{1.2\%} \times cnvprb \tag{8.3}$$

Since the branching fractions are well known (1.20 % and 98.8%), by measuring the $\gamma\gamma$ to Dalitz ratio in the data we can infer the conversion probability.

We check this method with π^0 Monte Carlo. The π^0's are generated as described in section 5.7, and the Monte Carlo decays them to $\gamma\gamma$ and $e^+e^-\gamma$ with the correct branching fractions. The material scale of the Monte Carlo has been set to give a conversion probability of 5.17%, which is the standard CDF material scale, as described in section 8.1. We find that before applying any event selection, the $\gamma\gamma$ to Dalitz ratio of the Monte Carlo is 4.36, which is within 1% of the expected value. However, after applying the Level 2 trigger parameterization, the $\gamma\gamma$ to Dalitz ratio goes up to 4.76, an increase of 9%. The origin of this bias appears to be in the E_T cut of the trigger. $\gamma\gamma$ events have a slightly harder E_T spectrum than Dalitz events. Since the two decays are generated with the same spectrum, this can only be a reconstruction effect. $\gamma\gamma$ events have a larger average radius of conversion, and therefore are more likely to have multiple tracks within the CEM cluster.

To account for this effect we assume that $\gamma\gamma$ events are weighted by 1.09, and take this correction as a systematic error.

We use the 8 GeV electron data. To isolate the double conversion π^0 sample we rely mostly on the dE/dx observed in the CTC to suppress fakes, and then we do a crude sideband subtraction to eliminate remaining backgrounds. The separation power of the dE/dx information is illustrated in Figure 8.1. The cuts are:

- high p_T photon > 8.0 GeV (trigger conversion)
- all four track $p_T > 500 MeV$
- $Q_{CTC} > 30$ for the three non-trigger tracks
- $|sep| < 0.3$ cm, $|\Delta \cot\theta| < 0.05$, both conversions
- $r_{cnv} > -4.0$ cm, unfit r_{cnv}, both conversions

The variable Q_{CTC} is a measure of the total ionization energy deposited in the CTC by the track.

An event is considered a Dalitz candidate if it has one or more conversions with a negative radius of conversion. We use the vertex fitted radius of conversion when making this distinction. However, if a conversion has an unfit radius of conversion less than -2.0 cm, then there is no vertex fit available. If the unfit radius is between -4.0 cm and -2.0 cm, then we consider the event a Dalitz candidate. Many of these events are probably fakes, and we rely on the sideband subtraction to remove them.

The diphoton mass spectrum of the two decays are shown in Figure 8.2. The mass is calculated using the raw track parameters. The signal to background ratio appears to be good in both samples. To remove remaining backgrounds we consider 0-300 MeV as the signal window, and 300-400 MeV as the sideband. We assume that the background is flat, so that the background estimate in the signal window is three times the number of sideband events.

Since Dalitz events are expected to be symmetric around r=0, the total Dalitz estimate is twice the number of negative radius events. The total $\gamma\gamma$ estimate is the number of positive radius events minus the number of Dalitz candidates expected to be found at positive radius. The event counting is summarized in Table 8.1.

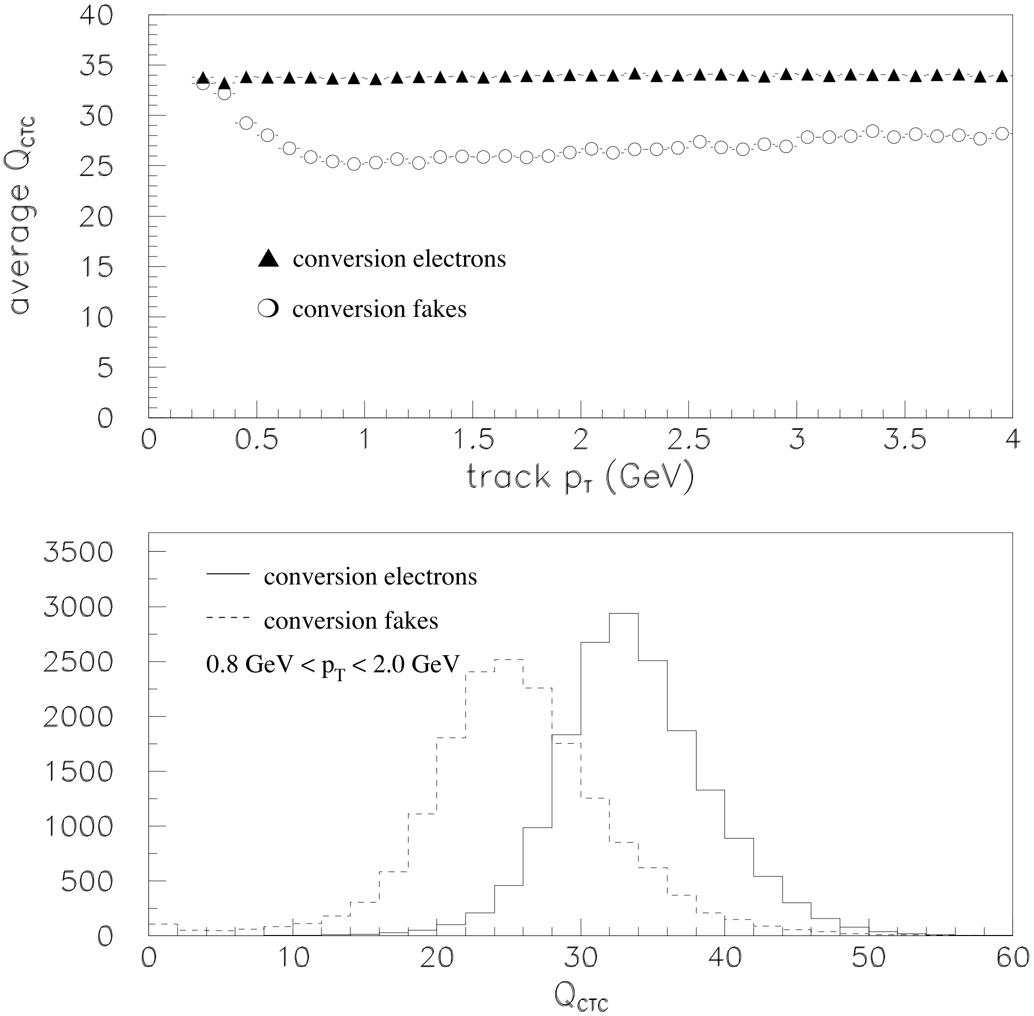

Figure 8.1: Illustration of the electron-pion separation power of dE/dx at low p_T.

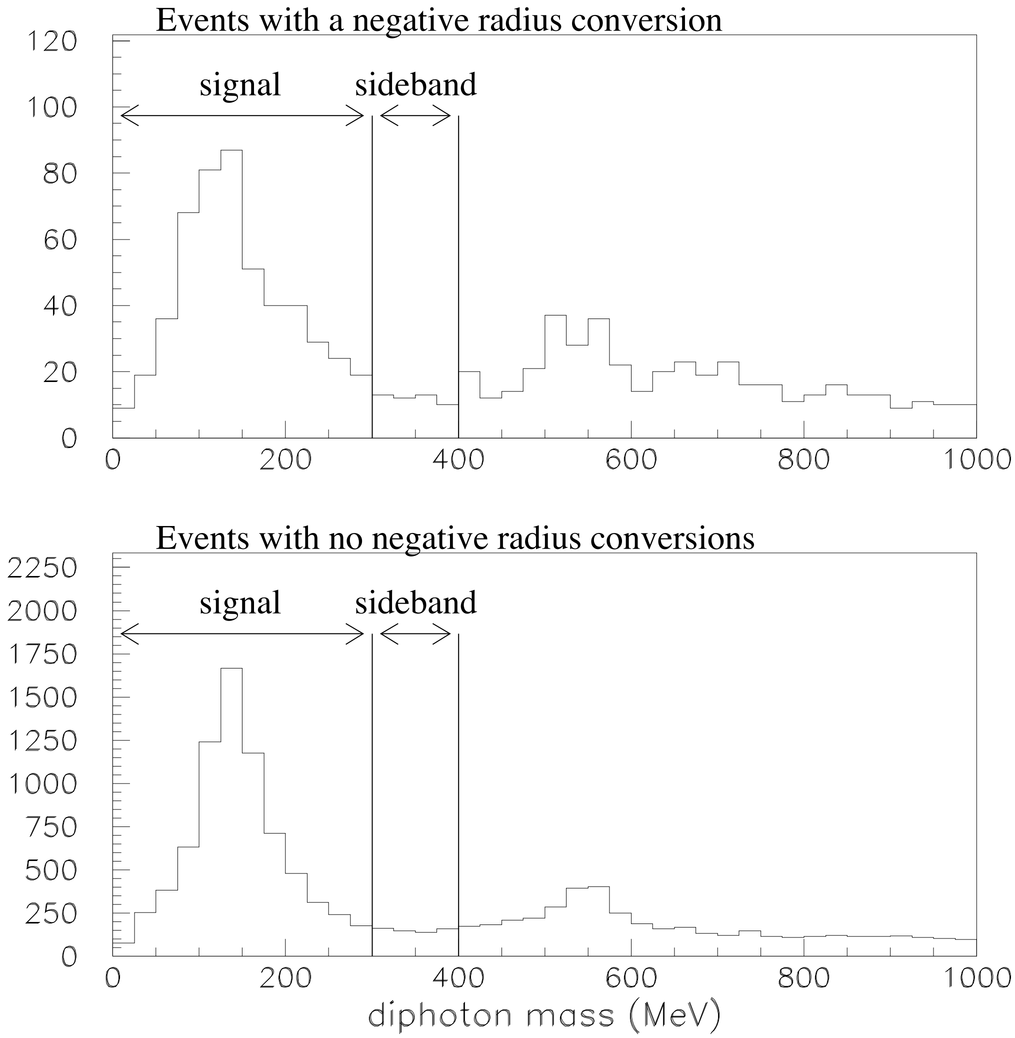

Figure 8.2: Diphoton mass spectrum of positive and negative radius events.

	π^0 window	sideband	back. sub. signal	total
neg. rad. sample	503	48	359 ± 31	718 ± 62 (Dalitz estimate)
pos. rad. sample	7352	608	5528 ± 114	5169 ± 136 ($\gamma\gamma$ estimate)

Table 8.1: Dalitz and $\gamma\gamma$ event counts.

As a check on the background subtraction, we lower the r_{cnv} cut from -4.0 cm to -9.0 cm. This should increase the fakes without adding many new Dalitz events. We find that the number of events in the negative radius π^0 window goes from 503 to 659, while the sideband increases from 48 to 98. The background subtracted Dalitz signal is 365, in agreement with the previous estimate of 359.

The $\gamma\gamma$ to Dalitz ratio measured in the data is 7.20 ± 0.65(stat) ± 0.65(sys). The conversion probability is

$$\begin{aligned} cnvprb &= 7.20 \times \frac{1.2\%}{98.8\%1.09} && (8.4) \\ &= 8.02 \pm 0.73(stat) \pm 0.73(sys)\% && (8.5) \end{aligned}$$

where we have included the weighting factor of 1.09.

However, this result is most likely an underestimate of the conversion probability, because the number of Dalitz events is probably over estimated. This is because some of the Dalitz candidates are positive radius conversions which are found at negative radius due to resolution. To get a rough idea of the size of this effect we fit the vertexed radius of conversion distribution near the origin to a sum of exponentials, as shown in Figure 8.3. The fit indicates that the Dalitz contribution to the negative radius conversions is about 82%. If we correct the event counting by this amount, we find that the conversion probability may be as high as 9.9 %.

In conclusion, the result of the Dalitz measurement of the conversion probability is significantly higher than the standard conversion probability as described in section 8.1.

8.3 Other evidence concerning the Run 1 material scale

In this section we summarize all other evidence concerning the material scale. These results are all related to the measurement of the W boson mass at CDF[40].

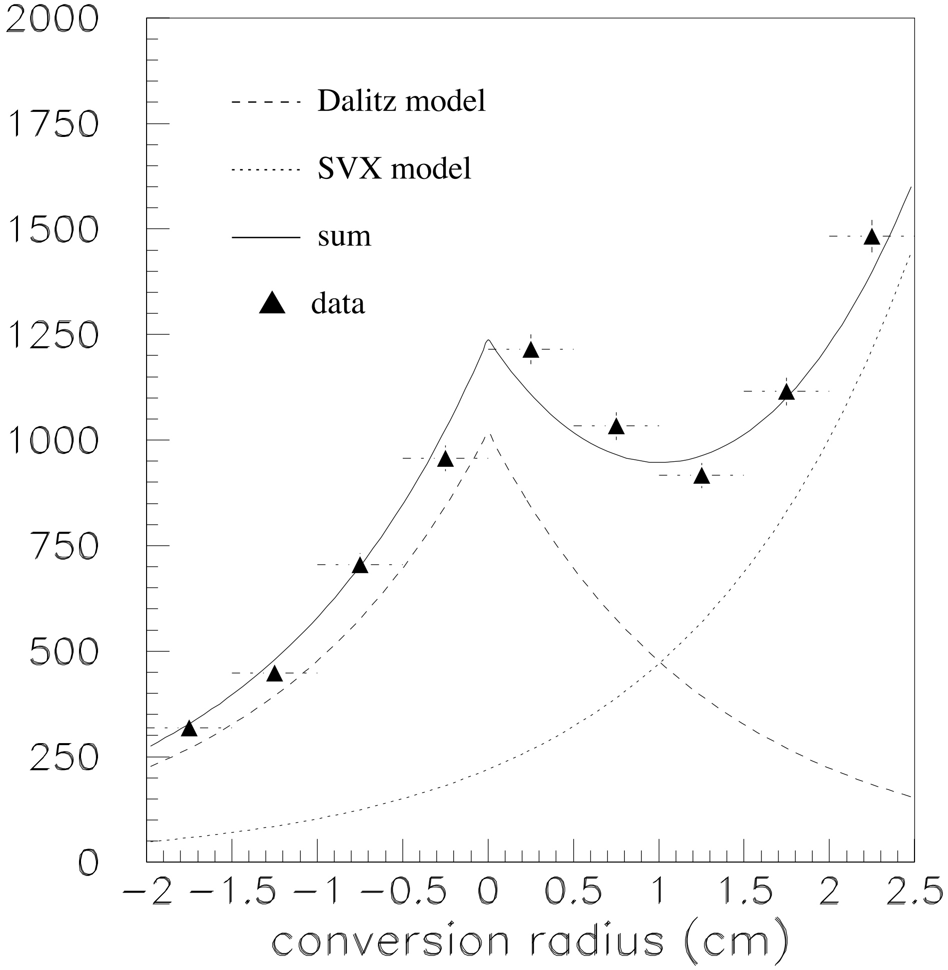

Figure 8.3: Estimate of the number of negative radius conversions due to SVX material. The solid line is the result of a fit to the data. The dotted and dashed are the Dalitz and SVX contributions separately. The curves are exponentials, all with the same decay constant.

8.3.1 E/p tail (from W mass analysis)

CDF has measured the mass of the W boson in the $e\nu$ decay channel, and this measurement requires a detailed simulation of the effect of bremsstrahlung on the electrons as they pass through the detector material. Consequently the material scale of the detector was studied in great detail. As a check on the standard material scale, the W mass group measured the rate of hard bremsstrahlung events in the $W \to e\nu$ data by looking at the high tail of the E/p distribution [37]. This method is sensitive to internal bremsstrahlung in the W data, and the Monte Carlo predicts that roughly 40 % of the events in the E/p tail are due to internal brem. To explain the remaining 60 % of the data, one finds that $X = 7.55 \pm 0.37\% X_0$, or a conversion probability of $5.70 \pm 0.28\%$. This result is in agreement with the standard CDF material scale.

8.3.2 Peak of the E/p distribution (from W mass analysis)

The W mass group found that the peak of the E/p distribution of the $W \to e\nu$ data is shifted slightly to the right of the prediction of the simulation when using the standard material scale. If one assumes that the material scale is incorrect, then the E/p peak in the Monte Carlo can be made to agree with the data by adding about 4.5 % of a radiation length to the default number of 7.34 %, for a total of 11.84 % X_0 [37]. This would correspond to a conversion probability of 8.80 %, which is much higher than the standard material scale, but similar to the material scale measured with Dalitz decays (described in section 8.2).

8.3.3 $J/\psi \to ee$ tail

The W mass group concluded that the discrepancy between data and Monte Carlo in the E/p peak region (described above) was unlikely to be due to an incorrect material scale. This conclusion is due in part to a study of the bremsstrahlung tail of the $J/\psi \to ee$ mass peak, which indicates that the material scale cannot be much larger than the standard material scale [37].

8.3.4 J/ψ mass

The momentum scale of the CTC is determined by comparing the mass of dimuon resonances such as the J/ψ and Υ as reconstructed by CDF to the world average masses [39]. The reconstructed mass has a small dependence on the inner detector material scale due to the energy loss experienced by the muons as they pass through the detector.

If the momentum scale of the CTC is set by using the standard CDF magnetic field database, and the standard material scale is used to correct for muon energy loss, then the masses of all five resonances ($J/\psi(1s), \psi(2s), \Upsilon(1s), \Upsilon(2s)$, and $\Upsilon(3s)$)

study	method	X (% X_0)	cnvprb (%)
standard	CTC inner cylinder	6.82 ± 0.37	5.17 ± 0.28
E/p tail	hard brem	$7.55 \pm 0.37 X_0$	5.70 ± 0.28
$j/\psi \to ee$	hard brem	agrees with above	agrees with above
E/p peak	soft brem	11.34	8.80
Dalitz	$\pi^0 \to \gamma\gamma$ / $\pi^0 \to \gamma ee$	$> 10.62 \pm 1.35$	$> 8.02 \pm 0.73(stat) \pm 0.73(sys)$
J/ψ mass	dE/dx	9.15	6.89
$\Upsilon(1s)$ mass	dE/dx	10.2	7.63

Table 8.2: Summary of Run 1 material scales. The three CTC inner cylinder results are highly correlated.

as reconstructed by CDF is low by a few MeV. In addition, the J/ψ mass has a strong dependence on the amount of material that the muons travel through, with the large X_0 muons giving the lowest mass.

In practice these small discrepancies are used to correct the CTC momentum scale. If we assume instead that the magnetic field database is correct, and that discrepancies are due to unexpected dE/dx in the inner detector, then we can calculate the material scale necessary to give the correct masses. The J/ψ mass is low by 1.05 MeV, and it changes by +0.34 MeV when the material is increased by a factor of 1.075. Therefore the implied material scale is a factor of 1.23 larger than the scale used, which is 7.43 % X_0, giving a material scale of 9.15 % X_0, and a conversion probability of 6.89 %. A similar exercise for the $\Upsilon(1s)$, which is low by 4.0 MeV, and changes by 0.8 MeV with a material scale factor of 1.075, gives an implied material scale of 10.2 % X_0, and a conversion probability of 7.63 %. These material scales are significantly higher than the standard CDF material scale.

8.4 Choice of the material scale for the photon cross section measurement

All material scale measurements described in this chapter are summarized in Table 8.2.

Unfortunately the various measurements give a wide variety of results, with some preferring a low conversion probability ($\sim 5\%$), and some a high ($\sim 8\%$). The three low results (conversions + CTC can, E/p tail, and $J/\psi \to ee$), which are the standard CDF run 1 material scales, are all direct methods. Among the high results, the Dalitz measurement is a direct method, while the E/p, J/ψ and Υ masses use a small effect to infer the material scale. Therefore the evidence for the high conversion probability is weaker than the evidence for the lower conversion probability. However the validity of the higher results cannot be ruled out, so to be conservative we have chosen a material scale with a central value and error which encompasses all of these results.

We choose the conversion probability such that both the smallest probability (5.17 %) and the result of the Dalitz measurement (8.02 %) are within one sigma. This value is

$$cnvprb = 6.60 \pm 1.43\% \tag{8.6}$$

which has a fractional error of 22%. This error translates directly to an error on the final cross section measurement, and dominates all other errors. Consequently, the conflicting data concerning the conversion probability is the limiting factor on the precision of the photon cross section measured with conversions.

8.5 Effective conversion probability

We make one correction to the conversion probability to account for the $r_{cnv} > 2.0$ cm cut. This cut eliminates π^0 Dalitz decays and γ^* events from the data sample, but it also removes a small number of external conversions. To measure the loss of efficiency, we release the r_{cnv} cut and reflect the negative radius conversion events about $r_{cnv} = 0.0$. This is shown in Figure 8.4. We subtract these events from the positive radius of conversion events, and we count the number of conversions which remain below $r_{cnv} < 2.0$ cm. We find that the r_{cnv} cut removes 2.96 % of the positive radius of conversion events, and we decrease the conversion probability by this amount. Our final result for the *effective* conversion probability is

$$cnvprb_{eff} = 6.40 \pm 1.43\% \tag{8.7}$$

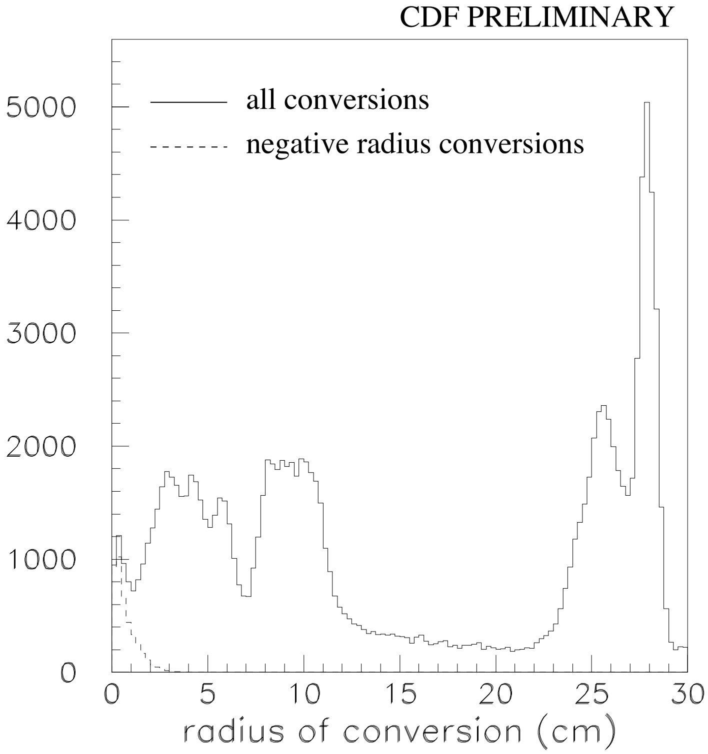

Figure 8.4: Efficiency of the $r_{cnv} > 2.0$ cm cut. Conversion candidates with negative radius of conversion are reflected about r = 0 and subtracted from the positive radius conversions. The remaining conversion candidates with $r_{cnv} < 2.0$ cm represent 3 % of all positive radius conversions.

Chapter 9

Systematic Errors

In this chapter we evaluate the systematic errors on the photon cross section measurement.

9.1 CEM scale and resolution

To measure the photon cross section as a function of p_T we bin the data according to the E_T of the photon measured with the calorimeter. Since the E_T measurement has an error, we expect that some events will be assigned to the wrong p_T bin. This may have important consequences on the observed cross section.

We classify all possible binning mistakes into the energy scale and the energy resolution. An error in the CEM energy scale would have the effect of systematically moving events from their proper p_T bin to a neighboring bin. This would increase or decrease the observed cross section, depending on the sign of the error. The CEM resolution also causes events near the bin boundaries to be improperly categorized. Since the cross section is a steeply falling function of p_T, small cross section bins tend to become polluted by their larger neighbors, and this has the effect of increasing the observed cross section in all bins.

The CEM energy scale has been set in the data by requiring that the observed $Z \rightarrow e^+e^-$ peak reproduce the Z mass value measured at LEP. This determines the CEM energy scale to 0.1%. However, as seen in section 6.4, the conversion E/p distributions prefer an E/p scale of as much as 1% for the 8 GeV electron data and 2% for the 23 GeV photon data. These scales may be due to errors in E_T or p_T, and in the case of the 23 GeV photon data there is evidence that the p_T measurement is at fault. To be conservative we assume that the CEM energy scale may be wrong by 1%.

To determine the effect of binning errors on the cross section we use a toy Monte Carlo. We generate a hypothetical photon p_T spectrum according to a power law with an exponent of -4.2775. This spectrum closely resembles the results of the NLO QCD calculation produced by the authors of reference [27]. We then scale the photon p_T by ±1% and compare the 'observed' spectrum to the true spectrum. We find that the cross section changes by ±3% in all p_T bins. Similarly, to determine the systematic due to the energy resolution we smear the photon p_T by the CEM resolution given in equation 3.4. We find that the cross section changes by a fraction of a percent, and we neglect this error.

9.2 Prompt electron background

After the E/p background subtraction there is one background which potentially remains. If a prompt electron (such as a W electron) is produced with a co-linear soft photon due to internal or external bremsstrahlung, then that photon may convert in the material of the inner detector. If one of the conversion tracks is lost, perhaps because it is too soft to be reconstructed by the CTC, then the remaining track may be vertexed with the prompt electron and form a high p_T conversion candidate. This scenario is shown schematically in Figure 9.1. This type of event may have an E/p of one, so it can appear as a spurious signal.

If we release the $\not\!\!E_T$ cut from the 8 GeV electron data we find clear evidence for W electrons in the final conversion sample. In Figure 9.2 we plot the $\not\!\!E_T$ versus electron E_T of all conversion candidates in the 8 GeV electron data without the $\not\!\!E_T$ cut. The cluster of events along $\not\!\!E_T \approx E_T$ is characteristic of W events.

In Figure 9.3 we show E_T versus $\not\!\!E_T$ for the 23 GeV photon data. In this dataset there is also some evidence for $W \rightarrow e\nu$ decays, but it appears to be a much smaller portion of the sample. We expect prompt electrons to contaminate primarily the 2 tower (8 GeV electron) data for the following reason. The bremsstrahlung photon p_T spectrum is steeply falling, so most brem photons which convert will produce low p_T tracks. The curvature of these tracks is large enough that we expect them to satisfy the 2 tower geometry.

Since W events have a high p_T neutrino in the final state, in the 8 GeV electron data most will be eliminated by the $\not\!\!E_T$ cut. However, any prompt electron, such as from a heavy flavor decay or Drell-Yan event, can fake a high p_T conversion in the same manner. To evaluate the importance of all prompt electrons in the final sample we rely on the SVX and VTX hit occupancies. If the radius of conversion of a photon candidate is in the CTC inner cylinder region, then these detectors should have hit occupancies consistent with noise and random charged particle overlap.

The VTX and SVX occupancies are measured by projecting the electron candidate track back into the detectors and looking for hits. The VTX occupancy is the ratio of found hits to expected hits, and for most VTX tracks the number of expected hits is 16. The SVX has four layers of silicon sensors, and we count the number of layers in which we find a silicon cluster.

The occupancies of the VTX and SVX for pure inner cylinder conversions and

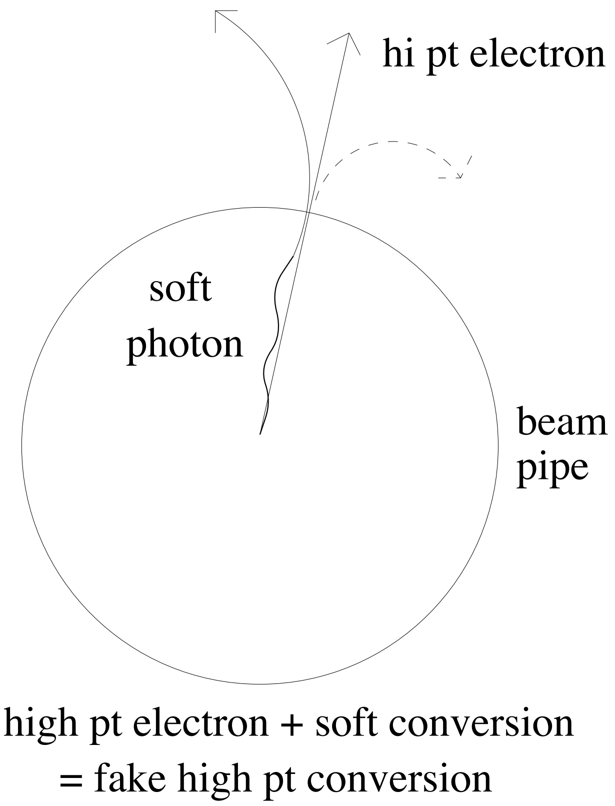

Figure 9.1: Schematic diagram of a prompt electron with a co-linear soft photon faking a high p_T conversion.

prompt electrons are shown in Figure 9.4. The VTX occupancy for pure inner cylinder conversions is measured by requiring that both tracks be SVX fiducial, but have less than three SVX hits. The reverse procedure gives the SVX occupancy. The occupancies for prompt electrons is taken from W events in the inclusive electron sample.

To measure the fraction of events due to prompt electrons we divide the inner cylinder candidates into two exclusive samples. The first sample contains conversions which are SVX fiducial but have less than three SVX hits. We assume this sample has no prompt electron component. All remaining events are in the second sample. In Figure 9.5 we plot the fraction of events which pass a VTX occupancy < 0.75 cut for sample 1 and sample 2 as a function of the $\not\!\!E_T$ for the 8 GeV electron data. Pure conversions pass at a rate of 92.8% independent of the event $\not\!\!E_T$. The second sample also pass with the same probability at low $\not\!\!E_T$, but fail in large numbers at high $\not\!\!E_T$, which is expected if these events are due to W electrons. This plot indicates that the

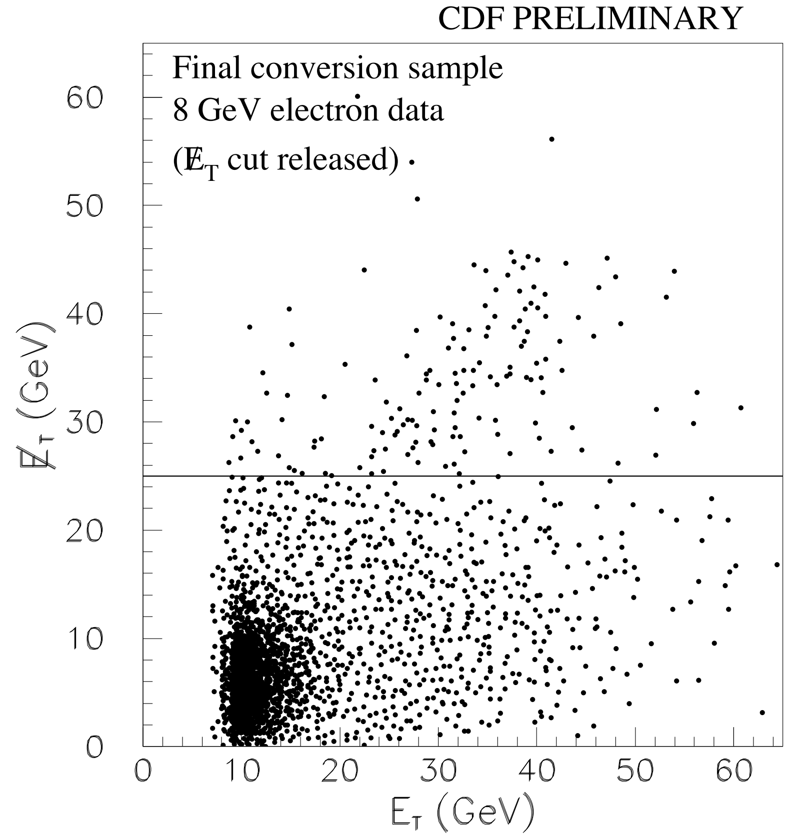

Figure 9.2: Electron E_T vs $\not\!\!E_T$ for the 8 GeV electron data, with the $\not\!\!E_T$ cut released. The cluster of events along the diagonal is characteristic of $W \to e\nu$ decays. The horizontal line marks the location of the $\not\!\!E_T$ cut.

prompt electron component of the 8 GeV electron data is small below $\not\!\!E_T < 25$ GeV, where we have placed our cut.

Figure 9.6 shows the VTX occupancy as a function of the photon candidate p_T for the 8 GeV electron data. The fraction of events which pass the VTX occupancy $<$ 0.75 cut is shown before and after the $\not\!\!E_T < 25$ GeV cut. The expected passing rate for pure conversions and prompt electrons are indicated by the solid and dashed lines on the plot. Below $p_T = 25$ GeV the data is consistent with being pure conversions, while the data above displays significant prompt contamination before the $\not\!\!E_T$ cut. With the $\not\!\!E_T$ cut applied the data appears more conversion-like. There are two p_T bins which show evidence for prompt contamination after the $\not\!\!E_T$ cut (the 27-30 GeV bin and the 45-52 GeV bin), while in the highest p_T bin the statistics is too poor to

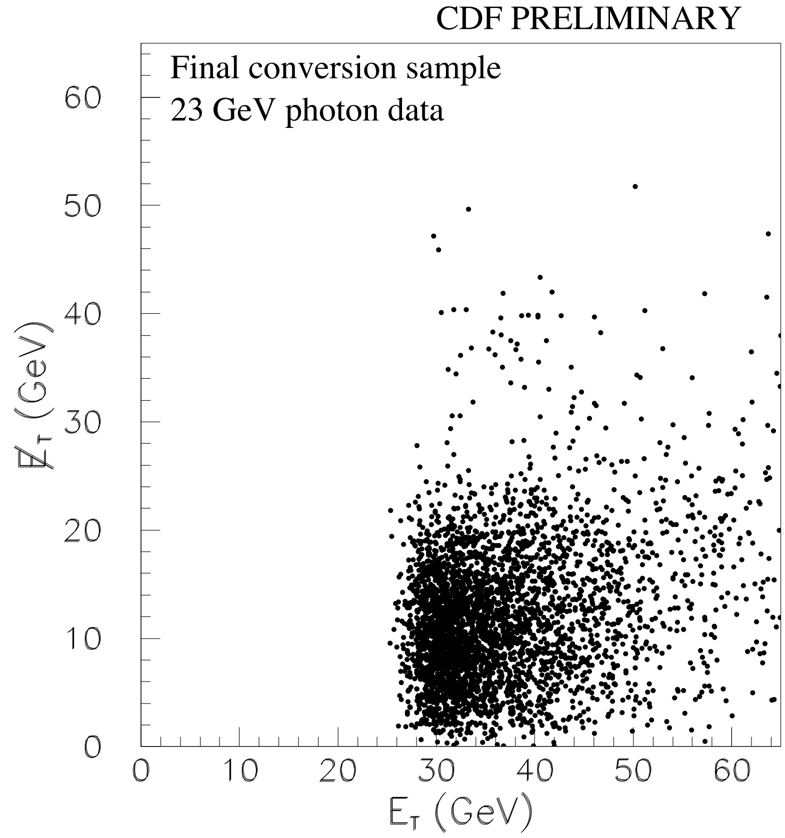

Figure 9.3: Electron E_T vs $\not\!\!E_T$ for the 23 GeV photon data.

discern much information. In addition, the data from 30-45 GeV have a lower VTX occupancy than is expected even for true conversions. We have no explanation for this other than a statistical fluctuation.

We use Figure 9.6 to determine a systematic error due to residual prompt electron contamination. Below $p_T = 25$ GeV we take no error, and above 25 GeV we take a one-sided 10% systematic. This error is large enough to accommodate the VTX occupancy of all the p_T bins except for the second to last which has a large statistical error bar.

Figure 9.7 shows the fraction of events failing the VTX occupancy < 0.75 cut versus photon candidate p_T for the 23 GeV photon data. We make no $\not\!\!E_T$ cut on this data, so we plot the VTX occupancy for all inner cylinder conversion candidates. The data is consistent with being dominated by pure conversions. We take a one-sided 3% systematic error for this data sample.

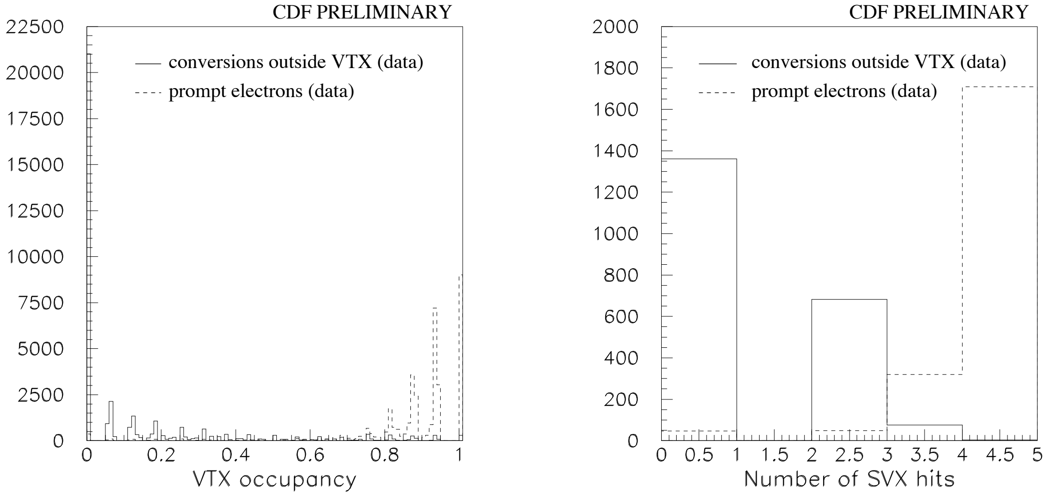

Figure 9.4: VTX and SVX occupancies for conversions and prompt electrons.

9.3 η/π^0 ratio

To determine the systematic error associated with the η/π^0 ratio, we vary the ratio in the Monte Carlo by $\pm 1\sigma$ from its nominal value of 0.678 ± 0.076 and perform the background subtraction again. The ratio of the number of signal candidates found is shown in Figure 9.8(a). The error is very small (one percent at 10 GeV). This is because the E/p distribution of a meson is determined by two-body decay kinematics, so the η and π^0 have a similar E/p. At low p_T, η's are more likely to have the second photon outside the CEM cluster (due to the larger opening angle in an η decay), and these events look like signal events and affect the background subtraction.

As a further check on the η/π^0 systematics, we try using a production ratio of one, which is the value used in previous CDF photon cross section analyses. This η/π^0 ratio was measured using events where the two photons land in separate CEM towers. The ratio of the number of signal candidates is shown in Figure 9.8(b). Using this production ratio changes the cross section by 5% at low p_T.

9.4 Trigger efficiency vs. time

There is some evidence that the efficiency of the 8 GeV electron trigger decreased for conversion events over the course of Run 1b [41], and we have adopted a systematic error to account for this possibility. To determine the systematic we have consulted the luminosity database to find the halfway point of Run 1b for the 8 GeV electron trigger, which is run 65350. We then count the number of events in our final 8 GeV

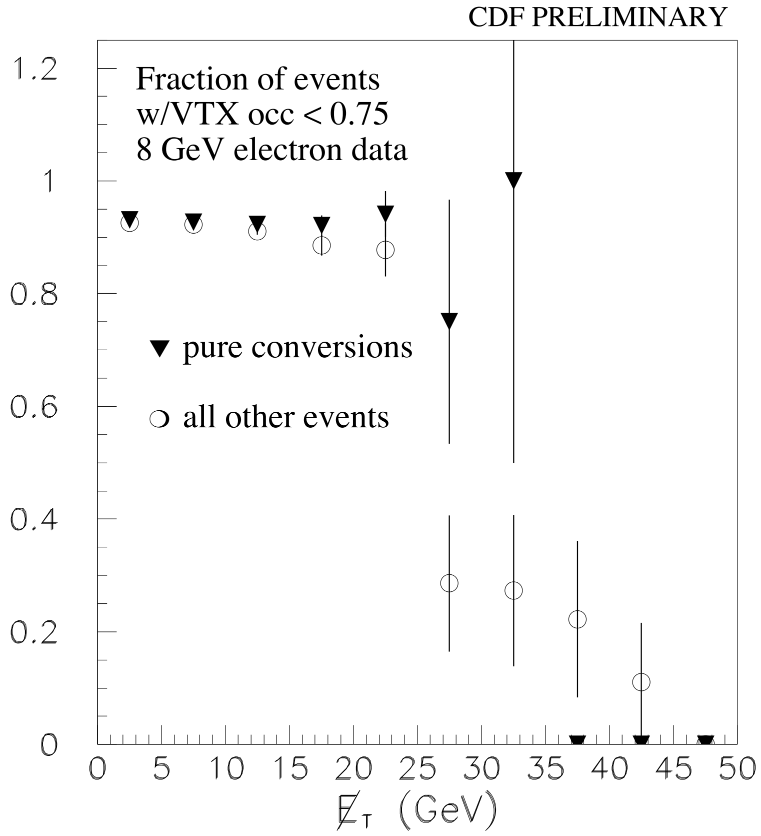

Figure 9.5: The fraction of inner cylinder conversion candidates which pass a VTX occupancy < 0.75 cut as a function of $\not\!\!E_T$, for the 8 GeV electron data. The pure conversion sample is selected by requiring that the candidate by SVX fiducial but have less than three SVX hits.

electron conversion sample which occurred before this run. We find that 47546 out of 88662 events are before run 65350, or 53.6 %. We take 53.6 % - 50.0 % = 3.6 % as a systematic error.

9.5 Other systematics

We take a systematic error from the following sources.

- Probability of conversion: The conversion probability adopted in chapter 8 is 6.60 ± 1.43 %, which has a fractional error of 22%. Since this error is large, and

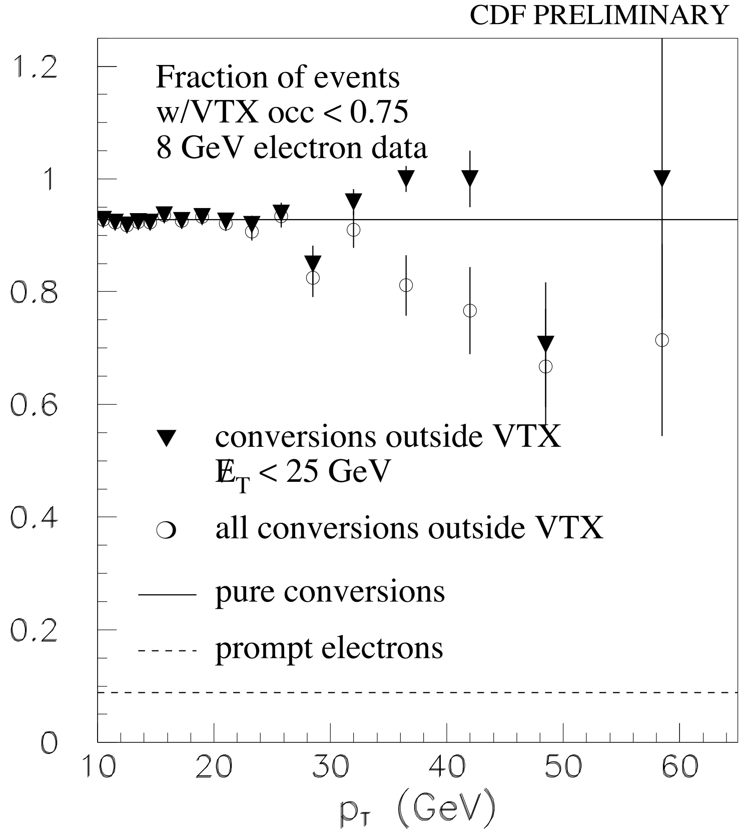

Figure 9.6: The fraction of inner cylinder conversion events which pass a VTX occupancy < 0.75 cut as a function of the photon candidate p_T, for the 8 GeV electron data. The expected passing rates for true conversions and prompt electrons are shown as the solid and dashed lines.

appears in the denominator of the cross section, the error on the cross section is asymmetric, and translates to $+27/-17\%$. This is the dominant error on the final result of the measurement.

- E/p model: The systematic error on the E/p background subtraction due to limitations of the E/p model is discussed in section 6.4. .
- Integrated luminosity: The integrated luminosity of our two data samples was measured previous to this work [36], [16]. The CDF procedure for estimating the integrated luminosity (using the beam-beam counters) is accurate to 4.1%.
- 8 GeV electron trigger efficiency: The Level 2 trigger simulation has eight free

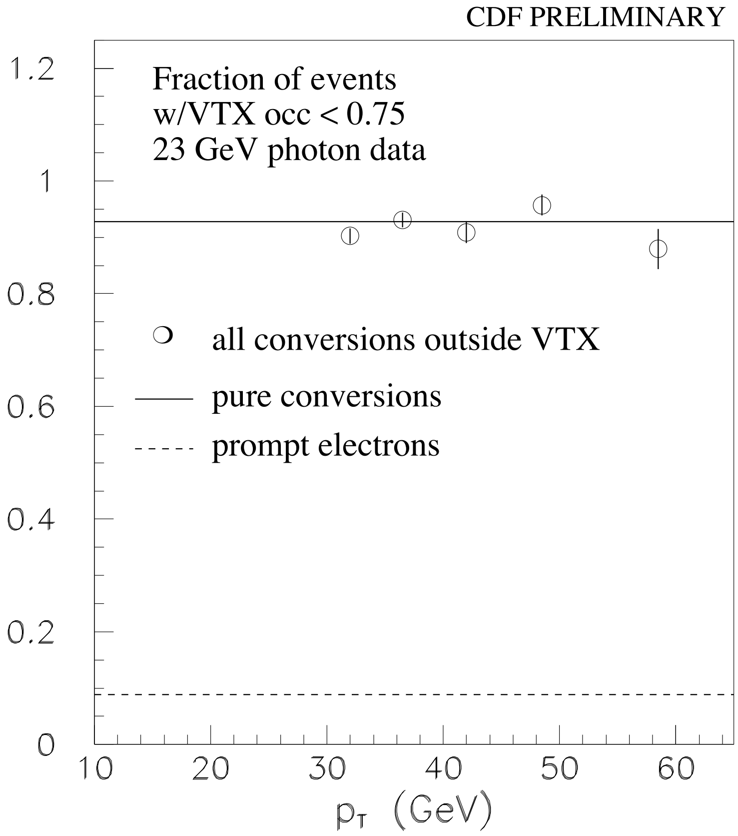

Figure 9.7: The fraction of inner cylinder conversion events which pass a VTX occupancy < 0.75 cut as a function of the photon candidate p_T, for the 23 GeV photon data. The expected passing rates for true conversions and prompt electrons are shown as the solid and dashed lines.

parameters: six which describe the E_T, p_T, and XCES thresholds, one for the trigger tower boundary correction, and one for the asymptotic efficiency. We vary each parameter one at a time by its reported error in the simulation and recalculate the efficiency. We find that the efficiency changes by less than a percent in all cases except for the trigger tower boundary correction and the asymptotic efficiency, which cause systematic errors of a percent. We take 1.4% systematic due to the 8 GeV electron Level 2 trigger parameterization.

- 23 GeV photon trigger efficiency: The Level 2 23 GeV photon trigger efficiency is known to 4.7%.

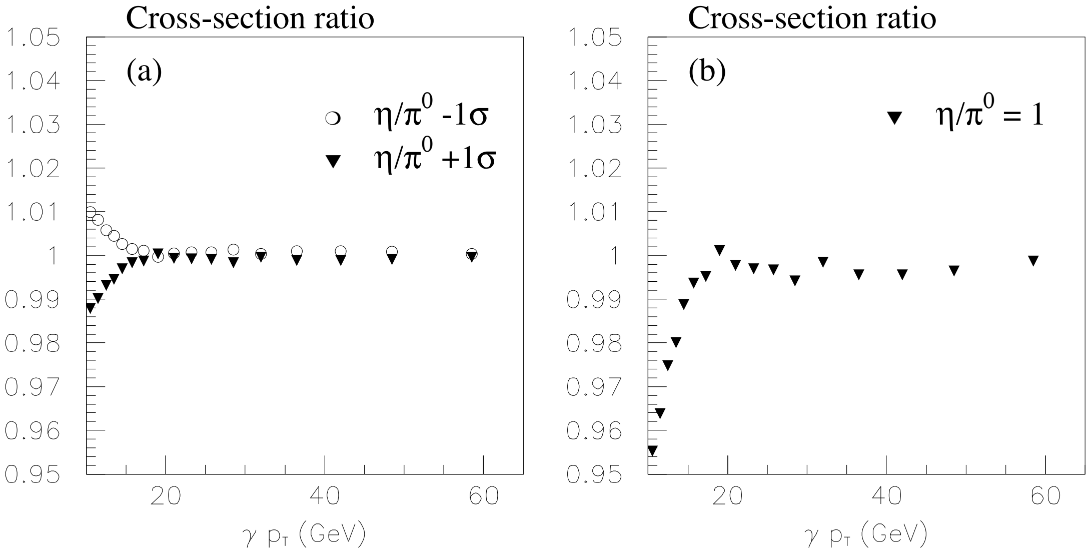

Figure 9.8: η/π^0 ratio systematic error.

- Tracking efficiency: The asymptotic tracking efficiency is known to 2%.
- Conversion identification efficiency: The conversion ID efficiency is known to 2%.
- Electron identification efficiency: The electron ID cuts are applied to the 8 GeV electron data by the Level 3 trigger. The efficiency is known to 3.5%.
- z_0 efficiency: The efficiency of the $|z_0| < 60$ cm cut is known to 1.2 %.

9.6 Total systematic error

The systematic errors are summarized in Tables 9.1. The total systematic error is determined by adding in quadrature the systematic errors in each p_T bin. These values are plotted in Figure 9.9 and listed in Table 9.2. Also shown in Figure 9.9 and Table 9.2 is the systematic error with the error due to the conversion probability and the integrated luminosity removed from the sum. These two errors affect only the overall normalization of the cross section, and therefore the remaining errors represent the systematic on the shape of the cross section as a function of p_T.

dataset	source	fractional error (%)
8 GeV electron	conversion probability	+27/-17
(2 tower)	E/p model	$\sim$ 11 at 10 GeV
	CEM scale	3.0
	prompt electron	10.0 above 25 GeV (one-sided)
	η/π^0 ratio	1.0 at 10 GeV
	luminosity	4.1
	Level 2 efficiency	1.4
	tracking efficiency	2.0
	conversion ID efficiency	2.0
	electron ID efficiency	3.5
	time dependence	3.6
	z_0 efficiency	1.2
23 GeV photon	conversion probability	+27/-17
(1 tower)	E/p model	$\sim 3.0 - 5.0$
	CEM scale	3.0
	prompt electron	3.0 (one-sided)
	luminosity	4.1
	Level 2 efficiency	4.7
	tracking efficiency	2.0
	conversion ID efficiency	2.0
	z_0 efficiency	1.2

Table 9.1: Summary of systematic errors.

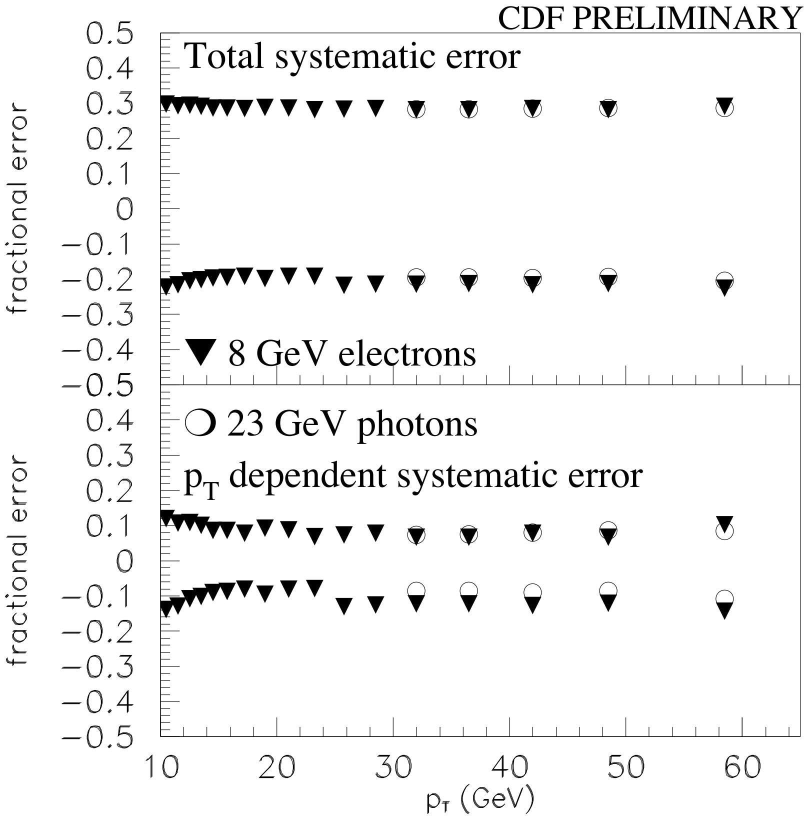

Figure 9.9: Systematic errors for the 8 GeV electron and 23 GeV photon datasets. The upper plot shows the total error, where all systematics errors are summed in quadrature. In the lower plot the normalization errors due to the uncertainty on the conversion probability and the integrated luminosity have been removed from the sum.

dataset	p_T	(+) total (%)	(-) total (%)	(+) p_T (%)	(-) p_T (%)
8 GeV electron	10-11	30	22	12.0	13.9
(2 tower)	11-12	29	22	10.7	12.8
	12-13	29	20	10.8	10.7
	13-14	29	20	10.1	10.2
	14-15	29	20	8.6	9.0
	15-16.5	29	20	8.6	8.7
	16.5-18	28	19	7.8	8.0
	18-20	29	20	9.3	9.5
	20-22	28	19	8.8	8.1
	22-24	28	19	6.8	7.9
	24.5-27	28	22	7.4	13.0
	27-30	28	21	7.8	12.5
	30-34	28	21	6.8	12.3
	34-39	28	21	6.8	12.2
	39-45	28	22	7.8	12.7
	45-52	28	21	6.8	12.1
	52-65	29	23	10.3	14.3
23 GeV photon	30-34	28	19	7.4	8.6
(1 tower)	34-39	28	19	7.6	8.6
	39-45	28	20	8.1	9.0
	45-52	29	19	8.6	8.5
	52-65	29	21	8.4	10.8

Table 9.2: Total systematic errors for the 8 GeV electron and 23 GeV photon datasets. The columns labeled 'total' have all systematic errors summed in quadrature. In the columns labeled 'p_T' the normalization errors due to the uncertainty on the conversion probability and the integrated luminosity have been removed from the sum.

Chapter 10

Cross section measurement

10.1 1 tower and 2 tower cross sections

The cross section is calculated according to

$$\frac{d\sigma^2}{dp_T d\eta} = \frac{N_{signal}}{A \cdot \epsilon \cdot \Delta p_T \cdot \Delta\eta \cdot \int \mathcal{L}} \tag{10.1}$$

For the final cross section measurement we adopt the results of the χ^2 fit background subtraction to determine the number of signal candidates (N_{signal}) in each p_T bin. The results of the χ^2 fit background subtraction for both data samples are listed in Table 6.2.

$A \cdot \epsilon$ is the acceptance times efficiency shown in Figure 7.15 and Tables 7.2 and 7.3 multiplied by the effective conversion probability of 6.40%. We measure the average cross section between -0.9 $< \eta <$ 0.9, so $\Delta\eta$ is 1.8. Δp_T is the bin width, and $\int \mathcal{L}$ is the integrated luminosity of $73.6pb^{-1}$ for the 8 GeV electron data and $83.72pb^{-1}$ for the 23 GeV photon data.

The cross section measured with the 8 GeV electron data and 23 GeV photon data is shown in units of pb/GeV as a function of p_T in Figure 10.1. The ratio of the two measurements is also shown above 30 GeV. In this plot only the statistical errors are shown.

As shown in Figure 7.15, the 1 tower and 2 tower data samples have very different acceptances above 30 GeV. For example, in the 34-39 GeV bin, the ratio acceptances (1 tower to 2 tower) is 5.4. However, the two cross section measurements are in perfect agreement (within statistical errors), as shown in Figure 10.1. This is a powerful cross check on the acceptance calculation of the Monte Carlo, and an internal consistency check of the measurement as a whole.

For our final cross section measurement we combine the two datasets by adopting the 23 GeV photon (1 tower) measurement above 30 GeV and the 8 GeV electron (2 tower) measurement below.

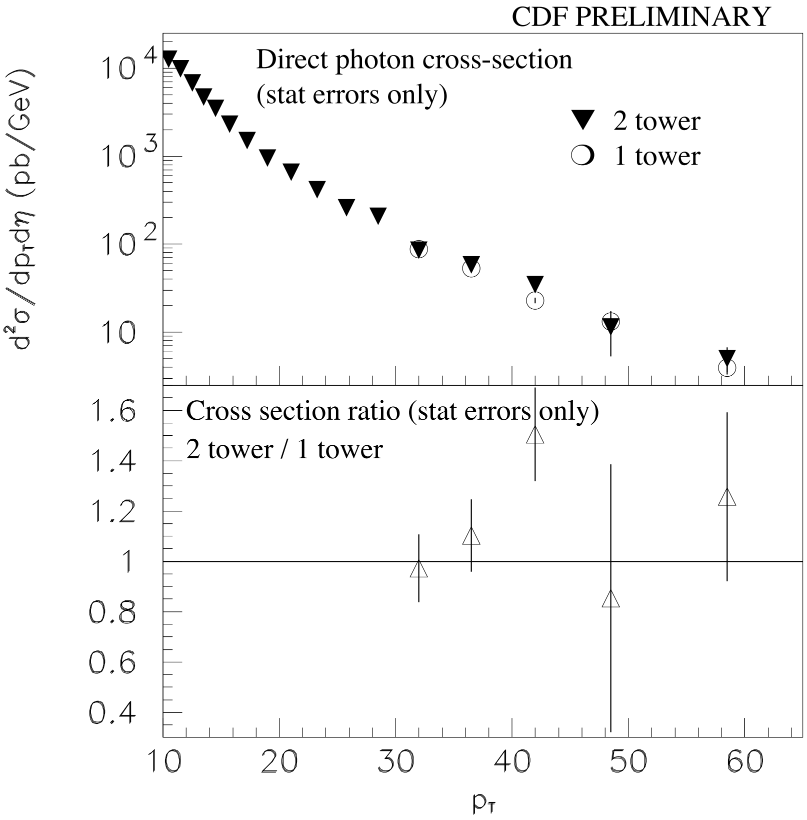

Figure 10.1: 1 tower and 2 tower cross section comparison. The top plot shows the absolute cross section measurement for the two datasets as a function of p_T. The lower plot shows the ratio of the two measurements in the p_T region of overlap. Only statistical errors are shown.

10.2 Error comparison with conventional CDF measurements

As noted in section 2.4, photon measurements at CDF traditionally rely upon non-conversion events from various photon triggers. These measurements use the CES and CPR chambers to distinguish the single photon signal from the multi-photon meson decays, so we refer to this method as the CES-CPR measurement. CDF has recently submitted the Run Ib CES-CPR photon cross section measurement to Physical Review D [15], and this is the measurement to which we compare our result. We first compare the precision of the conversion measurement with the CES-CPR measurement, and then we compare the measurements themselves to theory.

The statistical and systematic errors of the two CDF measurements versus p_T are shown in Figure 10.2. The CES-CPR measurement extends to 120 GeV, whereas the conversion measurement cuts off at 65 GeV. This illustrates one of the advantages of using non-conversion events: at high p_T, where the cross section is small, adequate statistics are still available if one does not pay the price of the conversion probability.

The sudden improvement in the statistical errors of both measurements around 30 GeV is due to the turn on of the 23 GeV photon trigger. For the conversion measurement the improved statistics is due to the recovery of the 1 tower events which are favored at high p_T. The statistics of the CES-CPR measurement improve because the low p_T photon triggers are prescaled by a factor of 80, whereas the high p_T triggers are not.

At the lowest p_T the conversion measurement has a clear statistical advantage over the CES-CPR measurement. This is due to the greater separation power of the E/p background subtraction compared to the CES-CPR background subtraction. At high p_T the signal purity of the data approaches 80%, so having a superior background subtraction is not as important in this region.

For both CDF measurements the systematic errors dominate over the statistical errors for most of the p_T spectrum. The total systematic error of the CES-CPR measurement is much smaller than the error on the conversion measurement. This is due to the large normalization error on the conversion measurement that results from the error on the total conversion probability.

Also shown in Figure 10.2 are the systematic errors if the normalization errors due to the integrated luminosity and the conversion probability are removed. The remaining errors could affect the shape of the cross section as a function of p_T, so we refer to this error as the p_T dependent error. The conversion measurement has a somewhat smaller p_T dependent error than the CES-CPR measurement, meaning that the shape of the cross section is measured more precisely by the conversion measurement.

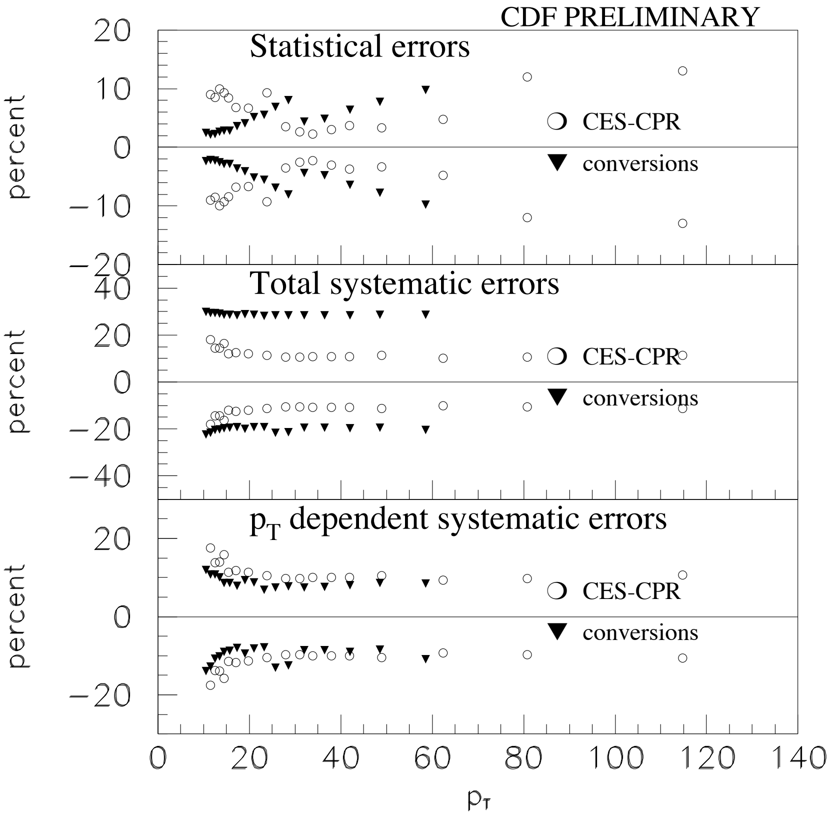

Figure 10.2: Statistical and systematic error comparison of the conversion cross section measurement with the CES-CPR measurement. The top plot shows the statistical errors of the two measurement. The middle plot shows the total systematic errors of the two measurements. The bottom plot shows the systematic errors after removing the normalization errors due to the luminosity and the total conversion probability.

10.3 Cross section comparison with theory

In Figure 10.3 we plot the conversion cross section measurement along with the CES-CPR cross section measurement and the NLO QCD calculation. The conversion cross section is also listed in Tables 10.1 and 10.2. The theory curve is taken from the authors of reference [27]. The calculation uses the CTEQ5M parton distribution functions, and the renormalization, factorization, and fragmentation scales have been set to the p_T of the photon. This calculation takes into account the suppression of the bremsstrahlung diagrams due to the isolation cut on the photon. In the lower half of Figure 10.3 the measurements are shown as (data-theory)/theory.

The CES-CPR measurement and the conversion measurement agree with each other both in shape and in normalization. The good agreement on the normalization is somewhat accidental, however, since the conversion measurement suffers from a large (+27%/-17%) normalization uncertainty due to the error on the conversion probability.

Nevertheless, both techniques give a precise measurement of the shape of the cross section as a function of p_T, and the measured shapes also agree well. This agreement is remarkable, since the two techniques have little in common with each other. The two measurements use independent data samples, independent background subtraction techniques, and have different acceptances, efficiencies, and systematics.

It is clear from Figure 10.3 that the two cross section measurements have a different shape from that predicted by the next-to-leading order QCD calculation. At low p_T, the measurements see an excess of about 30%, and at high p_T a deficit of about 25%. This shape difference can not be removed by changing the measurements within their systematic errors, or by recalculating the QCD prediction with a different renormalization or factorization scale. Since the two measurements agree well on the shape of the cross section, this is strong evidence that fundamental improvements in the calculation are needed to explain the data.

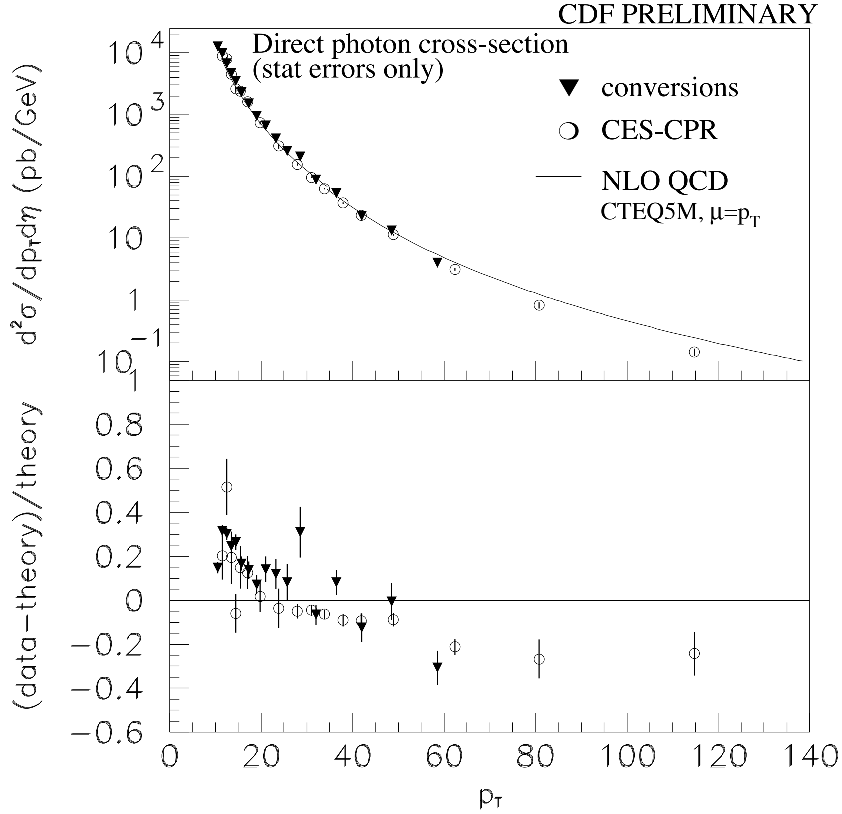

Figure 10.3: The isolated direct photon cross section. The result of the conversion technique is compared with CES-CPR and theory. The theory curve is from the authors of reference [27], and uses the CTEQ5M parton distribution functions with the all scales set to the p_T of the photon. Only the statistical error bars are shown. The CES-CPR measurement has a systematic uncertainty of ±10%, while the conversion measurement has a systematic uncertainty of +30%/-20%.

p_T (GeV)	$\langle p_T \rangle$ (GeV)	$\mathcal{A} \cdot \epsilon$	N_{signal}	$d\sigma/dp_T d\eta$ (pb/GeV)	stat error (%)	sys error (%)	NLO QCD (pb/GeV)
10-11	10.5	0.067	7152.3	12590	2.2	+30+/-22	10968
11-12	11.5	0.094	7761.2	9771	2.1	+29/-22	7433.6
12-13	12.5	0.106	6110.5	6773	2.2	+29/-20	5202.8
13-14	13.5	0.109	4319.7	4659	2.6	+29/-20	3743.4
14-15	14.5	0.108	3194.5	3483	2.9	+29/-20	2757.5
15-16.5	15.7	0.105	3059.3	2289	2.8	+29/-20	1962.5
16.5-18	17.2	0.096	1846.40	1509	3.5	+28/-19	1328.3
18-20	18.9	0.086	1391.2	950	4.1	+29/-20	887.6
20-22	20.9	0.077	862.9	658	5.1	+29/-19	577.2
22-24.5	23.2	0.068	596.3	413	6.0	+28/-19	369.3
24.5-27	25.7	0.063	344.6	258	7.7	+28/-22	238.4
27-30	28.3	0.056	272.2	207	8.8	+28/-21	157.9
30-34	31.9	0.047	135.9	85.9	13.5	+28/-21	94.6
34-39	36.3	0.041	101.4	58.5	14.4	+28/-21	49.1
39-45	41.6	0.036	63.9	34.5	18.7	+28/-22	26.2
45-52	48.1	0.032	21.7	11.4	53.3	+28/-21	13.4
52-65	57.8	0.030	16.6	5.0	33.5	+29/-23	5.7

Table 10.1: Summary of the 8 GeV conversion cross section measurement. This dataset has an integrated luminosity of $73.6pb^{-1}$. $\Delta\eta$ is 1.8, and the effective conversion probability, which is not included in the acceptance × efficiency shown here, is 6.40%. The NLO QCD theory was calculated by the authors of reference [27], and uses the CTEQ5M parton distribution functions with all scales set to the p_T of the photon.

p_T (GeV)	$\langle p_T \rangle$ (GeV)	$\mathcal{A} \cdot \epsilon$	N_{signal}	$d\sigma/dp_T d\eta$ (pb/GeV)	stat error (%)	sys error (%)	NLO QCD (pb/GeV)
30-34	31.9	0.212	723.0	88.4	4.8	+28/-19	94.6
34-39	36.3	0.220	564.3	53.1	5.3	+28/-19	49.1
39-45	41.6	0.238	315.5	22.9	7.4	+28/-20	26.2
45-52	48.1	0.250	224.9	13.3	8.5	+29/-19	13.4
52-65	57.8	0.261	130.5	4.0	11.3	+29/-21	5.7

Table 10.2: Summary of the 23 GeV conversion cross section measurement. This dataset has an integrated luminosity of $83.7 pb^{-1}$. $\Delta\eta$ is 1.8, and the effective conversion probability, which is not included in the acceptance × efficiency shown here, is 6.40%. The NLO QCD theory was calculated by the authors of reference [27], and uses the CTEQ5M parton distribution functions with all scales set to the p_T of the photon.

Chapter 11

Conclusions

We have developed a new technique for studying prompt photons at hadron colliders based on inner detector conversions, and applied it to measure the isolated direct photon cross section. The final result of our measurement is shown in Figure 10.3 and Tables 10.1 and 10.2. The power of the conversion method lies primarily in the E/p background subtraction, which achieves better signal separation than conventional methods. The greatest weakness of the conversion method is the sensitivity of the final cross section measurement to the total conversion probability. The large uncertainty on the conversion probability leads to an error of $+27\%/-17\%$ on the normalization of the cross section measurement, which is the dominant error in the analysis.

Another weakness of the conversion technique is the lack of a sophisticated CTC simulation which could model the unusual tracking systematics of conversions. Our simple simulation is not able to predict the p_T biases associated with conversion reconstruction, and this leads to E/p fits with low confidence levels in some p_T bins. We have adopted a systematic error on the background subtraction which is conservative enough to account for these shortcomings. This systematic is only important at low p_T, so its quantitative effect on the final result is small over much of the kinematic range. However, since the background subtraction plays a crucial role in all photon measurements, it is unsatisfying to have less than perfect fits, no matter how small the consequences. Future photon measurements with conversions would benefit greatly from a more detailed simulation.

The conversion technique results in a photon cross section measurement which agrees with previous measurements. Both the conversion measurement and the conventional measurements give precise information on the shape of the cross section as a function of p_T, and the measured shapes agree. The agreement is notable because the two methods have little in common with each other. This makes it unlikely that the measurements suffer from unknown systematic errors. Therefore, the poor agreement between data and theory is most likely due to shortcomings in the calculations. This conclusion has also been reached by many other authors [12], [23],[24].

The Tevatron collider and CDF have recently completed major upgrades with the aim of collecting a dataset 20 times larger than the current one within two years. CDF has replaced its entire central tracking system, with a new central drift chamber and a greatly expanded silicon vertex detector. The new inner detector represents about three times as much material as the previous inner detector, meaning that the conversion probability will be much larger in the new data. Consequently the conversion technique should become more powerful in the near future.

Bibliography

[1] www.cteq.org

[2] V.N. Gribov and L.N Lipatov, *Deep inelastic E P scattering in perturbation theory*, Sov. J. Nucl. Phys. **15** 438 (1972). V.N. Gribov and L.N Lipatov, *E+ E- pair annihilation and deep inelastic E P scattering in perturbation theory*, Sov. J. Nucl. Phys. **15** 675 (1972). G. Altarelli and G. Parisi, *Asymptotic freedom in parton language*, Nucl. Phys. **B 126** 298 (1977). Y.L. Dokshitzer, *Calculation of the structure functions for deep inelastic scattering and E+E- annihilation by perturbation theory in quantum chromodynamics*, Sov. Phys. JETP **46** 641 (1977).

[3] D.J. Gross and F. Wilczek, *Ultraviolet behavior of non-abelian gauge theories*, Phys. Rev. Lett. **30** 1343 (1973). H.D. Politzer, *Reliable perturbative results for strong interactions?*, Phys. Rev. Lett. **30** 1346 (1973).

[4] P.M. Stevenson, *Optimized perturbation theory*, Phys. Rev. D **23** 2916 (1981). H.D. Politzer, *Stevenson's optimized perturbation theory applied to factorization and mass scheme dependence*, Nucl. Phys. B **194** 493 (1982). P.M. Stevenson and H.D.Politzer, *Optimized perturbation theory applied to factorization scheme dependence*, Nucl. Phys. B **277** 758 (1986).

[5] E. Annassontzis *et. al.* (R806 collaboration), *High p_T direct photon production in pp collisions*, Z. Phys. **C 13** 277 (1982).

[6] M Bonesini *et. al.* (WA70 collaboration), *Production of high transverse momentum prompt photons and neutral pions in proton-proton interactions at 280 GeV/c*, Z. Phys. **C 38** 371 (1988).

[7] C. Albajar *el. al.* (UA1 collaboration), *Direct photon production at the CERN proton-antiproton collider*, Phys. Lett. **B 209** 385 (1988).

[8] A.L.S. Angelis *et. al.* (R110 collaboration), *Direct photon production at the CERN ISR*, Nuc. Phys. **B 327** 541 (1989).

[9] E. Anassontzis *et. al.* (R807/AFS collaboration), *High p_T photon and π^0 production, inclusive and with a recoil hadronic jet, in pp collisions at $\sqrt{s} = 63\,GeV$*, Sov. J. Nuc. Phys. **51** 5 (1990).

[10] J. Alliti *el. al.* (UA2 collaboration), *A measurement of the direct photon producution cross section at the CERN $p\bar{p}$ collider*, Phys. Lett. **B 263** 544 (1991).

[11] G. Ballocchi *et. al.* (UA6 collaboration), *Direct photon cross sections in proton-proton and antiproton-proton interactions at $\sqrt{s} = 24.3\,GeV$*, Phys. Lett. **B 436** 222 (1998).

[12] L. Apanasevich *el. al.* (E706 collaboration), *Evidence for parton k_T effects in high p_T particle production*, Phys. Rev. Lett. **81** 2642 (1998).

[13] B. Abbott *el. al.* (D0 collaboration), *The isolated photon cross section in $p\bar{p}$ collisions at $\sqrt{s} = 1.8\,TeV$*, Phys. Rev. Lett. **84** 2786 (2000).

[14] V.M. Abazov *el. al.* (D0 collaboration), *The ratio of isolated photon cross sections in $p\bar{p}$ collisions at $\sqrt{s} = 630\,GeV$ and $1800\,GeV$*. Phys. Rev. Lett. **87** 251805 (2001).

[15] D. Acosta *el. al.* (CDF collaboration), *Comparison of the isolated direct photon cross sections in $p\bar{p}$ collisions at $\sqrt{s} = 1.8\,TeV$ and $\sqrt{s} = 0.63\,TeV$*, FERMILAB-PUB-01-390-E, hep-ex/0201004 (2001).

[16] D. Partos, *Measurement of the $\sqrt{s}$ dependence of isolated direct photon production in proton-antiproton collisions*, Ph.D thesis, Brandeis University (2001).

[17] U. Baur, *el. al.*, *Report of the working group on photon and weak boson production*, hep-ph/0005226 (2000).

[18] See, for example, K. Ackerstaff *et. al.* (OPAL collaboration), *Measurement of the quark to photon fragmentaion function through the inclusive production of prompt photons in hadronic Z^0 decays.* Eur. Phys. J. **C 2** 39 (1998).

[19] L. Bourhis, M. Fontannaz, and J.Ph. Guillet, *Quark and gluon fragmentation functions into photons*, Eur. Phys. J. **C 2** 529 (1998).

[20] see, for example, D. Buskulic *et. al.*, *Inclusive production of neutral vector mesons in hadronic Z decays*, Z. Phys. **C 69** 379 (1996).

[21] D. Buskulic *et. al. First measurement of the quark-to-photon fragmentation function*, Z. Phys. **C 69** 365 (1996).

[22] P. Aurenche, A. Douri, R. Baier, M. Fontannaz, and D. Schiff, *Prompt photon production at large p_T in QCD beyond the leading order*, Phys. Lett. **B 140** 87 (1984). P. Aurenche, R. Baier, M. Fontannaz, and D. Schiff, *Prompt photon production at large p_T scheme invariant QCD predictions and comparison with experiment*, Nucl. Phys. **B 297** 661 (1988).

[23] L. Apanasevich *et. al.* *k_T effects in direct-photon production*, Phys. Rev. **D 59** 074007 (1999).

[24] H.L. Lai and H. Li, *Origin of the k_T smearing in direct photon production*, Phys. Rev. **D 58** 114020 (1998).

[25] P. Aurenche, M. Fontannaz, J.Ph. Guillet, B. Kniehl, E. Pilon, and M. Werlen, *A critical phenomenological study of inclusive photon production in hadronic collisions*, Eur. Phys. J. **C 9** 107 (1999).

[26] H. Baer, J. Ohnemus, and J.F. Owens, *Next-to-leading logarithm calculation of direct photon production* Phys. Rev. **D 42** 61 (1990). E. Berger and J. Qiu, *Calculations of prompt-photon production in QCD*, Phys. Rev. **D 44** 2002 (1991). L.E. Gordon and W. Vogelsang, *Polarized and unpolarized isolated prompt photon production beyond the leading order*, Phys. Rev. **D 50** 1901 (1994).

[27] M. Glöck, L.E. Gordon, E. Reya, and W. Vogelsang, *High-p_T photon production at $p\bar{p}$ colliders*, Phys. Rev. Lett. **73** 388 (1994).

[28] W. Vogelsang and A. Vogt, *Constraints on the proton's gluon distribution from prompt photon production*, Nucl. Phys. **B 453** 334 (1995).

[29] J. Huston, *et. al.*, *Study of the uncertainty of the gluon distribution*, Phys. Rev. **D 58** 114034 (1998)

[30] W. Trischuk and A. Warburton, *A parametrisation for the Run 1 low p_T CTC track finding efficiency*, CDF internal note 4423 (1997).

[31] W. J. Taylor, K. Byrum, and P. K. Sinervo, *Run 1b Level 2 CEM_8_CFT_7_5 and XCES electron trigger efficiencies*, CDF internal note 4691 (1998).

[32] F. Abe *el. al.* (CDF collaboration), *Measurement of $\sigma B(W \rightarrow e\nu)$ and $\sigma B(Z^0 \rightarrow e^+e^-)$ in $p\bar{p}$ collisions at $\sqrt{s} = 1.8\ TeV$*, Phys. Rev. Lett. 76 3070 (1996).

[33] A. Beretvas, A. Bhatti, P.F. Derwent, J.R. Dittman, B. Flaugher, and W.K. Sakumoto, *Event z vertex cut efficiency as a luminosity correction for Run Ib*, CDF internal note 5066 (1999).

[34] R.W. Kadel, *On the thickness of the CTC inner support cylinder*, CDF internal note 2804 (1994).

[35] R.W. Kadel, *Determination of the CDF inner detector materials using conversion electrons*, CDF internal note 2899 (1994).

[36] K. Byrum, *Luminosity for the Run1b electron binary dataset*, CDF internal note 5001 (1999).

[37] A. Gordon, *Measurement of the W boson mass with the Collider Detector at Fermilab*, Ph.D thesis, Harvard University (1998).

[38] F.A. Berends and R. Kleiss *Hard photon effects in $W^{\pm}$ and Z^{0} decay.*, Z. Phys. **C 27** 365 (1985).

[39] Young-Kee Kim, *Update on the momentum scale determination for the Run 1b W mass measurement*, CDF internal note 4757 (1998). Young-Kee Kim, *Momentum scale determination with Upsilon(1s) mass for the Run 1b W mass measurement.*, CDF internal note 4899 (1999).

[40] Affolder, T. *et. al.*, *Measurement of the W boson mass with the Collider Detector at Fermilab*, Phys. Rev. **D 64** 052001 (2001).

[41] Masa Tanaka, *personal communication.*

[42] R. Harris, *Measurement of eta/pi0 from isolated decays into two photons*, CDF internal note 1472 (1991).